Processing and Characterisation of Ruthenium Aluminium Alloys

by

ANIL BORAH

Department of Mechanical Engineering

Indian Institute of Technology Guwahati, INDIA

July, 2006

In memory

Of

My father

CERTIFICATE

It is certified that the work contained in this thesis entitled "**Processing and Characterisation of Ruthenium Aluminium Alloys",** *presented by* ***Mr. Anil Borah****, a student in the* ***Department of Mechanical Engineering, Indian Institute of Technology Guwahati****, India, for the award of degree of* ***Doctor of Philosophy*** *has been carried out under our supervision and that, this work has not been submitted elsewhere for a degree.*

(**Dr. P.S. Robi**)
Department of Mechanical Engineering
Indian Institute of Technology Guwahati
Guwahati – 781039 INDIA

(**Dr. A. Srinivasan**)
Department of Physics
Indian Institute of Technology Guwahati
Guwahati – 781039 INDIA

List of Figures

List of Tables

Acknowledgements

Perhaps there is not enough space and time to thank many individuals who at some point or another helped me in the completion of this thesis.

At the very inception, I am very much grateful to my thesis advisors Dr. P. S. Robi and Dr. A. Srinivasan for their patient guidance throughout my studies at IIT Guwahati. Their constant advice and encouragement made me confident enough to complete this work. Working with them was always a pleasure especially in tackling problems that were faced during the course of investigations with new ideas and solutions.

I sincerely acknowledge the Doctoral Committee chaired by Dr. U.S. Dixit and the members Dr. J.B. Barua and Dr. Dr. A.L. Muzumdar for spending their valuable time and energy in reviewing this thesis. The undersigned must also acknowledge all the faculty members of the Mechanical Engineering Department, IITG for their valuable suggestions and encouragements during this work.

I would like to convey grateful acknowledgement to Indian Space Research Organisation (ISRO), Government of India for the financial support under the RESPOND programme. The undersigned gratefully acknowledge the help received from Materials Characterisation Division, ISRO in carrying out the compression testing of the samples.

I am highly indebted to Mr. D.K. Sarma, Assistant Workshop Superintendent and all the staff of the workshops for extending their help in fabrication of the components related to the experimental set-ups for this work.

During my work, I had opportunity to work with a group of dynamic friends and colleagues. The undersigned is very much thankful for the cooperation and assistance received from the Project Associates Mr. Pranta Pratim Singha and Mr. Indrajit Talukdar.

I sincerely acknowledge the assistance received from Mr. Rituraj Saikia in sample preparation, cold compaction and hardness testing in the Material Science Laboratory. I would like to pay my sincere and heartfelt gratitude to Late Ramanada Das, who left us forever before completion of this work. I must sincerely acknowledge

him for his help. I acknowledge the help received from Mr. Bhanu Shankar Rajkhowa in the laboratory.

I am also thankful to Mr. Sidanada Sarma for carrying out XRD analysis reported in this work. Working with him has always been a source of new ideas. Many thanks to Mr. Chandan Borgohain and Mr. Kula Kamal Senapati for extend out their valuable time and energy in the SEM laboratory. My sincere thanks to Mr. Pranab Goswami and Mr. L.N. Sarma for lending me the rectifier circuits for the D.C Motor used in the attrition ball mill. Many a time Mr. Goswami also helped me in repairing electronic components.

I also wish to acknowledge the discussion and collaborations with Dr. S.K. Kakoty, Dr. D.C. Chakraborty, Dr. A.K. Dass, Dr. N. Chandiramani and Dr. P.K. Jha during this work. Several individuals in the technical and administrative staff at IITG deserve my sincere thanks and gratitude.

Finally, I thank my family. Most especially I wish to acknowledge my wife and best friend, Niva, for her love and support.

I consider myself privileged and fortunate to work in the Indian Institute of Technology Guwahati (IITG).

(ANIL BORAH)

Abstract

There is an ever increasing demand for materials usable at high temperatures and under extreme environmental conditions. The power generation sectors and aerospace industries are fostering the development of alternative materials with lower density, high strength and high application temperature. Material development coupled with improvements on the processing technology efforts of the last two decades has resulted in the availability of multi-component alloys with good high-temperature strength and oxidation resistance. However, it seems that the potential of the conventional materials has been exploited to the maximum extent and hence an intensified research is required in this area of newer materials development.

Intermetallic alloys have been identified as an emerging class of materials and have been the subject of studies for many years as the potential replacement for the existing high-temperature materials. A large number of intermetallic alloys such as Ni-Al based alloys, Ti-Al based alloys, Fe-Al based alloys, etc. has already been identified for high-temperature applications. However, the lack of a good combination of room temperature ductility and toughness together with high temperature strength and corrosion resistance are some of the major barriers for their application as high temperature structural materials. Hence, the successful development of newer materials based on intermetallic alloys depends on the improvement of these properties.

Though intermetallic ruthenium aluminide (RuAl) phase was identified in 1960, its properties amenable for high temperature structural applications have been unveiled only in the early nineties. These reports on the properties of Ru-Al alloys triggered the scientific research on RuAl. Ru-Al alloys exhibit a combination of high ductility and toughness, high strength and corrosion resistance at high temperatures. The intermetallic phase RuAl has a very high melting point (≈ 2060 °C). Due to these basic properties, RuAl is considered as a high-temperature structural material. However, there exist quite a few disagreements in the currently available binary and ternary phase diagrams of this alloy system. Past research activities were directed mostly on the Al rich side of the Ru-Al phase diagram, leaving the Ru rich side of the phase diagram relatively unexplored.

The large difference in the melting points of ruthenium (2334 °C) and aluminium (660 °C) and the high vapour pressure of aluminium often lead to aluminium losses with porosities in Ru-Al alloys produced by conventional solidification from the melt. On the other hand, the high enthalpy release in self-propagating high-temperature synthesis results in porous and inhomogeneous Ru-Al alloys. Therefore it appears that both these methods have failed to deliver homogeneous, porosity-free, and single-phase RuAl alloys.

In the present study, processing of Ru-Al alloys by a sequence of attrition milling of elemental powders, cold compaction and sintering has been reported. A comparison of the microstructure obtained for the Ru-Al alloys processed by solidification route has also been made. Six alloy compositions belonging to Ru-Al, Ru-Al-Ni and Ru-Al-Co alloy systems were processed and characterised by both the routes. The milled alloy powders that could be cold compacted were sintered. The alloys prepared by solidification route were heat treated at high temperature. The structure, microstructure, hardness (overall and microhardness of constituent phases) and temperature dependence of the electrical resistivity of these alloys were studied as a part of the present investigations. Attempts were also made to analyse the correlation between microstructure and properties in these alloys. Currently available ternary partial isothermal phase diagrams have been discussed with respect to the annealing temperature employed in the case of cast alloys.

A survey of the literature shows that (1) only a few investigations have been performed on milling characteristics of Ru-Al alloys, (2) the ternary alloy compositions reported in this work have not been investigated earlier, and (3) this is the first attempt to process the above alloys by powder metallurgy as well as casting techniques, thereby providing a means to compare the alloys prepared by both the routes.

The thesis is arranged in seven chapters. Chapter 1 would serve as a general introduction to the contents of the thesis. Chapter 2 is devoted to a literature review on topics related to this thesis work. Chapter 3 contains the details of the experimental techniques/procedures used in the present investigations including the design and fabrication of the experimental set-ups. Chapters 4 deals with the details of the experimental studies made on the $Ru_{47}Al_{53}$ alloy system. Similarly, chapters 5 and 6 discuss the experimental results of the Ru-Al-Ni and Ru-Al-Co alloy systems,

respectively. Chapter 7 would be the concluding chapter where an attempt is made to summarise the work done in this thesis and a brief mention of the future scope / extensions of the work.

Contents

Chapter 1

Introduction

The search for newer materials for use as components of high temperature gas turbines has led to the development of super alloys and intermetallic alloys since the beginning of the twentieth century. The motivation behind this trend stems from the fact that operation of the components at higher temperature leads to the development of higher efficiency engines, where as the ability to operate at high-temperatures is limited by the materials capable of withstanding the extreme mechanical and environmental conditions prevailing inside the engine.

Research in the area of high-temperature materials development started with the invention of nickel-chromium alloy in 1906. In the 1940s, nickel based super alloy operating at a temperature of 800 °C was introduced in the gas turbine engine for the first time. A number of alloys capable of withstanding higher temperatures were developed during the next two decades. The main thrust of these research activities was on understanding the material behaviour and development of new manufacturing techniques. The major developments (in chronological order) achieved until the late 1970s were the invention of stainless steels, hot work die steels, super alloys based on iron, cobalt and nickel, and development of new manufacturing techniques like directional solidification, investment casting and single crystal component casting. By the late 1980s, single crystal nickel based super alloys with operation temperatures of 1000 °C were commercially available. It was immediately apparent that the operating temperature of nickel based super alloys has almost reached its saturation limit.

Development of intermetallic materials for very high temperature applications was taking place in parallel. The materials investigated were mainly aluminides of nickel, titanium, iron and cobalt. These materials exhibited exceptionally high strength along with good ductility at high temperatures. However, the applications of these materials in engine components were impeded due to their very poor room temperature ductility and toughness. Numerous studies have been carried out during the past three decades to improve the ductility of these materials at ambient temperatures. The research efforts on improving the ductility of intermetallic alloys was focussed on

understanding the structural changes in these materials by ternary and quaternary solute additions, development of phase diagrams, improving the microstructure of these materials by proper heat treatment apart from development of new alloy systems. Though a better understanding of the phase diagrams and material behaviour could be achieved, the ambient temperature ductility of these materials could not be improved much. Presently, the use of these materials is confined to thermal barrier coating applications on the existing components. This has improved the operating temperatures of these components made of super alloys.

Research findings in the 1990s identified ruthenium aluminde (RuAl) as a promising material for structural applications at temperatures possibly beyond the capability of existing super alloys. This intermetallic alloy exhibits the unusual combination of properties like very high melting point, high strength at ambient and elevated temperatures, useful room temperature ductility and toughness, good oxidation resistance at elevated temperatures and high corrosion resistance to very severe chemical environment. Though RuAl was first identified as a phase in 1960s, its mechanical properties were highlighted in 1991. In spite of these promising properties, it took around another five years for the research community to gear up for active research in the development of this material. The last few years witnessed a growing interest in characterising the microstructure and properties of RuAl alloys, both by alloy addition and heat treatment. The binary Ru-Al and ternary Ru-Al-X (X = Co, Ni, Mo, B, etc.) alloys are being currently investigated.

Attempts to increase the ductility of intermetallic alloys have been the main thrust. Incorporation of ductile phases into fine composite microstructure, ductile phase strengthening in eutectic structures by engineering the microstructure with heat treatment, dispersion strengthening, solid solution strengthening by addition of substitution elements in to the matrix, etc are some of the methodologies employed to achieve the above goal. Some of these techniques have also been attempted in the development of ruthenium aluminide alloys with enhanced properties. The present trend is to develop ternary alloys based on the binary Ru-Al alloy system for reasons given below

Ruthenium, classified under the platinum group of material, is a costly material. The financial limitation of academic researchers and scientists to carry out basic research using ruthenium is one major bottleneck. Attempts are being made to

substitute ruthenium in the RuAl phase by elements like nickel, cobalt, molybdenum, etc with the intention of reducing the cost of these materials with out significantly affecting the properties. The lack of a viable or standard technique of processing ruthenium aluminide alloy has also dampened the enthusiasm created by the optimistic properties exhibited by this material. A technique of processing of this material so as to obtain a defect free component still remains a challenge. The inherent processing defects are due to the high melting point of ruthenium (~ 2334 °C), very high enthalpy of alloy formation (~ -124.1 ± 3.3 KJ/mol), the requirement of special refractory crucibles, large difference in the melting points of ruthenium and aluminium, etc. All the above factors contribute to the deterioration in mechanical properties of the alloys processed by solidification route.

The inherent advantages of powder metallurgy technique of processing over the solidification route led to a few attempts to process Ru-Al and Ru-Al-Ni alloy powders by powder metallurgy technique. The results reported by different authors were inconsistent. This may be due to difference in the equipments and process parameters used for mixing and subsequent solid state alloying during the processing. However, the successful processing of sintered product by powder metallurgy technique is yet to be reported. The very high internal energy of the ball milled powder mixture results in a highly reactive mixture, which ignites when exposed to ordinary air. The low diffusivity of ruthenium at typical sintering temperatures of ~1200 °C, results in improperly sintered product. This necessitates very high sintering temperatures along with a controlled (inert) atmosphere.

In spite of the above research efforts, exhaustive and complete phase diagrams for these materials covering the entire temperature and composition regions have not yet been evolved. The lack of consistency in the microstructure and compositions reported in Ru-Al alloy systems by different authors, shows that a systematic and exhaustive study of different parts of the binary and ternary phase diagrams of the Ru-Al system has to be carried out.

The research finding point out a few inconsistencies in the results mainly related to the microstructure of these alloys. Close observation of these will reveal that the microstructure obtained in these alloys is strongly influenced by the processing technique adopted. A viable processing technique by which these materials can successfully be produced needs to be identified. It is therefore necessary to investigate

the microstructural evolution in ruthenium aluminde alloys processed by different techniques and its correlation with its properties.

The present study has therefore been undertaken with the objectives of processing ruthenium aluminide (RuAl) alloys by powder metallurgy (P/M) technique as well as by solidification technique (ST), investigate and compare the microstructure and properties. Since ternary alloying and microstructural control are practical routes of further alloy development, it was also planned to partly replace ruthenium by nickel and cobalt.

Organisation of the thesis

The outline of this thesis is given below:

Chapter –1 introduces in brief the importance and evolution of the present work.

Chapter-2 summarises the literature survey on the high temperature materials *viz.*, super alloys, intermetallic materials like aluminides of nickel, titanium, cobalt, etc., and binary and ternary alloys of ruthenium aluminides. The crystal structure, mechanical properties and microstructure of aluminides have been discussed with more emphasis on ruthenium-based aluminides. The processing details of ruthenium aluminides have also been discussed at the end.

Chapter –3 describes the details of the experimental set-ups and various experimental procedures used to synthesize these materials and evaluation of their microstructures, hardness properties and electrical resistivity.

The results obtained for binary Ru-Al alloy are discussed in detail in chapter-4. The extent of alloying during attrition milling of binary Ru-Al alloy has been discussed in detail in this chapter. Comparison of the microstructures obtained for binary Ru-Al alloy produced by ST and P/M techniques is also discussed in this chapter.

Chapter-5 and chapter-6 present the results obtained for ternary Ru-Al-Ni and Ru-Al-Co alloys, respectively. The various phases for the different alloy compositions in these systems processed by both the techniques are also presented and discussed in the respective chapters.

The major conclusions drawn from the study and future scope for investigation in the related area are listed in chapter 7.

Chapter – 2

Literature survey

2.1 Introduction

The last 60 years saw an increased research effort in the area of high temperature materials development. The development of new materials and application of these materials went hand in hand, especially in areas of power generation, chemical industry, aircraft and space applications. The quest for development of materials, that can perform at very high temperatures stems from the fact that both thermodynamic efficiency and power of any heat engine generally increases with increase in the highest temperature of the thermodynamic cycle. For power generation as well as aero-engines, gas turbines are being used where the ability to operate at high-temperatures is dependent on the materials, which can withstand very complex mechanical and environmental conditions. Continuous research efforts over the past 60 years at development of newer materials for high temperature structural applications led to nickel, iron and cobalt based super alloys as well as several intermetallic alloys. During the various stages of alloy development several manufacturing techniques evolved which could control both the microstructure and properties of these materials. Creep resistance, thermal fatigue resistance, high temperature oxidation and corrosion resistance, high temperature strength retention, etc., are some of the important material properties for high temperature applications. These properties are dependent on the microstructure of these materials, which in turn depends on the manufacturing technique adopted.

This particular chapter summarizes the structure, properties, strengthening theories, and manufacturing techniques of some of the existing high temperature materials. Structure and properties of super alloys for gas turbine applications as well as intermetallic alloys with special emphasis on ruthenium aluminide alloys have been highlighted.

2.2 Super alloys

Super alloys are group of materials consisting of nickel, iron-nickel, and cobalt-based materials that exhibit high strength and stability at temperatures up to 85% of their melting points. The primary areas of application for such alloys are the gas turbine engine, both aircraft and power generation. Applications of these materials include compressor blades, vanes, spacers, discs, shafts, etc. The three groups of super alloys- Iron-nickel, nickel, and cobalt-base, which are further subdivided into cast and wrought alloys.

2.2.1 Nickel based super alloys

The development of nickel-based super alloys has been one of the major successes in materials development for high temperature structural use. The first nickel-based alloy developed was a nickel-chromium alloy in 1906 [1], which exhibited good oxidation resistance and was particularly useful for electrical heating elements. During 1920s it was established that this alloy with 20% chromium exhibited the best balance of oxidation resistance and strength along with better creep resistance than any other engineering materials available at that time. By 1929, a significant increase in creep resistance was observed in Ni-20%Cr alloy by the addition of small amounts of aluminium (Al) and titanium (Ti).

These metallurgical improvements led to the application of the first set of alloys: Nimonic 75 and Nimonic 80, in the gas turbine engines at an operating temperature of 800 °C by Frank Whittle in 1941, for overcoming the major drawback of creep failure. By that time it was established that alloys having face centred cubic (*fcc*) structure offered good creep resistance, which was linked, to the low stacking fault energy (SFE) favouring extended dislocation and inhibiting dislocation climb. The carbide network at the grain boundary due to addition of titanium along with carbides of chromium at the grain boundary regions inhibited grain boundary sliding during creep. Aluminium (Al) addition produced significant hardening by precipitation of Ni_3Al based on γ', which was exploited in Nimonic 80A. Substitution of Co for some of the nickel in Nimonic 90 raised the solubility temperature of γ' from 880 °C to 960 °C [2].

The key elements required for high temperature structural materials around 65 years ago was having a matrix of γ-nickel solid solution which was strengthened by precipitation of coherent ordered intermetallic phase γ' $Ni_3(Al,Ti)$ by a precipitation heat

treatment together with grain boundary strengthening by titanium carbide [2]. Further improvement in the high temperature properties in these wrought alloys was achieved by increasing the volume fraction of γ' and by solid solution strengthening. Nimonic 105 alloy was later developed, where the matrix and precipitates were strengthened by the addition of 5 at.% molybdenum (Mo) and 4.7 at.% Ti , respectively. The operating temperature of the alloys could be raised from750 °C to about 900 °C by inhibiting the grain boundary sliding phenomenon by the additions of 0.015 at.% boron and 0.1 at.% zirconium in these alloys. Further improvement in the high temperature properties of these alloys was hampered by the fact that alloys containing more than 40 % γ' were found to be difficult to deform due to poor workability. Nimonic 115 and Udimet 700 represent the limiting case of development of these alloys because the high strength in these alloys posed difficulties on their processing.

The challenges, in obtaining Ni-super alloy turbine blades having more than 40 % γ' phase, like the need for hot working and provision of cooling channels for blade air-cooling were overcome by development of investment casting technique in 1960s, thereby raising the application temperature further by 50 °C [2].

The sequence of materials developed subsequent to these was the G64, B1912, B1925, IN713, IN100, IN 738, IN939 alloys. A significant development in high temperature strength retention capability was the development of Mar-M200 alloy in 1965 in which γ-nickel solid solution was strengthened by high concentration of tungsten and γ'-phase was strengthened by the additions of tantalum (Ta) or niobium (Nb) The poor ductility in this alloy was improved by the addition of 1.5% hafnium (Hf). Though the investment casting raised the operating temperature to over 950 ^{o}C, the poor creep resistance at high temperatures limited its application as turbine blade material.

Development of directional solidification technique in 1960s was able to solve the creep failure initiation at grain boundary regions when these materials were subjected to high stress at high temperatures [2, 3]. The directional solidification eliminated the grain boundaries perpendicular to the blade edges; thereby the life of the components could be increased. The grain boundary sliding which was the main mechanism of failure in directionally solidified components was overcome by the production of single crystal turbine blades in the 1970s [2, 3]. The first generation single crystal alloy SRR99 was characterised by reduced tungsten and molybdenum and

addition of rhenium. The second-generation single crystal alloy CMSX-4, having 3 at.% rhenium further increased the temperature capability by 25 °C as compared to SRR99. The third generation of these alloys contain 6 at.% rhenium and provide a further improvement in the temperature capability by 30 °C. Rhenium addition made it possible to improve the temperature capability of these alloys over 1100 °C [1, 3]. At present, new alloys have been demonstrated in engines at metal temperatures of 1130 ^{o}C, which is about 87 % of the melting point of the alloy and a far more homologous temperature than any other structural material. It appears that this achievement has reached a near saturation temperature limit for the nickel based super alloys in high temperature applications.

2.2.2 Cobalt based super alloys

Cobalt based super alloys based on ternary cobalt-chromium–tungsten and cobalt-chromium-molybdenum systems are intended for use at temperatures up to 1000 °C. Following the development of these materials in the beginning of the 20th century, addition of W and Mo in the Co-Cr alloy system were found to strengthen further. Under the trade name 'Stellite' these were found useful as cutting tool materials, hard facing for oil-well drill bits, hot trimming dies, dredging cutters, ploughshares and internal combustion engine valves and valve seats. In the 1930s and early 1940s, cobalt based alloys based on ternary Co-Cr-Mo alloy system with low carbon addition was developed for corrosion resistant and high temperature applications.

These alloys have also been used extensively in defence and commercial aircraft turbine engines as high temperature structural components [4]. The strength and ductility of these alloys are lower than the nickel based alloys. These alloys are strengthened by a combination of carbides and solid solution elements. The presence of some nickel and carbon in cobalt-based alloys not only lowers the transformation temperature but also retains the *fcc* structure from room temperatures to 985 °C. Elements like chromium, tantalum, tungsten, molybdenum and nickel contributed to the solid solution strengthening effects as well as formation of carbides in the matrix where as chromium imparted corrosion resistance.

Carbon is an important alloying element in these alloys due to the formation of carbides in the matrix and influences hardness, ductility and wear resistance. A uniform distribution of fine carbides in the cobalt alloy matrix soluble at temperatures much

higher than the service temperatures, were obtained by precipitation hardening heat treatment which retained the strength at high temperatures [4]. HS-25, HS-21, HS-31, HS-151, SM 302and SM 302 are some of the commercial alloys for applications in the range of 815 °C–1100 °C [5, 6]. High temperature strength is obtained by the combined effect of solid solution hardening and precipitation of high melting point carbides of tantalum and tungsten. Boron and zirconium also contributed to the improvement in the high temperature strength by reducing the concentration of vacancies as well as grain boundary interactions. Rupture strength of up to 100 MPa could be obtained at 990 °C for the alloy SM302 produced by investment casting.

Haynes alloys 25 and 188, MAR-M 509 have been used by industries in areas of gas turbine, industrial furnace, fasteners, cables and marine hardware applications. The development of directional solidification followed by single crystal component manufacturing made it possible the development of higher thrust jet engines operating at higher temperatures [6].

2.2.3 Nickel-iron based super alloys

Nickel-iron based super alloys are characterised by their lower cost as compared to the nickel based super alloys that makes them more preferable than other alloys in high-temperature applications [2, 6]. Iron-based super alloys evolved from austenitic *fcc* matrix that is stabilized by at least 25 at.% Ni content. Cr addition renders solid solution strengthening of the austenitic matrix and oxidation resistance. Hardening by precipitation of intermetallic phases like γ' {Ni(Al, Ti)} and γ'' (Ni_3Nb), TiC in the matrix and grain boundary strengthening by the addition of boron and zirconium resulted in significant increase in high temperature rupture life and improvement in hot ductility. Vanadium improved the hot workability and notch ductility at service temperatures where as manganese (Mn) served as deoxidiser. The properties of these materials are controlled by the solution treatment and ageing hardening parameters.

Fe-Ni-based super alloys have been classified into several groups based on their composition and the strengthening mechanism [2, 6]. The main classifications are based on either (i) those strengthened by a Ti-rich intermetallic phase (γ') and contain 25-35 wt.% Ni, (ii) Fe-rich and contains at least 40 wt.% Ni as well as higher levels of solid solution strengthening and precipitate forming elements and (iii) Fe-Ni-Co alloy system strengthened by γ' intermetallic phase.

Another two important classes of Fe-Ni based alloys contain more nickel than iron [6]. The first group of these two classes of materials contain 3 to 5 wt.% of niobium (Nb) which is precipitated as a coherent strengthening γ'' (Ni_3Nb) phase and also form carbides in presence of carbon alloy. The iron acts as catalyst for the formation of the metastable γ'' phase. The alloys also contain small amounts of Ti and Al which precipitate as γ' in the matrix. Incoloy 706 and Inconel 718 represent this class of material. Inconel 718 is one of the strong and widely used superalloy for applications up to a temperature of about 650 °C.

2.3 Intermetallics

Intermetallics are defined as "a mixture of two metallic elements in specific proportions that form a crystal structure that is different from those of the constituent elements". An intermetallic compound or phase is a chemical compound based on a definite chemical composition that exists in a fixed or narrow range around a simple stoichiometric ratio. They constitute a unique class of metallic materials having long range ordered crystal structures below a critical ordering temperature [7].

Atomic bonding in intermetallics may be partly ionic or covalent and the materials having this type of bond generally exhibit high strength and low ductility at room and elevated temperatures. The atomic bonding may also be metallic but the atoms of the constituting elements take the preferred positions in the crystal lattice. The long range ordering of crystal lattice structure in intermetallics lowers the dislocation mobility and diffusion processes that contribute high melting point, high strength at room and elevated temperatures and better environmental resistance to these materials.

Intermetallics have been a subject of study for more many years starting from the 19th century as the potential material for high temperature applications. However, the poor ductility, brittleness and low fracture toughness exhibited by these materials restrict their use in structural components. In the past, these materials were used primarily as strengthening second phases in some alloys for structural applications. The discovery of improvement in the ductility of polycrystalline Ni_3Al alloys by Aoki and Izumi [8] in 1978 by the addition of small amounts of boron, led to the investigations for developing aluminides with increased high-temperature creep strength and good low temperature ductility for possible high temperature structural use. Although there

are a large variety of intermetallics with immense diversity in crystal structures, only a small fraction of these are tested to be useful at elevated temperatures [9]. Only a few of these aluminides will be discussed in the following sub-sections.

2.3.1 Titanium Aluminides

Intermetallic alloys based on titanium aluminides exhibit low density, high elastic modulus, better mechanical properties at high temperatures, higher oxidation resistance, low density, very high tensile strength at room and elevated temperatures, high fatigue strength at elevated temperature, and high thermal conductivity. These materials are not used as a structural material due to their very poor room temperature ductility.

Figure 2.1 shows the binary phase diagram of Ti-Al alloy system [10]. Two major alloys in this system, which have been developed and studied for high temperature structural applications are α_2 (Ti_3Al) with hexagonal $D0_{19}$ structure and γ (TiAl) with tetragonal $L1_o$ structure.

The Ti_3Al phase, having a composition in the range of 23 at.% to 35 at.% of Al, is stable up to a temperature of 1180 °C. They exhibit poor ductility (ε_f < 3%) at temperature below 600 °C [10] mainly due to the absence of slip. The low mobility of < c + a > dislocations contributes to stress concentrations at grain boundaries leading to premature fracture.

Various substitutional and interstitial elements such as Nb, V, Mo and Ta are alloyed with Ti_3Al in order to stabilise the (α + β) microstructure [11]. Nb additions improve ductility as well as oxidation resistance. Mechanical properties improve with the increasing addition of Nb. These alloys exhibit higher yield strength as well as good creep resistance up to 700 °C. The most popular example of these types of alloy is super α_2 with a composition of Ti-25Al-l0Nb-3V-lMo [12].

Recent alloys of Ti_3Al developed with compositions Ti-23Al-9Nb-2Mo-2V-0.9Si (MT 752) and Ti-23Al-9Nb-2Mo-0.9Si (MT 754) exhibited improved creep behaviour in the temperature range 650-750 °C as compared to the conventional alloy IMI 834 having composition Ti-10Al-0.4Nb-0.2Mo-2Zr-2Sn-0.6Si-0.2C [13]. The MT 75X alloys have enhanced creep strength equivalent up to 90 °C rise in temperature. These alloys show potential for some applications in the temperature range of 600 °C - 700 °C.

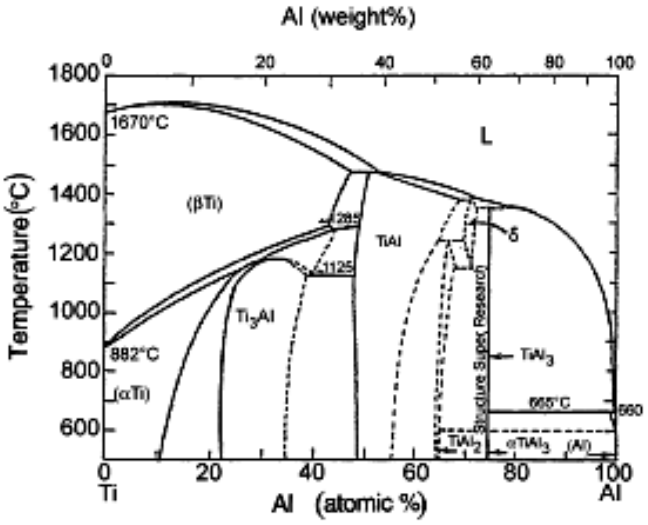

Fig 2.1: Ti-Al Phase diagram [10]

TiAl

TiAl is often designated as γ-phase having tetragonal $L1_o$ structure. TiAl is regarded as potential material for high temperature applications because of its low density, high specific strength, high specific stiffness, high temperature strength retention and better oxidation resistance. Studies [10, 14] revealed that TiAl based alloys have an extended composition range from ~ 35 at.% Al to 65 at.% Al and consists either of $\alpha_2 + \gamma$ phase mixture or the γ phase. Within the composition range of 49 at.% to 55 at.% Al, the primary phase is α. The γ-phase is formed during the phase transformation and results in the formation of lamellar structure. The variation in aluminium content between the solubility limits leads to constitutional disorder with excess Ti or Al atoms at the lattice sites. Above 53 at.% Al, single phase γ-TiAl, the solidification results in a peritectic reaction $L + \alpha \leftrightarrow \gamma$ [14]. Hence it is possible to develop alloys with different microstructures depending on the processing route and on the particular phase field chosen for the heat treatments.

The single-phase γ alloys exhibit low ductility at room temperature. The brittle to ductile transition occurs at 827 °C [14]. Single crystal TiAl shows anomalous increase in yield strength with temperature up to about 600 °C. This anomaly of positive temperature dependence results from the thermally activated cross-slip pinning. In contrast, considerable ductility and toughness can be achieved in the alloys with composition in the $(\gamma + \alpha_2)$ two-phase region as small volume fraction of α_2

enhances ductility. Reduction in the Al content (below 50%) to form α_2-Ti_3Al as a second phase in γ-TiAl results in improved ductility and fracture toughness [14]. Figure 2.2 shows the central portion of the binary Ti-Al phase diagram showing the compositional range for two-phase alloys [10]. Since the mechanical properties of TiAl based alloys are strongly dependent on the microstructure obtained, it is possible to meet the needs for the specific components by controlling their composition microstructure [15].

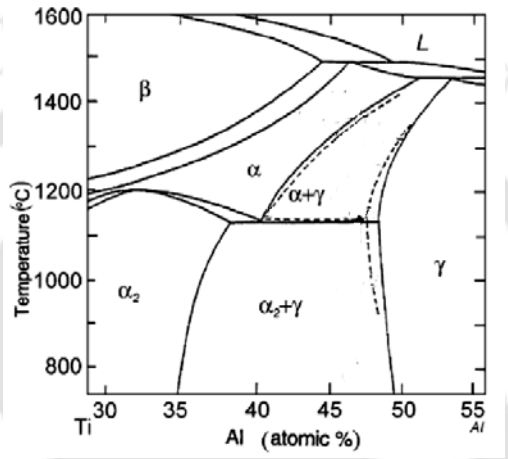

Fig 2.2: Central portion of the binary Ti-Al phase diagram showing the compositional range for two-phase alloys [10]

Oxidation resistance is observed to be independent of microstructure [11]. However, a reduction in Al content from 50 at.% to 48 at.% results in increasing the oxidation rate at 900 °C by a factor of four in binary Ti-Al alloys. Oxidation resistance of TiAl is higher than that of Ti_3Al due to its high Al content which provides a protective Al_2O_3 layer below 1000 °C, whereas at higher temperatures, complex scale formation increases the oxidation rates. Special pre-oxidation treatments as well as alloying with Nb, Ta and W improves the oxidation resistance of TiAl but at the expense of ductility.. The solubility of hydrogen in TiAl is high for hydride formation on cooling. No effects of hydrogen are observed in single-phase TiAl alloys whereas an embrittlement effect is seen in two-phase TiAl alloys containing Ti_3Al.

$TiAl_3$

TiAl possesses $D0_{22}$ crystal structure with lattice parameters $a = b = 0.3875$ nm and $c = 3.384$ nm [16]. The combination of properties such as low density (3.3

gm/cm^3), high melting point (~ 1340 °C) and good oxidation resistance makes $TiAl_3$ compound a potential material for lightweight high temperature structural applications. However, its extreme brittle nature restricts its application for structural use.

Extensive research has been carried out to change the crystal structure of $TiAl_3$ [10, 11, 15] with the aim of improving the ductility but without much success. Unlike the TiAl and Ti_3Al, $TiAl_3$ alloys do not exhibit anomalous positive temperature dependence on yield strength. $TiAl_3$ alloys deform by ordered twinning $(111)[11\bar{2}]$ and slip occurs along [110] and [100] directions [10]. (001)[110] slip and $(111)[11\bar{2}]$ twinning deformation increase the ductility slightly at elevated temperatures in this alloy. $TiAl_3$ alloys have been tried as oxidation resistant coating on Ti and TiAl based alloys. Application in thin film interconnections for microelectronic devices was reported where the $TiAl_3$ acts as a diffusion barrier [11].

2.3.2 Nickel aluminides

Nickel aluminides are reckoned as potential structural materials for the aerospace industry because of their high melting temperatures, low densities, good environmental resistances, high thermal conductivities, metal-like properties above the ductile-to-brittle transition temperature and low material cost. However, poor fracture toughness at low temperatures, low strength and low creep resistance at high temperatures hinder the structural use of these intermetallic alloys. Figure 2.3 shows the Ni-Al binary phase diagram [17]. Two intermetallic alloys *viz.,* Ni_3Al and NiAl have been extensively studied in the nickel aluminide system.

Ni_3Al

Ni_3Al falls in the composition range of ~ 73 at.% - 78 at.% Ni of the phase diagram, designated as the γ'-phase having cubic $L1_2$ crystal structure and is one of the promising aluminides for structural applications. Though Ni_3Al is an important phase imparting high temperature strength retention for Ni-based super alloys, the intrinsic strength of single phase Ni_3Al is insufficient for most of the structural applications beyond about 600 °C [18].

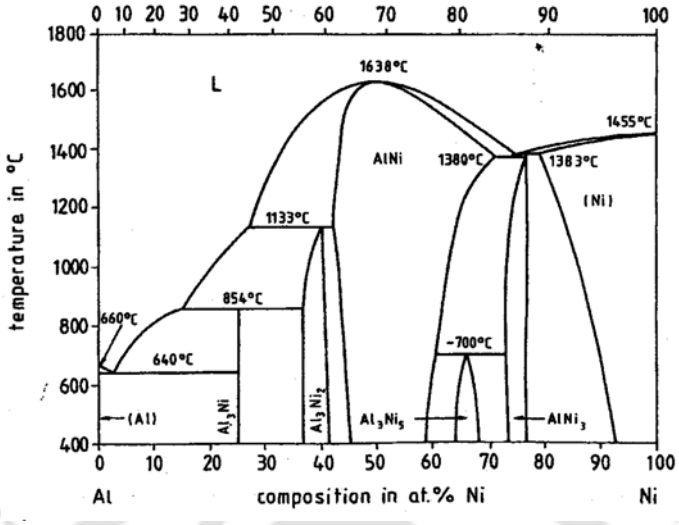

Fig 2.3: Ni-Al binary phase diagram [17]

Ni_3Al alloy exhibits an increasing flow stress with increasing temperature from room temperature to temperatures between 600 °C and 800 °C [11]. An anomalous positive temperature dependence of the compressive yield stress for Ni_3Al single crystals and Al-rich Ni_3Al alloys was reported by Golberg *et al.* [19]. The peak temperature of the yield stress decreases with increasing Al content and was found to be orientation dependent. The single crystal Ni_3Al alloys are known to be ductile whereas the Ni_3Al alloy in the polycrystalline state exhibits brittle intergranular fracture at room temperature [20] and directionally solidified Ni_3Al alloys with columnar grains were found to be ductile. Thus, the brittleness of polycrystalline Ni_3Al is attributed to the grain boundary weakness [11]. Studies [21] also indicated that polycrystalline Ni_3Al alloy with controlled recrystallised microstructure was ductile. The present approaches of increasing the ductility of Ni_3Al alloys are by boron addition to a level <500 ppm and keeping the aluminium concentration below the stoichiometric composition. Boron segregates into grain boundaries, enhancing the cohesive strength of the boundary, thereby preventing grain boundary failure. Boron enriched boundaries emit dislocations to reduce the stress concentrations within the boundary [11]. Tensile properties of cast Ni-16Al-8.Cr-1.7Mo-0.5Zr-0.03B (at.%) alloy were found to be better than the commercial IN-713 at elevated temperatures [22]. Addition of Hf, Zr, Ta and Mo improve the high temperature strength, whereas, addition of Cr (up to 10 at.%) enhances the ductility at intermediate temperatures in between 400 °C to 900 °C in these alloys.

Ni_3Al alloys generally display good resistance to oxidation at above 1200 °C due to the formation of alumina (Al_2O_3) films on the surface. At lower temperatures, Al diffusion in Ni_3Al to the surface is slow thereby Al depletion occurs at the surface resulting in the Ni-Al scale formation which leads to spalling. Scale adherence is improved by the addition of Cr, Ti, Zr, and Hf [11]. The embrittlement caused by exposure to air or oxygen at 800 °C as well as the stress corrosion cracking caused by hydrogen at low temperatures are of major concern in Ni_3Al alloys. Micro-alloying with boron reduces the environmental embrittlement of Ni_3Al alloys. Jiang *et al.,* [23] has reported notable decrease in dislocation velocity due to the presence of hydrogen in single crystal Ni_3Al alloy, resulting in the strengthening.

NiAl

The NiAl alloys are attractive as high temperature materials due to the wide compositional stability, low density (5.35 - 6.50 gm/cm^3), good thermal conductivity, high melting point (1640 °C) and excellent oxidation resistance. The physical and mechanical properties of NiAl were reviewed in detail by Miracle [17] and Noebe *et al.* [24]. NiAl possesses simple cubic B2 crystal structure that consist of two interpenetrating primitive cubic cells in which Al atoms occupy one sublattice and Ni atoms occupy the second sublattice. The composition of NiAl phase at room temperature varies between 45 at.% to 59 at.% Ni and is stable up to the melting point.

In binary NiAl alloy, the lattice constant is maximum at the stoichiometric composition and decreased rapidly with deviation from stoichiometry [17, 24]. The lattice constant also depends on ternary additions like Cu, Co and Fe [17].

It was reported [17, 25] that the Young' modulus (E) and shear modulus (G) of NiAl alloys were found to decrease with increase in the temperature. Few empirical relations are also available correlating these properties with temperature.

The bonding in NiAl is a combination of metallic and covalent type of bonds. An increase in electron density between nearest neighbouring Ni-Al atom pair along <111> directions results in a strong covalent bond between Ni and Al atoms. A weak ionic repulsion exists between second nearest neighbouring atom pair (Ru-Ru or Al-Al) along <100> direction. The strong covalent bond along <111> directions and the weak bond along <100> directions produce the observed elastic anisotropy in NiAl. The

strength and character of atomic bonding induce high strength and low ductility in single crystal NiAl [17, 24].

Thermal conductivity studies in NiAl increased with increase in Al concentration and exhibited a maximum of about 92 W/m.K at the stoichiometric composition of NiAl [26].

Polycrystalline NiAl is very brittle due to the availability of only three independent slip systems along the <100> in NiAl crystals. Grain sizes below 20 μm enhance some ductility in this alloy [18]. Ductile phase toughening has become a common method to improve the toughness and ductility in polycrystalline NiAl. Improvement in ductility could be achieved by ductile phase toughening [27]. It was reported by Noebe *et al.* [24] that improvement in toughness can be achieved by the formation of a second phase of Ni_3Al around the β-NiAl grains.

The flow strength of NiAl is greatly increased by alloy additions like boron, carbon, beryllium, chromium lanthanum yttrium and zirconium. [17,24]. The most potent strengthening typically results from a distribution of ordered precipitates, aligned eutectic alloys and fine ceramic particles in the matrix. Creep tests on $Ni_{40}Al_{50}Fe_{10}$ alloy [28] revealed that an addition of Fe to NiAl increases the creep strength due to reduced coefficient of diffusion resulting in decreased dislocation climb rate at high temperatures.

NiAl is extensively used in gas turbine engines as coating material due to its high resistance to oxidation and corrosion. Since the diffusion rate of Al to the surface in NiAl is very high at elevated temperatures, aluminium diffuses from the grains to the surface. In an oxidising atmosphere, formation of a highly adherent layer of alumina (Al_2O_3) act as a protective layer on the surface imparting oxidation resistance in NiAl alloys. Micro-alloying with oxygen-active elements such as Y, Zr, Hf, Ce or La enhances this resistance [11].

2.3.3 Iron aluminides

Iron aluminides are regarded as potential materials for variety of high-temperature applications to operate beyond the operating temperatures of some ferrite and austenitic steels. These materials exhibit a combination of attractive physical, mechanical and chemical properties such as low density, high electrical resistivity, excellent oxidation, corrosion and sulfidation resistances in addition to low cost

compared to many commercial iron-based alloys. Two phases of iron aluminides, *viz.,* Fe_3Al and FeAl have been investigated extensively for development of high temperature materials. However, in the following paragraphs only FeAl will be discussed due to its high temperature capability.

FeAl

FeAl has an ordered cubic body centred B2 crystal structure similar to the NiAl. FeAl has a melting point of ~ 1370 °C and exhibits a density of 5.76 - 6.32 gm/cm^3. The Young's modulus of polycrystalline FeAl is ~ 250 GPa [29, 30]. The FeAl exists over a wide range of composition from 36 at.% to 50 at.% Al. The lattice parameter of FeAl phase increases with increase in Al concentration up to 50 at.%. Higher quenching temperatures result in lower values of lattice parameter due to the formation of large number of thermal defects [31].

FeAl alloys exhibit both <111> and <100> types of dislocations. Room and low temperature deformations occur by <111> dislocation on {110} and {112} planes respectively whereas deformation at elevated temperatures occurs by <100> dislocation [29]. The transition temperature for change in slip vector from <111> to <100> increases with the increase in Al concentration. For 35 at.% Al alloy, the transition temperature is about 1000 °C, where as for 50 at.% Al alloy this is below 400 °C [32]. Further studies revealed the presence of both type of dislocations at higher temperatures. Initial plastic flow in FeAl alloys occurs by <111> dislocations at all temperatures [29].

At low temperatures, single crystal FeAl exhibits some amount of compressional ductility whereas the stoichiometric polycrystalline FeAl does not exhibit compressional or tensile ductility. Failures in FeAl alloys containing < 40 at.% Al and > 40 at.% Al are by transgranular cleavage and intergranular failure respectively [32]. Environmental embrittlement, weak grain boundaries, vacancy hardening and embrittlement are found to be the causes for low tensile ductility and brittle fracture in FeAl alloys processed by powder metallurgy technique [32]. Increase in ductility and strength attributed to the delaying of cracking with the reduction of grain size was reported. Addition of elements like boron, zirconium, lithium, and

Cerium increased the ductility of FeAl alloys by refinement of grain size or by increasing the cohesive strength of the grain boundary [33-35].

The yield strength of FeAl alloys ranges from 332 MPa to 402 MPa, and it is insensitive to temperature below 600 °C [22, 32]. Above this temperature range, a sharp decrease in strength with increase in temperature was observed. An anomalous behaviour of increase of yield stress up to a temperature of 500 °C followed by softening was reported by Kupka [36] in Fe–45Al–4Cr–0.1Zr–0.02B alloy. Solid solution hardening by Mo, Zr, Ti, Ni and precipitation of carbides increases the high temperature properties of FeAl alloys [35,37]. Micro-alloying with boron enhances room temperature ductility and improve resistance to environmental embrittlement and enhanced high temperature strength.

2.3.4 Cobalt aluminide (CoAl)

CoAl is also characterised by a cubic B2 crystal structure (CsCl type). CoAl has good mechanical properties at elevated temperatures.

The phase diagram for binary Co-Al alloy system is shown in Figure 2.4 [38]. The CoAl phase forms congruently from the melt at 1640 °C and exhibits a homogeneity range extending from 22 at.% Al to almost 50 at.% Al at higher temperatures, but is stable in the range ~ 48 at.% Co to 58 at.% Co at room temperature.

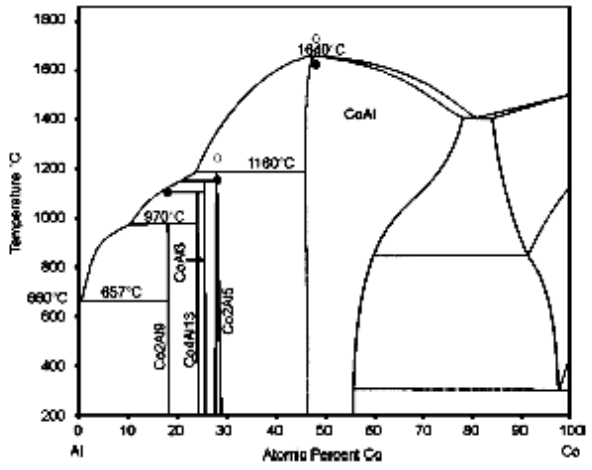

Figure 2.4: Phase Diagram of Co-Al [38]

The thermal conductivity of CoAl increased with the increase in Al concentration and exhibited a maximum of about 37 W/m.K at stoichiometric

composition [26]. Diffusion coefficient of Co in CoAl alloys decreases with increasing Al concentration up to the stoichiometric composition of CoAl. However, the diffusion coefficient of Co was found to be same in Al-rich $Co_{48}Al_{52}$ alloy, which is also same for stoichiometric CoAl [39].

Partial substitution of Co by Ni and Fe increases the creep resistance of CoAl alloys [11]. The strength is further enhanced on reinforcement with TiB_2 particulate.

Studies by Kimura *et al.* [40, 41] on the mechanical properties of ternary Co-Al-C alloys in the temperature range of 196 °C to 1000 °C revealed better combination of room temperature toughness and high temperature strength. These alloys exhibited anomalous positive temperature dependence of yield strength. Investigations [41] on annealed alloys having three-phase microstructure revealed that $C_{70}Al_{20}C_{10}$ alloy exhibited good balance of ductility and strength both at room and elevated temperatures as compared to the $Co_{69}Al_{24}C_7$ alloy. Microstructural modification achieved by hot forging and subsequent heat treatments enhanced the tensile ductility of both the alloys.

Mishima *et al.* [42] reported that quaternary Co-Al-Ni-Ti alloy, having three-phase microstructure with addition of 200-ppm boron, exhibited about 20% tensile ductility compared to the 10% ductility exhibited by ternary Al-Co-C alloys. The range of CoAl phase was found to extend up to 36.6 at.% Cu at 900 ^{0}C in Al-Cu-Co ternary alloys of constant Al concentration whereas low solubility of Ag and Au was observed in CoAl phase in ternary Al-Ag-Co and Al-Au-Co alloys, respectively. Different ternary phase formations were also observed in ternary Al-Cu-Co alloy system in contrast to the other two alloy systems [43].

2.3.5 Ruthenium aluminide (RuAl)

The intermetallic RuAl as a phase was first identified in 1960 by Obrowski in the binary Ru-Al alloy system [44]. Subsequently, Wopersnow and Raub [44] reported the properties of RuAl *viz.,* corrosion resistance in some very aggressive environments, malleability, hardness, and resistivity. The potential use of this material for high temperature structural use was not realised until Fleischer *et al.* [45, 46] published the unusual combination of physical, chemical and mechanical properties like high strength at room and elevated temperatures along with reasonably good room temperature toughness of Ru-Al alloys in the late 1980s. The elastic properties of RuAl phase reported by them are shear modulus, G = 104 GPa, bulk modulus, K = 207 GPa,

Young's modulus, E = 267 GPa and Poisson's ratio, ν = 0.286. The composition dependence of elastic properties of binary Ru-Al alloys revealed better toughness in the Ru-rich side and high brittleness in the Al-rich end of the binary phase diagram. Addition of 0.5 at.% B increases small amount of ductility in the alloys of Al-rich composition. Addition of 2 to 5 at.% scandium (Sc) increases the high temperature strength without diminution of ductility of RuAl alloys. The good ductility observed for RuAl is due to the presence of dislocations with <100>, <110> and <111> types of Burgers vectors.

The review by Wolff [44] on the development, processing, physical and mechanical properties of binary RuAl contributed to a better understanding of this alloy. The efficacy of multiphase alloy systems of RuAl with emphasis on the high temperature strength and room temperature ductility was highlighted by Wolff *et al.* [47] which also mentioned the successful development of RuAl based spark plug electrode. Mucklich and Ilic´ [48] have recently discussed in detail the physical properties, microstructure and processing of this intermetallic alloy.

Ruthenium aluminide (RuAl) is a potential high-temperature intermetallic phase having B2 (CsCl) crystal structure. Figure 2.5 shows the crystal structure of B2 RuAl. The structure is basically like two interpenetrating cubic sub-lattices of ruthenium (Ru) and aluminium (Al) atoms, with each Al atom at the body centre of Ru sublattice and vice-versa. Freeman *et al.* [49] studied the electronic properties like density of state, band structure and bonding charge density of RuAl by using computational techniques. Good agreement in the values of lattice constant, bulk modulus and formation energy was observed with the experimental results. The bonding between Ru atoms is smooth d-d type bonding along <100> direction whereas the bonding between Ru and Al atoms along <111> is not directional which have resulted in imparting good ductility to RuAl phase.

Lattice constant of RuAl have been determined by both experimental studies and theoretical calculations. Villars and Clavert reported the lattice constant of RuAl as 0.303 nm where as Fleischer observed the lattice constant as 0.29916 ± 0.00008 nm for stoichiometric RuAl [50]. The same study indicted a monotonic variation in lattice constant with variation in Al/Ru ratio within the stoichiometric composition as well as with solute addition. For Ru-rich composition, the lattice constant remains same as the excess Ru precipitates as second phase. Addition of Co and Fe reduces the lattice

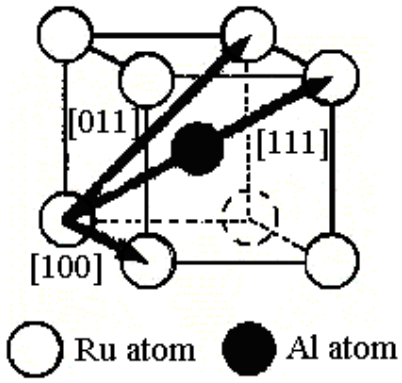

Fig 2.5: Crystal structure of B2 RuAl

while Ti addition causes an increase in lattice constant of RuAl phase [50]. Fleischer [50] determined the lattice constant of stoichiometric RuAl as approximately 0.29884 nm while the off-stoichiometric composition exhibited an increasing trend. The maximum value of the lattice constant was 0.29906 ± 0.000084 nm at 50.3 at.% Ru while towards the Al rich side of the phase diagram the maximum value was 0.29943 ± 0.000097 nm for 46.2 at.% Ru. Gobran *et al.* [51] also observed dependence of lattice parameters on compositions of binary Ru-Al alloys.

It was reported by Chakravorty and West [52] that the lattice constants of RuAl in $R_{22}Al_{50}Ni_{28}$ and $Ru_{17}Al_{39}Ni_{44}$ alloys were temperature dependent and exhibited values within the range of 0.2908 to 0.2944 nm, respectively. The investigation carried out in a range of ternary alloys based Ru-Al-Ni system revealed that the lattice constants of β2-RuAl were in the range of 0.2946-0.2949 nm [53] and was increasing linearly with increase in nickel content. Horner *et al.* [54] also observed a gradual increase in lattice constant of RuAl phase with increase in Ru concentration in Ru-Al-Ni ternary alloys. Experimental studies by Liu *et al.* [55] on milled powders based on three ternary Ru-Al-Ni alloy systems also exhibited a reduction in lattice constant with the increase in Ni concentration.

Bozzolo *et al.* [56] evaluated the lattice constant of binary Ru-Al and ternary Ru-Al-Ni alloys as a function of Ni concentration and found that the values were in close agreement with the experimental data. Freeman *et al.* [49] computed the lattice constant of RuAl as 0.302 nm. Wolff *et al.* [47] observed that the lattice constant remained almost same with Co addition of up to 13 at.% and beyond this it decreased. Ni addition resulted in a linear decrease in the lattice constant of the RuAl phase.

Almost linear decrease in lattice constant was observed with additions of Ir [57, 58], and Co [58] in the RuAl phase. Addition of Cu was found to decrease the lattice constant of B2 crystal in ternary Ru-Al-Cu alloys [59].

Figure 2.6 shows the binary phase diagram based on Al-Ru alloy system reported by Massalaski [60]. The figure shows that RuAl phase is stable over a small deviation from stoichiometric composition at room temperature where as it is stable over the composition range between 45 and 52 atomic percentage of Ru at elevated temperature. The recent phase diagram reported by Mucklich and Ilic′ [48], shown in Figure 2.7, indicates that the RuAl phase exist within the composition range from 46.5 at.% Ru to 50 at.% Ru at room temperature. At elevated temperature, there is only a small extension in the Ru-rich direction. The RuAl phase does not extend much beyond ± 2 at.% Ru of its stoichiometry in the ruthenium-rich end of the phase diagram even at high temperatures. The experimental investigation by Boniface and Cornish [61] showed that the RuAl phase formed between the composition range of 42 ± 3 at.% and 54.1 ± 1 at.% Ru. Prins *et al.* [62] observed reasonable match of Ru-Al phase diagram calculated by CALPHAD technique and the experimental data. Gobran *et al.* [51] investigated the composition range of single phase RuAl and observed that the phase boundaries extended up to 53.8 at.% Al and 54.5 at.% Al. at room temperature and at 1200 °C respectively. They also observed the phase Ru_2Al_3 to be stable at room temperature. This composition range differs from earlier reported values [60, 61]. Ilic′ *et al.* [63] observed the shifting of eutectic composition to Ru-rich direction of $Ru_{74}Al_{26}$ from the existing composition of $Ru_{70}Al_{30}$ [60]. Mi *et al.* [64] examined the intermediate phases and their reactions in the Al-rich part (up to 40 at.% Ru) of the binary Al-Ru phase diagram and observed the occurrence of a new Al_5Ru_2 phase at 28.6 at.% Ru.

Electrical resistivity measurements by Smith and Lang [65] revealed minimum resistivity and maximum thermo-electromagnetic frequency for the RuAl phase with equiatomic compositions of Ru and Al. Electrical resistivity increases rapidly in the ruthenium-rich direction than in aluminium rich compositions. $Ru_{53}Al_{47}$ and $Ru_{50}Al_{50}$ have similar thermal conductivity whereas the thermal conductivity of the aluminium rich $Ru_{47}Al_{53}$ samples was found to be far lower. They attributed this low thermal conductivity to off-stoichiometry defect structure in the aluminium rich samples. Results also showed the sensitivity of thermal conductivity of RuAl alloys to the

microstructural variations. $Ru_{54.2}Al_{45.8}$ showed maximum thermo-emf of ≈ 11 μV/K at 20 °C with lower electrical resistivity of ≈ 15 μΩ-cm at 20 °C. Same values of electrical resistivity were reported elsewhere [66].

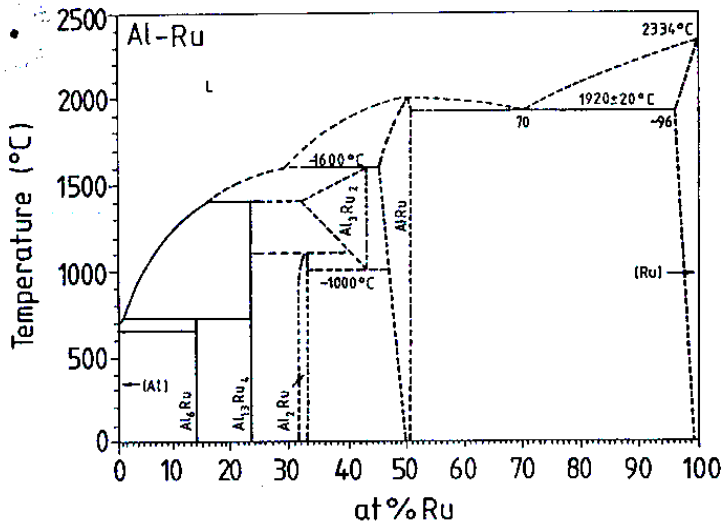

Fig 2.6: Binary phase diagram of Al-Ru [60]

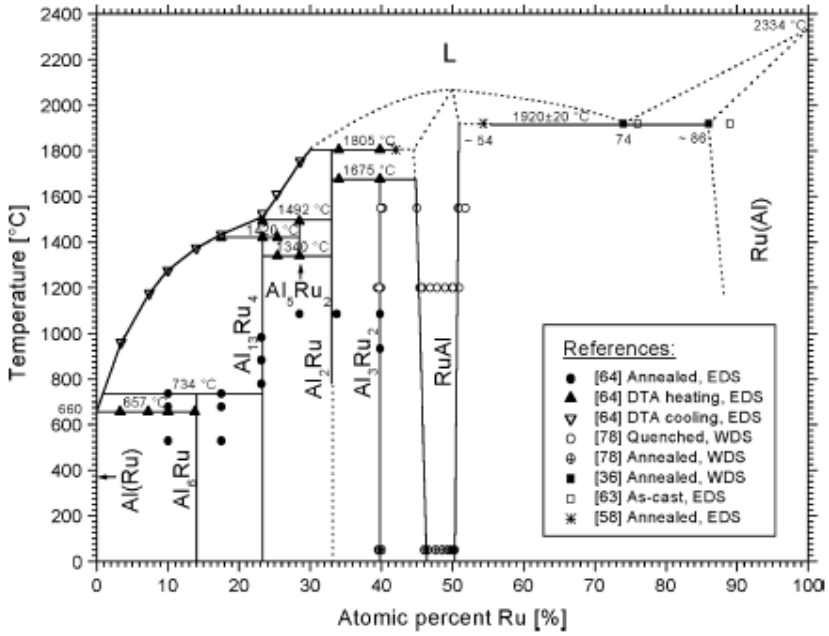

Figure 2.7: Binary Ru-Al phase diagram proposed on the recent literature [48]

Anderson and Lang [66] investigated the thermal conductivity and electrical resistivity, in the temperature range from 25 °C to 450 °C, for $Ru_{47}Al_{53}$, $Ru_{50}Al_{50}$ and $Ru_{53}Al_{47}$ alloys processed by reactive hot isostatic pressing (RHIP). Stoichiometric and Ru-rich RuAl alloys seemed to be good thermal conductors and have similar thermal

conductivity of ≈ 70-80 W/m/K whereas Al-rich RuAl alloys exhibited lower thermal conductivity ≈ 45 W/m/K. The low thermal conductivity in Al-rich RuAl alloy was attributed to a high degree of porosity and intergranular cracking observed in this alloy.

Tryon *et al.* [67] studied the thermal expansion behaviour of RuAl alloys. Coefficients of thermal expansion (CTE) of RuAl alloys of near stoichiometric compositions are in the range of $5.5x10^{-6}$/K to $11x10^{-6}$/K within the temperature range of 127 °C - 900 °C. CTE for RuAl was observed to be lower than other B2 intermetallics like FeAl, CoAl and NiAl. CTE values of the alloys were found to be insensitive to the minor variations in compositions of the alloys.

Ternary alloying and microstructural control are practical routes for further improvement of high-temperature properties of Ru-Al alloys [47]. Apart from modifying the physical and mechanical properties, there is also a possibility of cost reduction by replacing ruthenium by other cheaper elements. However, partial replacement of Ru is almost invariably accompanied by the loss of ductility in the monolithic form. Wolf [68] have highlighted that this problem can be alleviated by the incorporation of ductile second phases and by dispersion strengthening. Ultra fine-grained structure provides another possible means of improving the properties of the RuAl phase in which ruthenium was partially substituted by other elements.

Fleischer and co-workers studied the effect of addition of Co, Fe, Ti, Sc, B, Cr, Si, Ce, rhenium (Re) and yttrium (Y), its effects on mechanical properties and correlation with defect structure in Ru-Al alloys [45, 46, 50, 69-71]. They concluded that the constitutional defects were required to maintain the B2 crystal structure. They also reported the appearance of second phases in the microstructure after limited accommodation of constitutional defects in Ru-rich direction. Fleischer used the lattice constant and density measurement to calculate the cell occupancy and concluded that excess Al atoms produce vacancies. Iron, cobalt and titanium additions up to 5-wt% in RuAl [70] increased the compressive strength. The increase in the strength observed for RuAl phase was at the expense of room temperature toughness for all alloy additions with one exception being boron. Boron addition resulted in a ductilising effect on RuAl [71]. The maximum improvements in strength and compressional ductility of RuAl-based alloys was by addition of 0.5 at.% boron. The subsequent study by Fleischer [72] revealed that random distribution of boron in the RuAl alloy matrix enhances the toughness and ductility in these alloys. Addition of boron was found to lower the shear

moduli of these alloys without altering the lattice constant. The oxidation properties of RuAl alloys were found to be good up to about 1100 °C. Al-rich compositions showed better oxidation resistance, which was attributed to the formation of a protective layer of Al_2O_3 at the surface. The alloys containing Sc, Y, and Cr also showed better oxidation resistance. Alloys with Sc, in particular, possess combination of good strength and oxidation resistance [46].

The partial isothermal sections at 1000 °C and 1250 °C of the Ru-Al-Ni ternary phase diagram developed by Chakravorty and West [52, 53] are shown in Figures 2.8 (a) and (b), respectively. They found extensive solubility of Ru and Ni in the B2 phase. However the continuous mutual solubility was interrupted by a miscibility gap. Strong microstructural stability was observed in the microstructure having two phases *viz.*, RuAl and NiAl due to their extensive mutual solubility and very small difference in their lattice constants. During the solidification of these alloys, the primary dendrites were the high melting point RuAl phase thereby leaving a Ni-rich phase to form towards the later part of the solidification [47] . The authors also determined the phase boundaries of different phases present in the alloy taking isothermal sections of different Ru-Al-Ni ternary alloys in the range 0 to ~ 50 at.% Al.

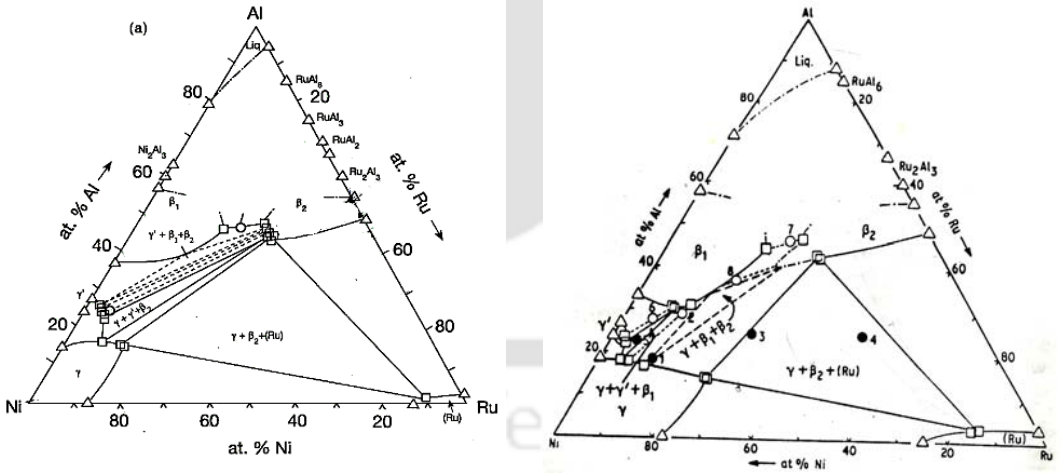

(a) (b)

Figure 2.8: Partial isothermal sections of Ru-Al-Ni ternary alloys [53] (a) at 1000 °C and (b) at 1250 °C

Wolff and Sauthoff [73] observed a combination of good ductility and strength in the ternary Ru-Al-Ni alloys consisting of multiphase mixtures with RuAl as one phase. However, despite good strengthening at low and intermediate temperatures, the Ru-Al-Ni alloys exhibit a rapid loss in their resistance to deformation at elevated

temperatures. The authors found no evidence to support the absence of the miscibility gap. A first principle based computational approach predicted the B2 single phase to exist across the ternary phase diagram [56]. Horner *et al.* [54] reported complete solid solubility between RuAl and NiAl. Tryon and Pollock [74] ruled out the possibility of the existence of a miscibility gap between RuAl and NiAl phases at temperatures 1000 °C and 1100 °C and proposed a continuous B2 phase across the ternary Ru-Al-Ni alloy system. The authors commented that homogenisation of Ru-Al-Ni alloys is very slow which leads to the conclusion of existence of a miscibility gap. The very slow inter-diffusion coefficient reported for Ru in binary Ni alloys [75] reflects that the homogenisation process in Ru-Al-Ni alloys is also very slow. Horner *et al.* [54] studied microhardness of ternary Ru-Al-Ni alloys. Multiphase alloys were found to be stronger than the single-phase alloys and exhibited an increase in hardness with the increase in Ni-content with a maximum hardness in alloy $Ru_{26}Al_{37}Ni_{37}$. The maximum hardness value with single-phase structure was observed in $Ru_{29}Al_{47}Ni_{24}$ alloy.

Constitution of ternary Ru-Al-Ti alloy system has been evaluated by Khataee *et al.* [76]. RuAl-TiAl exhibited continuous mutual solid solubility between the isostructural B2 phases. The ternary alloy system found to undergo ordering across the range of quenching temperatures (1250 °C - 700 °C), resulting in the formation of a *G*-phase close to the ideal composition of $Ti_6Al_{16}Ru_7$.

Mi and Grushko [59] studied the Al-rich part of the ternary Ru-Al-Cu alloy system. Partial isothermal reactions at different temperatures revealed the formation of three stable periodic phases designated as ω (Al_7Cu_2Ru), *C* ($Al_{58}Cu_{30}R_{12}$) and C_1 ($Al_{71}Cu_7Ru_{22}$). The single phase Ru-Al-Cu was found to contain 45-52 at.% Al at different Cu/Ru ratios. Isothermal sections at different temperatures resulted in the variation in Cu concentration. Cu concentration in single phase RuAl was found to decrease at higher temperature

Wolff and Sauthoff [77] investigated the possibility of dual-phase alloys by the addition of substitutional solutes like Ni, Co and Ti in RuAl. Mechanical properties of the alloys revealed that the multiphase alloys of Ru-Al-Ti and Ru-Al-Co systems exhibited substantial ductility along with higher strength compared to the single-phase alloys. Good ductility was observed in Ru-Al-Ti dual phase alloys with addition of up to 70 at.% of Ti. Ru-Al-Co alloys exhibited a high degree of deformability with Co addition up to 50 at.%. Ductility reduced rapidly for compositions above 50 at.% Co. In

both cases a continuous interfacial necklace structure with eutectic grain boundary resulted in the improved ductility. The Ru-Al-Ni alloys exhibited a drastic loss of ductility with Ni contents above 5 at. %. In this system the continuous interfacial layer was not observed and the hardening was attributed to the solid solution strengthening. Hardness values obtained by very high level of additions of Co and Ti were attained in Ni alloys at levels of 5-10 at % of Ni. The same report reveals that off-stoichiometric compositions in the ruthenium rich end resulted in the enhanced ductility due to the formation of a continuous eutectic (RuAl + Ru) phase at the grain boundaries.

Investigation of constitution of Al-Ir-Ru ternary alloy system together with hardness measurement was reported by Hill *et al.* [57]. The RuAl phase extended across the ternary alloy from IrAl to RuAl and existed in a very narrow composition range of about 2 at.% towards the Al-rich direction. A new phase was discovered with composition $Ru_{27}Al_{53}Ir_{20}$ that formed peritectically from the RuAl phase. Hardness measurements indicated that the hardness of the RuAl phase increased with Ir substitution and maximum Vickers hardness (1009) was observed for the $Ru_{11}Al_{58}Ir_{31}$ alloy composition. Hardness behaviour of pseudo-binary alloys based on RuAl-CoAl and RuAl-IrAl [58] exhibited linear increase in hardness with increase in alloy additions.

Microstructure and phase compositions of Ru-Al-Mo alloys were investigated by Reynolds and Johnson [78]. The RuAl- (Mo, Ru) eutectic exhibited a room temperature yield stress of 1500 MPa and was found to have lamellar morphology. The eutectic in this system consisted of RuAl fibres imbedded in an hcp- (Ru, Mo) matrix. They reported a peritectic reaction consisting of RuAl and hcp (Mo, Ru) solid solution in this system. The alloys consisting of RuAl and hcp (Mo, Ru) solid solution exhibited combination of superior room temperature fracture toughness and a high melting temperature. Mo-rich eutectic alloys were found to be brittle and harder than the Ru-rich eutectic alloys due to the precipitation of the σ (Mo_5Ru_3) phase. The Ru-Al-Mo alloys exhibited poor oxidation resistance.

Fleischer *et al.* [45] first reported the unusual deformation behaviour of RuAl alloys as compared to other aluminides such as NiAl, FeAl and CoAl. Transmission electron microscopy (TEM) investigations on annealed RuAl and $Ru_{53}Al_{47}$ alloys revealed the presence of dislocations having <111> and <100> Burgers vectors in the RuAl matrix of the undeformed material. Dislocations were also observed in the Ru-

phase of $Ru_{53}Al_{47}$ alloy. The deformed $Ru_{53}Al_{47}$ alloy was characterised by the presence of three dislocations having <100>, <110> and <111> Burgers vectors. Majority of the dislocations were found on {110} plane with <110> Burgers vector. The authors proposed the possibility of dissociation of both <110> and <111> dislocations into super partial (1/2) <111> in the region of dislocation core.

Unusual deformation characteristics exhibited by Ru-Al alloys were also investigated by Pollock *et al.* [79-83] at low temperatures. Strain rate sensitivities were measured in a number of polycrystalline RuAl based alloys with an abrupt change of strain rate from ~ 10^{-4} s^{-1} to 10^{-2} s^{-1} at room temperature. The temperature dependence of flow stress (both at -196 $^{\circ}$C and room temperature) and room temperature strain rate sensitivities exhibited by all the binary alloys was observed to be low [79]. Studies on dislocation characteristics and operative slip system [80] on (RuAl + 0.5% B) alloy at low temperatures revealed the presence of <100>, <110> and <111> Burgers vectors after 1-2% deformation in compression. <100> and <110> dislocations were observed in approximately equal densities with a low distribution of <111> dislocations on {110} plane. The authors also noted that <111> dislocations might have evolved from reactions between glissile <100> and <110> dislocations.

Studies by Pollock *et al.* [82] on the deformation behaviour of Ru-Al alloy containing boron (B) and platinum (Pt) exhibited a change in the deformation mode. The addition of platinum resulted in a change in the generally observed deformation mode by <110> and <100> dislocations in binary Ru-Al alloys to <111> and <100> dislocations in the $Ru_{48}Al_{50}Pt_2$ with 0.5at.% B alloy. High distribution density of <111> dislocations was observed in this alloy as compared to binary RuAl alloys. The platinum-containing alloy exhibited higher flow stress as well as slightly higher strain rate sensitivity compared to the stoichiometric RuAl alloy. Deformation and flow behaviour of RuAl alloys containing Boron at a temperature range of 300°C to 700 °C was characterised by the occurrence of serrated yielding, flow stress plateau, maxima in work hardening rate, and strain rate sensitivity [83]. A flow stress increase following static aging confirmed the effects of solute impurities at mobile dislocations. Anomalous strengthening peaks were also observed in stoichiometric RuAl alloys within the temperature regime 500 °C to 727 °C. Deformation studies at elevated

temperatures also revealed an unchanged dislocation substructure with respect to the low temperature deformations.

Deformation studies by Feng *et al*. [84] on Ru-Al-Ta alloys ($Ru_{25}Al_{25}Ta_{50}$ and $Ru_{32}Al_{13}Ta_{55}$) revealed the low compressional ductility of $Ru_{25}Al_{25}Ta_{50}$ alloy as compared to that of $Ru_{32}Al_{13}Ta_{55}$. Microstructural studies revealed a continuous Heusler phase (R_2AlTa) with a Ru-rich phase at the interdendritic boundaries in $Ru_{25}Al_{25}Ta_{50}$ alloy whereas $Ru_{32}Al_{13}Ta_{55}$ alloy contained a single phase B2 structure with Ru-rich phase at the interdendritic boundaries. $Ru_{32}Al_{13}Ta_{55}$ alloy exhibited similar dislocation substructure after deformation both at 25 °C and 700 °C with <111> as major dislocations on {110} plane. <100> dislocations were observed as pairs at 25 °C with low densities.

The reports available indicate that the microstructure of the Ru-Al alloy systems is strongly dependent on the processing technique adopted. The techniques adopted for the processing of RuAl alloys are briefly described in the subsequent paragraphs.

2.3.6 Processing of Ru-Al alloys

Information regarding processing of RuAl alloys in the literature are limited. The works carried out to investigate the microstructure and properties of these materials were either on samples prepared by arc melting or reactive hot isostatic pressing. The following paragraphs highlight these processing techniques and other possible techniques of manufacturing these alloys.

Processing by Solidification route

Ingot metallurgy is one of the most inexpensive and simple ways to produce metallic materials. However, production of RuAl intermetallics alloys by this conventional method encounters several difficulties. High melting point of ruthenium (2300 °C) coupled with high heat of formation of ruthenium aluminide (~ -124.1 ± 3.3 kJ/mol) [62] imposes a number of difficulties on the processing of this aluminide by solidification route. Volatilisation of aluminium results in inhomogeneous alloy composition with high porosity in these alloys. The process is also complicated by the severe attack on the conventional refractory crucibles materials used for furnace lining. The most commonly employed method for processing Ru-Al alloys is arc melting (cold crucible technique) in which the molten alloys undergo fast solidification. Even cold

crucible technique results in chemically inhomogeneous materials due to the rapid solidification and at the same time porous materials are obtained due to the volatilisation of aluminium. It appears that melting techniques unavoidably lead to the formation of (i) continuous networks of secondary interfacial phase, (ii) composite eutectic structure or (iii) near-single phase alloy. Literature survey of Ru-Al alloys within the single-phase region processed by arc melting technique revealed that microstructures obtained were not purely single phase. The existence of Ru-rich secondary phases in the microstructures confirms the above statement. The presence of secondary phase undoubtedly affects the material properties and behaviour.

The low melting point of aluminium (660 °C) along with the high vapour pressure at the very high processing temperature of the alloy leads to loss of aluminium from the melt making the composition control extremely difficult. Since the RuAl phase exists in the narrow compositional range, the production of single-phase RuAl alloys *via* ingot metallurgy route is a complex and near impossible task. RuAl alloys produced by cold crucible technique possess a near single phase microstructure with the primary RuAl phase (grey) and a Ru-rich intergranular layer (white) is shown in Figure 2.9 [85]. During solidification, the primary phase solidifying from the melt is the RuAl phase. The Ru-rich phase (white) solidifying towards the later part of the solidification process forms an eutectic layer (Ru + RuAl) around the primary RuAl phase. Hence, it appears that comparatively low melting point Ru-rich Ru-Al alloys with lamellar microstructure at the eutectic regions are easier to produce by this technique.

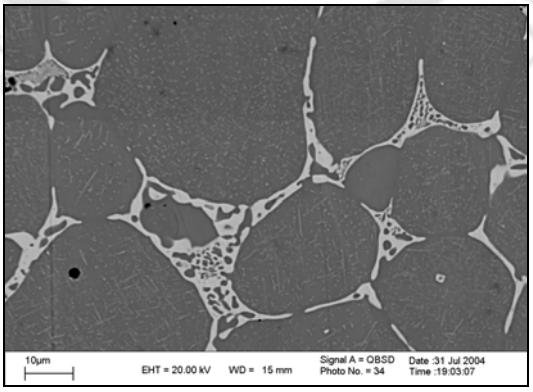

Fig 2.9: SEM micrograph of as-cast microstructure of RuAl alloy of nominal composition of $Ru_{47}Al_{53}$ [85]

Powder Metallurgy techniques

Process routes based on powder metallurgy (reactive hot sintering) offer a number of advantages in the processing of high temperature intermetallics, particularly when the highly exothermic reaction between the constituent elements is harnessed in active sintering. This technique enables more precise control of composition and manufacture of single phase RuAl or fine dispersed microstructures. In the case of RuAl-based alloys, some of the advantages offered by powder metallurgy route are [86]:

a. The intrinsic enthalpy of reaction between Ru and Al is a thermally efficient driving force for densification, circumventing the high furnace temperature necessary for melting or sintering
b. The Ru source material is converted directly from the powder which is the primary product of the refining process.
c. The reaction can be propagated within a sealed system which limits volatilisation losses and contamination
d. Reaction and densification by pressurization can be carried out simultaneously, for example, in a hot press.

However samples processed by this route were associated with presence of porosity.

Reactive powder processing based on reactive hot isostatic pressing (RHIP) has been successfully employed by I.M. Wolf [86] in the production of homogeneous, near full density RuAl based alloys and with near net shape structural components at a temperature lower than the melting point of RuAl. In the absence of external pressure, the reaction was driven close to completion, resulting in the formation of single phase RuAl. Pressurisation retarded the reaction and resulted in a partially reacted multiphase structure. The enhanced thermal conductivity and heat transfer during pressurisation lowered the maximum temperature attained. Heat treatment for extended period of time following the compaction under pressure resulted in the conversion of the multiphase structure into a single-phase structure. The study also revealed a modified the microstructure for the off-stoichiometric two-phased Ru-Al alloys processed by RHIP. The second phase in Ru-Al alloys produced by melt processing develops a continuous

network of a secondary interfacial phase whereas in powder processing there is a fine dispersion discrete ruthenium or aluminium in the matrix.

Gobran *et al.* [87] investigated the effects of Ru and Al particle sizes and compaction pressure on the reaction mechanism during reactive sintering and densification of RuAl alloys. The studies revealed that the particle size ratio of Ru and Al in the powder mixture affected the reaction temperature, intensity of the reaction and final density of the reactive sintered product. An increase in the Ru:Al particle size ratio increased the reaction temperature during reactive sintering. In all the cases, the reaction temperatures observed were below the melting point of Al. Lower Ru:Al particle size ratio led to the higher density and resulted in a single phase RuAl material. RHIP material exhibited higher theoretical density (94.4%) as compared to that of the reaction-sintered material (81%).

Cortie and Boniface [88] highlighted a modified hot isostatic pressing (HIP) method by hot pressing blends of pre-reacted powdered RuAl and the individual elements. The HIPing mixtures containing pre-reacted RuAl powder retarded the peak temperature reached during the self-propagating reaction. The author highlighted the possibility of producing near net shape products using this technique. The resultant product exhibited partially reacted multiphase structure due to the lack of insufficient temperature. Subsequent homogenisation of the product did not yield a single-phase structure.

Ball Milling/Mechanical Alloying (MA)

An alternative way of producing RuAl alloy is by solid-state reaction, namely mechanical alloying (MA). Since the invention of the mechanical alloying process by J.S. Benjamin during 1960s, it has become an alternative technique for processing a variety of materials including superalloys and intermetallic alloys. The process has been utilized in different areas of material processing and applied to different material systems such as oxide dispersion strengthened materials, composites, amorphous materials, nanocrystalline alloys etc. MA is a solid-state reaction process, in which a mixture of elemental powders is milled in a high-energy attrition-milling chamber. The set up consists of a water-cooled chamber in which the powder mixture is introduced along with hardened steel or ceramic balls. Milling of the powder mixture is facilitated by the rotation of a mechanical impellor at high speed in a controlled (usually inert)

atmosphere. During the milling operation, a series of high-energy collisions of the powder mixture takes place between the hardened balls and between balls and the vial wall. These impacts cause plastic deformation, fracture and cold welding of powder particles trapped at the collision points, and lead to the formation of composite particles. One of the requirement of the mechanical alloying is that at least two elements are required in the powder mixture and one of the element should be ductile and the other brittle.

During the milling process, the brittle powder constituent easily gets fractured whereas the ductile phase undergoes sever plastic deformation and gets flattened out due to impacts of the balls. The flattened particles may envelope the fragmented particles during the milling resulting in a layered composite structure. This composite structure becomes increasingly finer with continued milling. The reduction of the particle size increases the surface area to volume ratio of the particles. Depending on the type of elements used, the thickness of the layers may be reduced even to nanometer level. Under these circumstances the diffusion between the elemental metals becomes increasingly operative and result in a solid-state reaction to form a new alloy of the powder constituents. The key factors that are identified for controlling the mechanical alloying process are [89]-

- Activation energy, which is related to the formation of defect density during collisions involving the balls, the vial and the powder particles,
- Temperature, which is associated with the plastic deformation of the powder particles and the sliding between the powder particles and the high energetic balls,
- Crystallite size, which is related to the formation of nanometer crystalline structures during milling and,
- Crystal structure, which is related to the change in the diffusivities with the change in the crystal structure during milling.
- The type and nature of the elements in the powder mixture.

In some alloy systems the solid-state mechanical alloying reaction are activated spontaneously especially with very fine sized composite powder mixture [89]. It has to be noted that full mechanical alloying may not be obtained in all alloy systems. However, the formation of a composite structure plays a vital role in determining the reaction kinetics during subsequent heat treatment of milled powder. The main factors

influencing the high-energy ball milling process are the size of the balls, density of ball material, powder properties and characteristics, ball to powder weight ratio, the impeller speed, etc.

Increased dislocation density, high lattice defects and very high total surface energy due to the fine particle size on milling lead to low activation energies for the reactions. The most important advantage offered by mechanical alloying is the solid state processing nature, which makes it extremely suitable for producing high temperature intermetallics, especially the alloy systems with constituent elements having widely differing melting points. In addition, MA is found to be a feasible mean for the alloy formation that exists within a very narrow composition range. Moreover, the potential ability to form fine-grained intermetallics by MA would further increase its strength.

Hellstern *et al.* [90] first studied the effects of ball milling on RuAl alloy processed by reactive sintering. Observation of nano sized (~ 7 nm) RuAl particles was reported after 32 hours of milling. The observed heat release of 6 kJ/mol revealed that the milled powder mixture was strained to a very high level.

Liu *et al.* [91-93] reported the production of RuAl by mechanical alloying from elemental Ru-Al powder mixture. Structural evolutions during milling exhibited the abrupt formation of RuAl phase after 4 hours of milling [91, 92]. Complete transformation of the elemental powders to RuAl occurred after 25 hours of milling for a composition of $Ru_{50}Al_{50}$ carried out in a Spex TM mill. In another study by the same authors, RuAl phase formation was reported only after 35 hours of milling and subsequent annealing of the milled powders [93]. The as-milled single-phase RuAl powders exhibited high stability and underwent reordering, strain relaxation and grain growth at elevated temperatures. The studies indicated stagnation of all the above-mentioned phenomena at elevated temperatures.

Liu and Mucklich [94] reported the synthesis of RuAl/ZrO_2 nano composite by mechanical alloying of stoichiometric elemental Ru + Al mixture with 10 at.% and 20 at.% of ZrO_2. The presence of ZrO_2 was found to retard the reaction for formation of RuAl phase. RuAl phase formation was observed after 15 hours of milling and the complete transformation of the powders to RuAl occurred after 35 hours of milling. ZrO_2 was found to be uniformly dispersed in the RuAl matrix after subsequent

annealing. The milled powders exhibited high thermal stability at elevated temperatures.

Synthesis of nanocrystalline ternary Ru-Al-Ni alloys was reported by Liu *et al.* [55]. Structural evolution during milling of powder mixtures corresponding to the compositions of $Ru_{25}Al_{50}Ni_{25}$, $Ru_{30}Al_{50}Ni_{20}$ and $Ru_{40}Al_{50}Ni_{10}$ revealed that the powder compositions with lower Ni-content required longer milling time to obtain the final single phase. The as-milled powders exhibited high stability, reordering, strain relaxation and grain growth at elevated temperatures.

2.3.7 Motivation and challenges in the processing of Ru-Al alloys

The above literature survey shows that ruthenium aluminide alloys have been mainly processed by solidification (arc melting) and RHIP techniques. A few attempts have also been made to prepare Ru-Al based powders by mechanical alloying of elemental powders. The former techniques suffer from limitations such as porosities, volatilisation of Al and hence lack of control on Al content of the final product, difficulty in deformation processing and machining of the as cast ingots, composition variation (inhomogeneity) in the cast ingot, etc. Hence, the P/M technique seems to be a viable option to process these alloys since it overcomes most of the above limitations. However, the reports in the literature are limited to processing the Ru-Al alloy powders by mechanical alloying technique only. Applications demand near net shaped alloy products and hence information related to compaction and sintering of the alloy powders is required. Since no such information is available in the literature, the viability and the challenges in P/M processing of these alloys remain unexplored. A comparative study of alloys prepared through the solidification and P/M techniques would help in deciding the appropriate synthesising technique for these alloys.

2.3.8 Aim of the present investigation

The information available from the literature survey indicates that there is a great interest in developing binary and ternary ruthenium aluminide alloys for high temperature structural use. However, applications of these materials require proper processing technique, investigation of the microstructural evolution during processing and evaluation of mechanical and physical properties. There appears to be several issues and trends with regard to the phase diagrams, processing, microstructure and

properties of those alloys, which have not yet been fully explored. Some of these issues are highlighted below:

- The phase diagrams for both binary as well as various ternary Ru-Al-X (where, X = solute elements) systems are not completely explored.
- The various processing techniques and its effect on the microstructure need to be established.
- The sintering characteristics of the milled binary Ru-Al and ternary Ru-Al-X (where, X = solute elements) alloy powders have not been studied so far.
- The mechanical properties of Ru-Al alloys are strongly dependent on factors like alloy composition, type of solute addition, and the processing route adopted.
- The effect of heat treatment on these alloys needs to be established for the stability of the microstructures.
- A better understanding regarding the microstructural evolution during processing of these alloys by different techniques remains to be established.

The present study was therefore undertaken with the objectives of processing of binary Ru-Al, ternary RuAl-Ni and Ru-Al-Co alloys by solidification route as well as by powder metallurgy technique, investigation and comparison of the microstructure and properties of these materials. The solidification technique involves arc melting and heat treatment whereas the powder metallurgy technique of processing involves a sequence of attrition ball milling of the powder mixture, degassing of the milled powders, cold compaction followed by sintering at high temperature. The main objectives of the present investigation in brief are:

1. Study the extent of mechanical alloying during the attrition ball milling operation.
2. Study the microstructure of the milled powders as well as the microstructure of the sintered milled powder compact.
3. Study the effects of substitution of Ru with nickel and cobalt in Ru-Al alloys.
4. Microstructural characterisation of Ru-Al, ternary RuAl-Ni and RuAl-Co alloys processed by solidification route.
5. Determination of properties of the Ru-Al alloys processed by solidification method and powder metallurgy route.

6. Comparison of the structure and properties of the above alloys processed by mechanical alloying and solidification method.

Chapter-3

Experimental Procedures

The objectives of the present work have been highlighted in the previous chapter. The properties of the alloys depend on the microstructure, which are being influenced by the processing conditions. Hence, it was decided to study the mechanical properties and microstructure of Ru-Al, Ru-Al-Ni and Ru-Al-Co alloys processed by casting route as well as powder metallurgy technique. The subsequent sections explain in detail the experimental procedures followed in the present investigations. The experimental set-ups that were designed and fabricated for carrying out the investigations are also described.

3.1 Experimental set-ups

During the course of the present investigations, different set-ups were fabricated for experimental studies. The details of these set-ups are outlined in the following sub-sections.

3.1.1 Design and fabrication of the attrition mill

Mechanical alloying by attrition milling has gained considerable attention in recent years as an effective tool to produce alloy powders at a faster rate. High-energy ball milling has been widely used in laboratories and industry to process powder materials. One of the applications of high-energy ball milling process is to enable mechanical alloying of two or more metals. To achieve mechanical alloying, the milling must be performed under an inert atmosphere. The conventional mixing of powders in a ball mill results in a uniform mixture of elemental powders. However in this process, alloy formation does not take place. During attrition milling, alloying takes place in the solid state. The attrition milling chamber consists of a double walled cylinder, in which water is circulated in the annular region between the two walls, and a mechanical impeller. The powder mixture along with hardened steel balls in appropriate weight ratio is placed in the milling chamber and the impeller is rotated at

sufficient speed (rpm) with the help of DC motor. Inert gas can be admitted into the milling chamber for providing the required atmosphere during the milling process.

Figure 3.1 shows the 3D-view of the attrition mill designed and fabricated for the present studies. The assembled diagram for the milling chamber with impeller is shown in Figure 3.2. The details of the impeller and chamber are shown in Figures 3.3 (a–d). A summary of the features, which have been incorporated in the design of the milling chamber, are:

- Mainframe structure to hold the motor driven milling assembly with provision for height adjustment of the milling chamber.
- A 0.5 hp DC motor whose speed could be set at any desired constant value between 100 to 1400 rpm with an electronic circuit, for propelling the impeller.
- Provision for continuous inert gas purging in the chamber during the milling process.
- Continuous cooling of the milling chamber walls by cold water circulation.

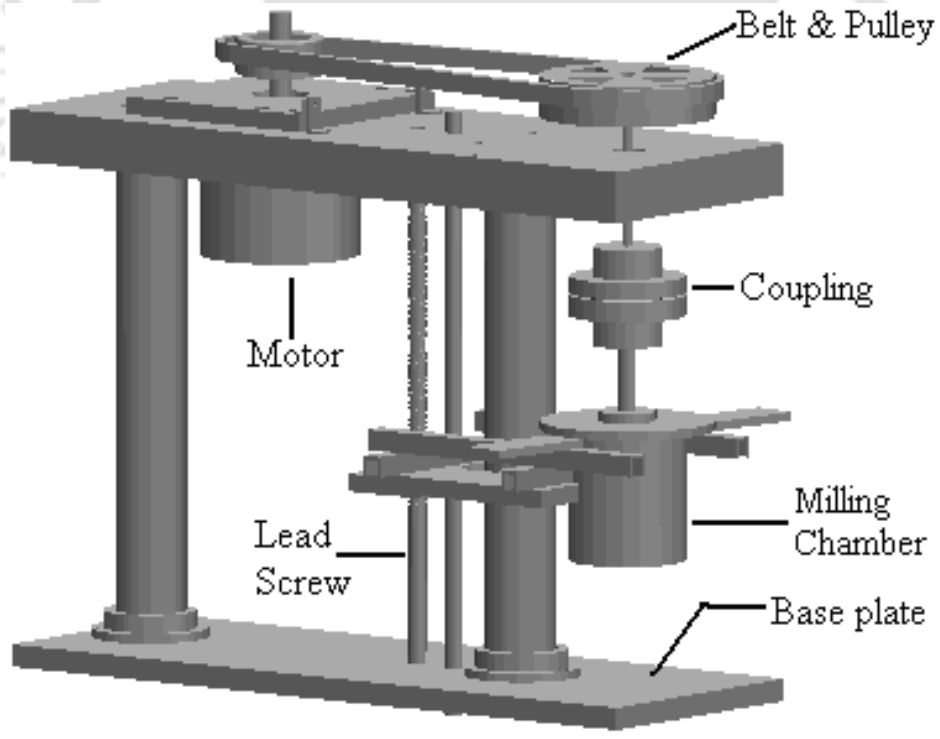

Figure 3.1: Assembled diagram for the attrition milling machine

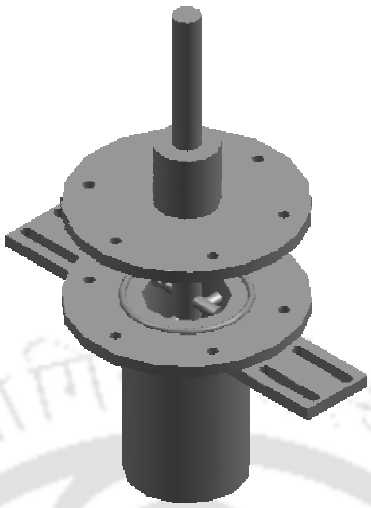

Figure 3.2: Assembled diagram for milling chamber

3.1.2 Fabrication of glove box

Handling of the milled powder requires care, especially when the materials have a high affinity for oxygen. Aluminium powder becomes highly reactive due to the severe plastic deformation and size reduction during the milling process. During the milling operation, powder samples need to be taken out at regular time intervals for structural analysis. Although most of the mechanical energy expended during mechanical alloying is converted into heat energy, the powder absorbs a large part of the energy. In addition, as the particle size reduces to nanometer sizes, the high surface area to volume ratio (S/V) becomes very high. This high S/V ratio makes the powder particles highly pyrophoric when they come in contact with oxygen. To prevent this, handling of the milled powders in either an oxygen-free or an inert atmosphere is necessary. Therefore an inert gas glove box was designed and fabricated, which is shown in Figure 3.4.

The glove box of dimensions 1.5 m (L) × 1.0 m (W) × 1.0 m (H) was made with welded mild steel sheets covering on five of its sides and a poly methyl metha-acrylate (PMMA) sheet covering the front side. A pair of 8-inch neoprene rubber gloves (Make - Sigma-Aldrich) was fixed to the PMMA sheet to permit manipulation inside the box. Neoprene O-rings provide the necessary vacuum isolation for the gloves and the door. Air inside could be pumped out using a rotary pump (not shown in Figure 3.4) and inert gas can be purged through an inlet valve.

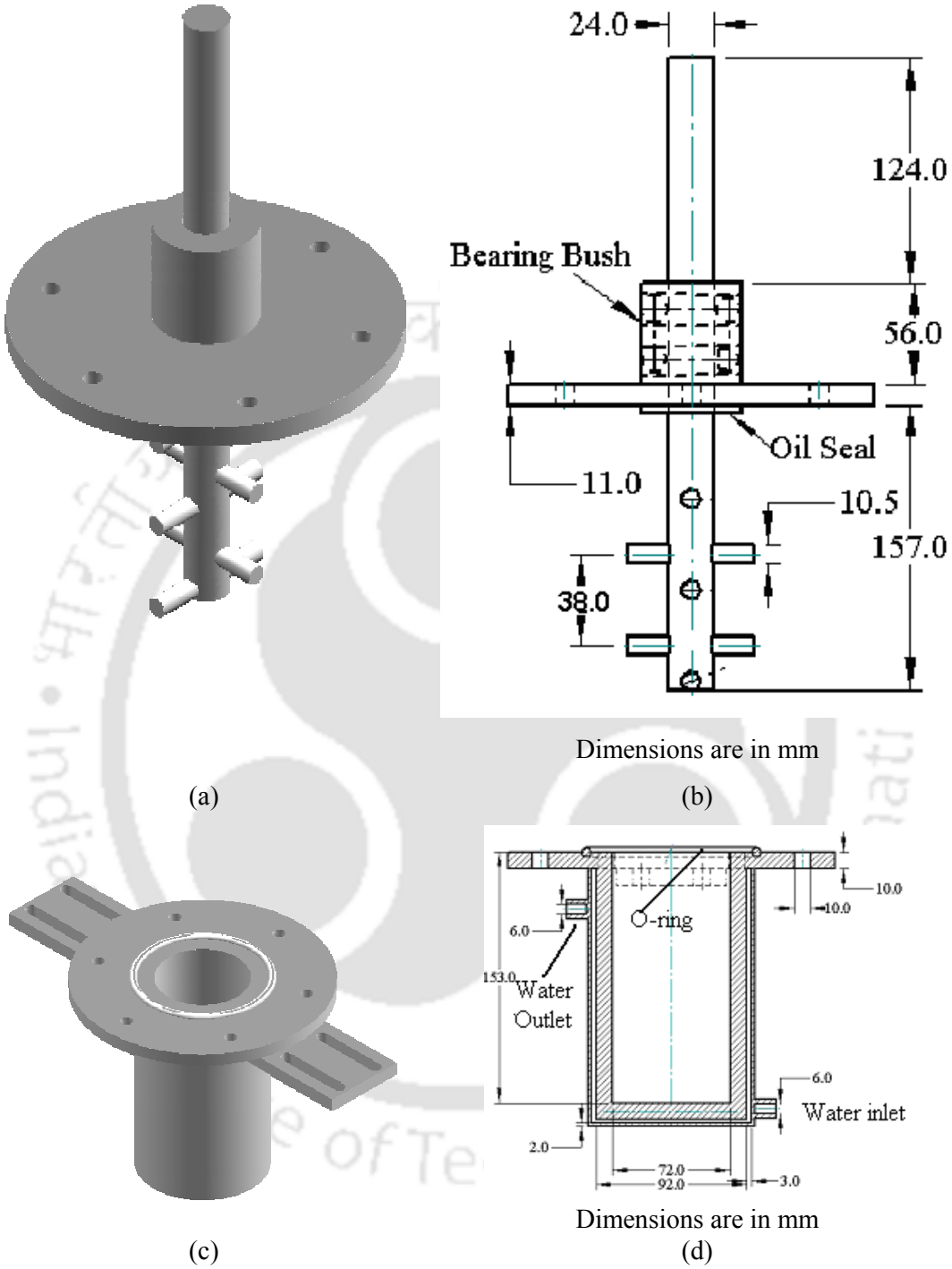

Figure 3.3: Details of the impeller and milling chamber (a) Part view of the impeller, (b) orthographic view of the impeller, (c) Part view of the milling chamber and (d) Cross-sectional view of the milling chamber

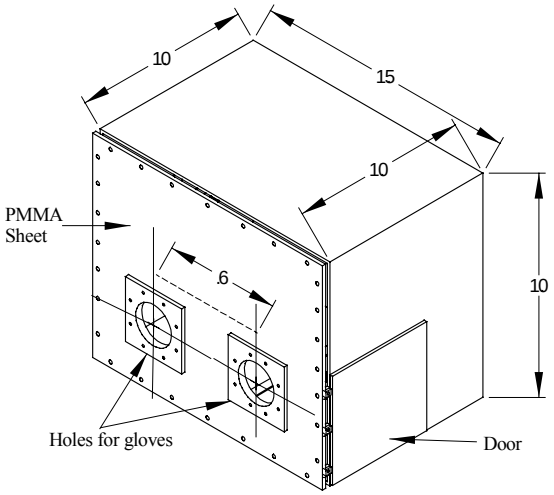

(Dimensions are in metres)
Figure 3.4: Diagram for the Glove Box

3.1.3 Fabrication of cold compaction die and punch

It is necessary to cold compact the milled alloy powder before sintering. Cold compaction die was designed and fabricated. The cold compaction die was a split die having 10 mm bore. The split die was fabricated to facilitate easy removal of the cold compacted cylindrical pellets from the die after compaction. Both punch and die were made of EN-24 steel. The top punch, bottom punch and the pressure pad were heat treated to enhance their compressive strengths. The diagram of the die and punch assembly is shown in Figure 3.5 and the detailed view of one part of the split-die is shown in Figure 3.6.

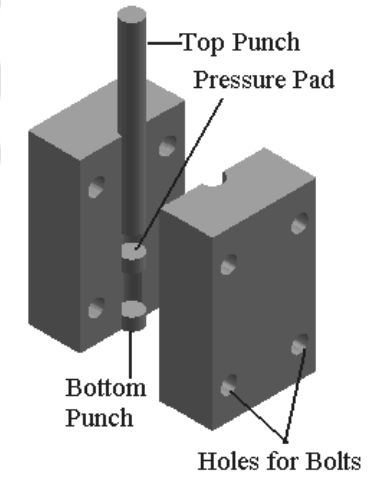

Figure 3.5: Split-die for cold compaction

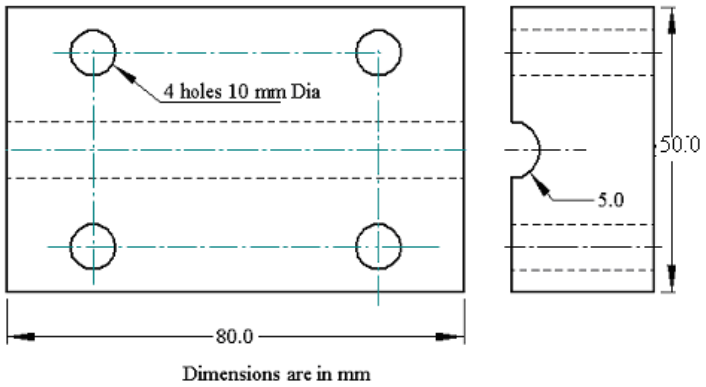

Figure 3.6: Detailed views of one part of the split-die

3.1.4 Degassing unit

A process control agent (PCA) is added to facilitate the milling operation. After completion of milling, the PCA, which usually decomposes at low temperatures, is to be removed from the alloy powder prior to further processing. In addition, it is also required to remove any gases adsorbed on the powder surface, before cold compaction. A degassing set up was fabricated for this purpose. The set-up consists of a copper tube of 40 mm ID, 1 mm wall thickness and 300 mm long, closed at one end, in which the milled powder mixture was placed. The lower part of the pipe was placed inside an electric furnace, while the other end was connected to a rotary pump. A low pressure of $< 10^{-2}$ mbar was maintained while the closed end was slowly heated to a temperature of 300 ˚C. A water-cooling arrangement was provided so as to avoid heating of the neoprene O-ring at the flanged area of the pipe. The temperature inside the pipe was held at 300 °C for 2 hours and then slowly cooled to room temperature. Figures 3.7 and 3.8 show the part view and the detailed view of the degassing unit, respectively.

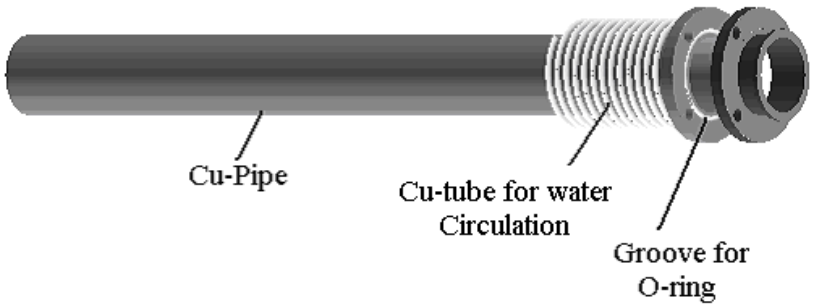

Figure 3.7: Part view of degassing unit

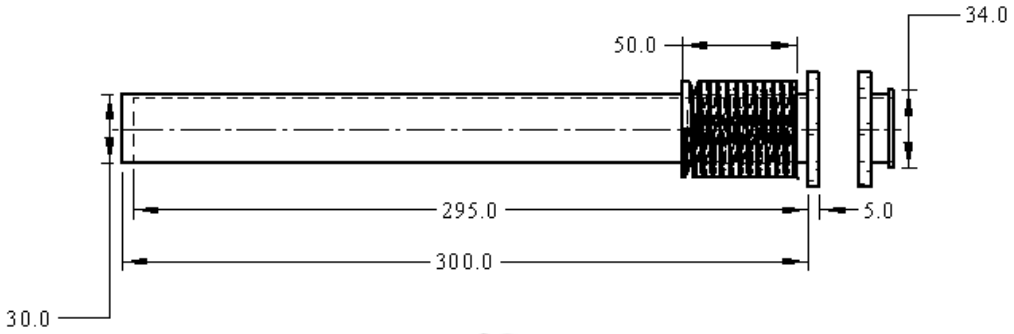

(Dimensions are in mm)

Figure 3.8: Detailed view of the degassing unit

3.1.5 Sintering furnace

The furnace used for the sintering of the cold compacted pellets was a commercial 1700 °C tubular furnace with inert gas purging facility (OKAY Electric Furnace, Make - Bysakh & Co). The furnace temperature can be maintained at any set temperature with an uncertainty of ± 2 °C with the help of a PID temperature controller.

3.2 Experimental procedures and principles

In the following sub-sections details of the experimental procedures and the principles of the techniques that were used in the course of these investigations are outlined.

3.2.1 Mechanical alloying of Ru-Al and Ru-Al-X (X = Ni, Co) powder mixtures

Mechanical alloying of the elemental powder mixtures were carried out in the attrition mill using 9.5 mm diameter hardened steel balls. A total weight of 100 grams of powder mixture was used for each batch of mechanical alloying. Elemental ruthenium powder of purity > 99.4% with average size of 4 μm (obtained from Impala Platinum Holdings, South Africa), aluminium powder of purity 99.7% and average particle size 7 μm (obtained from Burgoyne), nickel powder of purity 99.9% and average particle size 30 μm (obtained from s.d. fine –Chem Ltd, Boisar) and cobalt powder of purity 99.9% and average particle size of ± 100 mesh size (~ 149 μm) (obtained from Aldrich Chemical Company, Inc. USA) were used as starting materials for mechanical alloying. SEM micrographs for the elemental powders are shown in

Figure 3.9 (a-d). It can be seen that the ruthenium powder has a spongy shape, aluminium powder has irregular rounded shape whereas nickel and cobalt powders have spherical shapes.

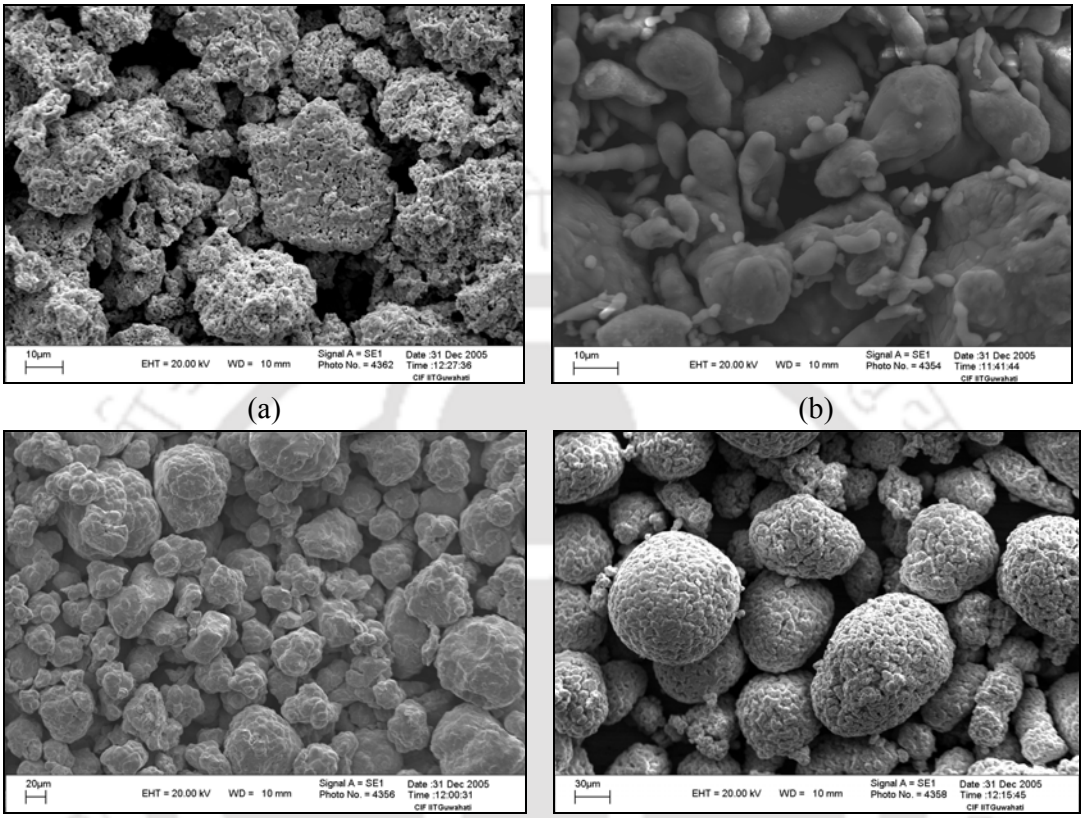

Figure 3.9: SEM micrographs corresponding to the elemental (a) Ruthenium, (b) aluminium, (c) Nickel and (d) Cobalt powders

The nominal compositions of the alloys that were studied are as follows:

1. $Ru_{47}Al_{53}$
2. $Ru_{32}Al_{50}Ni_{18}$
3. $Ru_{43}Al_{39}Ni_{18}$
4. $Ru_{38.5}Al_{16.5}Ni_{45}$
5. $Ru_{32.5}Al_{32.5}Co_{35}$
6. $Ru_{23.5}Al_{21.5}Co_{55}$

Initial mixtures of Ru and Al powders were corresponding to the compositions $Ru_{50}Al_{50}$ and $Ru_{49}Al_{51}$. Milling of these two powder compositions did not result in the formation of intermetallic RuAl phase even up to 100 hours of milling. However,

milling of the $Ru_{47}Al_{53}$ powder composition resulted in the formation of RuAl phase and is reported in this present study.

Since alloying is one of the practical routes for further alloy development, ruthenium was substituted in part by nickel and cobalt. This would reduce cost of these platinum group metal alloys and at the same time would modify the physical as well as mechanical properties. The selected ternary Ru-Al-Ni alloy compositions investigated in the present study are shown on the partial isothermal section at 1250 °C of the ternary phase diagram [53]. Since $Ru_{32}Al_{50}Ni_{18}$ composition (point "1" in Figure 3.10) is basically $(Ru,Ni)_{50}Al_{50}$, in this alloy composition ruthenium is substituted by nickel while maintaining the stoichiometric composition. This alloy composition falls in the single-phase (β_2) region of the ternary Ru-Al-Ni phase diagram. The alloy compositions consisting of $Ru_{43}Al_{39}Ni_{18}$ (point "2" in Figure 3.10) and $Ru_{38.5}Al_{16.5}Ni_{45}$ (point "3" in Figure 3.10) are selected from two-phase (β_2 + Ru) and three-phase (γ + β_2 + Ru) regions of the isothermal section shown in Figure 3.10, respectively. In the Figure 3.10, B2-RuAl is designated as "β_2" and Ni solid solution as "γ".

The partial isothermal section at 550 °C of Ru-Al-Co alloy system is shown in Figure 3.11 [77]. The alloy compositions, *viz.,* $Ru_{32.5}Al_{32.5}Co_{35}$ (point "1" in Figure 3.11) and $Ru_{23.5}Al_{21.5}Co_{55}$ (point "2" in Figure 3.11) are selected from the two-phase (β + Ru) and three-phase (β + γ + α) fields, respectively. In this figure RuAl and Co-solid solution are designated as "β" and "α", respectively.

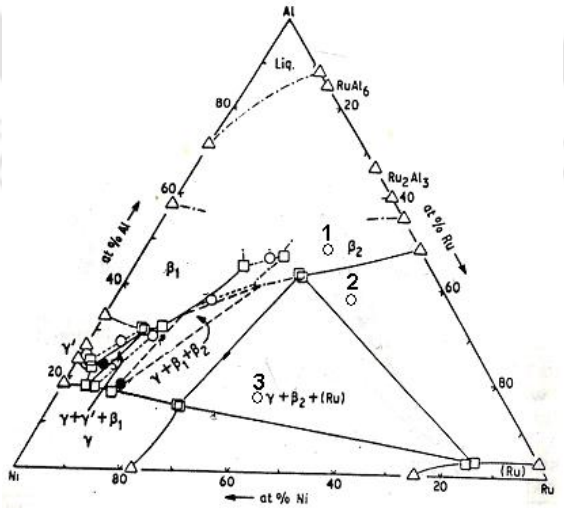

Figure 3.10: Partial isothermal section of Ru-Al-Ni alloy system at 1250 °C [53]

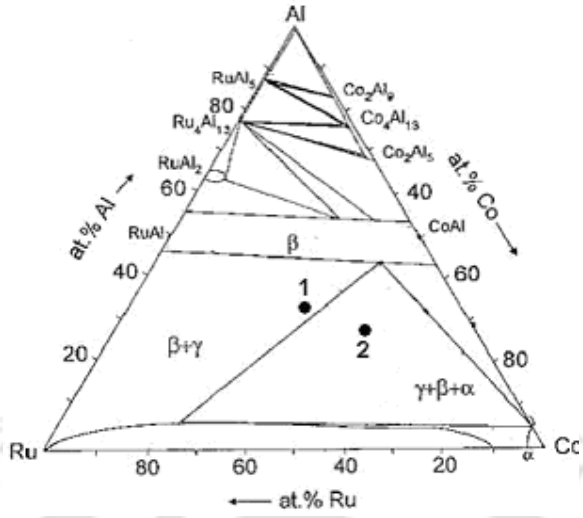

Figure 3.11: Partial isothermal section of Ru-Al-Co alloy system [77]

A constant ball to powder weight ratio of 10:1 was maintained throughout the milling process. The milling chamber was continuously purged with dry, high purity (99.999%) argon gas during milling. Water circulation through the water cooling jacket surrounding the milling chamber was ensured both during the milling process and till the powder samples were transferred out of the milling chamber. 1 wt.% stearic acid ($C_{18}H_{36}O_2$) was introduced as process control agent (PCA) at the starting of the milling process and 0.5 wt.% stearic acid was added after every 10 hours of milling. Milling was carried out at a constant impeller speed of 400 rpm. The mill was operated continuously for 5 hours followed by 2 hours rest. Whenever sample of milled powder mixture was taken out for analysis, it was ensured that the entire operation was performed inside the inert gas glove box under argon atmosphere. The extracted samples were then sealed and preserved in vacuum desiccator under residual argon atmosphere.

3.2.2 Characterisation using X-ray diffraction

Structural analyses of the milled powder samples were carried out using a commercial X-ray diffraction system (SEIFERT XRD 3003 T/T). Cu K_α radiation (λ=1.5405 Å) with a nickel filter was used for all analysis. The instrument was calibrated with a standard silicon reference sample. The XRD patterns were recorded with 40 kV acceleration potential and 30 mA tube current. The theta-theta goniometer was used in the reflection (Bragg-Brentano) geometry shown in Figure 3.12. A thick layer of milled powder sample spread over a poly methyl metha-acrylate (PMMA) plate

was used for recording the X-ray diffraction (XRD) patterns. The XRD data provides the variation of intensity/counts per second (cps), recorded by the detector (scintillation counter) as a function of 2θ, where θ is the glancing angle. XRD patterns were recorded by varying 2θ from 10° to 80° in steps of 0.05°.

A typical XRD pattern of milled Ru-Al powder mixture corresponding to the composition $Ru_{47}Al_{53}$ is shown in Figure 3.13. Sharp crystalline (Bragg) peak in the XRD pattern is the typical signature of a crystalline material. With an increase in the milling duration the powder mixture is subjected to large plastic deformations due to the impact of the hardened steel balls within the milling chamber. Continuous impact of the balls inside the milling chamber increases the micro-strain in the constituent phases and also reduces the sizes of the crystallites. These phenomena of increase in micro-strain and reduction in crystallite size are reflected in the XRD pattern by observation of peak broadening. A new phase formation during milling process is confirmed by observation of a new XRD pattern usually with the appearance of new peaks specific to the new phase formed. Figure 3.13 shows a typical peak broadening phenomena for the peaks labelled as 1 and 1^* corresponding to the reflection from a specific plane at different duration of milling. The intensity is also observed to be reduced with increase in the milling time. New phase formation is confirmed by observation of new XRD peaks (e.g., peak labelled as 2) as shown in figure.

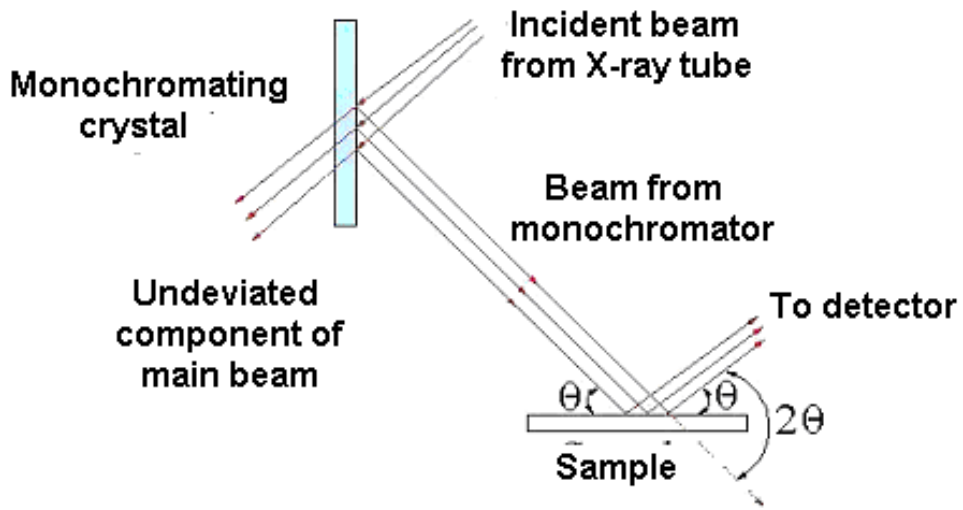

Figure 3.12: Ray diagram of an X-ray diffractometer.

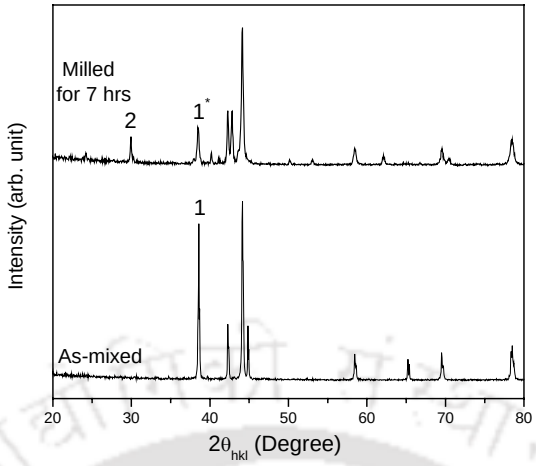

Figure 3.13: A typical XRD pattern for Ru-Al powder mixture

Indexing of different XRD peaks was carried out by a search-and-match process with the ICDD (International Centre for Diffraction Data) powder diffraction file (PDF) data file. The powder diffraction files that were used to index the reflections from different elements/phases are given in the Table 3.1. The extent of alloying was determined qualitatively by monitoring the relative intensities of the different peaks. In this thesis the phases are written within square brackets to differentiate them from the respective elements.

Table 3.1: PDF data files for elements and phases

Element/phase	PDF file	System	Crystal structure	Lattice parameter (Å)
Al	04-0787	Cubic	*fcc*	a = 4.0494
Ru	06-0663	Hexagonal	*hcp*	a = 2.7058 c = 4.2819
Ni	04-0850	Cubic	*fcc*	a = 3.52
Co	01-1278	Hexagonal	*hcp*	a = 2.51 c = 4.07
RuAl	29-1404	Cubic	*B2*	a = 2.95
NiAl	02-1261	Cubic	*B2*	a = 2.88
CoAl	03-1192	Cubic	*Simple*	a = 2.86
$RuAl_2$	19-0045	Orthorhombic	*fco*	a = 8.012 b = 4.717 c = 8.785
Al_2O_3	82-1468	Hexagonal	*RC*	a = 4.7589 c = 12.99

The crystallite sizes of different phases present in the milled powder samples and the micro-strain in the phases resulting from the milling process were estimated

from the full width at half maximum (FWHM) of the respective XRD (X-ray diffraction) peaks using the Williamson-Hall method [95]. The peak broadening (β_{hkl}) observed in the XRD pattern during milling can be attributed to particle size (β_s) and micro-strain (β_ε) effects. β_s of a Bragg reflection (*hkl*) originating from a finite size of powder follows the Scherrer equation [96],

$$\beta_s = \frac{k\lambda}{B\cos\theta_{hkl}} \qquad (3.1)$$

where, λ is the wavelength of X-rays, θ_{hkl} is the Bragg angle (peak maximum), B is the mean effective size of the crystallite in the coherent scattering region normal to the reflecting planes and $k = 1$. The strain induced peak broadening is given by Wilson formula [95],

$$\beta_\varepsilon = 4\varepsilon\tan\theta_{hkl} \qquad (3.2)$$

where, ε is micro-strain in the crystallites which is assumed to be proportional to the square root of the dislocation density [95].

The strain induced broadening (β_ε) and broadening due to size effect (β_s) are assumed to be mutually independent. The FWHM (β_{hkl}) observed in the XRD pattern can be correlated to β_ε to β_s using the relation,

$$\beta_{hkl} = \beta_s + \beta_\varepsilon = \frac{\lambda}{B\cos\theta_{hkl}} + 4\varepsilon\tan\theta_{hkl} \qquad (3.3)$$

B and ε were estimated from the plots of $\beta_{hkl}\cos\theta_{hkl}$ versus $4\sin\theta_{hkl}$ for all the peaks.

In order to estimate the mean particle size and the micro-strain in as-milled powders, analysis of the X-ray peak profiles was carried out. For this, the XRD data was collected at a step size of 0.002° s^{-1} with 10 s sampling time at each step. The X-ray peak profile from a single reflection could be approximated to a Lorentzian curve. Multiple (up to three) Lorentzians were used for analysing overlapping peaks. Figure 3.14 shows a typical fit in which the open circles correspond to the XRD data, the dotted line corresponds to the sum of the three Lorentzian profiles and the solid lines represent the individual Lorentzian fit for the three peaks. The full width at half maximum (FWHM) was obtained from the fit parameters for the various peaks.

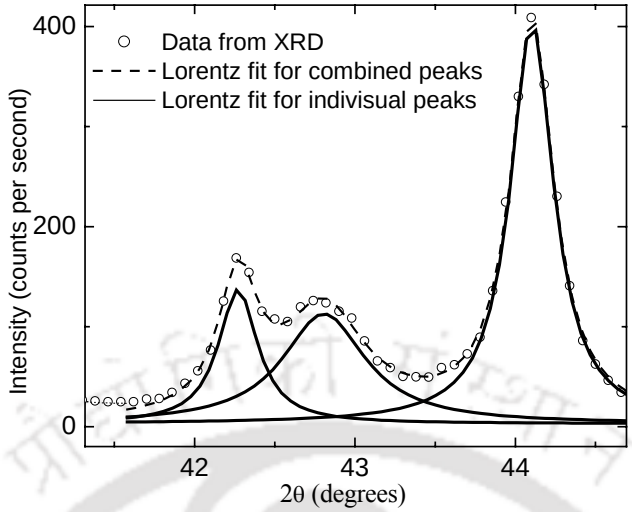

Figure 3.14: Lorentzian curve fitting and peak separation for milled powder mixture

3.2.3 Processing of Ru-Al and Ru-Al-X (X = Ni, Co) alloy powders

The milled powder mixtures were first degassed in the degassing unit in order to remove the PCA. The degassed powder mixtures were cold compacted using 10 mm diameter die under a pressure of 500 MPa. Camphor dissolved in methanol was applied on the die and punch surface as lubricant during cold compaction to minimise friction between the die and punch as well as to avoid cold welding of the alloy powder on to the die surface. The cold compacted cylindrical pellets were then pre-sintered at a temperature of 300 °C for 3 hours in order to remove the lubricant used during cold compaction. These pellets were subsequently sintered at a temperature range of 1450 °C in the sintering (tubular) furnace for 24 hours and then furnace cooled to room temperature. The typical heating cycle used in sintering of cold compacted pellets is shown in Figure 3.15. Argon gas was continuously purged through the tube of the furnace during the entire sintering cycle. The density of the sintered samples was measured by Archimedes' principles. Xylene was used as the immersion fluid for density measurements of the sintered pellets.

3.2.4 Processing of Ru-Al and Ru-Al-X (X = Ni, Co) by casting technique

For processing by solidification route, the elemental powders of compositions mentioned in section 3.2.1 were mixed in an agate mortar and pestle. The powder

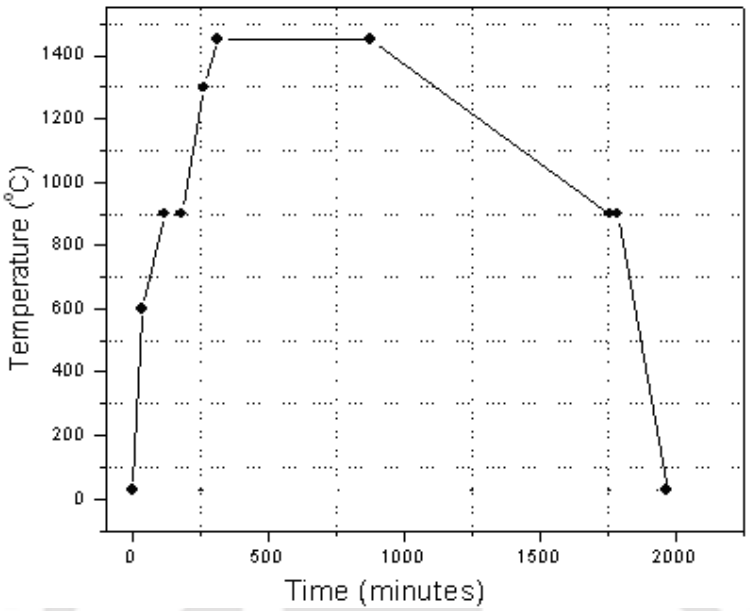

Figure 3.15: A typical heating cycle used in sintering

mixture was compacted at a pressure of 200 Mpa in a die and punch assembly to obtain a rectangular rod approximately of size 30 mm (L) × 12 mm (W) × 10 mm (B). This was done to prevent the loose powder particles from flying off during the arc melting stage. These cold compacted rods were kept in the water-cooled copper hearth of a laboratory level arc furnace and evacuated to a pressure of 10^{-5} mbar. The evacuated furnace chamber was then filled with high purity (99.9%) argon gas. Melting of the compacted rod was carried out by striking the arc between a tungsten electrode and the compacted specimen. The alloy was melted 2-3 times to ensure homogeneity of the cast alloy. The samples were then allowed to solidify in the furnace hearth. The cast alloys were subsequently annealed at 1450 °C for 24 hours in the tubular furnace (*cf.* section 3.1.5) under argon atmosphere. Annealing Ru-Al-Co alloys at 1450 °C resulted in the melting and hence these alloys were annealed at 900 °C for 8 hours.

3.2.5 Microstructural characterisation of Ru-Al and Ru-Al-X (X = Ni, Co) alloys processed by powder metallurgy and casting routes

Following sub-sections outline the details of the microstructural characterisation techniques used in this investigation including the sample preparation for the studies.

Sample preparation

Cylindrical shaped sintered alloy pellets of 1-2 mm thickness were obtained by sectioning arc melted rods using a precision saw machine (Buehler ISOMET 2000 Precision Saw) equipped with diamond wheel. These sliced samples were mounted in thermosetting resins using a hot mounting press (Simplimet 2 Mounting press, Buehler). These mounted samples were polished with a variable speed grinder polisher (Ecomet, Buehler) using SiC polishing papers of grit sizes 250, 350, 400 and 600 in a sequence. Subsequently, the samples were diamond polished with 10 μm, 5 μm and 3 μm sized diamond paste. Final polishing was carried out using 0.5 μm sized alumina suspension in distilled water on a polishing cloth. As-cast as well as cast and annealed samples were also prepared using similar methods for microstructural studies.

For morphological studies of as-milled powder mixtures, small quantity (around 0.3 grams) of powders was sprinkled on polished copper studs of diameter 8 mm. Studies on the milled powders were also carried out using resin mounted polished samples. In this, the milled powder mixture was first mixed with thermosetting resin grains in an agate mortar and pestle. Then this mixture was hot mounted using hot mounting press. The powder particles settle on the lower part of the mounting resin due to higher density. The mounted samples were subsequently polished using 0.5 μm sized alumina suspension in distilled water on a polishing cloth

Characterisation by optical microscope

Microstructural observation of the polished sintered as well as cast samples was carried out using Carl Zeiss Axiotech upright reflected beam optical microscope. The image of the specimen was captured by a CCD (charged coupled device) camera fitted on the top of the instrument. The image from the CCD camera is read into a computer memory and processed by KS-300 image analysis software.

Characterisation by scanning electron microscope (SEM)

A finely focused electron beam scan across the surface of the sample generates secondary electrons, backscattered electrons and characteristic X-rays. These signals are collected by detectors to form images of the sample on a cathode ray tube screen. The electron–solid interaction and the imaging modes are depicted in the Figure 3.16. Secondary Electron (SE) imaging shows the topography of surface features a few

nanometers (nm) across. Materials are usually viewed at magnifications up to 100,000x without the need for extensive sample preparation and in a non-destructive way. Backscattered Electron Imaging gives the image based on composition contrast. Features as small as 10 nm can be resolved and composition variation within ± 0.2 at.% can be determined. Features seen in the SEM image may then be immediately analysed for elemental composition using energy dispersive X-ray spectroscopy (EDS). Electron imaging was carried out to observe the microstructure of the samples at high magnification using Leo make 1430 VP model scanning electron microscope (SEM). Composition analysis during the microstructural characterisation was carried out using OXFORD INCA EDS system attached with the SEM. The reported compositions are the average of at least 4 independent determinations in each case. Extra pure cobalt was used as standard reference while determining compositions of constituent phases in the sample. Imaging of different specimens was obtained with 10-20 keV energy and 10-20 mm working distance. All EDS spectra were recorded at 20 keV energy with 15 mm working distance. During imaging as well as EDS analysis, probe current varied between 3.4 nA to 500 pA and filament current varied between 2.40 A to 2.73 A. All chemical compositions reported in this study refer to as atomic percentage (at.%) only, unless otherwise mentioned.

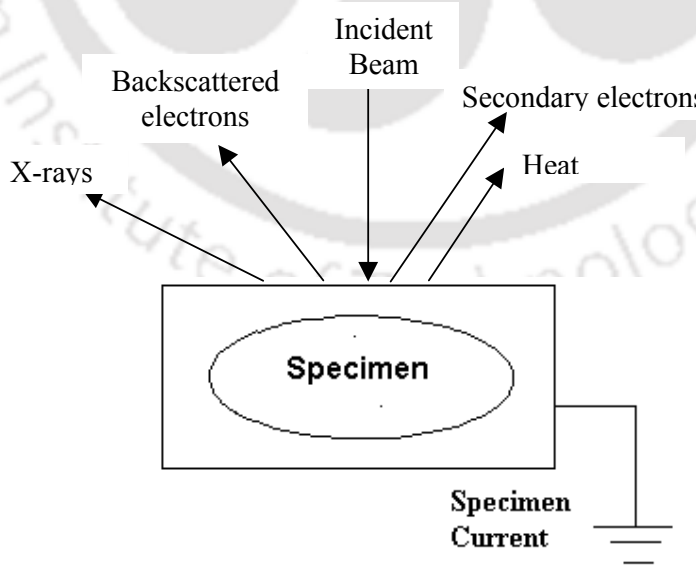

Figure 3.16: Electron-solid interaction and the imaging mode in SEM

3.2.6 Mechanical properties of Ru-Al and Ru-Al-X (X = Ni, Co) alloys processed by powder metallurgy and casting routes

In the following sub-sections, the experimental procedures of hardness and compression testing followed in the course of the investigations on sintered as well as on cast alloy samples are described.

Overall/Microhardness

Indentation hardness is of major engineering interest for metals and its alloys. Many metallurgical problems require the determination of hardness over very small areas such as constituent phases. One of the popular measurement methods is Vickers hardness testing. The Vickers hardness test uses a square-base diamond pyramid as the indenter. The included angle between opposite faces of the pyramid is 136°. Figure 3.17 shows the geometry of Vickers square pyramidal indenter. Because of the shape of the indenter, this is frequently called the diamond-pyramid hardness test. The diamond-pyramid hardness number (DPH), or Vickers hardness number (VHN, or VPH), is defined as the load divided by the surface area of the indentation (expressed usually in kg. mm^{-2}). In practice, this area is determined from microscopic measurements of the diagonal length of the square impression (indentation). The VHN may be determined from the following equation:

$$VHN = \frac{2F\sin(\theta/2)}{d^2} \approx \frac{1.854F}{d^2} \qquad (3.4)$$

where, F = applied load, kg

d = average length of diagonals, mm

θ = angle between opposite faces of diamond = 136 ^{o}

Careful preparation of the sample surface is necessary prior to indentation hardness measurement. The specimens were given a metallographically polished finish. In the present investigation, hardness of the alloys processed by powder metallurgy and casting routes were determined using a microhardness tester (Microhardness Tester, Micromet 2101, Buehler) at room temperature. For microhardness measurement of the constituent phases in the alloy, indentations were made on the respective phase(s) using varying loads ranging from 5 -100 gmf. On the other hand, a load of

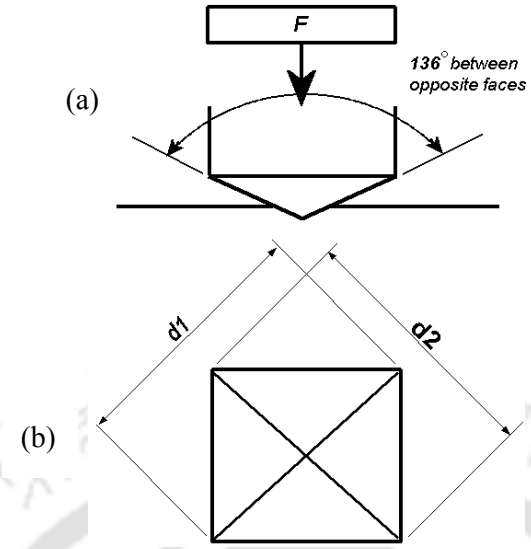

Figure 3.17: (a) Geometry of Vickers square pyramidal indenter and (b) d1 and d2 are the diagonals of the indentation made on the sample by a Vickers pyramidal indenter.

300 gmf was used to make the indentation extending over the different constituent phases present in the alloy material to determine the overall hardness value of the alloy material. Total indentation (loading) time of 25 seconds was used for the microhardness as well as overall hardness measurements. The diamond-pyramid indentation diagonals were measured with the microscope attached with the microhardness tester and were later confirmed using optical microscope / SEM observation. Figure 3.18 shows measurement of diagonals of such an indentation made on the cast and annealed $Ru_{43}Al_{39}Ni_{18}$ alloy by SEM. As far as possible, the measurements of the microhardness values of all constituent phases present in the alloys were performed. However, in certain cases, the fine size of the phase or the lack of optical contrast has made it difficult to evaluate the hardness of some of these phases. The microhardness values reported in this thesis are the average values of at least ten independent indentations made on each sample composition under identical loading conditions.

Compression testing

Compression testing on non-standard sintered samples was carried out on two alloy compositions ($Ru_{47}Al_{53}$ and $Ru_{38.5}Al_{16.5}Ni_{45}$). Testing of other alloy compositions

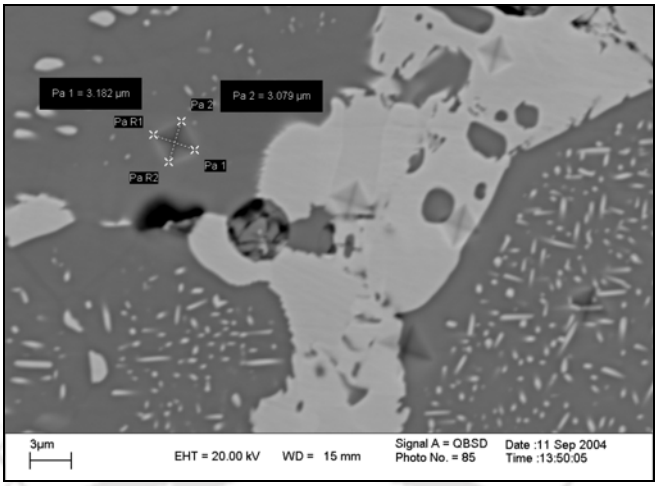

Figure 3.18: SEM micrograph showing a Vickers indentation made on the cast and annealed $Ru_{43}Al_{39}Ni_{18}$ alloy

was not possible because of the difficulty encountered in cold compacting the milled powders into cylindrical samples. The sintered samples were surface grounded at the two opposite faces to have parallel surfaces. This test was carried at room temperature. The scientists in the Materials Characterisation Division, ISRO, performed this test using standard procedures.

3.3 Determination of electrical properties of Ru-Al and Ru-Al-X (X = Ni, Co) alloys processed by powder metallurgy and casting routes

The electrical resistivity of the specimen was measured using the van der Pauw techniques for an arbitrarily shaped specimen [97]. The alloy specimens processed by powder metallurgy and casting routes were first polished to form plates of uniform thickness of ~ 0.8 mm. The specimens were accommodated in a sample stage made of alumina containing four stainless steel probes (pressure contact type). The probes were connected with stainless steel wires to a constant current source (Keithely, 220) and a nano voltmeter (Keithely, 2192). The sample stage was inserted into a tube into which argon gas could be purged. This tube was inserted into a tubular furnace. Electrical resistivity was measured from room temperature to 600 °C at intervals of 200 °C. All measurements were made under argon environment. The sample temperature was controlled within ± 3 °C during the measurement.

3.3.1 van der Pauw technique

The van der Pauw method involves applying a current and measuring voltage using four small contacts on the periphery of an arbitrarily shaped sample of uniform thickness. This method is particularly useful for measuring the electrical resistivity of very small samples because geometric spacing of the contacts is unimportant. Moreover, effects due to the sample size, which is the approximate probe spacing, are irrelevant.

Using this method, the electrical resistivity can be derived from a total of eight measurements that are made around the periphery of the sample with the configurations shown in Figure 3.19 [98]. Once all the voltage measurements are taken, two values of resistivity ρ_1 and ρ_2 are computed as follows:

$$\rho_1 = \frac{\pi}{\ln 2} f_1 t_s \frac{V_2 + V_4 - V_1 - V_3}{4} \tag{3.5}$$

$$\rho_2 = \frac{\pi}{\ln 2} f_2 t_s \frac{V_6 + V_8 - V_5 - V_7}{4} \tag{3.6}$$

where, V_1 to V_8 are voltages (in V), t_s is the sample thickness (in cm), and f_1 and f_2 are geometrical factors based on sample symmetry, which is unity for perfect symmetry. f_1 and f_2 are related to the voltage ratios Q_1 and Q_2, where,

$$Q_1 = \frac{V_2 - V_1}{V_4 - V_3} \tag{3.7}$$

$$Q_2 = \frac{V_6 - V_5}{V_8 - V_7} \tag{3.8}$$

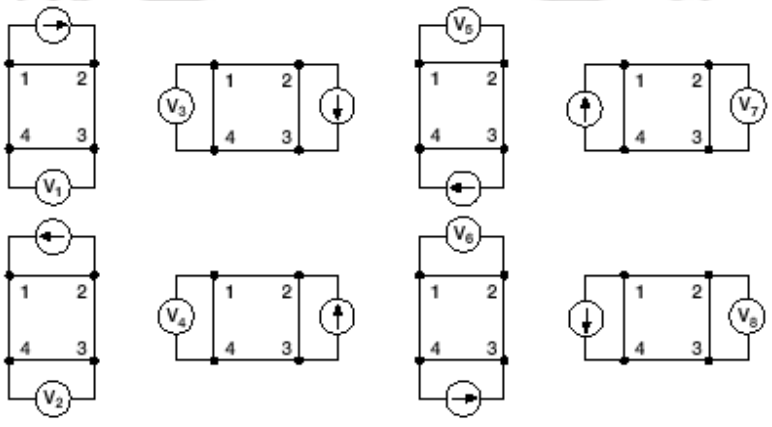

Figure 3.19: van der Pauw resistivity conventions [98]

Also, Q and f are related as follows:

$$\frac{Q-1}{Q+1} = \frac{f}{0.693} arc\cosh\left(\frac{e^{0.693/f}}{2}\right) \tag{3.9}$$

A typical plot of the function f versus Q is shown in Figure 3.20 [98]. The value of f can be found from the plot once the value of Q is determined. Once, ρ_1 and ρ_2 are determined, the average resistivity of the specimen can be obtained.

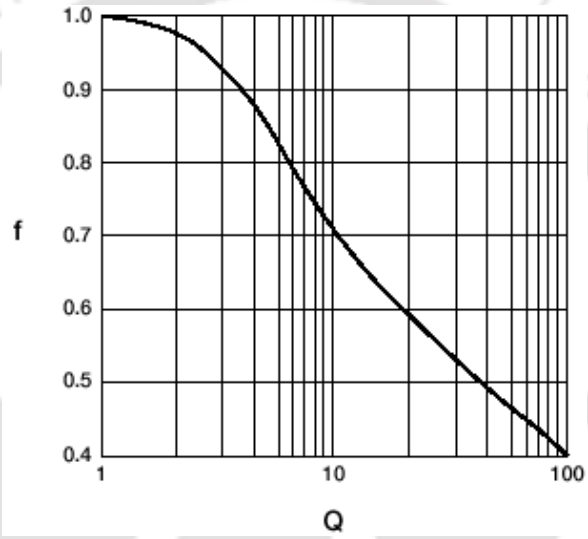

Figure 3.20: Relationship between f and Q [98]

Chapter –4

Results and discussion on binary Ru-Al alloy

The results of the studies carried out on Ru-Al alloys processed by powder metallurgy as well as by casting routes are summarised in the following sub-sections. The alloy composition of $Ru_{47}Al_{53}$ has not been investigated earlier by powder metallurgy route. The results of the microstructural investigations, hardness testing and electrical resistivity measurements of the alloys are presented in the following sub-sections.

4.1 Binary Ru-Al alloy processed by powder metallurgy route

The milling characteristics, microstructure of milled powder as well as sintered pellets, compression test results, microhardness and electrical resistivity data of the sintered alloy are presented and discussed in the following sub-sections. The milling characteristics and the extent of alloying are explained using XRD patterns and SEM-EDS data of samples milled for different time periods. The micro-strain and average crystallite size of different phases present in the milled powder mixture were determined from W-H plots.

4.1.1 Milling characteristics

Figure 4.1 shows the XRD patterns of Ru + Al elemental powder mixture with composition of $Ru_{47}Al_{53}$, milled for various time periods. This powder mixture as well as the composition will henceforth be referred to as Ru-Al powder mixture and RuAl composition respectively for the sake of convenience. In the case of the as-mixed Ru-Al powders, all the peaks expected within the 2θ range of 20° to 80° for Ru {i.e. (100), (002), (101), (102), (110) and (103) planes} and Al {i.e. (111), (200), (220) and (311) planes} are observed. Ru (100) and Ru (103) peaks overlap with Al (111) and Al (311) peaks, respectively. The reflections from Al planes were not discernible in the XRD pattern obtained after 2 hours of milling. No new peaks were observed at this stage of milling. XRD pattern obtained for the powder mixture milled for 7 hours revealed the presence of new peaks, which could be indexed to RuAl phase (ICDD file # 29-1404). These new peaks arising from the (100), (110), (111), (200) and (210) planes of the

RuAl phase are shown in Figure 4.1. Milling beyond 7 hours resulted in broadening of all the RuAl and Ru peaks present in the XRD pattern.

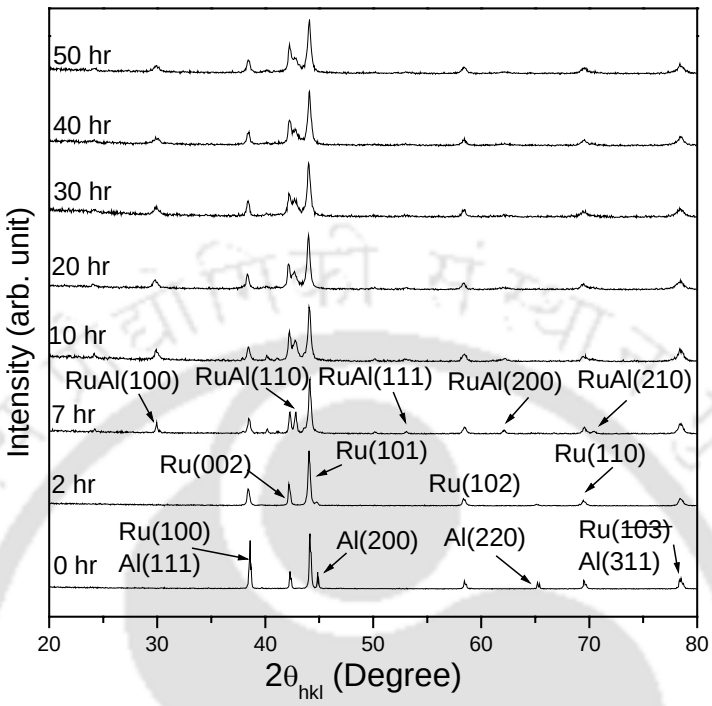

Figure 4.1: XRD patterns of Ru-Al elemental powder mixture milled for various time periods

The William-Hall plots (W-H plots) obtained from the XRD patterns of Ru-Al powder mixture milled for various durations are shown in Figures 4.2 (a) and 4.3 (a) for Ru and RuAl phases, respectively. The variation of average crystallite size and micro-strain induced in Ru phase as a function of milling time are shown in Figures 4.2 (b-c), respectively. The corresponding variations in RuAl phase are shown in Figures 4.3 (b-c), respectively. The average crystallite size of Ru decreased rapidly during the initial phase of milling. Since Ru is very brittle at room temperature, Ru particles fragment rapidly, resulting in a drastic reduction in crystallite size during the initial stage of milling. The size of Ru crystallites after 7 hours of milling was determined to be 826 nm, which reduced to 120 nm after 50 hours of milling. The size of RuAl crystallites formed after 7 hours of milling was determined to be 64 nm, which subsequently decreased to a size of 17 nm after 50 hours of milling. In both these cases, the micro-strain increased sharply with increasing periods of milling and attained a saturation value. The maximum micro-strains obtained for the Ru and RuAl crystallites were 0.00449 after 30 hours of milling and 0.00332 after 10 hours of milling, respectively.

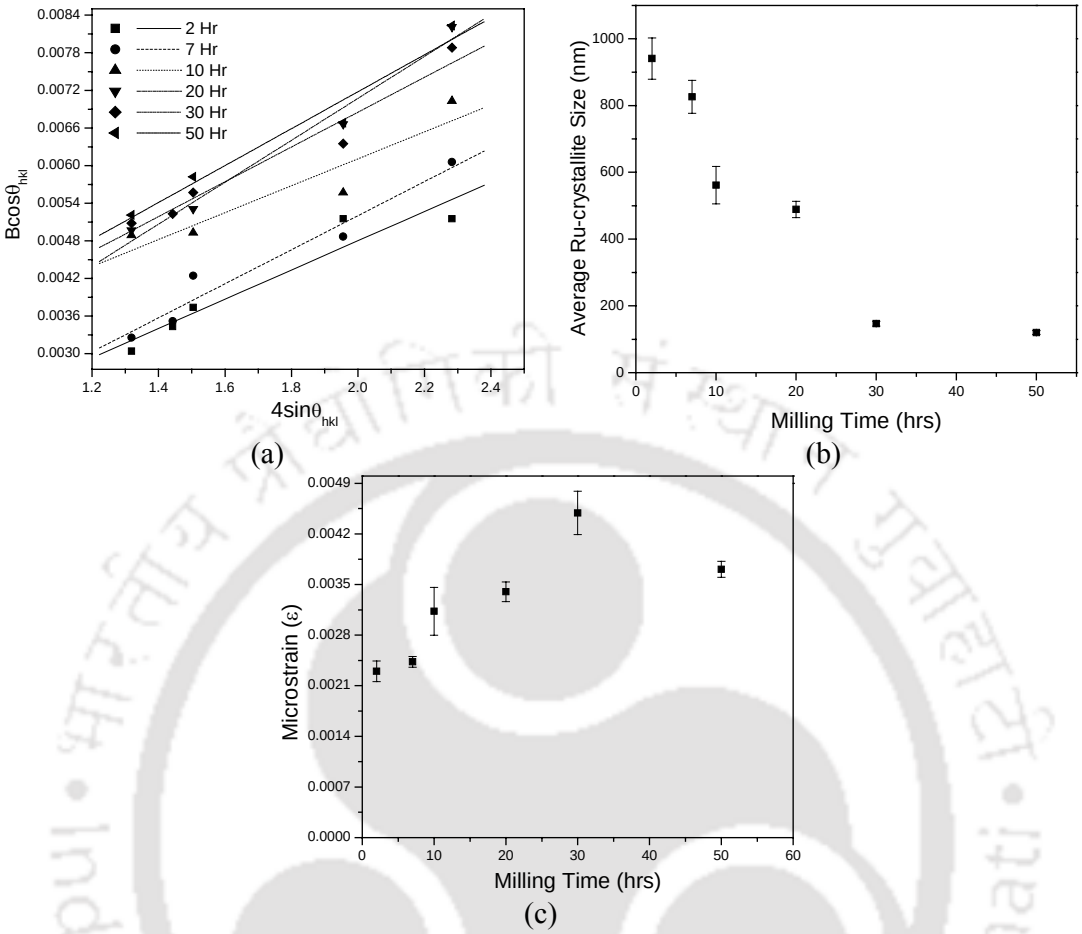

Figure 4.2: (a) W-H plot for Ru in different durations of milling of Ru-Al powder mixture, (b) Variation of Ru crystallite size with milling time and (c) Variation of micro-strain in Ru with milling time

Figure 4.4 (a) shows the XRD pattern of the Ru-Al powder mixture milled for 50 hours together with the XRD pattern of heat-treated powder mixture milled for 50 hours. The heat treatment was annealing at 1450 °C for 8 hours. Very sharp diffraction peaks corresponding to the reflections from the RuAl phase are visible along with two low intensity peaks at 2θ values of 35.5° and 57.8°, which could be best indexed to reflections from Al_2O_3. These low intensity peaks did not show up in the XRD patterns of the as-milled powder mixture. Small amount of unreacted Al might have oxidised during annealing of the powder mixture resulting in these two extra peaks seen in the XRD pattern. Reflections from unreacted Ru can also be seen in the XRD patterns. The XRD pattern revealed the stability of RuAl phase at high temperature (1450 °C).

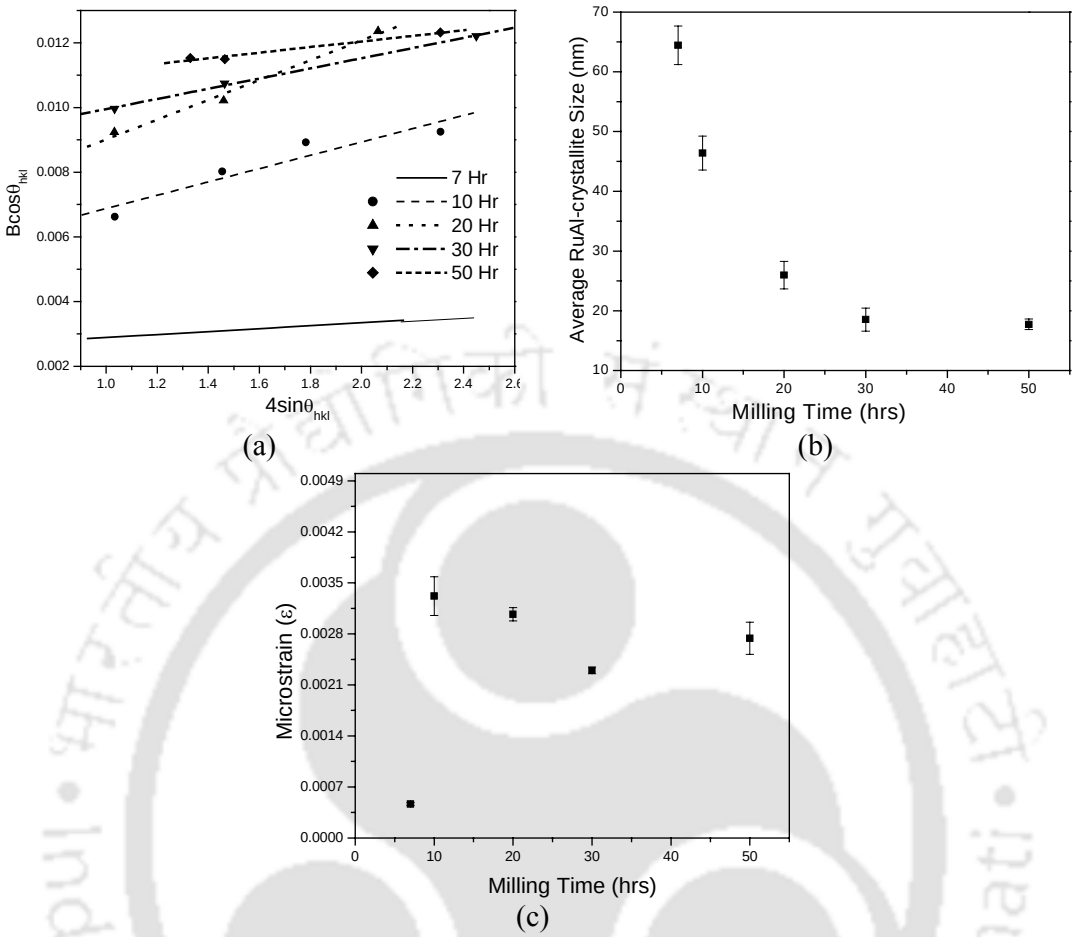

Figure 4.3: (a) W-H plot for RuAl in different durations of milling of Ru-Al powder mixture, (b) Variation of RuAl crystallite size with milling time and (c) Variation of micro-strain in RuAl with milling time

The W-H plots for the [Ru] and RuAl phases in the annealed powder mixture are shown in Figure 4.4 (b). The average crystallite sizes of Ru and RuAl present in the annealed powder sample were determined to be 190 nm and 83 nm and the micro-strains in Ru and RuAl were found to be 0.00217 and 0.00182, respectively.

4.1.2 Milled powder microstructure

SEM secondary electron (SE) micrographs of as-milled Ru-Al powder mixture milled for 2 hours are shown in Figures 4.5 (a-b). The EDS spectrum obtained, taken over a large area, for determining the overall composition of the powder mixture is shown in Figure 4.5 (c). The EDS analysis revealed an overall composition of $Ru_{56}Al_{44}$ of the powder mixture shown in Figure 4.5 (a). Figure 4.5 (a) shows a large number

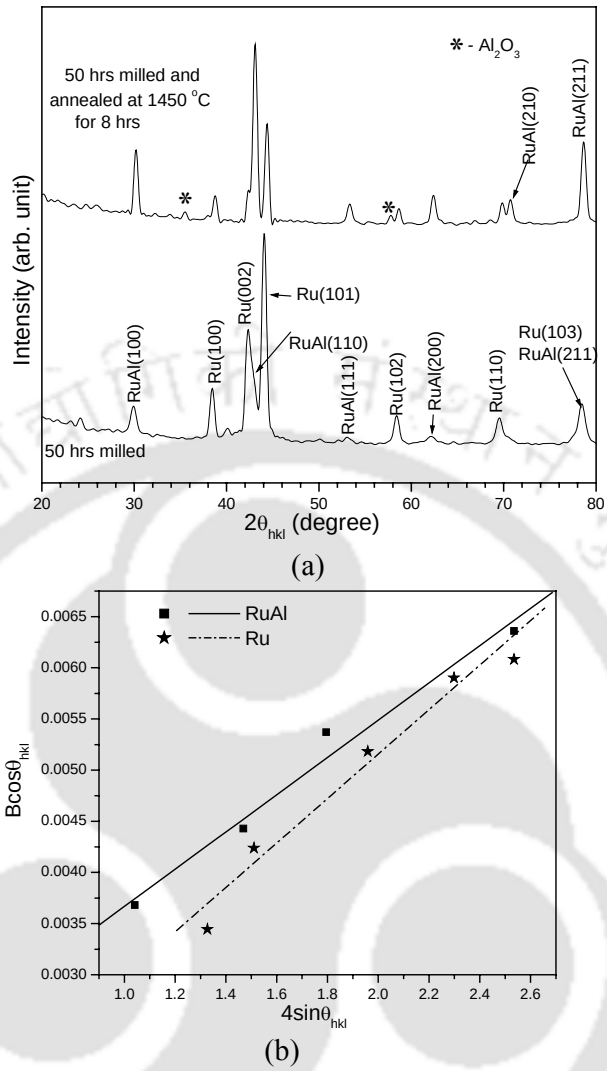

Figure 4.4: (a) XRD patterns of the as-milled Ru-Al powder mixture milled for 50 hours together with the annealed powder mixture milled for 50 hours and (b) W-H plots of Ru and RuAl in the Ru-Al powder mixture milled for 50 hours and subsequently annealed at 1450 °C

of fine particles, labelled as "A", along with coarse clusters consisting of a mixture of fine Ru and Al, labelled as "B". High magnification SEM micrograph of the powder cluster shown in Figure 4.5 (b) revealed flake-like morphology with the surface features indicating the presence of a thin layer on the surface. EDS spectra corresponding to the regions "A" and "B" of Figure 4.5 (a) are shown in Figures 4.5 (d-e), respectively. EDS analyses revealed a composition of $Ru_{33}Al_{67}$ for the region "B" and $Ru_{35}Al_{65}$ for the region labelled as "A". Both these regions "A" and "B"

correspond to the $RuAl_2$ phase. However, the formation of a ductile Al layer over brittle Ru particles during the milling process cannot be ruled out.

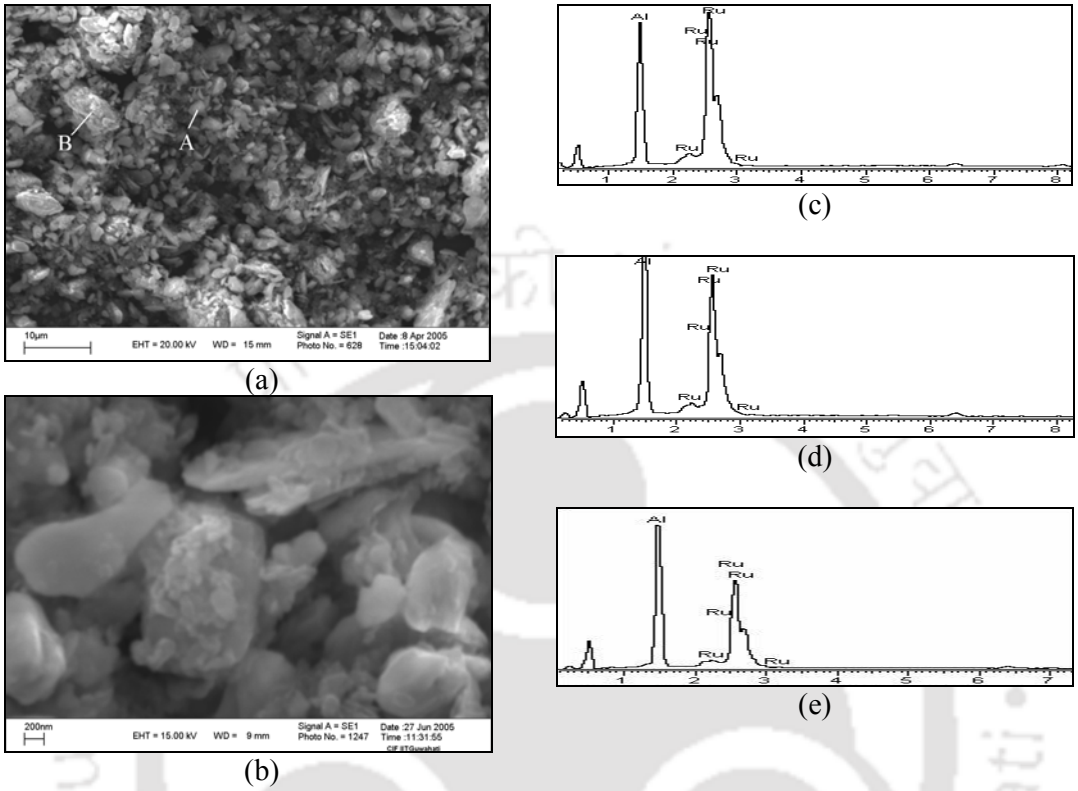

Figure 4.5: (a-b) SEM micrographs of Ru-Al powder mixture milled for 2 hours at low and high magnification, respectively; EDS spectra corresponding to the (c) overall composition of the powder mixture, (d) particle labelled as "A" and (e) particle labelled as "B" shown in Figure 4.5 (a)

To ascertain whether the particles were coated with the ductile Al layer, loose powders were mounted in thermosetting resin and subsequently polished for metallographic observations. Figures 4.6 (a-b) show the SEM micrographs of polished powder mixture milled for 2 hours. Figures 4.6 (c-d) show the EDS spectra corresponding to the powder particles labelled in the Figures 4.6 (a-b). Coarse powder particles labelled as "A" and "C" in Figure 4.6 (a) are ruthenium rich particles with average composition of $Ru_{87}Al_{13}$. Nanometer sized particles labelled as "B" and "D" in Figure 4.6 (a) are metastable phases with average composition of $Ru_{67}Al_{33}$ and fine particles of RuAl labelled as "E" in the Figure 4.6 (b) of composition $Ru_{44}Al_{56}$ were also observed in the milled powder mixture. EDS analysis clearly shows the formation of RuAl phase even after 2 hours of milling, although the same was not detectable by X-ray diffraction.

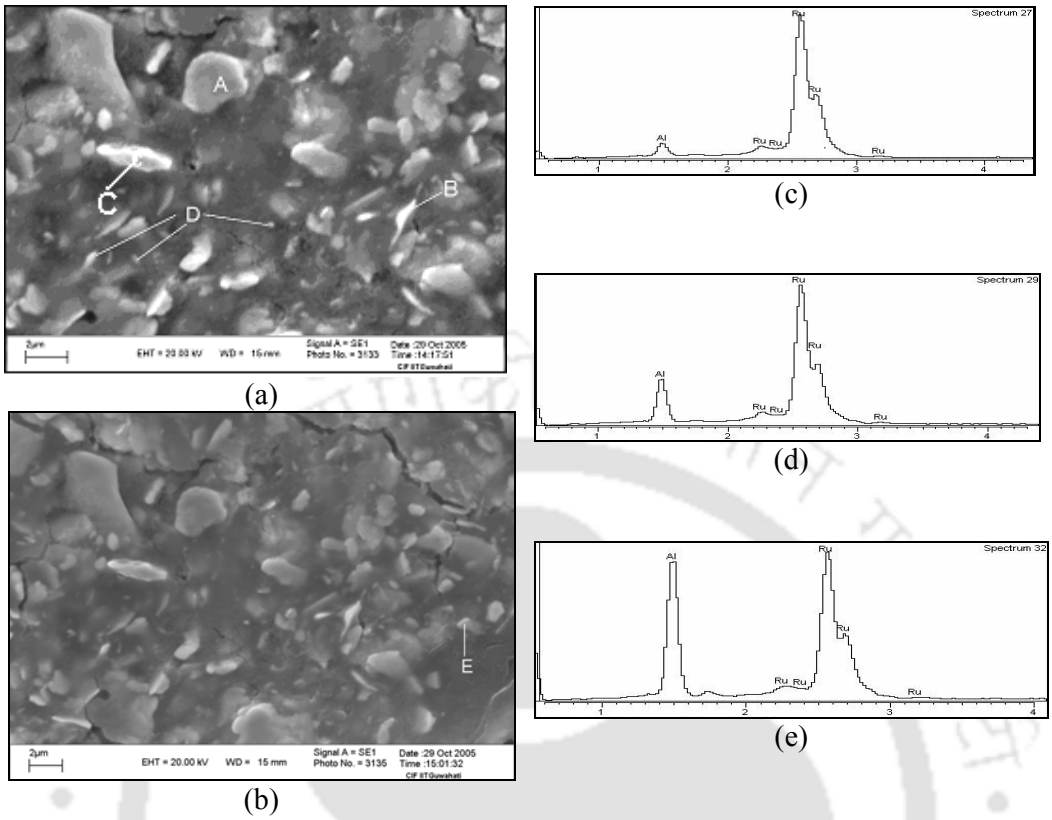

Figure 4.6: (a)–(b) SEM micrographs of polished Ru-Al powder mixture, which has been milled for 2 hours. EDS spectra corresponding to the (c) particles labelled as "A" and "C" in Figure 4.6 (a), (d) particles labelled as "B" and "D" in Figure 4.6 (a) and (e) particle labelled as "E" in Figure 4.6 (b)

Figures 4.7 (a-b) show SEM micrographs of the Ru-Al powder mixture milled for 7 hours. There was not much variation in the size of the powder particles as compared to the 2 hours of milling. However, a morphological change from flake-like appearance to semi-rounded shapes was observed with surface features typical of plastic deformation and cold welding processes during milling. Figure 4.7 (c) shows the EDS spectrum corresponding to the overall composition of the powder. The EDS analysis revealed an overall composition of $Ru_{46}Al_{54}$ for the powder mixture milled for 7 hours. When compared to the 2 hours milled powder mixture, number of sub-micron sized particles was more in the 7 hours milled powder mixture, indicating increased fragmentation of the brittle constituents during extended milling. Figure 4.8 (a) shows SEM micrograph of powder mixture milled for 7 hours and polished. EDS spectra corresponding to the powder particles labelled "A", "B" and "C" are shown in Figures 4.8 (b-d), respectively. Analyses of the above spectra revealed that the very fine particles (labelled as "A") are RuAl phase with a composition of $Ru_{48}Al_{52}$ and the

coarse particles (labelled as "B") belong to the metastable phase of composition $Ru_{67}Al_{33}$. The larger particles labelled as "C" were identified as [Ru] phase of composition $Ru_{95}Al_5$.

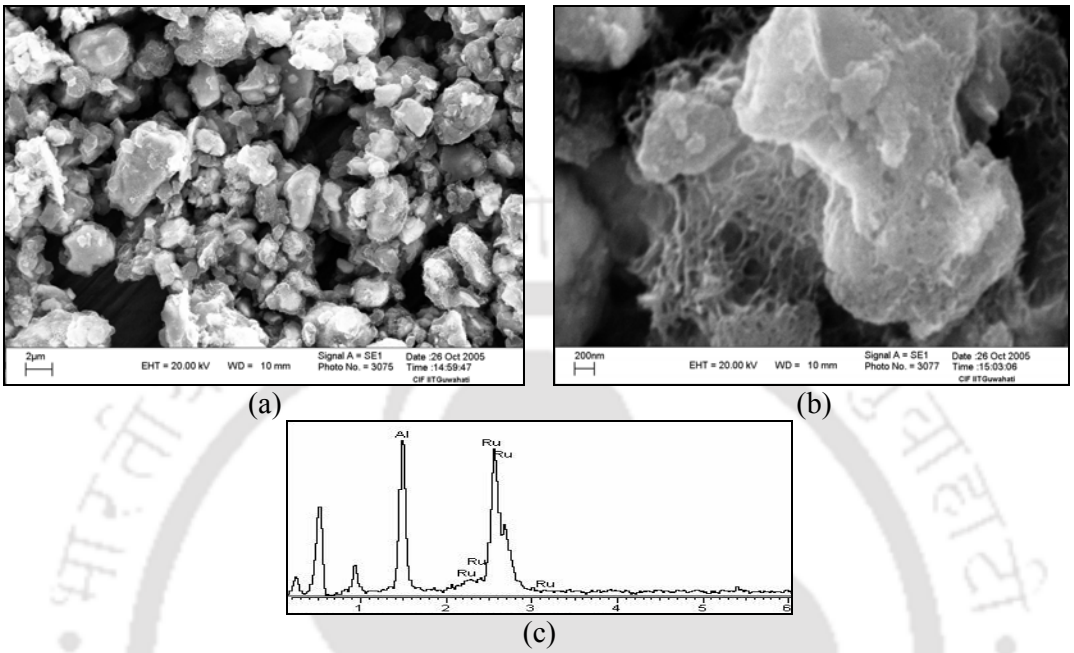

(a) (b)

(c)

Figure 4.7: (a-b) SEM micrographs of Ru-Al powder mixture milled for 7 hours at low and high magnification, respectively and (c) EDS spectrum corresponding to the overall composition of the Ru-Al powder mixture milled for 7 hours

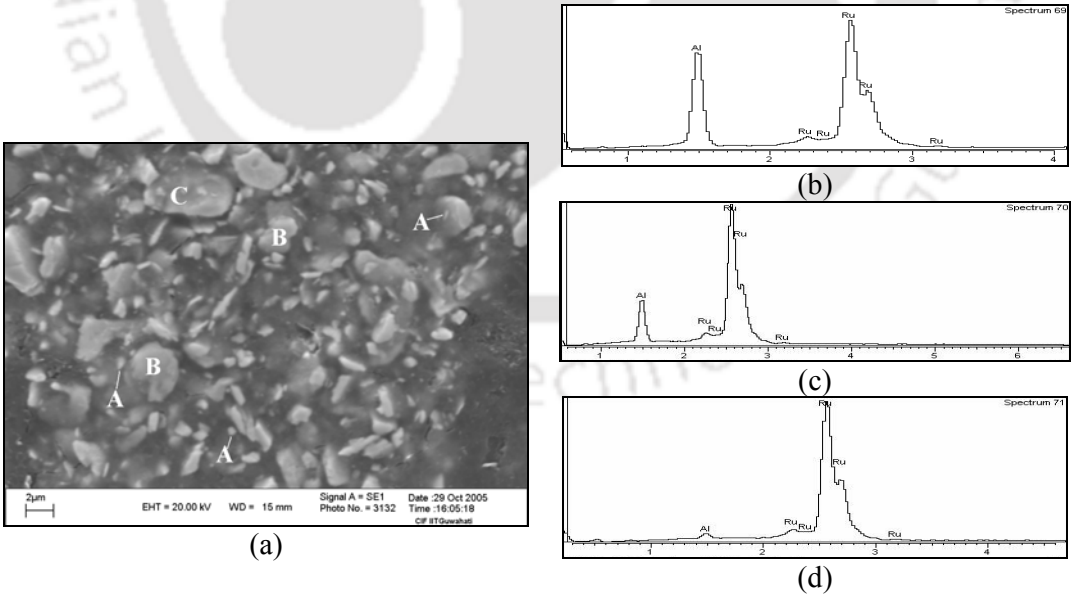

(a) (b) (c) (d)

Figure 4.8: (a) SEM micrograph of polished Ru-Al powder mixture milled for 7 hours. EDS spectra corresponding to the (b) particles labelled as "A", (c) particles labelled as "B" and (d) particle labelled as "C" in Figure 4.8 (a)

Figures 4.9 (a-b) show the SEM micrographs of Ru-Al powder mixture milled for 20 and 50 hours, respectively. Powder particle size reduced with increased milling time. The particle surface features indicate the occurrence of extensive cold welding during these stages of milling. EDS analyses indicated that the overall compositions of the powder mixtures milled for 20 and 50 hours were the same as that of the powder milled for 7 hours. This shows that the overall composition of the powder mixture stabilised after 7 hours of milling. Better SEM micrographs for the polished powder mixture milled for 20 and 50 hours could not be obtained for analyses due to fine size of the powder particles.

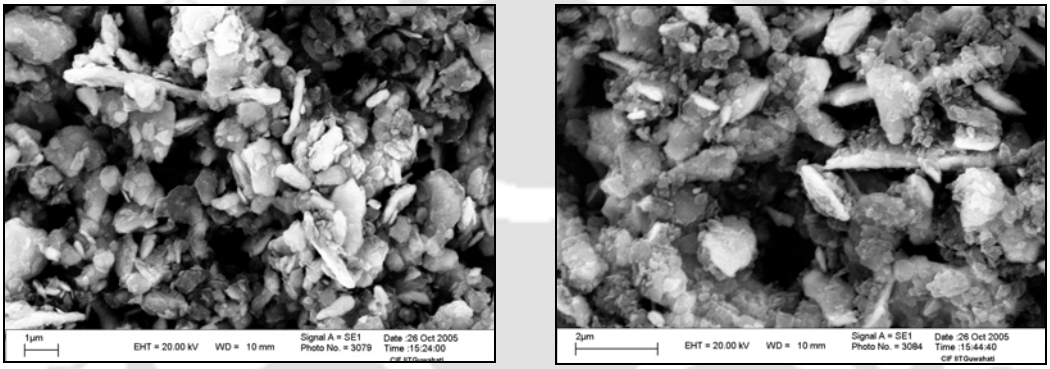

(a) (b)

Figure 4.9: SEM micrographs of Ru-Al powder mixture milled for (a) 20 hours and (b) 50 hours

Discussion

Though the XRD analysis confirmed the RuAl phase formation after 7 hours of milling, the EDS data shown by Figure 4.6 (e) provides the evidence of RuAl phase formation even after 2 hours of milling. This was not evident from the XRD pattern of the 2 hours milled powder mixture since the amount of RuAl phase formed after 2 hours of milling was very small to be detected by the XRD technique. The XRD patterns revealed the presence of peaks corresponding to the [Ru] phase even after 50 hours of milling. This indicates that all the Ru present in the starting powder mixture was not fully consumed during the milling process. Broadening of the XRD peaks corresponding to reflections from (002), (101), (102), (110) and (103) planes of Ru and (100), (110), (111), (200) and (211) planes of RuAl could be observed in Figure 4.1. The FWHM of these peaks increased with an increase in milling time. The peak broadening observed is a result of the reduction in the crystallite size and an increase in

the micro-strain induced during the milling process. Average crystallite size of 17 nm and 120 nm could be obtained after 50 hours of milling for RuAl and [Ru] phases, respectively.

Reflections from aluminium crystallites were not discernible corresponding to the powder mixtures milled beyond 2 hours. Increase in the milling time led to the disappearance of the XRD peaks corresponding to Al planes, while the Ru peaks persisted even up to 50 hours of milling. The disappearance of Al peaks in comparison with Ru peaks can be related to the atomic scattering factors of the elements. The element with the lower atomic number (Z) and hence lower atomic scattering factor, has a lower XRD peak intensity. On continued milling, as the elements are used up in the formation of the alloy, the XRD peaks corresponding to the element with lower Z tend to disappear more rapidly than the element with higher Z. Accordingly, in the Ru-Al alloy system, Ru peaks (Z = 44) persist while Al (Z = 13) peaks disappear during prolonged milling. Subsequent reaction occurring, results in the formation of RuAl, which is evident from the XRD pattern of powders milled for 7 hours. Comparison of the XRD patterns observed at various periods of milling [as indicated by the normalised intensity ratio of the RuAl (100) and Ru (100) peaks] indicate no observable increase in the RuAl phase beyond 7 hours of milling. This shows that the RuAl phase formation is more or less complete by 7 hours of milling and further milling leads to size refinement only.

The overall composition corresponding to the 2 hours milled powder mixture shows reduced aluminium content (overall composition of $Ru_{56}Al_{44}$) as compared to the composition of the starting (as-mixed) powder mixture ($Ru_{47}Al_{53}$). This anomaly may be due to the nature of the mechanical alloying process itself. During the first stage of mechanical alloying, the elemental powders undergo plastic deformation and cold weld to the ball / wall surface. The ductile aluminium undergoes severe plastic deformation and is more likely to adhere to the ball/wall surfaces. Hence, this may lead to an apparent decrease in the Al content in the sampled powder mixture. The subsequent increase in the Al content in the powders milled for longer periods supports this explanation. Similar observations have also been made by Mucklich *et al.* [91, 92].

Recent studies [91,92] reported the abrupt formation of the RuAl phase after 4 hours of milling and complete transformation of the elemental powders to RuAl occurred after 25 hours of milling for a composition of $Ru_{50}Al_{50}$ carried out in a Spex

mill. In another study by the same authors, RuAl phase formation was reported after 35 hours of milling and subsequent annealing of the milled powders [93]. In the present work, the EDS study reveals a gradual formation of RuAl phase during the initial period of milling, though complete transformation to RuAl was not observed even after 50 hours of milling. The same milled powder after annealing at 1450 °C for 8 hours revealed the presence of unreacted Ru by XRD [*cf.* Figure 4.4 (a)]. The diffusion coefficient of Ru in RuAl is not available in the literature. However, an approximate diffusion coefficient value of $(2.4 \pm 1.3) \times 10^{-13}$ cm^2/s of Al in RuAl has been estimated at 1000 °C [48]. It is also expected that the diffusion coefficient of ruthenium in RuAl is lower than that of aluminium in RuAl [48]. Annealing at 1450 ºC for 8 hours might not have been sufficient for any comparable diffusion of ruthenium from the 120 nm sized Ru crystallites into the surrounding RuAl phase. Hence unreacted ruthenium is observed in the annealed powders. Mucklich *et al.* [91, 92] have reported that no unreacted Ru was observed when the average crystallite size of Ru was ~ 10 nm. Since, the average crystallite size of Ru was more than one order higher (~ 120 nm) in the present study, the longer diffusion length requirement might have resulted in the presence of unreacted Ru. This leads to the conclusion that the complete RuAl phase formation can be achieved with sufficiently lower Ru crystallite size (i.e., ~ 10 nm), longer (more than 8 hours) annealing time and/or higher (more than 1450 ºC) annealing temperature.

Annealing of the Ru-Al powder mixture at 1450 ºC for 8 hours resulted in the increase in the average crystallite sizes of Ru and RuAl with concomitant reduction in micro-strains. In the present study, the average crystallite size of Ru increased from 120 nm to 190 nm and that of RuAl increased from 17 nm to 83 nm after this annealing treatment. Mucklich *et al.* [93] reported achieving RuAl crystallite size of the order of ~ 80 nm after annealing at 1000 ºC for 5 hours. These authors also observed a stagnation of the grain growth after 3 hours of annealing time. Though, higher annealing temperature as well as higher annealing time was used in the present study, the average RuAl crystallite size obtained was also of the same order as that reported earlier. This leads one to presume that the RuAl crystallite might not grow beyond this value of about 83 nm in this process.

4.1.3 Microstructure of the sintered Ru-Al powder compact

The 50 hours milled Ru-Al powder mixture was cold compacted and subsequently sintered at 1450 ºC for 24 hours. The sintered Ru-Al alloy exhibited 97% theoretical density indicating a porosity level of ~3%. Porosities of the order of 4-11% were reported by Gobran *et al.* [87] in binary Ru-Al alloys processed by reactive hot pressing technique. Figures 4.10 (a-b) show the backscattered (BSE) and SE micrographs of the sintered RuAl sample, respectively. Figure 4.10 (a) shows three distinct regions labelled as "W", "G" and "B", corresponding to the white, grey and black regions, respectively. From the SE micrograph [*cf.* Figure 4.10 (b)], the black region appears to be either voids or grain boundaries. These voids might have appeared due to removal of loosely bound individual grains during the specimen polishing stage. Further, these voids cannot be porosities since the area fraction of the black region determined by image analysis was found to be 30%, where as mass density measurement revealed the porosities to be only 3%. This leads to the conclusion that the sintered samples exhibit poor bonding characteristics. The low diffusivity of elements in this alloy system requires higher temperature and time for the completion of the sintering process. As long as the sintering process is not complete, the bonding between individual grains across the grain boundary would be weak. Hence during the polishing stage, voids are formed on the surface due to abrasion.

EDS analyses shown in Figure 4.10 (c) revealed the composition of the grey region [labelled as "G" in Figure 4.10 (a)] as $Ru_{56}Al_{44}$ and "W" region shown in Figure 4.10 (d) as [Ru] phase with a composition of $Ru_{95}Al_5$. The grain sizes of these phases (grey and white) were approximately in the range from 2 μm to 8 μm.

Discussion

The microstructure of the sintered Ru-Al alloy was observed to be consisting of two phases, *viz.,* RuAl and [Ru]. The metastable $RuAl_2$ and $Ru_{67}Al_{33}$ phases formed during milling were eliminated by inter-diffusion on sintering of the milled powder compact and resulted in the RuAl phase (composition $Ru_{56}Al_{44}$) and [Ru] phase (composition $Ru_{95}Al_5$). At present there is no report on the microstructure of sintered Ru-Al alloy in the literature. In the present study, the sintered Ru-Al alloy processed from powder mixture milled for 50 hours exhibited poor bonding characteristics between the individual grains. Grain sizes as large as 8 μm were observed. The

diffusion rate of Ru in RuAl appears to be slow. According to the current binary Ru-Al phase diagram reported in a recent review article [48] and from the reported RuAl phase boundaries [51], this composition of $Ru_{47}Al_{53}$ falls within the RuAl phase. However, the sintered powder compact did not result in the complete formation of RuAl phase. This could be attributed to one or more of the following reasons, (i) Large crystallite size obtained for Ru on milling (*cf.* section 4.1.2), (ii) low inter-diffusion coefficient of Ru in RuAl, (iii) insufficient pressure applied during cold compaction of the powder compact (though a pressure of 500 MPa was used for cold compaction) (iv) combination of sintering temperature and time was inadequate.

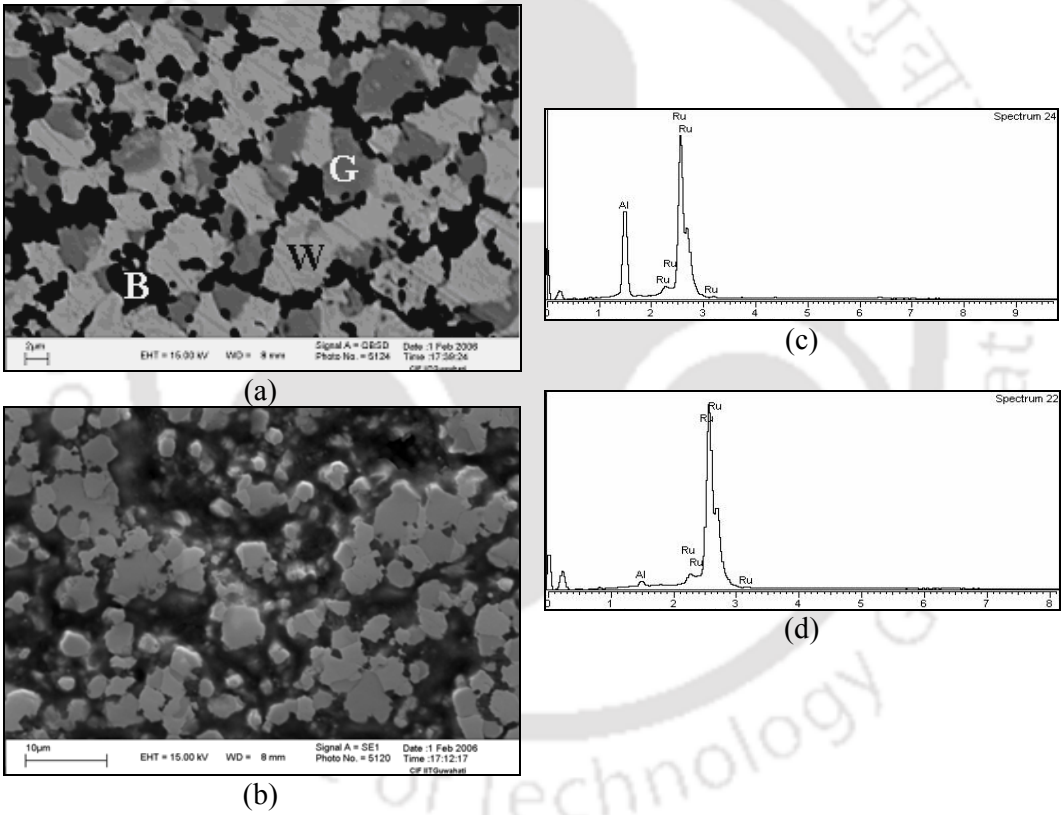

Figure 4.10: (a-b) SEM micrographs of the sintered Ru-Al powder compact (a) BSE micrograph and (b) SE micrograph; EDS spectra for the (c) region labelled as 'G' and (d) region labelled as 'W' in Figure 4.10 (a)

4.1.4 Mechanical properties of sintered Ru-Al alloy

Microhardness of the constituent phases in the sintered Ru-Al alloy was determined using a load of 10 gmf. The microhardness values of the constituent phases determined at room temperature were 276 (VHN) and 383 (VHN) corresponding to the grey (RuAl) and white (Ru) phases, respectively. The overall hardness of the sintered alloy could not be determined due to the voids [region B of Figure 4.10 (a)] present on the sample surface.

Ultimate strength of 66 MPa was obtained for the sintered sample by compression testing on non-standard cylindrical specimens. This value is very low compared to the value ~ 1000 MPa reported in the literature [45] for cast Ru-Al alloy. The Young's modulus and yield strength values could not be determined since non-standard samples were used. The low ultimate strength value is mainly due to the poor bonding characteristics of the sintered sample.

4.1.5 Electrical resistivity

The result obtained from the electrical resistivity (ρ) measurement for the sintered Ru-Al alloy from the room temperature to 600 ºC is shown in Figure 4.11. An electrical resistivity value of 83 μΩ-cm was obtained at room temperature, which increased linearly to a value of 124 μΩ-cm at 600 ºC. The temperature dependence of electrical resistivity of the sintered alloy was observed to be linear within the investigated temperature range. The variation of electrical resistivity as a function of temperature was fitted to linear regression from which the temperature coefficient of resistivity (α) was estimated to be 0.07 $°C^{-1}$.

At present no data on electrical resistivity of sintered Ru-Al alloy is available in literature for direct comparison of the results obtained in the present study. However, the obtained electrical resistivity values for the sintered alloy was observed to be higher when compared to the reported values for the alloy with a nominal composition of $Ru_{47}Al_{53}$ manufactured by RHIP technique (~ 65 μΩ-cm at room temperature and ~ 80 μΩ-cm at 450 °C) [66]. Anderson and Lang [66] reported a single-phase RuAl microstructure for their alloy. In the present study, the microstructure of the sintered RuAl alloy was observed to have two phases, *viz.,* RuAl and [Ru]. The presence of extra [Ru] phase in the microstructure and the poor bonding characteristics between the

grains are some of the reasons behind the higher electrical resistivity exhibited by the sintered Ru-Al alloy sample studied in the present investigation.

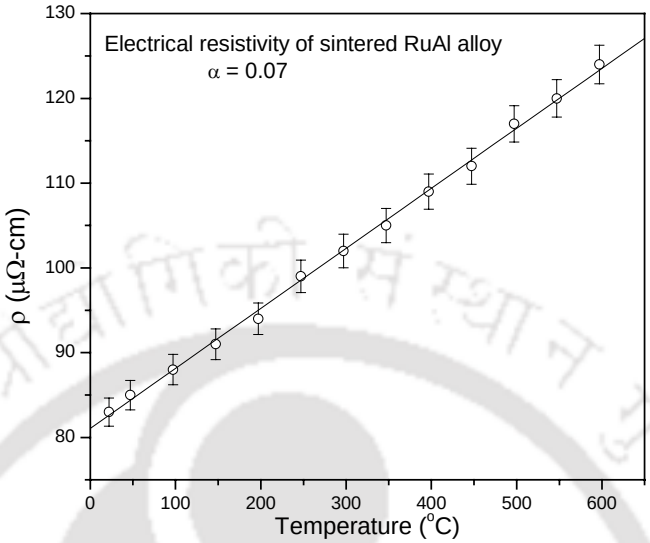

Figure 4.11: Plot of electrical resistivity with temperature for sintered Ru-Al alloy

4.2 Ru-Al alloy processed by casting route

The solidified alloy in as-cast as well as cast and heat-treated conditions were sliced and prepared for microstructural study, hardness and electrical resistivity measurements. The results obtained are summarised in the following sub-sections.

4.2.1 XRD analysis of cast Ru-Al alloy

XRD patterns for both as-cast and cast and annealed Ru-Al alloys are shown in Figures 4.12 (a-b), respectively. All the XRD peaks seen in the Figure 4.12 (a) could be indexed to reflections from RuAl and Ru planes alone. Hence the XRD pattern shows that the as-cast structure of the Ru-Al alloy consisted of [Ru] and RuAl phases only. The XRD pattern for the cast and annealed Ru-Al alloy [*cf.* Figure 4.12 (b)] shows reflections from (100), (102), (110) and (103) planes of Ru, which did not show up in the XRD pattern for the as-cast alloy. Ru or an [Ru] phase might have been precipitated out on annealing treatment resulting in the XRD reflections from those planes.

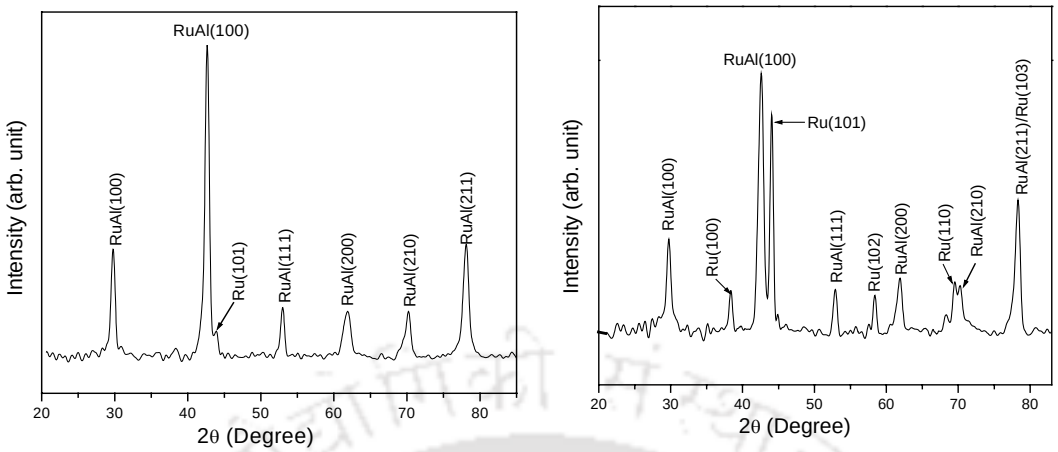

Figure 4.12: XRD patterns corresponding to cast Ru-Al alloy in (a) as-cast and (b) annealed conditions

4.2.2 SEM microstructural study of cast Ru-Al alloy

SEM back-scattered micrographs of the as-cast sample with a target composition of $Ru_{47}Al_{53}$ under different magnifications are shown in Figures 4.13 (a-b). Figure 4.13 (c) shows the EDS spectrum taken at low magnification for the determination of the overall alloy composition. Analysis of the spectrum revealed a composition of $Ru_{59}Al_{41}$ for the alloy showing a reduction in aluminium content with a concomitant increase in ruthenium content. Due to the large difference in melting points between aluminium and ruthenium as well as the fact that aluminium vaporises above 1950 ºC, aluminium loss by volatilisation occurs during the arc melting stage. Volatilisation of aluminium results in the formation of porosities and inhomogeneity in chemical composition of the cast alloy. The back-scattered electron micrograph shown in Figure 4.13 (b) revealed primary dendrites of RuAl phase (of composition $Ru_{56}Al_{44}$) labelled as "I", surrounded by a continuous network of eutectic lamellae. The EDS spectrum for regions labelled as "I", "H" and "G" and the overall eutectic composition are shown in Figures 4.13 (d-g), respectively. Composition analysis by EDS indicated that the eutectic lamellae are composed of alternate layers of white [Ru] phase of composition $Ru_{87}Al_{13}$ (labelled as "H") and grey phase of composition $Ru_{63}Al_{37}$

(labelled as "G"). The overall composition of the eutectic lamellae was determined as $Ru_{76}Al_{24}$.

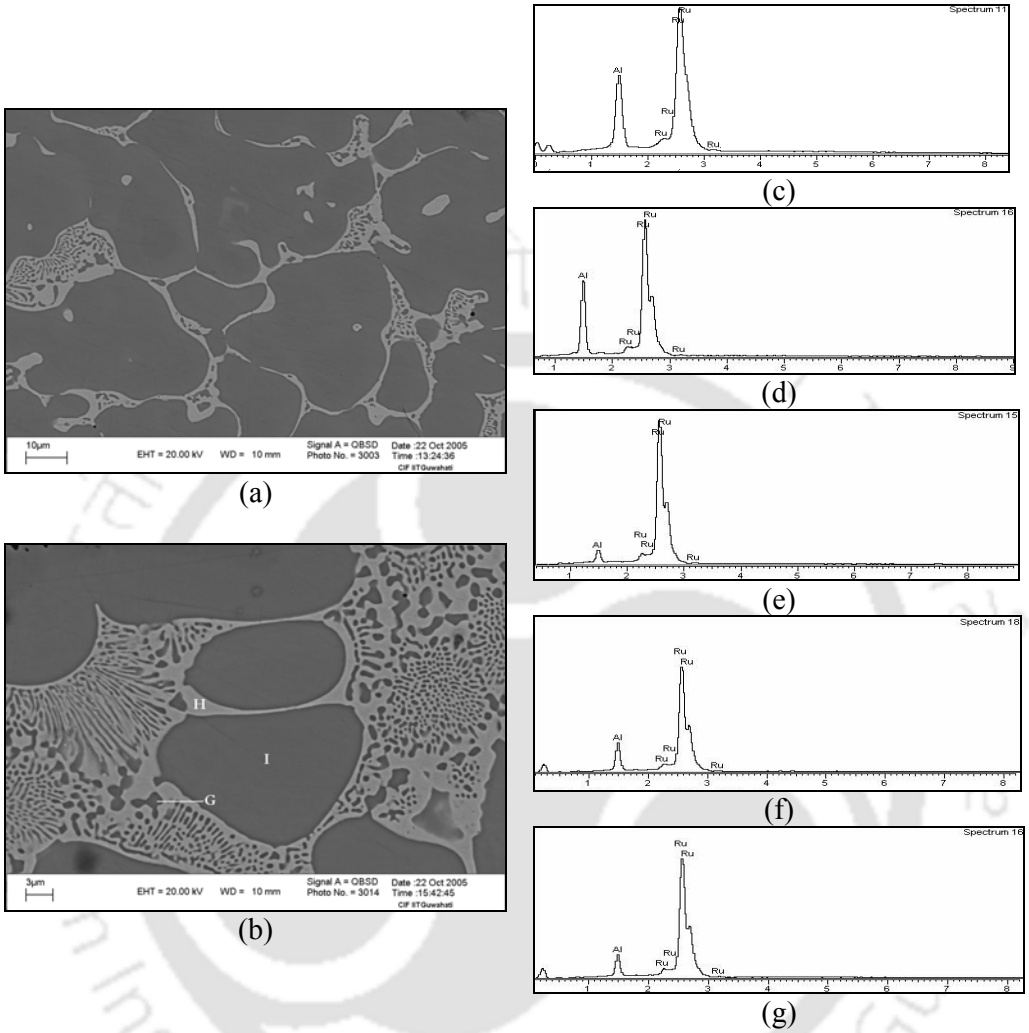

Figure 4.13: (a-b) SEM micrographs of as-cast Ru-Al alloy sample at low and high magnification, respectively; EDS spectra corresponding to the (c) overall composition of the alloy, (d) region "I" in Figure 4.13 (b), (e) region "H" in Figure 4.13 (b), (f) region "G" in Figure 4.13 (b) and (g) overall composition of the lamellar region

The cast Ru-Al alloy sample after heat treatment at 1450 ºC for 24 hours showed the presence of a second phase precipitates in the form of fine needles distributed uniformly in the primary RuAl phase as evident from Figures 4.14 (a-b). During heat treatment, a morphological change was observed in the eutectic mixture. Though the structure after the heat treatment consists of a mixture of white [labelled as "W" in Figure 4.14 (b)] and grey [labelled as "G" in Figure 4.14 (b)] regions, the features do not represent a lamellar structure. The EDS spectra for the constituent

phases of the eutectic mixture are shown in Figures 4.14 (c-d), respectively. Analyses revealed the grey phase (labelled as "G") as $Ru_{55}Al_{45}$ and white phase (labelled as "W") as $Ru_{98}Al_2$, respectively. The EDS analysis shown in Figure 4.14 (e) indicated an average composition of $Ru_{60}Al_{40}$ for the precipitate phase. This corresponds to precipitates of Ru_3Al_2, which has not been shown in the existing binary Ru-Al phase diagrams. EDS analysis shown in the Figure 4.14 (f) corresponding to the grey region along with the precipitated phases revealed an overall composition of $Ru_{56}Al_{44}$.

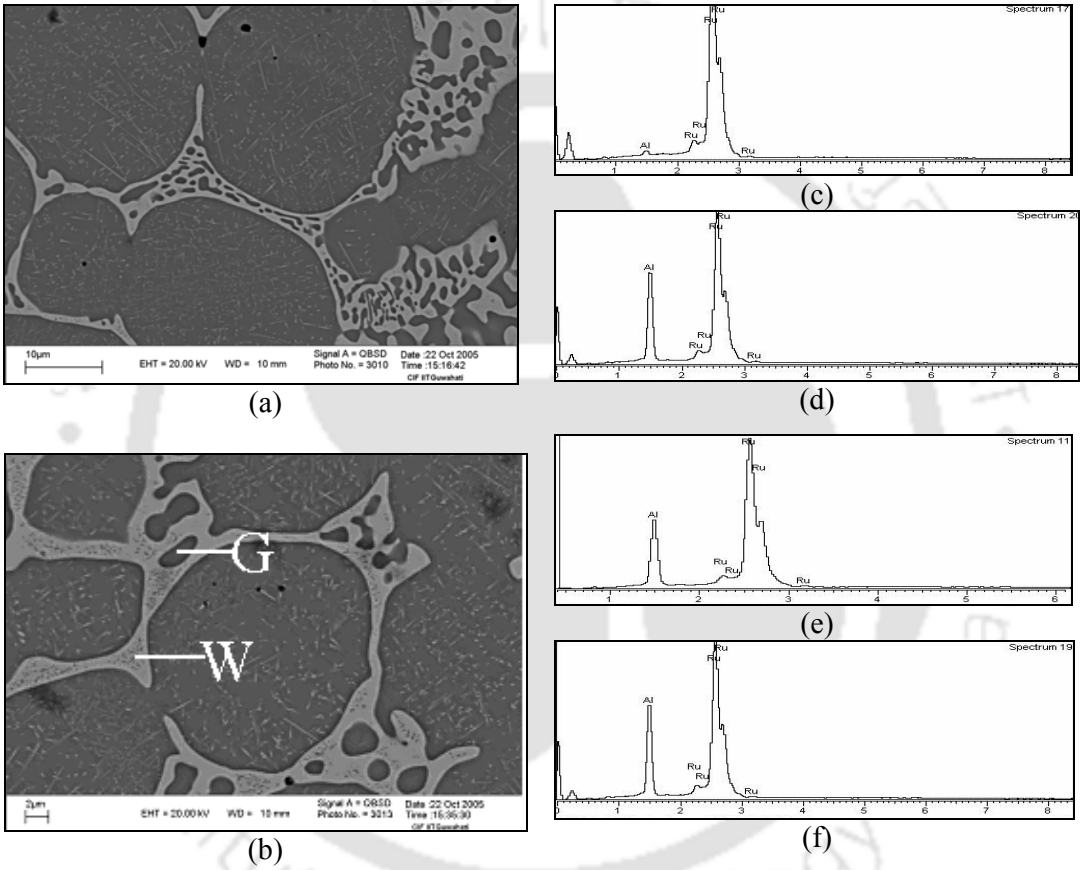

Figure 4.14: (a-b) SEM micrographs of cast and annealed Ru-Al alloy sample at low and high magnification, respectively; EDS spectra corresponding to the (c) white region "W", (d) grey region "G", (e) needle shaped precipitates in the grey region and (f) overall composition of the grey region in Figure 4.14 (b)

Additionally, a ruthenium rich white layer with a composition of $Ru_{97}Al_3$ was observed around the macroscopic gas porosity regions as seen in Figure 4.15 (a) indicating aluminium loss from the alloy in these regions after the annealing treatment. The EDS spectrum for the white layer is shown in Figure 4.15 (b).

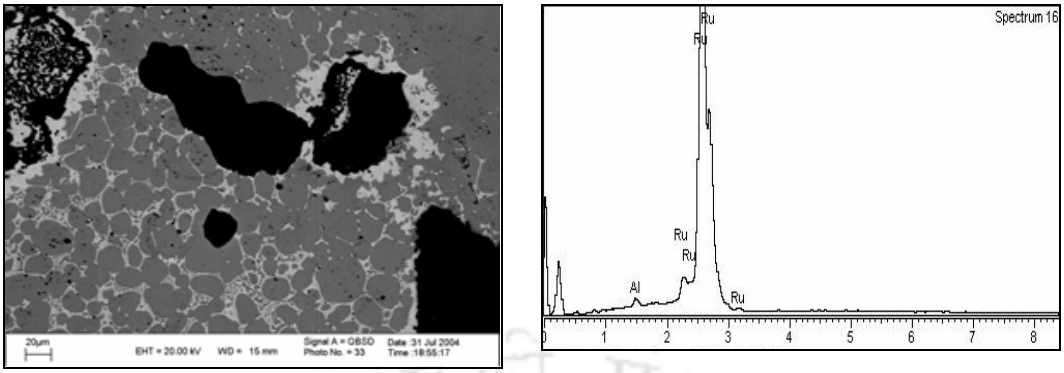

(a) (b)

Figure 4.15: (a) SEM micrograph of cast and annealed Ru-Al alloy showing the Ru-rich white layer around macroscopic porosity region and (b) EDS spectrum for the white layer

Discussion

Both XRD and SEM-EDS studies on as-cast Ru-Al alloy revealed that the alloy structure is composed of RuAl and [Ru] phases. [Ru] phase is having varying compositions one with composition of $Ru_{87}Al_{13}$ [region "H" in Figure 4.13 (b)] and the other with composition of $Ru_{63}Al_{37}$ [region "G" in Figure 4.13 (b)]. The binary phase diagram of the Ru-Al system indicates the eutectic composition to be $Ru_{70}Al_{30}$ [60] as per Figure 2.6 and $Ru_{74}Al_{26}$ [48] as per Figure 2.7. Ilic *et al.* [63] proposed the eutectic composition as $Ru_{76}Al_{24}$. In this investigation the observed composition for the eutectic mixture is in good agreement with their proposal. The shift in the eutectic composition towards the ruthenium rich side of the phase diagram can be attributed to the high cooling rate during the casting process resulting in non equilibrium solidification. The binary Ru-Al phase diagram indicates a composition of 54 at.% Ru at 1920ºC for the RuAl phase which decreases to 50.3 at.% at room temperature. Ilic *et al.* [63] also reported the composition of this β-RuAl phase as $Ru_{56}Al_{44}$. Rapid cooling of the melt in the water-cooled copper hearth leads to non-equilibrium solidification. This results in an alloy with an RuAl phase containing 56 at.% of ruthenium. The rapid non-equilibrium solidification during arc melting therefore results in a shift in the RuAl phase and the RuAl + [Ru] eutectic compositions towards ruthenium rich end of the binary phase diagram.

Both XRD and SEM-EDS analyses on the cast Ru-Al alloy annealed at 1450 ºC revealed two interesting features. The first concern was the appearance of a Ru-rich

white layer around macroscopic porosity regions after annealing. Al diffusion into the free surface (porosity) from the surrounding matrix results in the formation of the Ru-rich layer in the region surrounding the porosity. The second concern was the evidence of precipitation of a [Ru] phase in the annealed β-RuAl matrix. Since the solidification of the alloy took place under non-equilibrium condition, the primary RuAl phase was enriched in ruthenium. The excess ruthenium is precipitated out of the solid solution in the form of needles during heat treatment at 1450 ºC. The ruthenium concentration in the ruthenium rich phase of the eutectic lamellae is increased from 87 at.% to 97 at.% after heat treatment. Simultaneously, an increase in the aluminium concentration is observed in the RuAl phase in the eutectic lamellae indicating inter-diffusion of individual species of Ru and Al in the [Ru] phase and RuAl phase during heat treatment. This precipitation reaction from the super saturated primary RuAl phase during heat treatment indicates the possibility of precipitation hardening in this alloy. The presence of such small needle shaped precipitates of *hcp* α-Ru in Ru-Al alloys was also noticed by Fleischer *et al.* [45]. However, no further details of these precipitates are available. It has to be pointed out that the Ru-Al phase diagrams presented by Massalski (*cf.* Figure 2.6) and Mucklich *et al*. (*cf.* Figure 2.7) show distinct differences. However, the existing works have concentrated more on the Al rich side of the Ru-Al phase diagram with quite a few disagreements among one another. The Ru rich side of the Ru-Al phase diagram has not been explored in such details. Hence the presence of Ru_3Al_2 in the binary phase diagram cannot be ruled out, especially for samples, which were annealed after casting. Repeated studies on different samples indicated an overall composition of Ru_3Al_2 for the precipitated needles. A detailed study of compositions in this region of the Ru-Al phase diagram is required to resolve this matter.

4.2.3 Hardness measurement of the cast Ru-Al alloy

Overall hardness of as-cast and heat-treated Ru-Al alloy samples were determined as 290 VHN and 334 VHN, respectively. The overall hardness value for the as-cast Ru-Al alloy was observed to be higher than the reported value of 240 ± 10 (VHN) [77] for the as-cast alloy with a nominal composition of $Ru_{50}Al_{50}$. The higher value of overall hardness (290 VHN) exhibited by the as-cast Ru-Al alloy prepared in

the present study compared to the reported value of 240 ± 10 (VHN) could be attributed to lower Al-content in the alloy (overall composition of $Ru_{59}Al_{41}$). Fleischer *et al.* [45] reported a value of overall hardness of ~ 370 VHN for an annealed alloy with a composition of $Ru_{55}Al_{45}$. In the present case an overall hardness value of 334 VHN was obtained for the cast and annealed alloy with a composition of $Ru_{59}Al_{41}$. Fleischer *et al.* [45] reported that the binary Ru-Al alloys show higher toughness towards the Ru-rich compositions whereas it was brittle towards the Al-rich compositions. The higher Ru content in the present cast and annealed Ru-Al alloy might have resulted in the lower overall hardness value.

An increase in the overall hardness value in Ru-Al alloy after heat treatment is evident from the investigation. This could be attributed to the precipitation of Ru_3Al_2 needles within the RuAl phase. This also confirms the occurrence of precipitation hardening in this alloy. The microhardness RuAl-phase with precipitated needles in the annealed Ru-Al alloy [*cf.* Figure 4.14 (b)] was determined as 457 VHN at a load of 5 gmf.

4.2.4 Electrical resistivity

The results obtained from the electrical resistivity (ρ) measurements of the cast Ru-Al alloy annealed at 1450 ºC from room temperature to 600 ºC are shown in Figure 4.16. A resistivity value of 54 μΩ-cm was obtained at room temperature, which increased linearly to a value of 90 μΩ-cm at 600 ºC. Comparatively large fluctuations were observed at higher temperatures than at low temperatures.

The electrical resistivity values obtained for the heat-treated alloy was observed to be lower than the reported value for alloys having nominal composition of RuAl (~65 μΩ-cm at room temperature and ~80 μΩ-cm at 450 °C) [66]. It should be noted that those values were reported for the alloy manufactured by using RHIP technique. However these values were observed to be higher as compared to the reported values for the alloys with nominal composition of $Ru_{50}Al_{50}$ (~15 μΩ-cm at room temperature and 30 μΩ-cm at 425 °C) and $Ru_{53}Al_{47}$ (~12 μΩ-cm at room temperature and ~ 25 μΩ-cm at 425 °C) manufactured using the same technique [66]. The high degree of porosity present in the cast alloy might have impeded the flow of electrical current in the specimen resulting in high values of electrical resistivity.

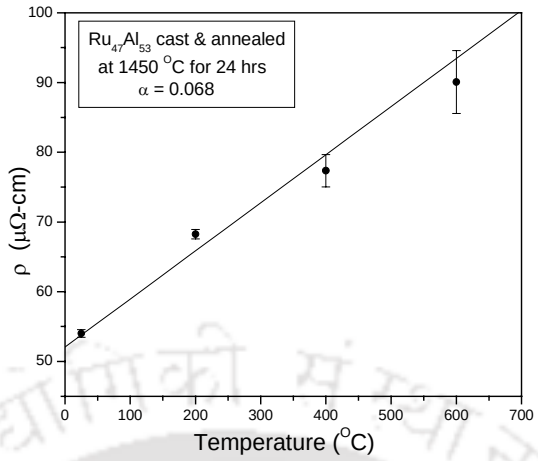

Figure 4.16: Plot of electrical resistivity with temperature for cast Ru-Al alloy annealed at 1450 °C

4.3 Summary and Conclusions

The highlights and the new findings of the current investigations on binary Ru-Al alloy are summarised below:

- RuAl phase could be formed by mechanical alloying just after two hours of milling in the indigenously developed attrition mill. This is worth comparing with the four hours of milling time for the formation of this phase reported by Lie *et al.* carried out in a Spex mill.
- XRD analysis of as milled powders reveals that there was no further formation of the RuAl phase beyond seven hour of milling. Milling beyond seven hours led to size refinement only, leaving behind unalloyed Ru. A comparison of the average crystallite sizes of Ru and RuAl phases with those reported by Liu et al suggests that the larger Ru crystallite size (~120 nm), which did not refine further could be the reason for the lack of further RuAl phase formation.
- Annealing studies of milled powders confirmed the stability of the RuAl phase at 1450 °C.
- Sintered samples of milled and cold compacted RuAl powders exhibited poor bonding characteristics, although 97% theoretical density was achieved after sintering for 24 hours at 1450 °C. A higher sintering

temperature and / or extended sintering time is recommended for achieve better bonding characteristics.

- Sintered Ru-Al powder compacts exhibited a low electrical resistivity value (83 μΩ-cm) at room temperature with a low temperature coefficient of resistivity (0.07 $°C^{-1}$) reflecting the potentiality this alloy for high temperature electrical contact application such as aircraft spark-plug electrode material. These electrical properties are expected to improve with improved sintering.
- SEM studies on cast alloy after annealing revealed the presence of needle-shaped intermetallic phase of composition Ru_3Al_2 in the primary RuAl phase. This is the first report of this intermetallic phase in RuAl phase diagram.
- SEM studies on cast alloy after annealing revealed a morphological change in the eutectic constituents, which is also a new finding.
- An increase in the overall hardness value in the cast alloy after annealing confirms the occurrence of precipitation hardening in this alloy, which has also been observed for the first time in RuAl alloy system.

Chapter-5

Results and discussion on Ru-Al-Ni alloy system

5.1 Introduction

Three alloy compositions of Ru-Al-Ni alloy system, *viz.*, $Ru_{32}Al_{50}Ni_{18}$ (point "1" in Figure 3.10), $Ru_{43}Al_{39}Ni_{18}$ (point "2" Figure 3.10) and $Ru_{38.5}Al_{16.5}Ni_{45}$ (point "3" in Figure 3.10) were processed by powder metallurgy as well as by casting routes using the procedures outlined in chapter 3. $Ru_{32}Al_{50}Ni_{18}$ falls in the single-phase (β_2) region, $Ru_{43}Al_{39}Ni_{18}$ falls in the two-phase (β_2 + Ru) region and $Ru_{38.5}Al_{16.5}Ni_{45}$ falls in the three-phase (γ + β_2 + Ru) region of the isothermal section shown in the Figure 3.10. These alloy compositions have not been studied earlier both by powder metallurgy as well as by casting techniques. The results of the microstructural investigations, hardness testing and electrical resistivity measurements of the alloys processed by powder metallurgy as well as by casting routes are summarised in the following sub-sections.

5.2 Processing of $Ru_{32}Al_{50}Ni_{18}$ alloy by powder metallurgy route

The elemental powder mixture of Ru + Al + Ni consisting of the composition $Ru_{32}Al_{50}Ni_{18}$ was attrition milled for 50 hours. The variation in crystallite size and micro-strain of various phases during milling was studied and the results obtained are presented in the following sub-sections.

5.2.1 Milling characteristics

Figure 5.1 shows the XRD patterns of powder mixture corresponding to the composition $Ru_{32}Al_{50}Ni_{18}$ milled for various time periods. After 10 minutes of milling, the peak observed at 2θ value of 38.66° corresponds to overlapping reflections from Ru (100) and Al (111) planes. Similarly, the peak observed at 2θ value of 78.61° corresponds to overlapping reflections from Ru (103) and Al (311) planes. In the same manner, it was observed that the peak at 2θ value of 44.80° corresponds to overlapping reflections from Ni (111) and Al (200) planes. There was no evidence of any new phase formation even up to 50 hours of milling. It was observed that the reflections from Al

and Ni planes showed a rapid decrease in intensity with a simultaneous increase in their peak widths. Hence the reflections from Al and Ni planes were not discernible in the XRD patterns after milling for 20 hours and 40 hours, respectively.

The W-H plots corresponding to Ru, Al and Ni reflections in the XRD patterns of as-milled $Ru_{32}Al_{50}Ni_{18}$ powder mixture are shown in Figures 5.2 (a-c), respectively. The corresponding crystallite size and micro-strain variations with milling time are shown in Figures 5.3 (a-c) and 5.4 (a-c), respectively. Figure 5.3 (b) indicates saturation in the average crystallites size of Al within the period from 5 hours to 10 hours of milling.

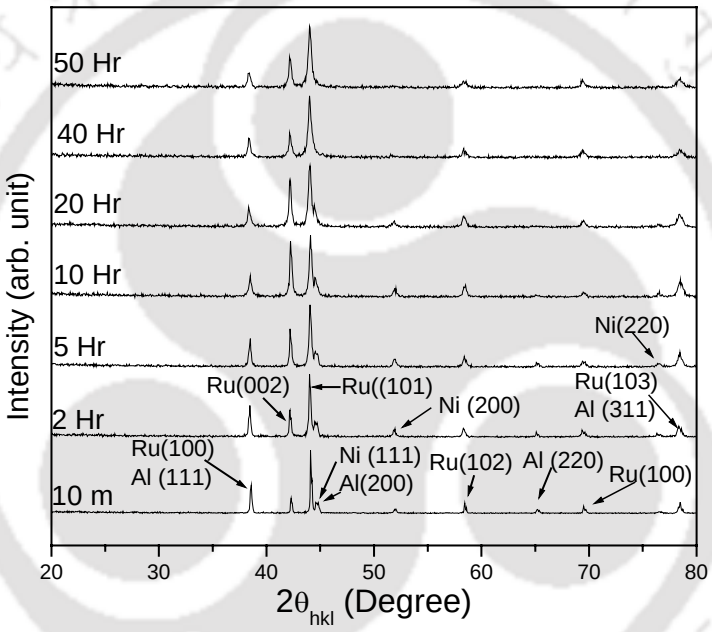

Figure 5.1: XRD patterns of $Ru_{32}Al_{50}Ni_{18}$ elemental powder mixture milled for various time periods

Micro-strains observed in Ru in the powder mixture with milling time did not reveal any systematic trend, whereas micro-strains in Al and Ni were found to increase with milling time. The average crystallite sizes of Ru, Al and Ni were estimated to be 466 nm, 313 nm and 401 nm, respectively after 2 hours of milling. After 10 hours of milling their average crystallite sizes were reduced to 193 nm, 50 nm and 31 nm, respectively. On continued milling, Ru crystallites attained an average size of 130 nm after 50 hours of milling. Ni and Al crystallite sizes were 18 nm and 50 nm after 20 and 10 hours of milling, respectively. In all the phases the reduction in the average crystallite size was observed to stagnate after some hours of milling. The micro-strain in

Ru was estimated to be 0.0029 after 50 hours of milling and that of Al and Ni were 0.002 and 0.0091 after 10 and 20 hours of milling, respectively.

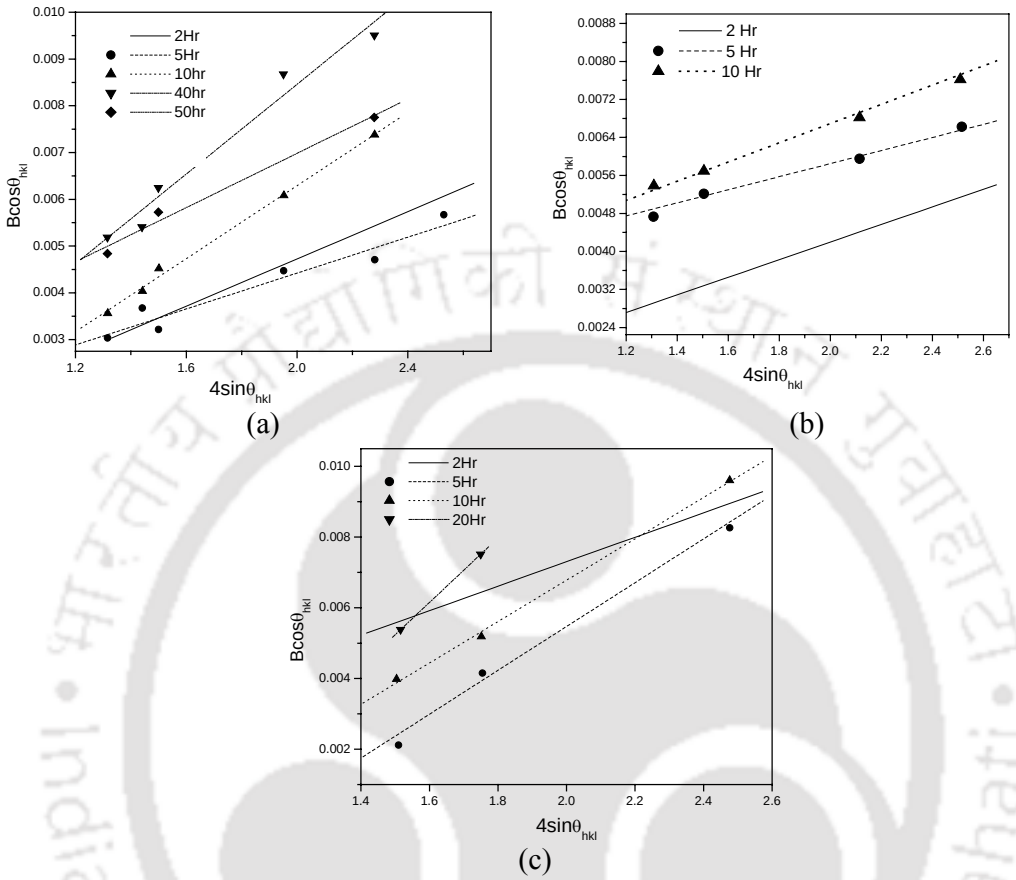

Figure 5.2: W-H plots corresponding to (a) Ruthenium, (b) Aluminium and (c) Nickel in milled $Ru_{32}Al_{50}Ni_{18}$ powder mixture

5.2.2 Milled powder microstructure

Figure 5.5 shows the as-milled $Ru_{32}Al_{50}Ni_{18}$ powder microstructure milled for 2 hours. The milled powder mixture consisted of a mixture of coarse flaky particles and fine rounded sub-angular particles. Figure 5.6 (a) shows high magnification view of a fine particle shown in Figure 5.5 after 2 hours of milling. The size of the particle is approximately 2.4 μm. EDS spectrum of the particle is shown in Figure 5.6 (b). The EDS analysis of the particle showed a composition of $Ru_{82}Al_{18}$ for the fine particle indicating that some amount of Al has gone into Ru to form a solid solution during the milling process.

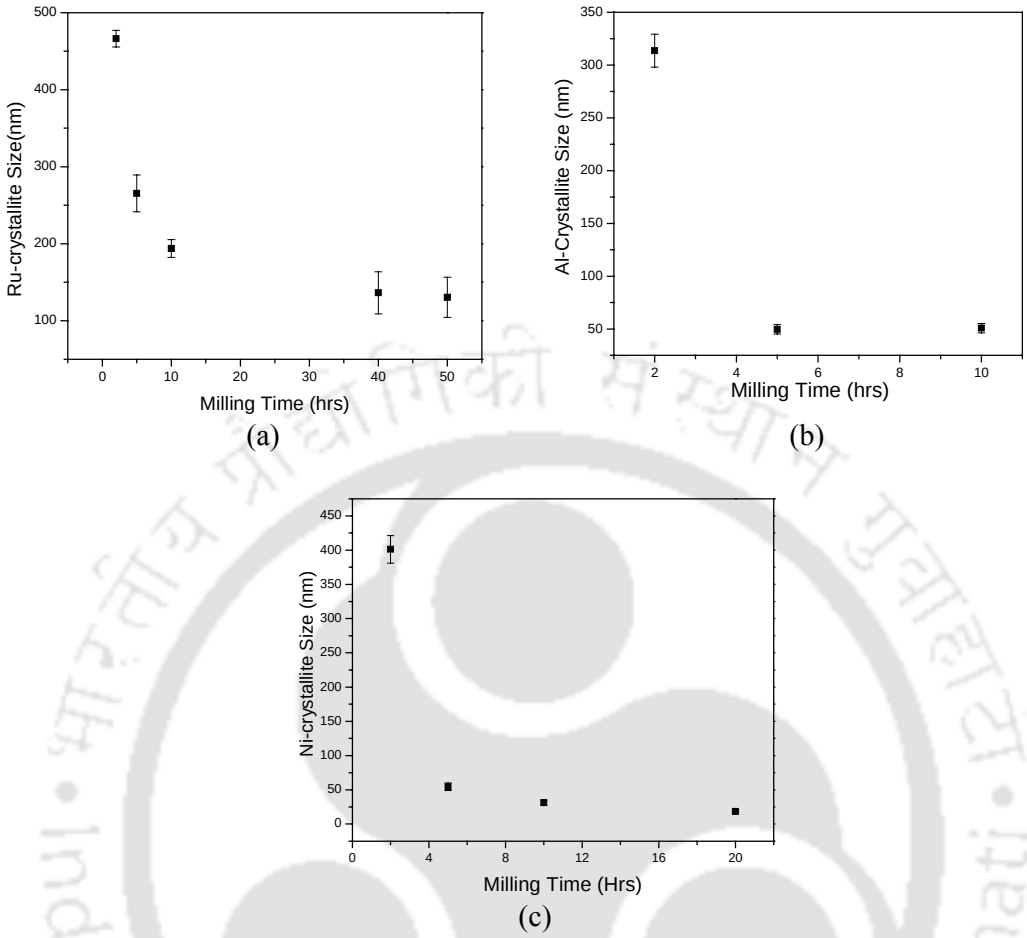

Figure 5.3: (a) Variation of crystallite size with milling time corresponding to (a) Ru-crystallite size, (b) Al-crystallite and (c) Ni-crystallite in milled $Ru_{32}Al_{50}Ni_{18}$ powder mixture

To investigate whether Al is adhering to the surface of these fine particles, as-milled powders were mounted in resin, polished and viewed under SEM. Figures 5.7 (a-b) show the SEM photomicrographs of polished particles milled for 2 hours. EDS analysis shown in Figure 5.7 (c) revealed that the particles similar to those shown at the centre of Figure 5.7 (a) correspond to a [Ru] phase having a composition of $Ru_{86}Al_5Ni_9$. Analysis of the EDS spectrum [spectrum shown in Figure 5.7 (d)] corresponding to the coarse particle shown in Figure 5.7 (b) revealed to be Ni solution having a composition of $Ni_{90}Al_{10}$. These analyses indicate the initiation of weak alloying even on 2 hours of milling, although this does not lead to a new phase formation even up to 50 hours of milling.

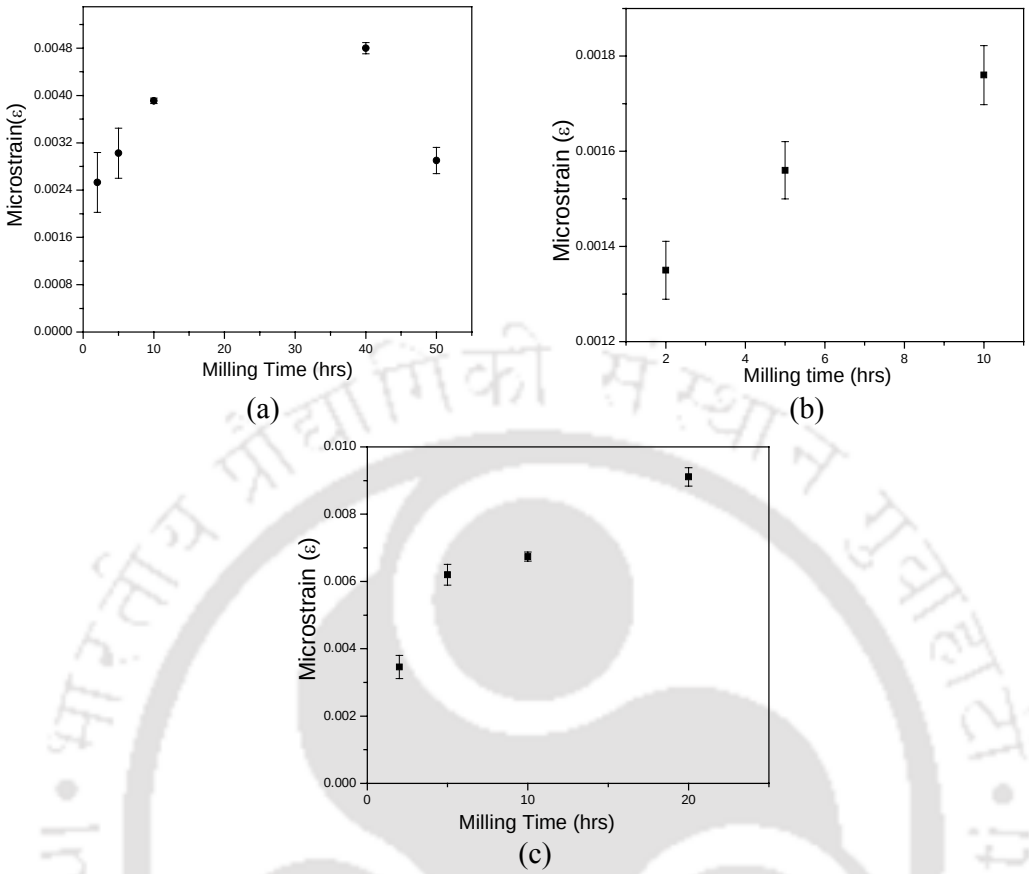

Figure 5.4: Variation of micro-strain with milling time corresponding to (a) Ru, (b) Al and (c) Ni in milled $Ru_{32}Al_{50}Ni_{18}$ powder mixture

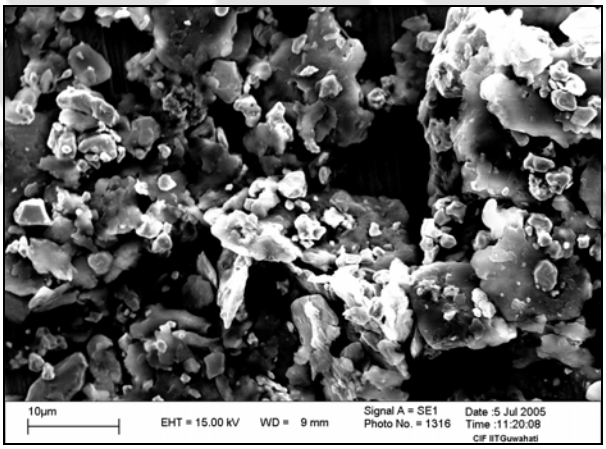

Figure 5.5: SEM micrograph of $Ru_{32}Al_{50}Ni_{18}$ powder mixture milled for 2 hours at low magnification

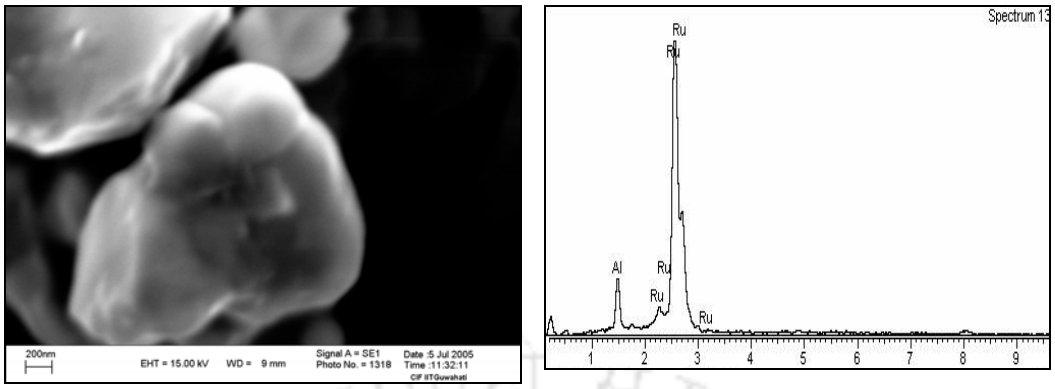

(a) (b)

Figure 5.6: (a) SEM micrograph of a fine powder particle in $Ru_{32}Al_{50}Ni_{18}$ powder mixture milled for 2 hours and (b) EDS spectrum for the central particle

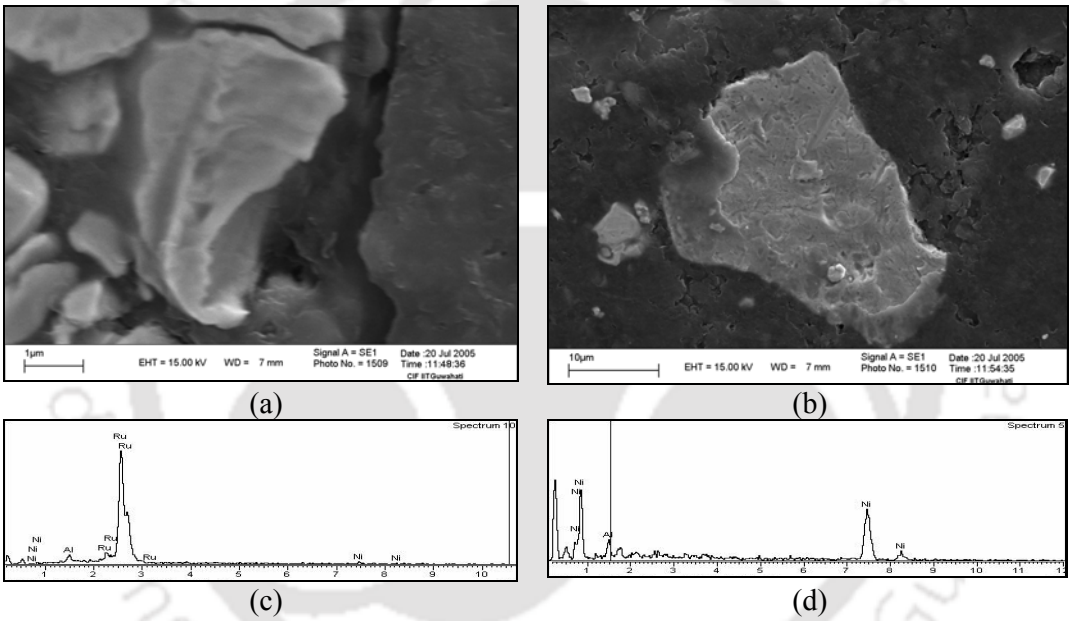

(a) (b)

(c) (d)

Figure 5.7: (a-b) SEM micrographs of polished $Ru_{32}Al_{50}Ni_{18}$ powder particles milled for 2 hours, (c) EDS spectra corresponding to the (a) particle in centre of the Figure 5.7 (a) and (d) coarse particle shown in Figure 5.7 (b)

Figures 5.8 (a-c) show the as-milled $Ru_{32}Al_{50}Ni_{18}$ powder microstructures milled for 5, 20 and 50 hours, respectively showing reduction in particle size. The fine particles appeared to be more clustered with increase in milling time. The particle surface morphology indicates features of cold welding between the constituent particles. This effect increases with increase in milling time.

Due to the very small size of the particles as a result of milling for 50 hours, satisfactory micrographs could not be obtained by the SEM. Figure 5.9 (a) shows the SEM micrograph of a polished particle after 50 hours of milling. Analysis of the EDS

spectrum of the particle shown in Figure 5.9 (b) revealed a composition of $Ru_{69}Al_{23}Ni_8$ indicating higher degree of mechanical alloying compared to the 2 hours milled powders.

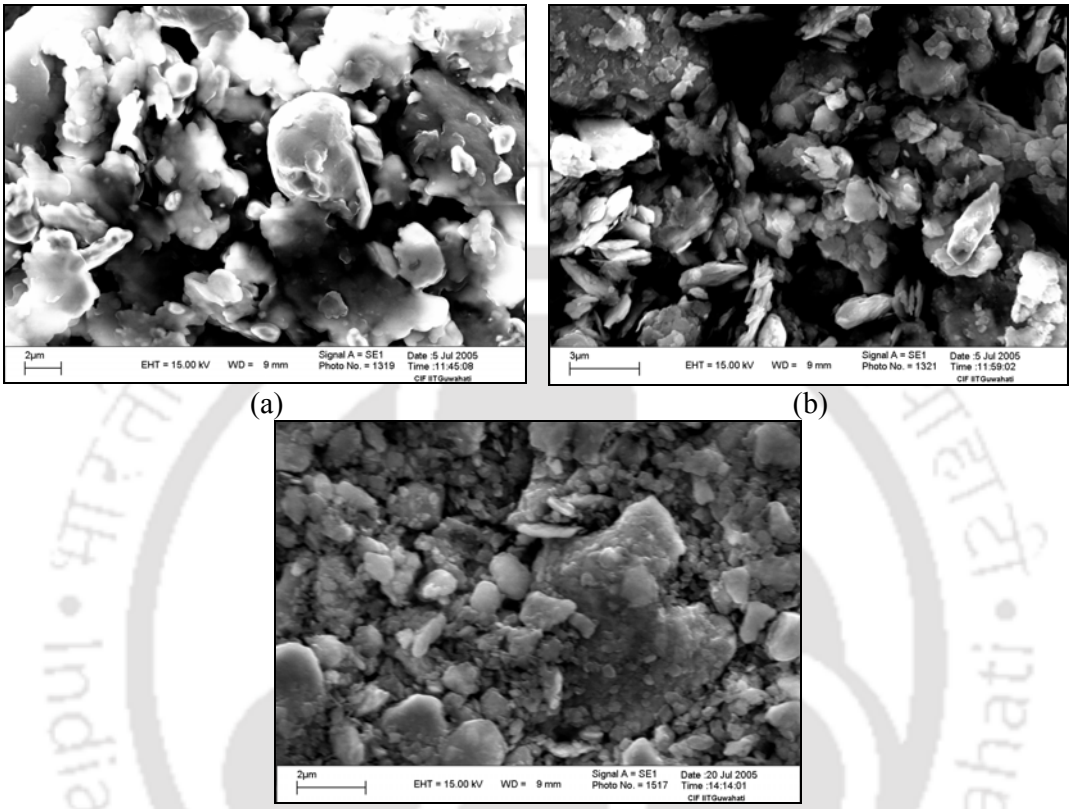

(a) (b)

(c)

Figure 5.8: SEM micrographs of the as-milled $Ru_{32}Al_{50}Ni_{18}$ powder mixture milled for (a) 5 hours, (b) 20 hours and (c) 50 hours

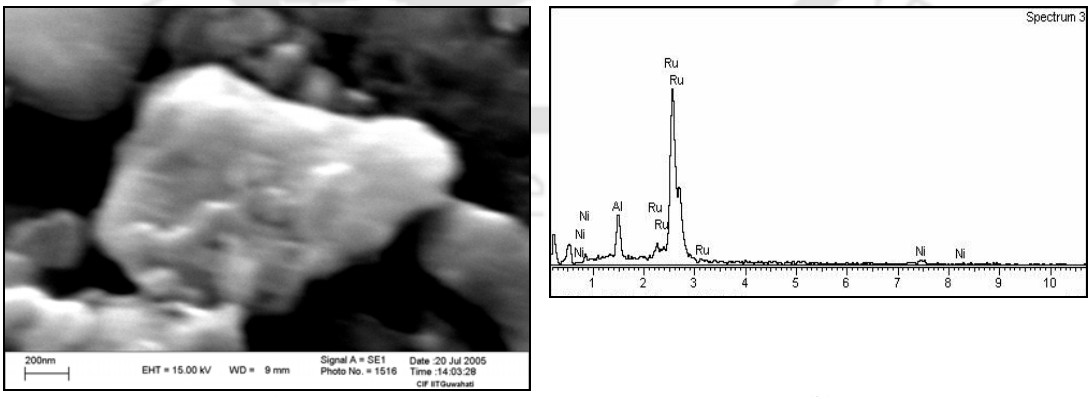

(a) (b)

Figure 5.9: (a) SEM micrograph of a polished particle in $Ru_{32}Al_{50}Ni_{18}$ powder mixture milled for 50 and (b) EDS spectrum corresponding to the particle shown in Figure (a)

Discussion

XRD patterns of as milled Ru + Al + Ni powder mixture of composition $Ru_{32}Al_{50}Ni_{18}$ did not reveal the formation of any new phase even after milling for 50 hours. The gradual disappearance of the XRD peaks corresponding to reflections from nickel and aluminium planes (*cf.* Figure 5.1) can be explained as follows. Figures 5.1 5.3 show a drastic reduction the average crystallite sizes of Al and Ni during the initial stages of milling with simultaneous increase in peak width. If one considers the lower atomic number of Al and Ni as compared to Ru, one expects a drastic reduction in the intensities of the Al and Ni peaks as compared to Ru peaks (due to the lower atomic scattering factor). All these factors lead to the apparent disappearance of the Al and Ni peaks in the XRD patterns of powders milled beyond 20 hours.

Liu *et al.* [55] reported the formation of (Ru,Ni)Al phase in $Ru_{50-x}Al_{50}Ni_x$ ($0 \leq x \leq 25$) on milling for 4 hours, which was not observed in the present investigations, even after 50 hours of milling. One possible reason for this could be the relative sizes of Ru, Ni and Al obtained in the present work and by Liu *et al.* [55]. Liu *et al.* [55] reported Ru crystallite sizes of the order of 10 nm, whereas the average crystallite size in the present studies did not reduced below 130 nm. Since, finer particle refinement is required for inducing mechanical alloying, the same might not have been possible in the present studies.

Although no alloying phenomenon was discernible from XRD analysis for powders milled for 50 hours, EDS analyses [*cf.* Figures 5.7 (c-d)] indicate the presence of Ru particles having composition $Ru_{86}Al_6Ni_9$ and Ni particles having composition $Ni_{90}Al_{10}$ in powders milled for 2 hours. The degree of alloying increased with the milling time as evidenced by the compositional variation of the Ru and Ni particles with increase in the milling time.

5.2.3 Cold compaction

Powder mixture of composition $Ru_{32}Al_{50}Ni_{18}$ milled for 50 hours could not be compacted at a pressure of 500 MPa. The green compacts exhibited very poor bonding between the powder grains. Flaky morphology observed from SEM studies might be the reason for poor cold compaction behaviour exhibited by this powder. Attempts to hot press the compacts failed mainly due to fusion of the powders with the die-and-punch assembly as a result of the exothermic reaction following the formation of RuAl above

700 °C. Hence compacts suitable for sintering work could not be prepared in this alloy system.

5.3 Alloy processed by casting technique

Microstructural studies, microhardness measurements and electrical resistivity measurements were carried out on the alloy processed by arc melting technique. The results obtained are presented in the following sub-sections.

5.3.1 XRD analysis of cast $Ru_{32}Al_{50}Ni_{18}$ alloy

Figures 5.10 (a-b) show the XRD patterns corresponding to the cast $Ru_{32}Al_{50}Ni_{18}$ alloy in as-cast as well as annealed conditions, respectively. Six XRD reflections were observed in the XRD pattern for the as-cast alloy [*cf.* Figure 5.10 (a)] within a 2θ range of 20° to 90°. The XRD reflections at 2θ values of 30.23° and 43.22° could be indexed to both RuAl and NiAl since the XRD reflections from RuAl and NiAl planes are very closely spaced at these 2θ values. Hence it is not possible to assign the observed peaks to either RuAl or NiAl conclusively. XRD reflections of other NiAl planes were not observed in the XRD pattern. The NiAl formation in the cast alloy might have been of very low quantity resulting in very low intensity reflections to be detected by X-ray diffractometer.

The XRD pattern corresponding to the cast $Ru_{32}Al_{50}Ni_{18}$ alloy annealed at 1450 °C for 24 hours [*cf.* Figure 5.10 (b)] shows extra peaks other than the (Ru,Ni)Al peaks. These peaks could be identified as reflection from [Ru], which might have precipitated during the heat treatment. The weak peak observed at 2θ value of 35.46^o could not be indexed since only one peak was observed in the XRD pattern.

5.3.2 SEM microstructural study of cast $Ru_{32}Al_{50}Ni_{18}$ alloy

Microstructure of the as-cast $Ru_{32}Al_{50}Ni_{18}$ alloy is shown in Figures 5.11 (a) and 5.12 (a). EDS analysis [spectrum shown in Figure 5.11 (b)], revealed an overall composition of $Ru_{39}Al_{45}Ni_{16}$ for the alloy indicating Al loss with simultaneous increase in Ru concentration compared to the starting composition. SEM observation indicated the alloy structure composed of primary dendrite of $Ru_{46}Al_{45}Ni_9$ [white region labelled as "W" in the Figure 5.12 (a)] surrounded by a Ni enriched $Ru_{17}Al_{37}Ni_{46}$ phase [black

region labelled as "B" in the Figure 5.12 (a)]. The EDS spectra corresponding to the regions "W" and "B" of Figure 5.12 (a) are shown in Figures 5.12 (b-c), respectively.

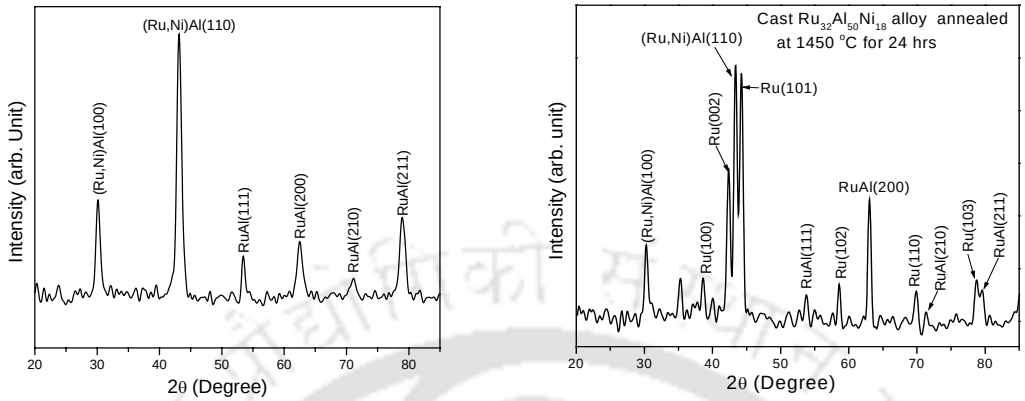

(a) (b)

Figure 5.10: XRD patterns corresponding to cast $Ru_{32}Al_{50}Ni_{18}$ alloy in (a) as-cast and (b) annealed conditions

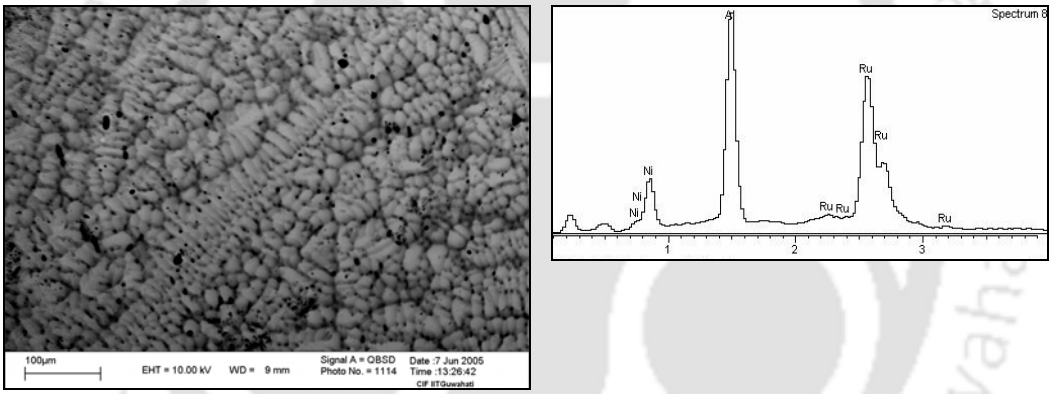

(a) (b)

Figure 5.11: (a) SEM micrograph of as-cast $Ru_{32}Al_{50}Ni_{18}$ alloy at low magnification and (b) EDS spectrum corresponding to the overall composition of the alloy

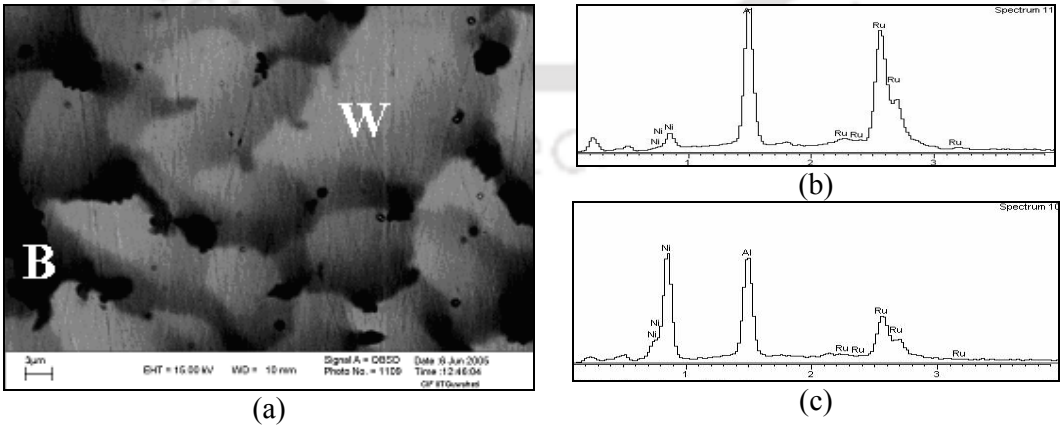

(a) (b) (c)

Figure 5.12: (a) SEM micrograph of as-cast $Ru_{32}Al_{50}Ni_{18}$ alloy at high magnification; EDS spectra corresponding to the (b) region "W" and (c) region "B" shown in (a)

Microstructure of the cast $Ru_{32}Al_{50}Ni_{18}$ alloy annealed at 1450 ^{o}C for 24 hours is shown in Figure 5.13 (a). A morphological change in the microstructure was observed after heat treatment. The microstructure of the alloy composed of two phases, *viz.*, light and dark grey phases labelled as "A" and "B", respectively. EDS analysis of the spectrum shown in Figure 5.13 (b) indicated an overall composition of $Ru_{44}Al_{45}Ni_{11}$ for the region consisting of light and dark grey phases. The EDS spectra corresponding to the regions "A" and "B" are shown in Figures 5.13 (b-c), respectively. From the EDS analyses, the compositions of the light (region "A") and dark grey (regions "B") phases were identified as $Ru_{45}Al_{45}Ni_{10}$ and $Ru_{38}Al_{45}Ni_{17}$, respectively. Additionally, a white layer was observed around porosity regions when viewed at high magnification. The white layer around porosity is shown in Figure 5.14 (a). Analysis of the EDS spectrum shown in Figure 5.14 (b) revealed a composition of $Ru_{87}Al_2Ni_{11}$ for this white layer. It was observed (as also reported in [53,54,73]) that better metallographic contrast could not be obtained for the two phases at higher magnification of the alloy. This might be due to the small variation in the compositions of the two phases.

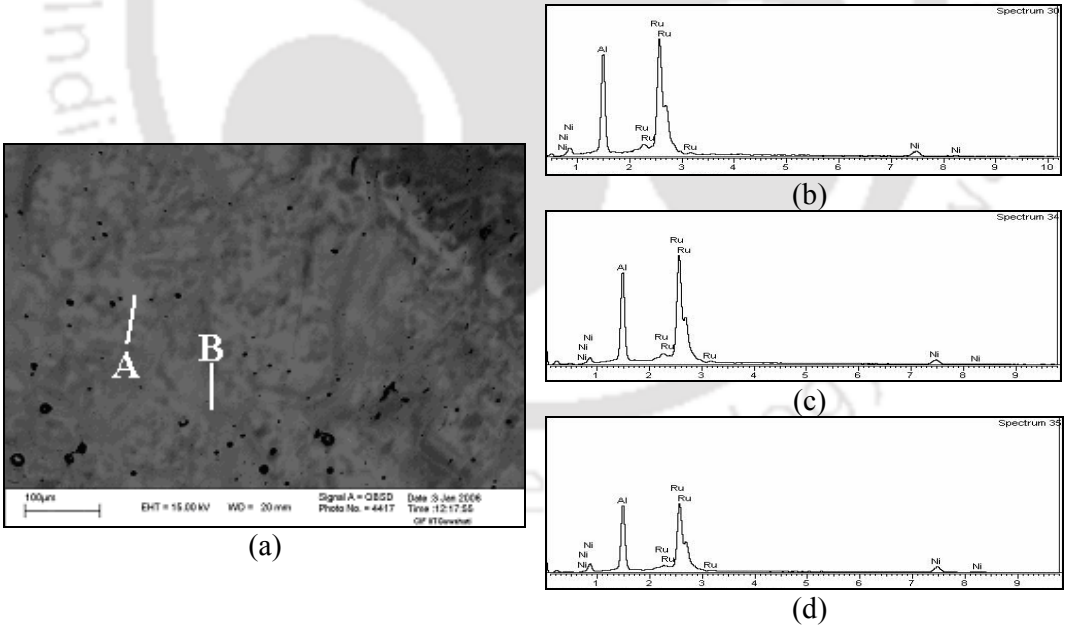

(a) (b) (c) (d)

Figure 5.13: (a) SEM micrograph of the cast and annealed $Ru_{32}Al_{50}Ni_{18}$ alloy; EDS spectra corresponding to the (b) overall composition, (c) region labelled as "A" and (d) region labelled as "B" in the (a)

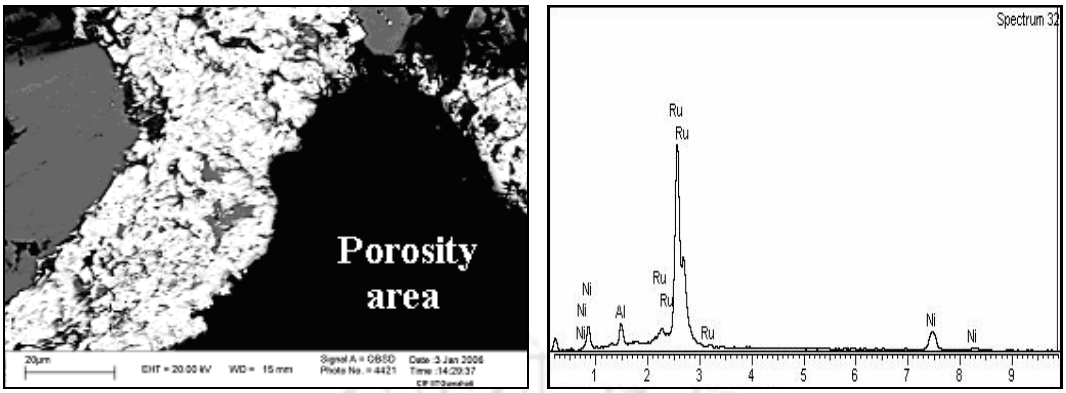

Figure 5.14: SEM micrograph showing a Ru-rich white layer around porosity in cast and annealed $Ru_{32}Al_{50}Ni_{18}$ alloy and (b) EDS spectrum corresponding to the white layer

Discussion

Both XRD and SEM studies of as-cast $Ru_{32}Al_{50}Ni_{18}$ alloy revealed that the alloy microstructure was composed of two-phases, each with varying amounts of Ru, Ni and Al. Since the RuAl and NiAl reflections are very closely spaced, it is not possible to assign the observed peaks to either RuAl or NiAl conclusively. Hence one can say that the structure consists of two phases [*cf.* Figure 5.12 (b)], each containing a mixture of RuAl and NiAl phases in varying amounts, leading to the ternary compositions, $Ru_{46}Al_{45}Ni_9$ (white region) and $Ru_{17}Al_{37}Ni_{46}$ (black region), respectively. Similar conclusions have also been drawn by other researchers [73]. Considering the positions of the overall composition ($Ru_{39}Al_{45}Ni_{16}$), the white ($Ru_{46}Al_{45}Ni_9$) and black ($Ru_{17}Al_{37}Ni_{46}$) phases in the phase diagram of Ru-Al-Ni [53], the amount of white and black phases could be estimated as 77 wt.% and 23 wt.%, respectively. Reports [53,77] show that the primary RuAl phase can accommodate up to 25 at. % Ni when processed at 1250 °C. Hence the observation of 9 at.% nickel in the primary RuAl (white phase) in the present studies is in agreement with the reported data of solubility of nickel in the RuAl phase. The melting points of β_2-RuAl (~ 2060 °C) and β_1-NiAl (~ 1638 °C) are significantly different and during solidification, Ru-rich β_2 phase will solidify first. As more of the primary β_2-phase (white) is formed, the unsolidified melt gets enriched in nickel. At the final stage of (the non-equilibrium) solidification, the nickel enriched molten material solidifies at the inter-dendritic region forming the black β_1 phase. Since

the last part to solidify would have the lowest solidus temperature and would contain a higher concentration of low melting point elements (such as Al and Ni in this case), the composition of the black phase ($Ru_{17}Al_{37}Ni_{46}$) is understandable. Earlier investigation [54] on such ternary alloys revealed the dendritic structure suggesting solidification of Ru-rich β_2 phase earlier than the Ni-rich β_1 phase. To ascertain the microstructure of the alloy under near equilibrium condition, the heat treatment (annealing) was carried out.

XRD and SEM studies on microstructure of the cast $Ru_{32}Al_{50}Ni_{18}$ alloy after annealing confirmed that the near equilibrium microstructure at 1450 °C consists of single (Ru,Ni)Al phase. This is in accordance with the findings of Chakravorty-and-West [52] and Horner *et al.* [54] who reported the equilibrium compositions at 1250 °C and 1500 °C, respectively. The observation of slightly higher Ru in the light grey phase as compared to the dark grey phase is also in line with the observation already reported [54]. Horner *et al.* [54] reported the compositions of $Ru_{45}Al_{48}Ni_7$ and $Ru_{36}Al_{47}Ni_{17}$ respectively for light and dark grey phases in an alloy with an overall composition of $Ru_{40}Al_{47}Ni_{13}$. Similar compositions ($Ru_{45}Al_{45}Ni_{10}$ and $Ru_{38}Al_{45}Ni_{17}$) for the respective phases were obtained in the present study. An additional white Ru-rich phase around porosities [*cf.* Figure 5.14 (a)] might have resulted due to Al loss during annealing treatment at 1450 °C. Since the equilibrium structure analysis discounts porosities, the annealed $Ru_{32}Al_{50}Ni_{18}$ can be essentially considered as a single-phase alloy. It has to be mentioned that this annealed alloy contained the specific feature of Ru-rich layered porosities as observed in Figure 5.14 (a). The presence of the same in earlier works cannot be confirmed due to the low magnification micrographs presented in the earlier report [54].

It has been reported that Ru has a low inter-diffusion coefficient in Ni based binary alloys [75]. Additionally homogenisation of Ru-Al-Ni alloys has also been reported to be time consuming [74]. Both these two above factors suggest that homogenisation would occur in Ru-Al-Ni alloys over a very long period of time. Hence the observation of two (Ru,Ni)Al phases with slightly varying compositions, indicate that the heat treatment time of 24 hours was not sufficient for the complete diffusion of elements to form a single (Ru,Ni)Al phase.

5.3.3 Hardness measurement of the cast $Ru_{32}Al_{50}Ni_{18}$ alloy

Overall hardness values of 528 VHN and 640 VHN were obtained for the cast $Ru_{32}Al_{50}Ni_{18}$ alloy in as-cast and annealed conditions, respectively. Microhardness values were obtained for the different phases in as-cast alloy using 100 gmf indentation load. The average microhardness values for the black (β_1) and white (β_2) phases [*cf.* Figure 5.12 (a)] were determined to be 570 VHN and 629 VHN, respectively. The microhardness values reported for the respective phases were ~ 680 VHN and ~ 770 VHN, respectively for annealed $Ru_{17}Al_{39}Ni_{44}$ alloy [53]. In the present study similar to the values reported lower hardness values were obtained for β_1 phase with β_2 slightly harder than β_1. It is worth mentioning that the phase compositions reported [53] for the β_1 and β_2 are different from the compositions obtained in the present study.

The microhardness values of different constituent phases in the cast and annealed alloy were determined using the same load of 100 gmf. The average microhardness values obtained for the Ru-rich phase around porosity and rest of the region (grey phase consisting of light and dark grey phases) were 774 VHN and 660 VHN, respectively. Due to brittle nature of Ru (*hcp* crystal structure), this Ru-rich phase has a higher hardness value compared to the grey phase. A hardness value of ~ 780 VHN has been reported for Ru-phase in $Ru_{25}Al_{25}Ni_{50}$ alloy [53]. In the present study comparable hardness value was obtained for this phase.

Overall hardness values of the alloy in as-cast and annealed conditions are comparable to the hardness values reported [53,54,73] for Ru-Al-Ni ternary alloys. Increase in the overall hardness after annealing of $Ru_{22}Al_{50}Ni_{28}$ alloy consisting of β_1 (NiAl) + β_2 (RuAl) phases has also been reported [53]. The increase in the overall hardness of the alloy in the present study after annealing treatment could be attributed to the Ru-rich layer of composition $Ru_{87}Al_2Ni_{11}$ and thereby increasing the overall hardness of the alloy as compared to the as-cast alloy.

5.3.4 Electrical resistivity

Figure 5.15 shows the variation of electrical resistivity (ρ) with temperature for the cast $Ru_{32}Al_{50}Ni_{18}$ alloy annealed at 1450 °C for 24 hours. The electrical resistivity data obtained as a function of temperature was fitted to a linear regression from which the temperature coefficient of resistivity (α) was estimated to be 0.16 $°C^{-1}$. It can be

seen that the data did not lead to a good linear fit, mainly because of the porosities present in the cast sample. Electrical resistivity of the alloy increases from 88 μΩ-cm at room temperature to 181.1 μΩ-cm at 600 °C.

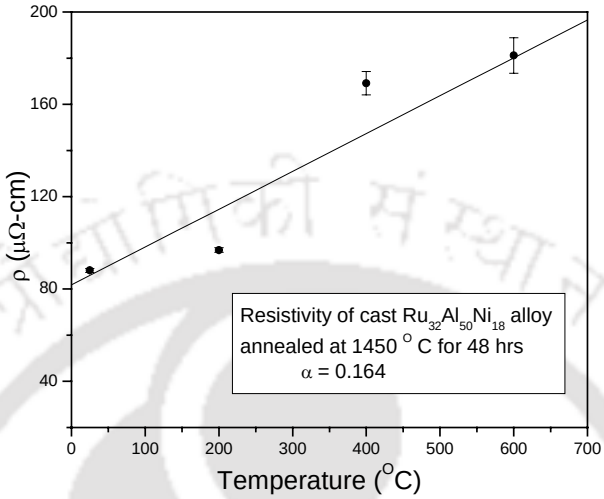

Figure 5.15: Plot of electrical resistivity with temperature for the cast $Ru_{32}Al_{50}Ni_{18}$ alloy annealed at 1450 °C

5.4 Summary and Conclusions

The highlights and new findings in the current investigations on $Ru_{32}Al_{50}Ni_{18}$ alloy are summarised below:

- SEM EDS data revealed the presence of $Ru_{85}Al_6Ni_9$ phases, indicating weak alloying of powders milled for 50 hrs.
- The powder mixture milled for 50 hours exhibited very poor bonding between the individual powders grains when cold compacted at 500 MPa. Hence cold compaction is not possible with these milled powders.
- The as-cast alloy was composed of two phases, which on annealing resulted in a near single (Ru, Ni)Al phase.
- Annealing of the cast alloy resulted in an increase in the overall hardness

5.5 Processing of $Ru_{43}Al_{39}Ni_{18}$ alloy by Powder metallurgy route

The elemental powder mixture of Ru + Al + Ni with the composition $Ru_{43}Al_{39}Ni_{18}$ was attrition milled for 50 hours. The crystallite size and micro strain for the various phases due to milling for different time periods were studied and the results obtained are presented in the following sub-sections.

5.5.1 Milling characteristics

Figure 5.16 shows the XRD patterns of $Ru_{43}Al_{39}Ni_{18}$ powder mixture at various stages of milling up to 50 hours. For the starting powder mixture (as-mixed), all the expected XRD reflections from Ru, Al and Ni planes can be seen in the Figure 5.16. In the starting powder mixture, reflections from Ru (100) and Ru (103) planes were seen to be overlapping with reflections from Al (111) and Al (311) planes, respectively. Similarly reflections from Ni (111) planes were overlapping with the reflection from Al (200) planes. No evidence of any new phase formation was observed from the XRD patterns even after 50 hours of milling. Broadening of the all the XRD peaks was observed during the initial stages of milling. It can be seen from Fig. 5.16 that the reflections from Al and Ni planes showed a rapid decrease in intensity with a simultaneous increase in their peak widths. Hence the reflections from Al and Ni planes were not discernible in the XRD patterns after milling for 10 hours and 15 hours, respectively.

The W-H plots corresponding to Ru and Ni reflections in the XRD patterns of as-milled $Ru_{43}Al_{39}Ni_{18}$ powder mixture are shown in Figures 5.17 (a-b), respectively. The corresponding crystallite size and micro-strain variations with milling time are shown in Figures 5.18 (a-b) and Figures 5.19 (a-b), respectively.

Micro-strain observed in Ru in the powder mixture with milling time did not reveal any systematic trend. The average crystallite size of Ru and Ni was estimated to be 217 nm and 239 nm, respectively after 5 hours of milling. After 15 hours of milling their average crystallite sizes were reduced to 182 nm and 30 nm, respectively. On continued milling, Ru crystallites attained an average crystallite size of 120 nm after 50 hours of milling. The micro-strain in Ru was estimated to be 0.00293 after 50 hours of milling and that of Ni was 0.00691 after 15 hours of milling. The variation of crystallite size and micro-strain of Al with milling time could not be determined since XRD reflections from Al planes could not be obtained after 10 hours of milling.

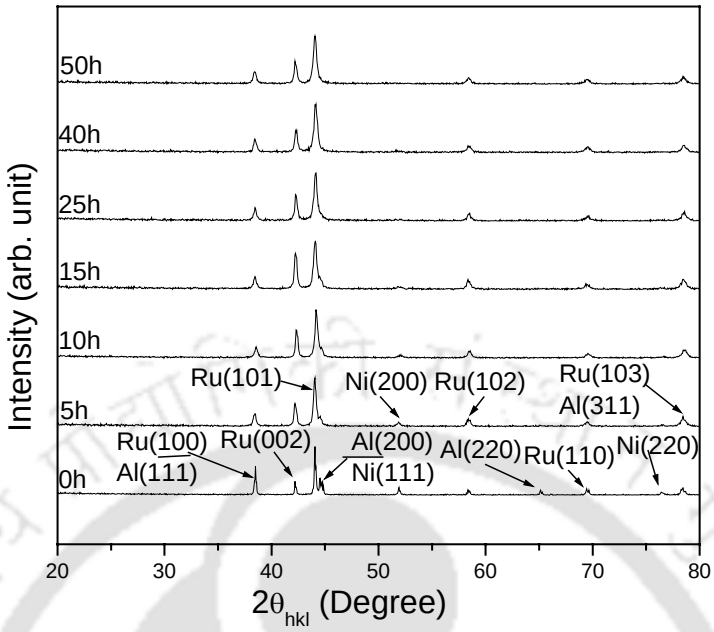

Figure 5.16: XRD patterns of $Ru_{43}Al_{39}Ni_{18}$ elemental powder mixture milled for various time periods

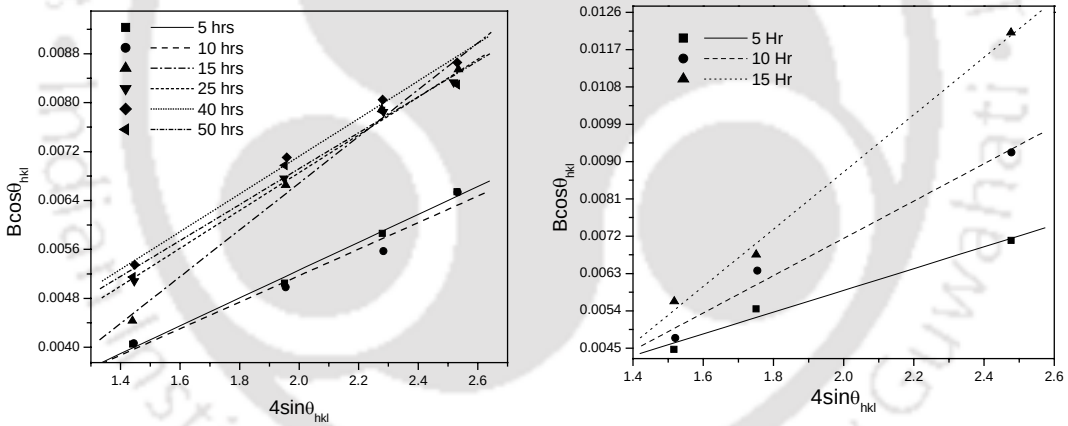

(a) (b)

Figure 5.17: W-H plots corresponding to (a) Ruthenium and (b) Nickel in the as-milled $Ru_{43}Al_{39}Ni_{18}$ powder mixture

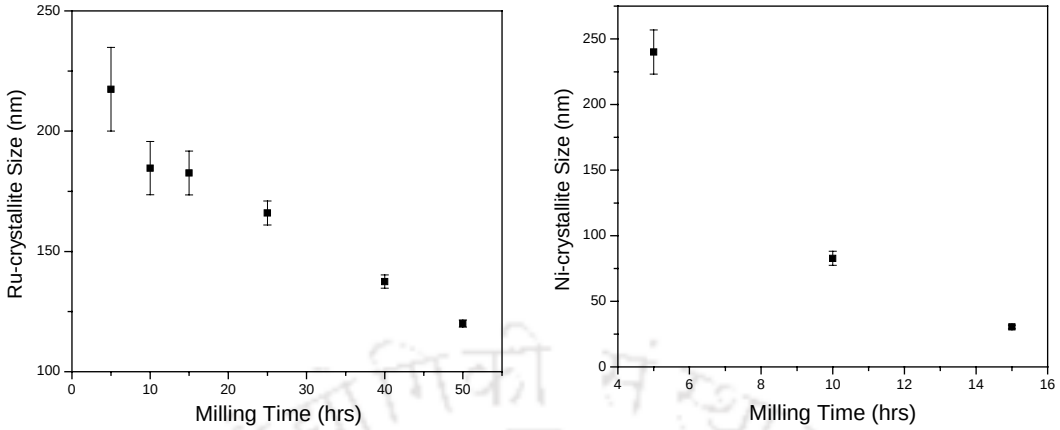

Figure 5.18: Variation of crystallite size with milling time corresponding to (a) Ruthenium and (b) Nickel in the as-milled $Ru_{43}Al_{39}Ni_{18}$ powder mixture

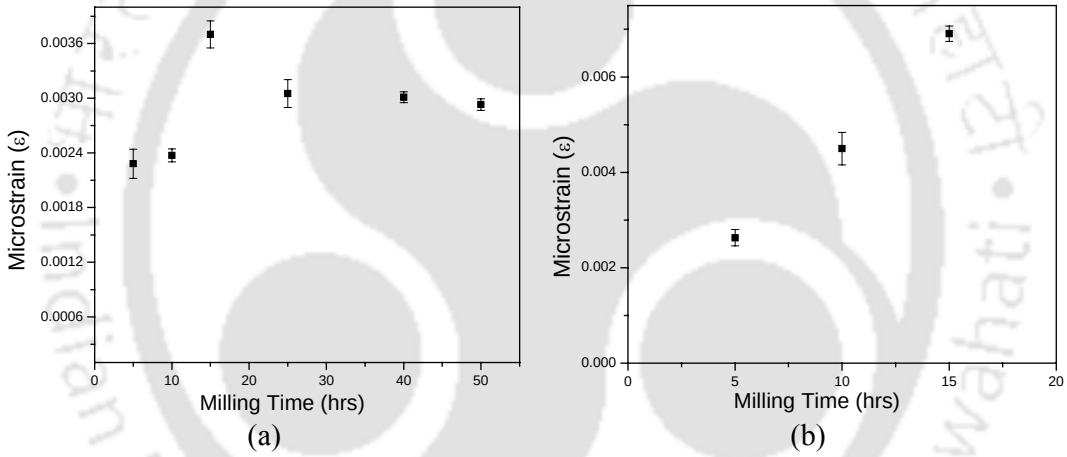

Figure 5.19: Variation of micro-strain with milling time for (a) Ruthenium and (b) Nickel in the as-milled $Ru_{43}Al_{39}Ni_{18}$ powder mixture

5.5.2 Milled powder microstructure

Microstructure of as-milled $Ru_{43}Al_{39}Ni_{18}$ powder mixture milled for 5 hours is shown in Figures 5.20 (a) and 5.21 (a). Micrograph reveals aggregates or clusters (labelled as "B") in the powder mixture. Smaller particles (labelled as "A") were found to be dispersed over these clusters of powder particles are seen in the Figure 5.20 (a). EDS spectra for the regions labelled as "A" and "B" are shown in Figures 5.20 (b-c), respectively. EDS analyses of the region labelled as "A" revealed that smaller particles seen were [Ru] containing small amounts of Al and Ni of average composition $Ru_{94}Al_5Ni_1$, whereas the region labelled as "B" was identified as aluminium with Ru

and Ni (of overall composition $Ru_{27}Al_{61}Ni_{12}$ corresponding to the region "B"). It can be inferred from Figures 5.20 (a-c) that the Ru particles get fragmented and embedded onto Al matrix in the course of milling. To investigate the alloying phenomena in the powder mixture during milling, as-milled powders were mounted in resin, polished and viewed under SEM. Figure 5.21 (a) shows the SEM micrograph of polished powder particles milled for 5 hours. EDS analysis shown in Figure 5.21 (b) revealed that all the particles [labelled as "A", "B" and "C" in Figure 5.21 (a)] are Ru-rich particles having an average composition of $Ru_{83}Al_{16}Ni_1$.

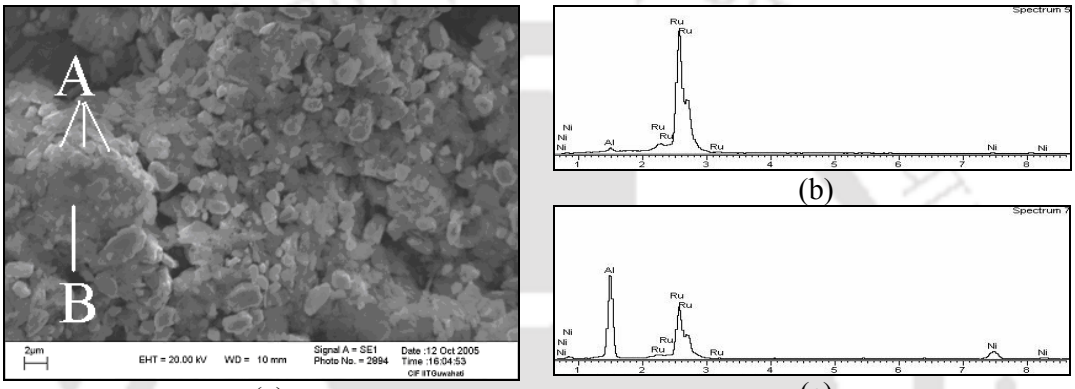

(a) (b) (c)

Figure 5.20: (a) SEM micrograph of $Ru_{43}Al_{39}Ni_{18}$ powder mixture milled for 5 hours: EDS spectra for (b) regions "A" and (c) region "B" in Figure (a)

SEM micrographs of the powder mixture milled for 25 hours are shown in Figures 5.22 (a-b). The powder mixture exhibited a flaky morphology with evidence of dispersion of very fine powder particles over it. In the polished powder sample, particles labelled as "B", "C" and "D" shown in Figure 5.22 (b) have an average composition of $Ru_{63}Al_{29}Ni_8$ and a typical EDS spectrum for the these particles is shown in Figure 5.22 (c). EDS spectra for the particles labelled as "A" and "E" in Figure 5.22 (b) are given in Figures 5.22 (d-e), respectively. The particles labelled as "A" and "E" were identified to have compositions of $Ru_{28}Al_{51}Ni_{21}$ and $Ru_{57}Al_{27}Ni_{16}$, respectively.

Discussion

Disappearance of XRD reflections from Al and Ni planes after 10 and 15 hours of milling was evident in the XRD patterns (*cf.* Figure 5.16) for as-milled powder mixture of composition $Ru_{43}Al_{39}Ni_{18}$. The disappearance of XRD reflections from Al and Ni planes could be attributed to the same reasons provided in the earlier discussions on $Ru_{47}Al_{53}$ and $Ru_{32}Al_{50}Ni_{18}$ powder mixtures (*cf.* sections 4.1.2 and 5.2.2). The

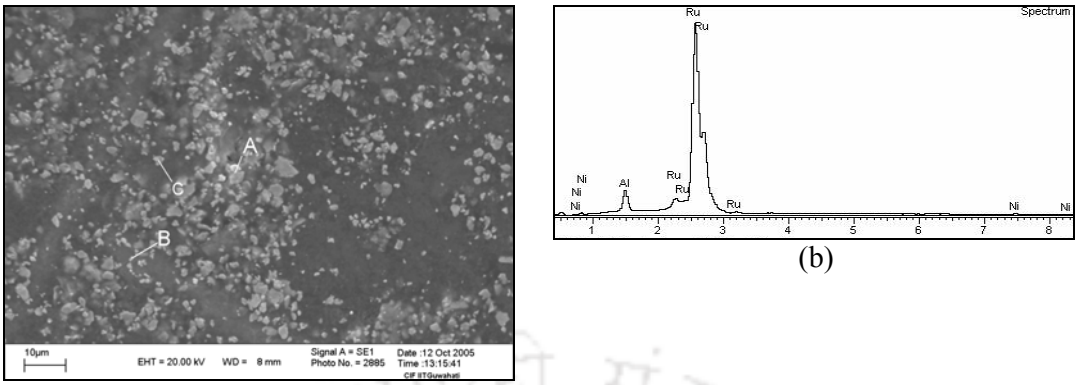

Figure 5.21: SEM micrograph of polished $Ru_{43}Al_{39}Ni_{18}$ powder mixture milled for 5 hours: (b) EDS spectra of particles labelled as "A", "B" and "C"

average crystallite size and micro-strain of Ru and Ni in the milled $Ru_{43}Al_{39}Ni_{18}$ powder mixture were of the same order as the ones obtained for the $Ru_{32}Al_{50}Ni_{18}$ powder mixture. Similar to the case of milled $Ru_{32}Al_{50}Ni_{18}$ powder mixture, the XRD analysis of milled $Ru_{43}Al_{39}Ni_{18}$ powder mixture did not reveal any new phase formation, However, SEM studies of polished $Ru_{43}Al_{39}Ni_{18}$ powder mixture milled for 25 hours revealed the formation of (Ru,Ni)Al phases [particle labelled as "A" in Figure 5.22 (b)]. The amount of formation of these phases was very low to be detected from the powder X-ray diffraction patterns. The high average crystallite size obtained for Ru (120 nm) might have hindered the formation of (Ru,Ni)Al phase during milling.

5.5.3 Microstructure of the sintered powder compact

The $Ru_{43}Al_{39}Ni_{18}$ powder mixture milled for 50 hours was cold compacted and subsequently sintered at 1450 ºC for 24 hours. The microstructure of the sintered alloy is shown in Figures 5.23 (a-b). The sintered alloy exhibited 85.5% theoretical density and composed of three phases, *viz.*, white (labelled as "W"), grey (labelled as "G") and black (labelled as "B") as seen in the backscattered SEM photomicrograph [Figure 5.23 (a)]. However, the black regions were voids created by the removal of some weakly bonded grains during polishing as seen clearly in the SEM photomicrograph in SE mode [Figure 5.23 (b)]. This indicates that sintering at 1450 °C for 24 hours does not yield a fully sintered sample in this case. The density measurements lend support to this conclusion. From EDS analyses, the white [region "W" in Figure 5.23 (a)] and grey [region "G" in Figure 5.23 (a)] regions were identified as phases with compositions

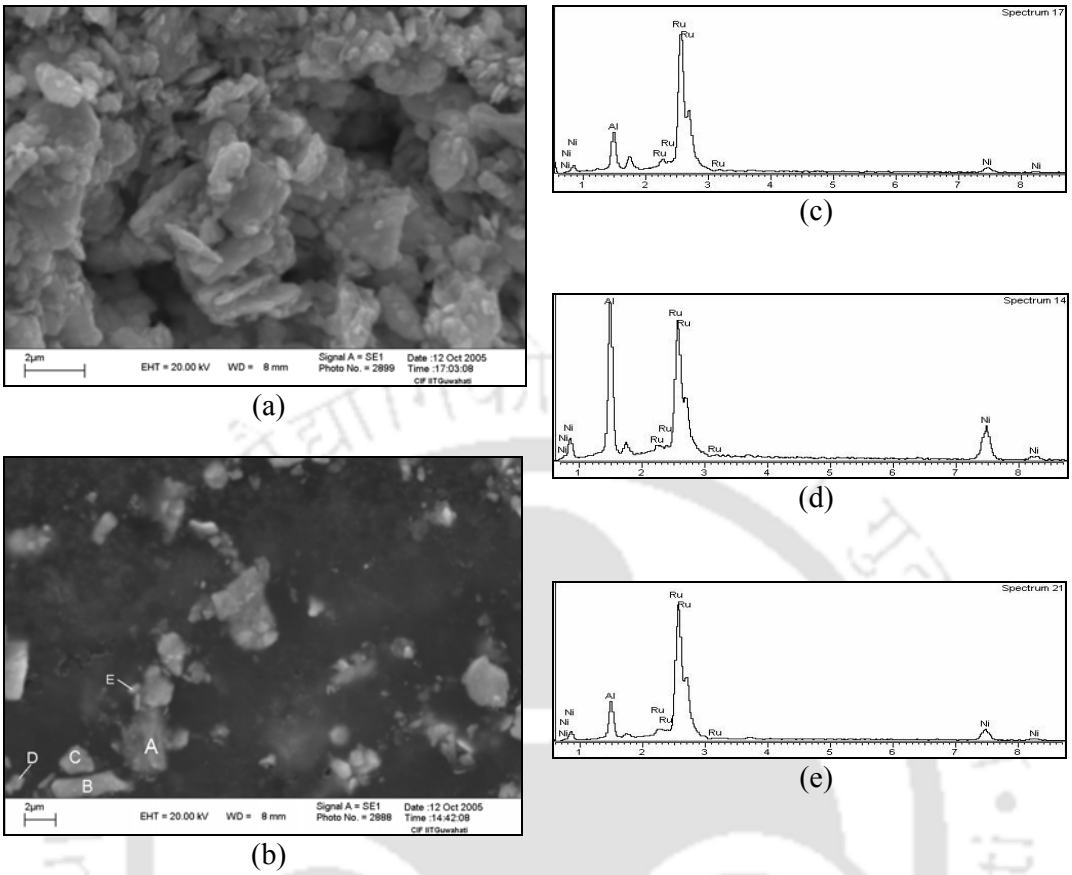

Figure 5.22: SEM micrographs of $Ru_{43}Al_{39}Ni_{18}$ powder mixture milled for 25 hours (a) as-milled (b) polished: EDS spectra corresponding to the particles (c) labelled as "B", "C" and "D" (d) labelled as "A" and (e) labelled as "E" in Figure (b)

$Ru_{82}Al_5Ni_{13}$ and $Ru_{15}Al_{60}Ni_{25}$, respectively. Since the composition of the loosely bound grains, which were removed during polishing stage, could not be analysed, it is not possible to make any comparison with the phase diagram. The EDS spectra for the white (W) and grey (G) regions are shown in Figures 5.24 (a-b), respectively.

5.5.4 Hardness measurement of the sintered $Ru_{43}Al_{39}Ni_{18}$ alloy

Indentations were not visible since the different phases present were very fine and precise measurements could not be obtained. Hence hardness testing of this sintered alloy sample could not be reported.

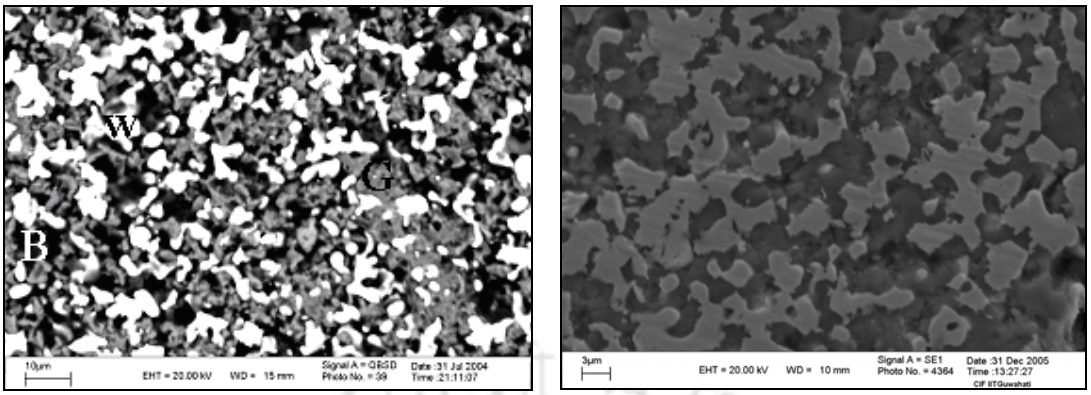

(a) (b)

Figure 5.23: SEM micrographs of the sintered $Ru_{43}Al_{39}Ni_{18}$ alloy in (a) backscattered (b) SE mode

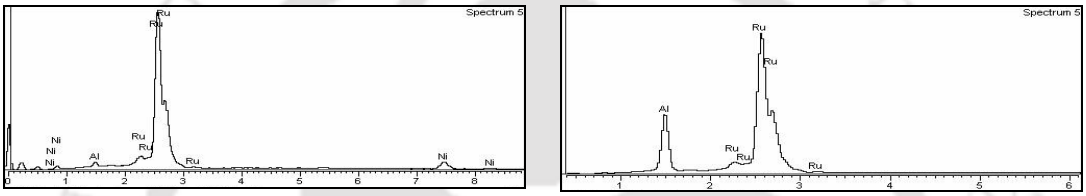

(a) (b)

Figure 5.24: EDS spectra for (a) white (W) region and (b) grey (G) region, in Figure 5.23 (a)

5.5.5 Electrical resistivity

Figure 5.25 shows the variation of electrical resistivity (ρ) of the sintered $Ru_{43}Al_{39}Ni_{18}$ alloy plotted against temperature. Approximately linear increase in the electrical resistivity with increase in temperature was observed for sintered $Ru_{43}Al_{39}Ni_{18}$ alloy. This alloy exhibited lower values of electrical resistivity as compared to the sintered $Ru_{47}Al_{53}$ alloy. The electrical resistivity of the alloy increases from 20 μΩ-cm at room temperature to 76 μΩ-cm at 600 °C with a temperature coefficient of electrical resistivity (α) of 0.1 $°C^{-1}$.

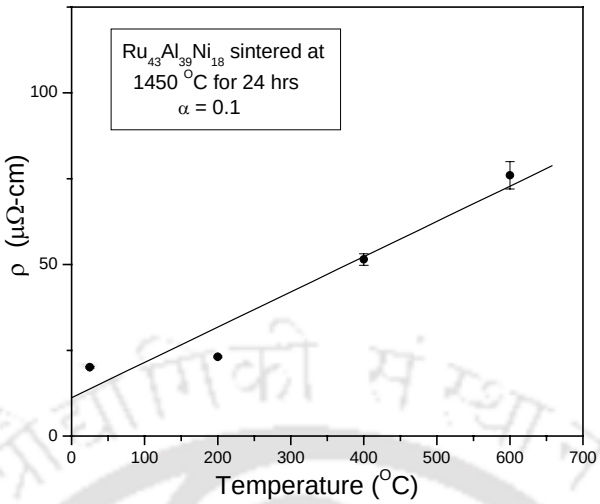

Figure 5.25: Plot of electrical resistivity with temperature for the sintered $Ru_{43}Al_{39}Ni_{18}$ alloy

5.6 Alloy processed by casting technique

The $Ru_{43}Al_{39}Ni_{18}$ cast alloy was processed by arc melting using the same procedures mentioned earlier. The solidified alloy in as-cast and annealed conditions is studied and the results are presented in the following sub-sections.

5.6.1 XRD analysis of the cast $Ru_{43}Al_{39}Ni_{18}$ alloy

Figures 5.26 (a-b) show the XRD patterns of the cast $Ru_{43}Al_{39}Ni_{18}$ alloy sample in as-cast and annealed conditions, respectively, within the range of 2θ value of 20^o to 85^o. XRD reflections seen in the Figure 5.26 (a) could be indexed to reflections from RuAl and Ru planes. The XRD pattern for cast $Ru_{43}Al_{39}Ni_{18}$ alloy sample annealed at 1450 °C for 24 hours [*cf.* Figure 5.26 (b)] shows similar type of XRD reflections as in the case of the as-cast sample. However, reflections from Ru planes were more intense than that of obtained for the as-cast sample. Two additional peaks corresponding to reflections from (100) and (002) planes of Ru were also observed in the XRD pattern of the alloy in the annealed state. This indicates that Ru or a Ru-rich phase might have been precipitated during annealing treatment.

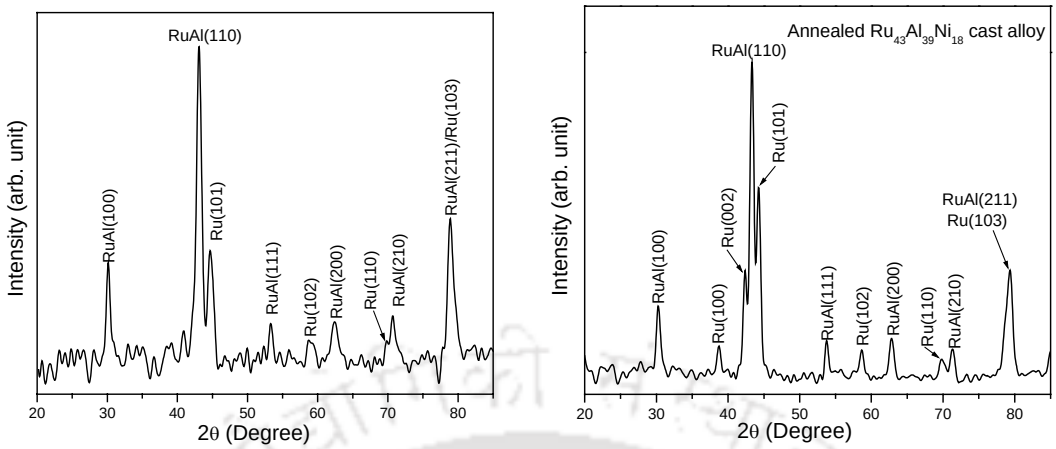

Figure 5.26: XRD patterns corresponding to cast $Ru_{43}Al_{39}Ni_{18}$ alloy sample in (a) as-cast and (b) annealed conditions

5.6.2 SEM microstructural study of cast $Ru_{43}Al_{39}Ni_{18}$ alloy

The as-cast structure of $Ru_{43}Al_{39}Ni_{18}$ alloy as shown in Figures 5.27 (a) and 5.28 (a), consists of three phases. The overall composition of the alloy was identified as $Ru_{46}Al_{35}Ni_{19}$ indicating loss of aluminium during casting. The EDS spectrum for the overall composition of the alloy is shown in Figure 5.27 (b). The three phases in the microstructure [*cf.* Figure 5.28 (a)] have been identified using EDS analyses as a white [Ru] phase labelled as "D" (composition $Ru_{64}Al_{12}Ni_{24}$), a dark grey γ-phase labelled as "F" (composition $Ru_{37}Al_{40}Ni_{23}$) adjacent to the white phase and a light grey β_2 [(Ru,Ni)Al] phase labelled as "E" (composition $Ru_{47}Al_{44}Ni_9$). The EDS spectra corresponding to the white [Ru phase, dark grey γ-phase and light grey β_2-phase are shown in Figures 5.28 (b-d), respectively.

Microstructure of the cast alloy annealing at 1450 °C for 24 hours shown in Figures 5.29 (a-c) revealed the presence of fine needle shaped entities, distributed in the grey region (labelled as "G") apart from regions labelled as "A" and "B". EDS spectra for the needle shaped phase and the grey matrix region "G" are shown in Figures 5.29 (d-e), respectively. Spot analyses of the needle shaped precipitated phase revealed an average composition of $Ru_{60}Al_{13}Ni_{27}$, whereas the average composition of the grey ("G") region was $Ru_{34}Al_{43}Ni_{23}$, indicating the latter to be the β_2-phase. The EDS

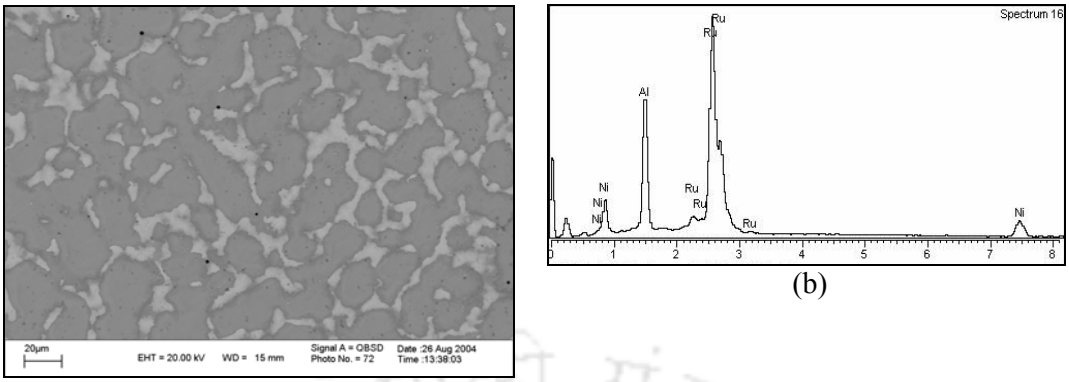

(a) (b)

Figure 5.27: (a) SEM micrograph of $Ru_{43}Al_{39}Ni_{18}$ alloy at low magnification and (b) EDS spectrum corresponding to the overall composition of the alloy

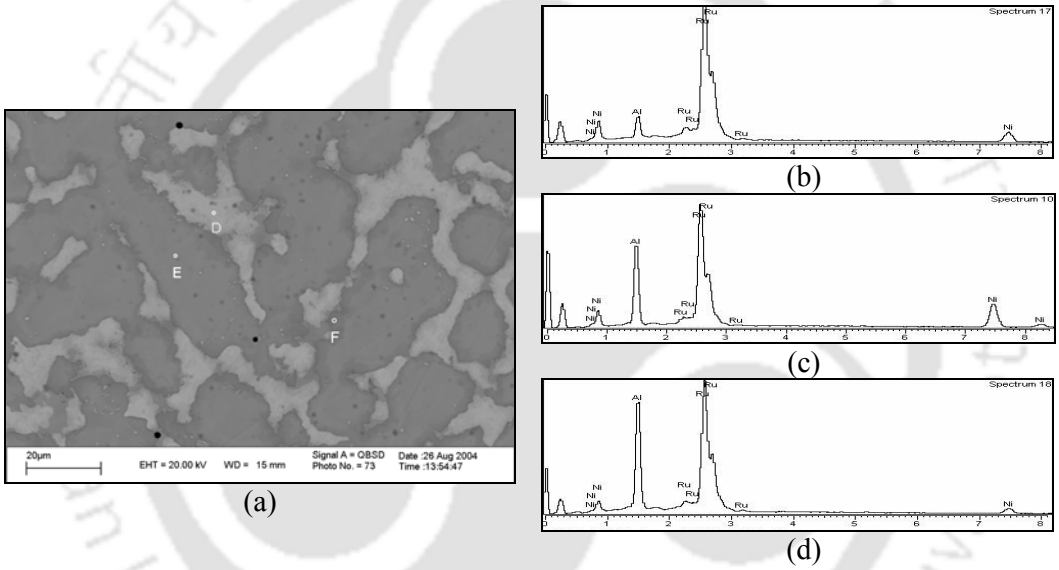

(a) (b) (c) (d)

Figure 5.28: (a) SEM micrograph showing as-cast microstructure of $Ru_{43}Al_{39}Ni_{18}$ alloy at high magnification: EDS spectra corresponding to the (b) region labelled as "A", (c) region labelled as "F" and (d) region labelled as "E" in Figure (a)

analysis shown in Figure 5.29 (f) revealed an overall composition of $Ru_{39}Al_{40}Ni_{21}$ for the region "G" with fine needle shaped precipitates. Grey β_2-phase regions devoid of the needle like disperse have also been observed in the micrographs shown in Figure 5.29 (b). These regions labelled as "G2" constitute a thin annular region (of typical thickness 3.5 µm) at the periphery of the grey β_2-phase containing the precipitates or grey regions within the white phase. EDS analysis shown in Figure 5.29 (g) revealed an overall (average) composition of $Ru_{35}Al_{43}Ni_{22}$ for this "G2" region. Analyses also indicate that there is only a marginal difference in the compositions of the grey β_2-

phase (region "G") and the grey phase (region "G2") depleted of the precipitated phase. Hence these are considered to be of same phase only. The white regions seen in the SEM micrograph [Figures 5.29 (b-c)] mainly consist of two types of lamellar structures [regions labelled as "A" and "B" in Figure 5.29 (b)]. Region "B" consists of a mixture of a white phase and a grey phase. Though the region "A" appears as a single-phase region, observation under very high magnification (micrographs not shown due to poor resolution) revealed that this region also composed of a mixture of two fine phases. The EDS analyses shown in Figures 5.29 (h-i) revealed an overall composition of $Ru_{59}Al_9Ni_{32}$ for the regions "A" and "B", respectively. The EDS spectra for the white and grey phases in the region "B" are shown in Figures 5.29 (j-k), respectively. The EDS analysed revealed the compositions of the white and grey phases in the region "B"' as $Ru_{80}Al_4Ni_{16}$ and $Ru_{39}Al_{37}Ni_{24}$, respectively. However, due to the very fine size of the grey phase, interaction of the electron beam with the neighbouring phases is possible rendering the EDS analysis data in these regions less accurate. Such difficulties have also been reported earlier [52, 53]. Since the overall composition of the region "A" is the same as that of region "B", region "A" can be considered as region "B" but with finer constituent phases. This could be confirmed when region "A" was viewed under higher magnification.

Discussion

XRD analysis of as-cast $Ru_{43}Al_{39}Ni_{18}$ alloy showed the presence of two phases in its structure [*cf.* Figure 5.26 (a)]. However, SEM analysis [*cf.* Figure 5.28 (a)] indicated the presence three phases in the as-cast alloy, *viz.*, white Ru-phase, metastable dark grey γ-phase and light grey β_2 (Ru,Ni)Al phase. The formation of the metastable dark grey γ-phase of composition $Ru_{37}Al_{40}Ni_{23}$ around white phase may be attributed to the coring during solidification. Since the percentage of this phase in the alloy is very low as compared to the other two phases, it could not be observed in the XRD patterns. It was expected that with proper heat treatment the alloy structure could result in a two-phase structure, as pointed out by the equilibrium phase diagram. XRD pattern for cast and annealed $Ru_{43}Al_{39}Ni_{18}$ alloy [*cf.* Figure 5.26 (b)] showed all the reflections from Ru planes present in the XRD pattern of the as-cast alloy. More amounts of Ru or a Ru-rich phase has precipitated out from the (Ru,Ni)Al phase during annealing treatment,

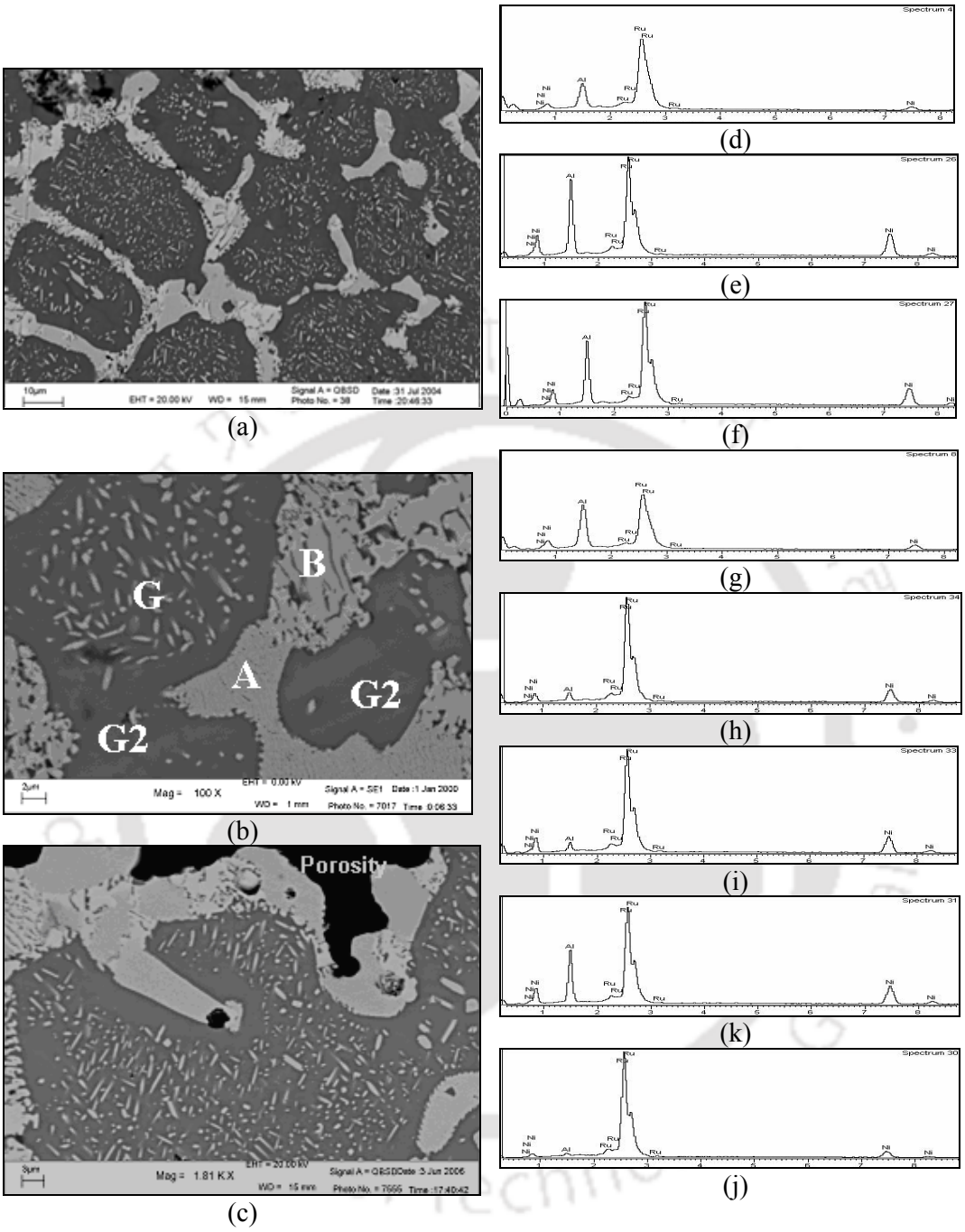

Figure 5.29: (a-b) SEM micrographs of the cast $Ru_{43}Al_{39}Ni_{18}$ alloy annealed at 1450 °C at low and high magnification respectively and (c) SEM micrograph showing white Ru rich layer around porosity regions; EDS spectra corresponding to the (d) precipitated phase in the region "G", (e) region "G" without the precipitated phase, (f) overall composition of the region "G" with precipitates, (g) region "G2", (h) overall composition of region "A", (i) overall composition of the region "B", (j) white in the region "B" and (k) black phase in the region "B"

resulting in the XRD reflections from all planes of Ru. The observation of two phases, *viz.*, β_2 and [Ru] in the annealed alloy is in accordance with earlier reports [53,73]. The metastable dark grey γ-phase observed in the as-cast alloy microstructure [region "F" in Figure 5.28 (a)] was eliminated on annealing treatment and resulted in the above two phases. The composition of $Ru_{80}Al_4Ni_{16}$ for [Ru] phase obtained in the present study was found to be similar to the reported composition ($Ru_{85}Al_3Ni_{12}$) for the same phase in an alloy of composition $Ru_{50}Al_{25}Ni_{25}$ [53]. Precipitation of Ru-rich needles of composition $Ru_{60}Al_{13}Ni_{27}$ in the grey β_2-phase occurred after annealing treatment. Precipitation of an unidentified phase has also been reported [53] in a Ru-Al-Ni ternary alloy. These Ru-rich needles have precipitated from the RuAl phase [region 'E' in Figure 5.28 (a)] of the as-cast alloy during annealing. During the annealing process, precipitation of [Ru] occurred in the β_2-phase [region "E" in Figure 4.28 (a)] in the as-cast alloy. While the Ru in interior of the β_2-phase contributed to the formation of the Ru-rich needles, the Ru at the periphery diffused into the A and B regions, leaving behind a precipitate-free zone [region "G2" in Figure 5.29 (b)] adjacent to the phase boundaries. The formation of a white Ru-rich layer around porosity [*cf.* Figure 5.29 (c)] was observed in this alloy after annealing as in the case of cast $Ru_{32}Al_{50}Ni_{18}$ alloy after annealing. Diffusion of Al into the free surface (porosity) from the surrounding matrix during annealing at 1450 °C results in the formation of the Ru-rich layer in the region surrounding the porosity.

5.6.3 Hardness measurement of the cast $Ru_{43}Al_{39}Ni_{18}$ alloy

Overall hardness of the as-cast and annealed $Ru_{43}Al_{39}Ni_{18}$ alloys was determined to be 696 VHN and 835 VHN, respectively. The micro indentations on different phases were made using 5 gmf load. The average microhardness values for the β_2-phase [region "E" in Figure 5.28 (a)] and [Ru] [labelled as "D" in Figure 5.28 (a)] were found to be 635 VHN and 849 VHN, respectively in the as-cast alloy. The average microhardness values of the constituent phases in the cast and annealed alloy were found to be as follows:

Grey β_2-phase with precipitates (Region "G" in Figure 4.46 (b)) = 848 VHN

White region [Region "B" in Figure 4.46 (b)] = 896 VHN

Grey phase depleted of precipitates [Region "G2" in Figure 4.46 (b)] = 796 VHN

Since there is no report on the hardness of this alloy composition in the literature, no direct comparison is possible. However, hardness values reported [53] for $Ru_{50}Al_{25}Ni_{25}$ alloys are given in the Table 5.1. It is evident from the data presented in table 5.1 that alloys in this region exhibit higher hardness, primarily due to the higher Ni content in the alloys. On annealing, there is a softening of the alloy, which has been interpreted as a result of the decrease in Ni content in the Ru phase with a consequent reduction in solid solution hardening [53]. Moreover, the Ni content in the Ru phase is higher when annealed at higher temperatures. The overall hardness values obtained for the alloy both in as-cast and annealed conditions in the present studies are comparable to the hardness values given in Table 5.1. However in the present case, the composition lies in the two-phase (β_2 + Ru) region of the ternary phase diagram. On annealing, unlike the case of the $Ru_{50}Al_{25}Ni_{25}$ alloy, the hardness increases in this alloy. This increase in overall hardness could be attributed to (i) an increase in the Ni content in the Ru and β_2 phase, leading to solid solution hardening and (ii) precipitation hardening due to the formation of Ru-rich precipitate needles in the β_2 phase. These two contributions result in a substantial increase in the overall hardness of the alloy as observed in the present studies. Overall hardness value of RuAl alloy containing ~ 8 at.% Ni has been reported to be ~ 750 VHN [53]. In the present study, the microhardness of β_2-phase ($Ru_{39}Al_{40}Ni_{21}$) was found to be 796 VHN in the precipitate-free region and 848 VHN in the region containing the needle-shaped precipitates. It is evident from the above that β_2 phase in the alloy undergoes precipitation hardening during annealing treatment.

Table 5.1: Hardness values for $Ru_{50}Al_{25}Ni_{25}$ alloy [53]

Treatment	Hardness, VHN	Phases present
As-cast	882	$\gamma + \beta_2 + Ru$
Annealing at 1250 ºC	773	$\gamma + \beta_2 + Ru$
Annealing at 1000 ºC	689	$\gamma + \beta_2 + Ru$

5.6.4 Electrical resistivity

Figure 5.30 shows the variation of electrical resistivity (ρ) with temperature for the cast $Ru_{43}Al_{39}Ni_{18}$ alloy annealed at 1450 ºC. The electrical resistivity increased from

144 μΩ-cm at room temperature to 269 μΩ-cm at 600 ºC. A linear increase in electrical resistivity was observed up to 600 ºC for this alloy. Linear fit to the data yielded a temperature coefficient of resistivity (α) value of 0.21 ºC $^{-1}$.

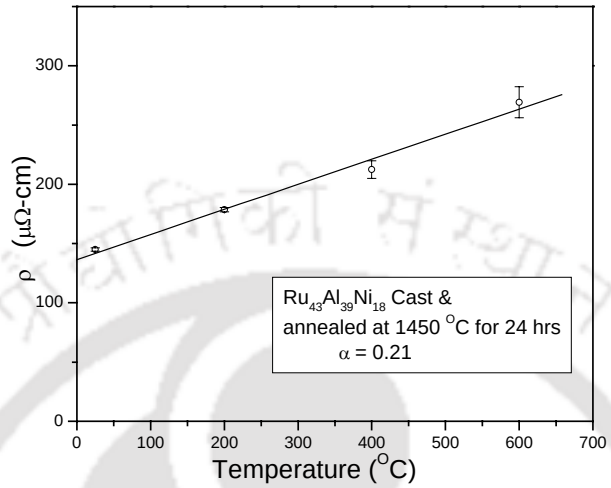

Figure 5.30: Plot of electrical resistivity with temperature for cast $Ru_{43}Al_{39}Ni_{18}$ alloy annealed at 1450ºC

5.7 Summary and Conclusions

The highlights and new finding in the current investigations on $Ru_{43}Al_{39}Ni_{18}$ alloy are summarised below:

- SEM EDS studies on the milled powders revealed the formation of $Ru_{28}Al_{51}Ni_{21}$ and $Ru_{57}Al_{27}Ni_{16}$ phases after 25 hours of milling.
- The milled powders could be cold compacted and sintered.
- The sintering studies revealed that higher sintering temperature/prolonged sintering time was required to achieve fully sintered alloy. The low theoretical density (85.5%) lends support this conclusion.
- The milled, compacted and sintered alloy exhibited a lower electrical resistivity than the binary Ru-Al alloy. Such a low electrical resistivity for any Ru-Al based alloy has not been reported earlier. However, the cast alloy after annealing exhibited a higher electrical resistivity which is more than seven times higher than that of the P/M processed alloy.
- The cast microstructure revealed the presence of a metastable γ-phase in addition to the already known Ru and β_2-(Ru,Ni)Al phases.

- Annealing the cast alloy at 1450 °C resulted in a morphological change in the microstructure. A needle shaped precipitate was formed in the β_2 phase after annealing. Hardness measurement revealed for the first time precipitation hardening as well as solid solution hardening in this alloy.

5.8 Processing of $Ru_{38.5}Al_{16.5}Ni_{45}$ alloy by powder metallurgy route

The composition $Ru_{38.5}Al_{16.5}Ni_{45}$ lies in the three-phase region (γ + β_2 + Ru), whereas the earlier two compositions were in the single-phase (β_2) and two-phase (β_2 + Ru) regions of the Ru-Al-Ni ternary phase diagram [*cf.* Figure 3.10], respectively. A study of this composition is expected to reveal the influence of γ-phase as well as the possibility of Ni substituting for Ru in the alloy. The elemental powder mixture of Ru + Al + Ni consisting of the composition $Ru_{38.5}Al_{16.5}Ni_{45}$ was attrition milled for 50 hours. The average crystallite size and micro-strain for the various phases due to milling for different time periods were studied and the results obtained are summarised in the following sub-sections.

5.8.1 Milling characteristics

Figure 5.31 shows the XRD patterns of $Ru_{38.5}Al_{16.5}Ni_{45}$ powder mixture at various stages of milling up to 50 hours. For the as-mixed powder, all the XRD reflections from Ru, Al and Ni planes can be seen in the Figure 5.31. In the as-mixed powder, reflections from Ru (100) and Ru (103) planes were seen to be overlapping with reflections from Al (111) and Al (311) planes, respectively. Similarly, reflections from Ni (111) planes were overlapping with the reflection from Al (200) planes. No evidence of any new phase formation was observed from the XRD patterns even after 50 hours of milling. Broadening of the all the XRD peaks were observed during the initial stages of milling. It can be seen from Figure 5.31 that the reflections from Al planes showed a rapid decrease in intensity with milling along with simultaneous increase in their peak widths. Hence the reflections from Al planes were not discernible in the XRD patterns after 5 hours of milling.

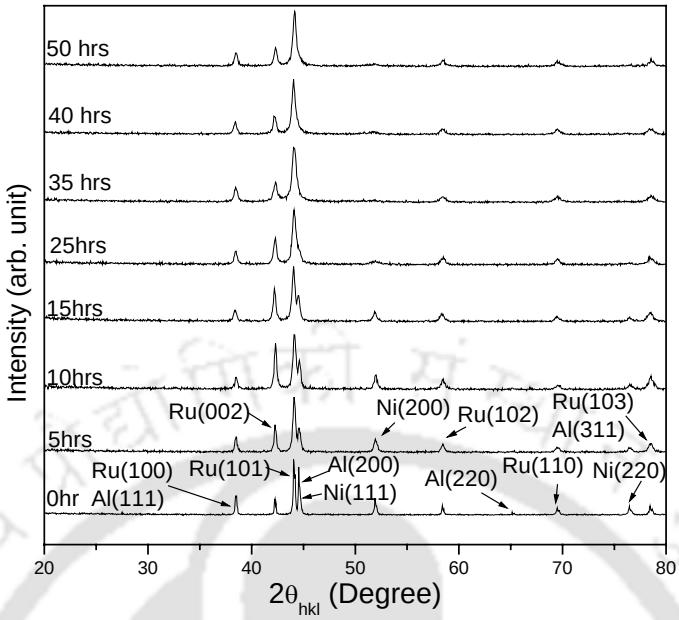

Figure 5.31: XRD patterns for the as-milled $Ru_{38.5}Al_{16.5}Ni_{45}$ powder mixture for various time periods

The W-H plots corresponding to Ru and Ni reflections in the XRD patterns of as-milled $Ru_{38.5}Al_{16.5}Ni_{45}$ powder mixture are shown in Figures 5.32 (a-b), respectively. The corresponding Ru and Ni average crystallite size and micro-strain variations with milling time are shown in Figures 5.33 (a-b) and Figures 5.34 (a-b), respectively. Micro-strain observed in Ru in the powder mixture with milling time did not reveal any systematic trend. Micro-strain in Ru increases sharply to a value of 0.00366 at 15 hours of milling from 0.00318 after 5 hours of milling and then almost remains constant up to 50 hours of milling. The average crystallite sizes of Ru and Ni were estimated to be 243 nm and 142 nm, respectively after 5 hours of milling. On continued milling, Ru and Ni crystallites attained average sizes of 98 nm and 20 nm after 50 hours of milling. The micro-strains in Ru and Ni were estimated to be 0.0033 and 0.01 after 50 hours of milling. The variation of average crystallite size and micro-strain of Al with milling time could not be determined since XRD reflections from Al planes could not be obtained after 10 hours of milling.

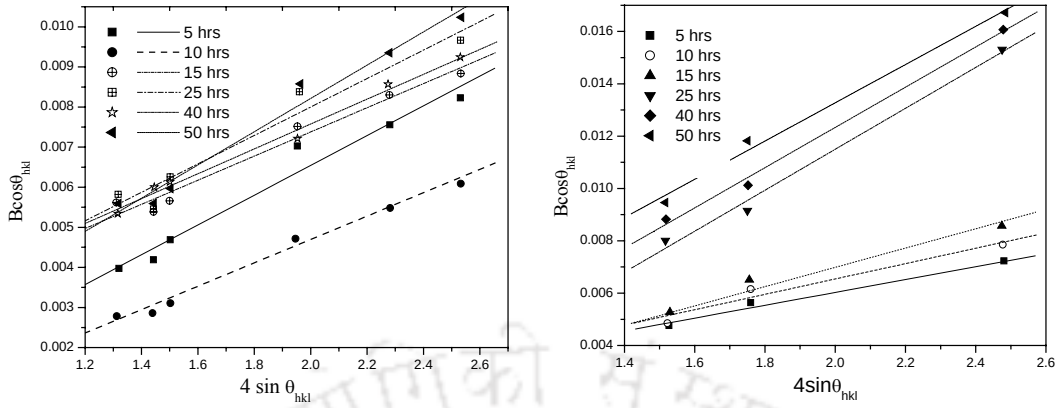

(a) (b)

Figure 5.32: W-H plots corresponding to the (a) Ru and (b) Ni in the as-milled $Ru_{38.5}Al_{16.5}Ni_{45}$ powder mixture

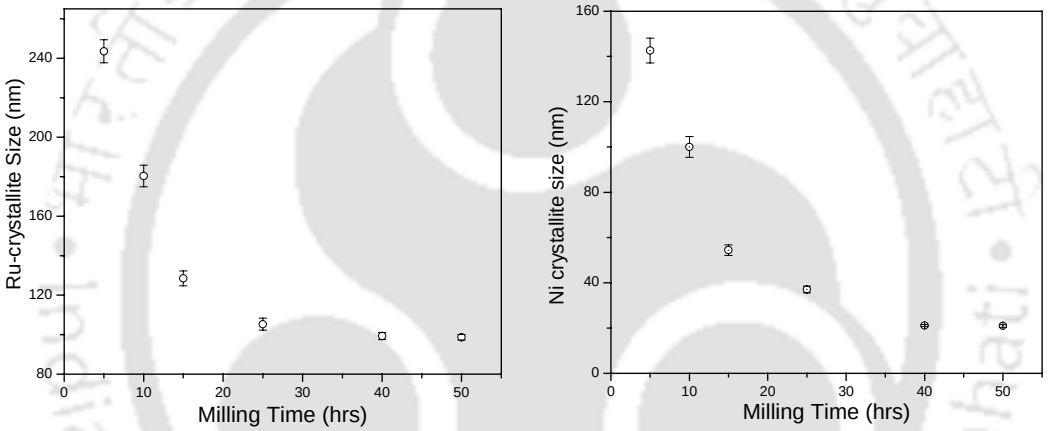

(a) (b)

Figure 5.33: Variation of average crystallite sizes with milling time corresponding to (a) Ru and (b) Ni

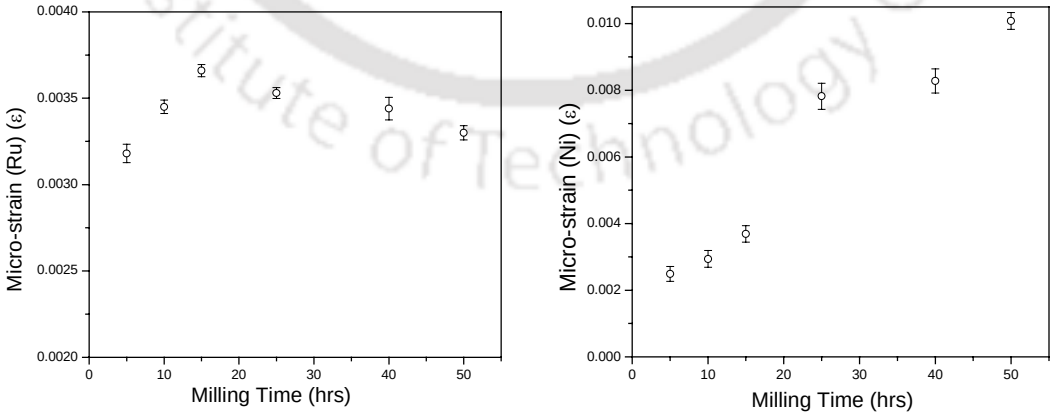

(a) (b)

Figure 5.34: Variation of micro-strain with milling time corresponding to the (a) Ru crystallite and (b) Ni crystallite

5.8.2 Milled powder microstructure

Microstructure of $Ru_{38.5}Al_{16.5}Ni_{45}$ powder mixture milled for 5 hours is shown in Figures 5.35 (a). The micrograph reveals flaky particles of various sizes formed due to severe plastic deformation of the powder particles as a result of milling. The EDS spectra for the particles labelled as "A", "B" and "C" are shown in Figures 5.35 (b-d), respectively. The fine particles (labelled as "A") in the Figure 5.35 (a) are Ru-rich particles containing small amounts of Ni and Al. The average composition of these particles was determined as $Ru_{68}Al_{14}Ni_{18}$. The coarse particles labelled as "B" are [Ni] with small amounts of Ru and Al with a composition of $Ni_{97}Al_2Ru_1$. In addition to these, particles with flaky morphology, labelled as "C" were also observed having average composition $Ru_{48}Al_{45}Ni_7$. The fine [Ru] particles resulted from the fragmentation of the brittle Ru particles during milling, whereas the flaky Ni rich particles were formed due severe plastic deformation of the ductile Ni particles. There is evidence of weak mechanical alloying with the formation of $Ru_{48}Al_{45}Ni_7$. However, the fine nature and the small amounts of this phase might have eluded detection by XRD.

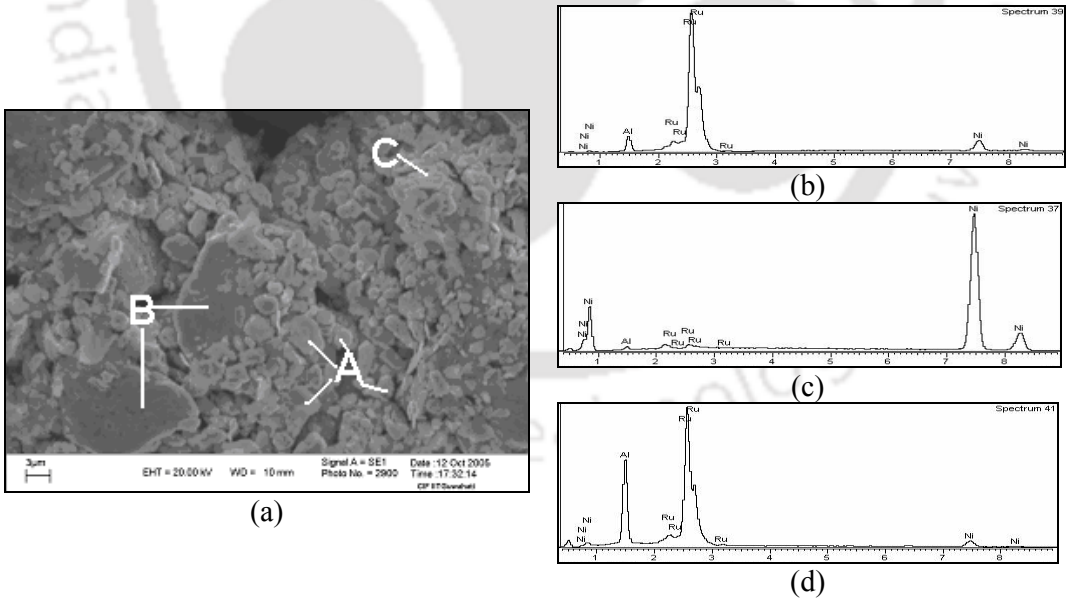

(a) (b) (c) (d)

Figure 5.35: (a) SEM micrograph showing the as-milled $Ru_{38.5}Al_{16.5}Ni_{45}$ powder microstructure milled for 5 hours; EDS spectra corresponding to the (b) particles labelled as "A", (c) particles labelled as "B" and (d) particles labelled as "C"

Milling for 25 hours led to the formation of agglomerations of fine powder particles. Figure 5.36 (a) shows the photomicrograph of the powder mixture milled for 25 hours. The particle sizes were finer as compared to 5 hours milled powder mixture. EDS spectra for the regions labelled as "A", "B", and "C" of Figure 5.36 (a) are shown in Figures 5.36 (b-d), respectively. Quantitative EDS analyses of the particles revealed average compositions of $Ru_{84}Al_4Ni_{12}$, $Ru_{24}Al_{11}Ni_{65}$, and $Ru_{36}Al_{20}Ni_{44}$ for the regions "A", "B", and "C", respectively. From Figure 5.36 (a), it is evident that Ni particles were reduced to smaller sizes when compared to 5 hours of milling. The strain hardening due to severe plastic deformation of the Ni-rich phases causes these particles to be brittle resulting in their fragmentation during the milling process.

Figure 5.37 (a) shows the microstructure of the powder mixture milled for 50 hours. Particles sizes were finer than those obtained after 25 hours of milling. A typical EDS spectrum obtained for the powder mixture is shown in Figure 5.37 (b). Quantitative analysis revealed an average composition of $Ru_{31}Al_{17}Ni_{52}$ for the milled powder mixture. These studies also revealed that the chemical composition of the powders was homogeneous due to the prolonged milling.

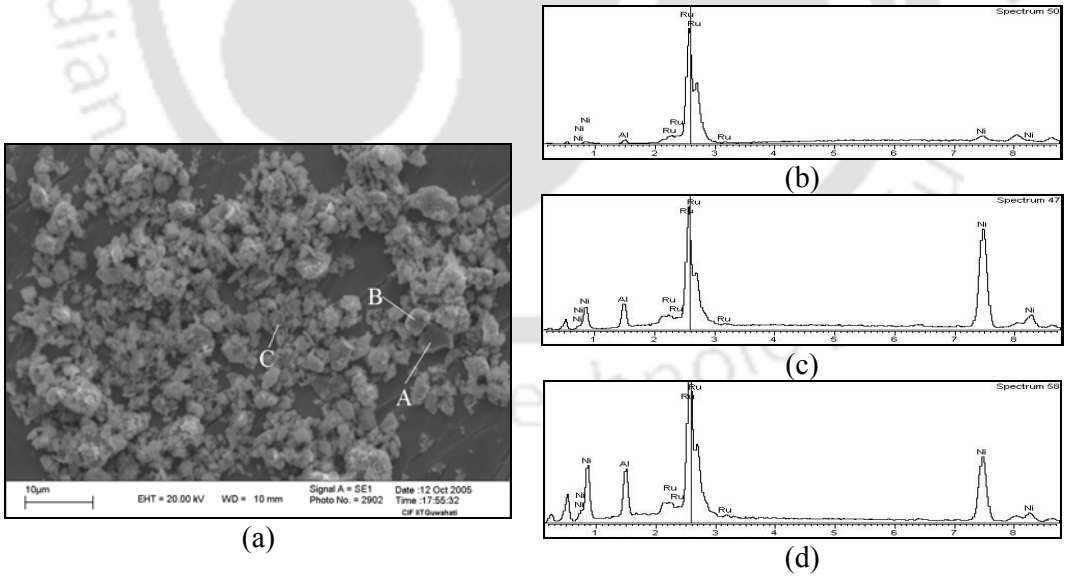

(a) (b) (c) (d)

Figure 5.36: (a) SEM micrograph of as-milled $Ru_{38.5}Al_{16.5}Ni_{45}$ powder mixture milled for 25 hours; EDS spectra corresponding to the (b) region labelled as "A", (c) region labelled as "B" and (d) region labelled as "C" in Figure (a)

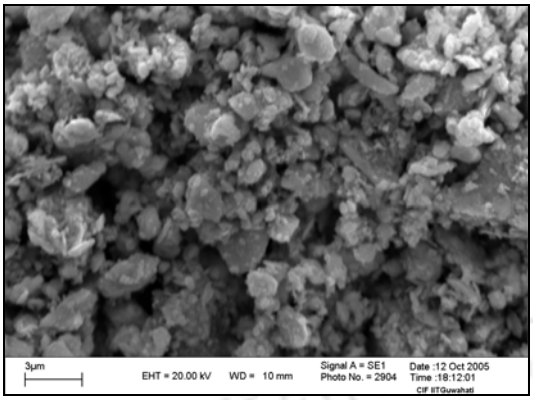

((a)

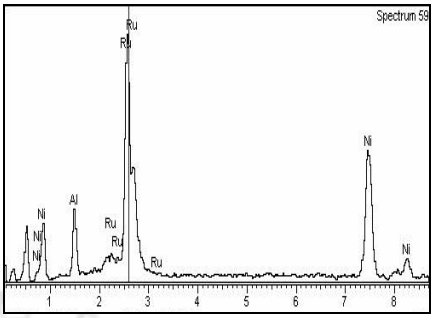

(b)

Figure 5.37: (a) SEM micrograph of as-milled $Ru_{38.5}Al_{16.5}Ni_{45}$ powder mixture milled for 50 hours and (b) EDS spectrum corresponding to the overall composition of the powder mixture

Discussion

XRD pattern (*cf.* Figure 5.31) for powder mixture after 5 hours of milling did not show any peak corresponding to reflections from Al planes. This observation is similar to the ones encountered in the case of $Ru_{47}Al_{53}$, $Ru_{32}Al_{50}Ni_{18}$ and $Ru_{43}Al_{39}Ni_{18}$ powder mixtures (*cf.* sections 4.1.2, 5.2.2 and 5.4.2). The variation in crystallite size and micro-strain corresponding to Ru and Ni in milled $Ru_{38.5}Al_{16.5}Ni_{45}$ powder mixture followed the same trend as observed for $Ru_{32}Al_{50}Ni_{18}$ and $Ru_{43}Al_{39}Ni_{18}$ powder mixtures. However, in this powder composition the final average crystallite size obtained for Ru was 98 nm, which was lower than the Ru average crystallite sizes obtained in $Ru_{32}Al_{50}Ni_{18}$ (130 nm) and $Ru_{43}Al_{39}Ni_{18}$ (120 nm) powder mixtures. In this powder mixture no new phase formation was evident from XRD patterns of powders milled up to 50 hours. However, EDS studies of $Ru_{38.5}Al_{16.5}Ni_{45}$ powder mixture milled for 25 hours revealed particles with ternary compositions. These observations indicate the formation of Ru and Ni-rich solid solutions during the course of milling. Unlike the other two Ru-Al-Ni compositions, this powder composition exhibited a chemical homogeneity on prolonged milling.

5.8.3 Microstructure of the sintered powder compact

The $Ru_{38.5}Al_{16.5}Ni_{45}$ powder mixture milled for 50 hours was cold compacted and subsequently sintered at 1450 ºC for 24 hours. The sintered alloy exhibited 94% theoretical density. The sintered alloy microstructure is shown in Figures 5.38 (a-b).

Analysis of the EDS spectrum shown in Figure 5.38 (c) revealed an overall composition of $Ru_{44}Al_{17}Ni_{39}$ for the alloy. The SEM micrograph shown in Figure 5.38 (a) showed that the microstructure of the alloy composed white, grey and black phases. The grey phase was seen in the white phase region. The constituent phases in the white region (white and grey) were identified as $Ru_{69}Al_2Ni_{29}$ and $Ru_{14}Al_8Ni_{78}$, respectively. The EDS spectra corresponding to the white and grey phases are shown in Figures 5.38 (d-e), respectively. The EDS analysis shown in Figure 5.38 (f) revealed a composition of $Ru_{10}Al_{62}Ni_{28}$ for the black phase. The smooth edges of the black phase as seen in the micrograph in SE mode [*cf.* Figure 5.38 (b)] indicate the possibility of liquid phase sintering to have occurred during the sintering process. For the Al:Ni ratio of 62:28 in the binary Al-Ni system, the liquidus temperature is below 1400 ºC [*cf.* Figure 2.3]. Hence, it is possible for the formation of a liquid phase while sintering the alloy having a phase of composition $Ru_{10}Al_{62}Ni_{28}$ at 1450 ºC. The compositions of the constituent phases in the white phase could not be determined because of the fine nature of the phases. In the composition analysis of the black phase, a large (~ 57 at. %) amount of oxygen was detected. Since it is not clear whether this high oxygen content represents the adsorbed oxygen or the oxidized part of the material, the composition of the black phase could not be determined accurately. It is worth mentioning that the milled and compacted powder mixture resulted in a well-sintered alloy. No further discussion based on the ternary phase diagram is attempted on this alloy since there is a lack of reliable composition data of three phases.

5.8.4 Mechanical properties of sintered $Ru_{38.5}Al_{16.5}Ni_{45}$ alloy

Overall Vickers hardness of the sintered $Ru_{38.5}Al_{16.5}Ni_{45}$ alloy was found to be 571 VHN. Microhardness of the constituent phases in the sintered RuAl alloy was determined using a load of 10 gmf. The microhardness values corresponding to the white and black regions were found to be 506 (VHN) and 691 (VHN), respectively.

Ultimate strength of 1533 MPa was obtained for the sintered alloy sample by compression testing on non-standard cylindrical specimens. The Young's modulus and yield strength values could not be determined since non-standard samples were used. This sintered alloy exhibited higher values of compressive strength compared to the sintered RuAl sample. The high ultimate compressive strength exhibited by this alloy is

attributed to the well-sintered characteristics of this sample compared to the RuAl sample which showed poor bonding characteristics.

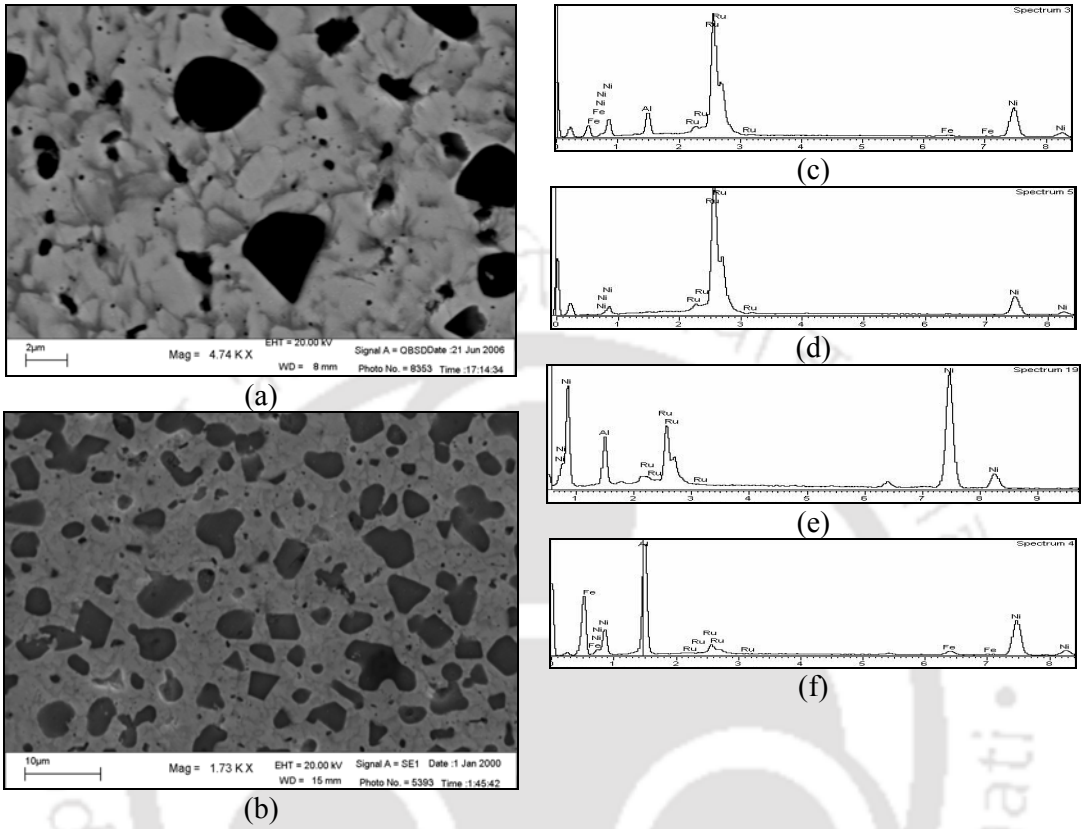

Figure 5.38: SEM micrographs of the sintered $Ru_{38.5}Al_{16.5}Ni_{45}$ alloy in (a) backscattered mode and (b) secondary electron mode; EDS spectra corresponding to the (c) overall composition of the alloy, (d) white phase, (e) grey phase and (f) black phase

5.8.5 Electrical resistivity

Variation of electrical resistivity (ρ) of the sintered $Ru_{38.5}Al_{16.5}Ni_{45}$ alloy with temperature is shown in Figure 5.39. The resistivity was found to increase from 27 μΩ-cm at room temperature to 39.2 μΩ- cm at 600 ºC. An approximately linear increase of electrical resistivity with temperature was observed up to 600 ºC. Linear fit to the data yielded a temperature coefficient of resistivity (α) value of 0.01 $ºC^{-1}$.

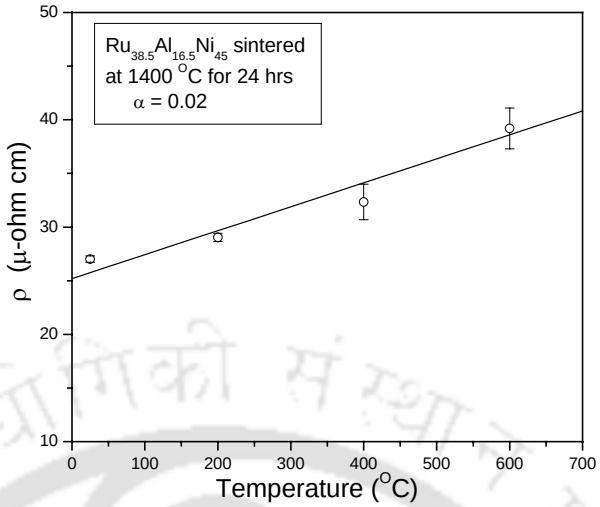

Figure 5.39: Plot of electrical resistivity with temperature for the sintered $Ru_{38.5}Al_{16.5}Ni_{45}$ alloy

5.9 Alloy processed by casting technique

Structure, microstructure, microhardness and electrical resistivity of the cast alloy were investigated both in the as cast as well as annealed conditions. The results obtained are presented in the following sub-sections.

5.9.1 XRD analysis of the cast $Ru_{38.5}Al_{16.5}Ni_{45}$ alloy

Figures 5.40 (a-b) show the XRD patterns corresponding to the cast $Ru_{38.5}Al_{16.5}Ni_{45}$ alloy in the as-cast as well as annealed conditions, respectively. Eight XRD reflections were observed in the XRD pattern [Figure 5.40 (a)] within a 2θ range of 20° to 85°. All the XRD reflections could be indexed to the reflections from either Ru or Ni planes. Hence one can infer from the XRD pattern that the cast alloy consisted of two-phases, *viz.,* [Ru] and [Ni].

Figure 5.40 (b) shows the XRD pattern for the cast $Ru_{38.5}Al_{16.5}Ni_{45}$ alloy annealed at 1450 °C for 24 hours. The XRD pattern showed no new peaks in the annealed alloy when compared to the as-cast alloy.

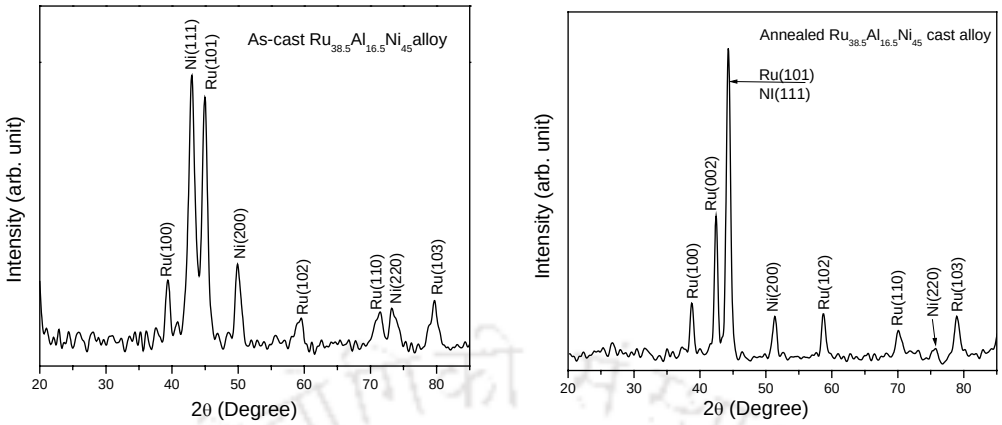

(a) (b)

Figure 5.40: XRD patterns corresponding to the (a) as-cast and (b) cast and annealed $Ru_{38.5}Al_{16.5}Ni_{45}$ alloy

5.9.2 SEM microstructural study of cast $Ru_{38.5}Al_{16.5}Ni_{45}$ alloy

Figures 5.41 (a-b) show SEM micrographs of as-cast microstructure of the $Ru_{38.5}Al_{16.5}Ni_{45}$ alloy. SEM image at low magnification shown in Figure 5.41 (a) revealed a dendritic growth of crystals along with micro porosities. EDS spectrum for the overall composition is shown in Figures 5.41 (c). Overall composition of the alloy determined by EDS analysis was $Ru_{39}Al_{13}Ni_{48}$ indicating aluminium loss with concomitant increase in nickel concentration. High magnification observation of the microstructure revealed a white phase (labelled as "A" and "B") and a black phase (labelled as "C) as seen in the Figure 5.41 (b). Features typical of coring were observed from the contrast variation in the region "A" of the back-scattered SEM micrograph. EDS spectra for the regions "A", "B" and "C" are shown in Figures 5.41 (d-f), respectively. Variation in composition across the white phase was observed, e.g., the compositions corresponding to the regions labelled as "A" and "B" in Figure 5.41 (b) were respectively $Ru_{66}Al_{7}Ni_{27}$ and $Ru_{56}Al_{9}Ni_{35}$. The black phase labelled as "C" in Figure 5.41 (b) was identified as $Ru_{28}Al_{15}Ni_{57}$.

Annealing of the cast alloy at 1450 °C for 24 hours resulted in a structural evolution as seen in Figure 5.42 (a). During the annealing process, the morphology of both white and black phases seen in the as-cast alloy has changed to a lamellar type of structure. EDS spectra of the overall compositions for white (labelled as "W") and black lamella (labelled as "B") are shown in Figures 5.42 (d-e), respectively. EDS analyses of the white and black lamella regions revealed the overall compositions

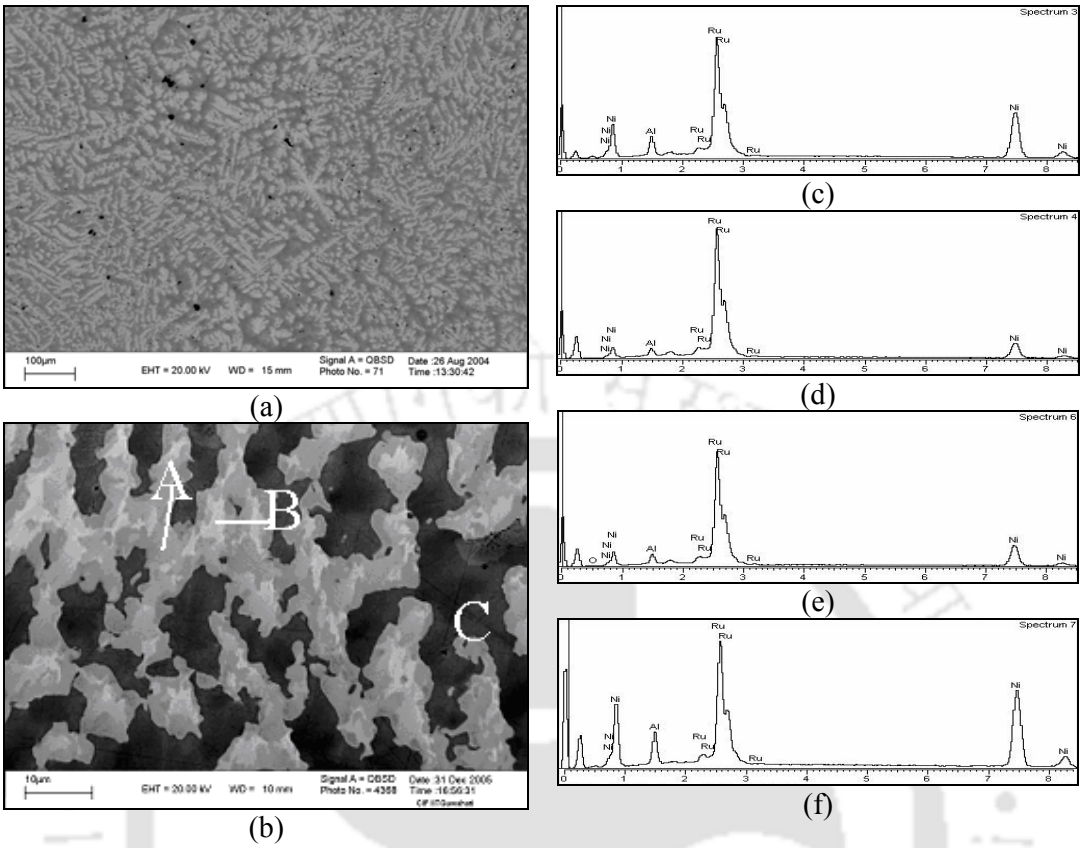

Figure 5.41: (a-b) SEM micrographs of as-cast $Ru_{38.5}Al_{16.5}Ni_{45}$ alloy at low and high magnification, respectively; EDS spectra corresponding to the (c) overall composition of the alloy, (d) region "A", (e) region "B" and (f) region "C"

corresponding to these two regions as $Ru_{51}Al_{10}Ni_{39}$ and $Ru_{33}Al_{13}Ni_{54}$, respectively. Figures 5.42 (b-c) show the SEM high magnification micrographs of black and white lamella regions, respectively. Analyses of the EDS spectra shown in Figures 5.42 (f-g) revealed the composition of the black (labelled as "B1") and white (labelled as "B2") regions inside black lamella as $Ru_{17}Al_{13}Ni_{70}$ and $Ru_{56}Al_{10}Ni_{34}$, respectively. Similar analyses shown in Figures 5.42 (h-i) identified the white (labelled as "W1") and black (labelled as "W2") inside white lamella as $Ru_{59}Al_{7}Ni_{34}$ and $Ru_{19}Al_{19}Ni_{62}$, respectively.

Discussion

Both XRD and SEM analyses confirmed a two-phase structure in the as-cast $Ru_{38.5}Al_{16.5}Ni_{45}$ alloy. SEM study showed evidence of coring in the white [labelled as "A" and "B" in Figure 5.41 (b)] and black phases. Coring is characteristic of the solidification of solid solution alloys.

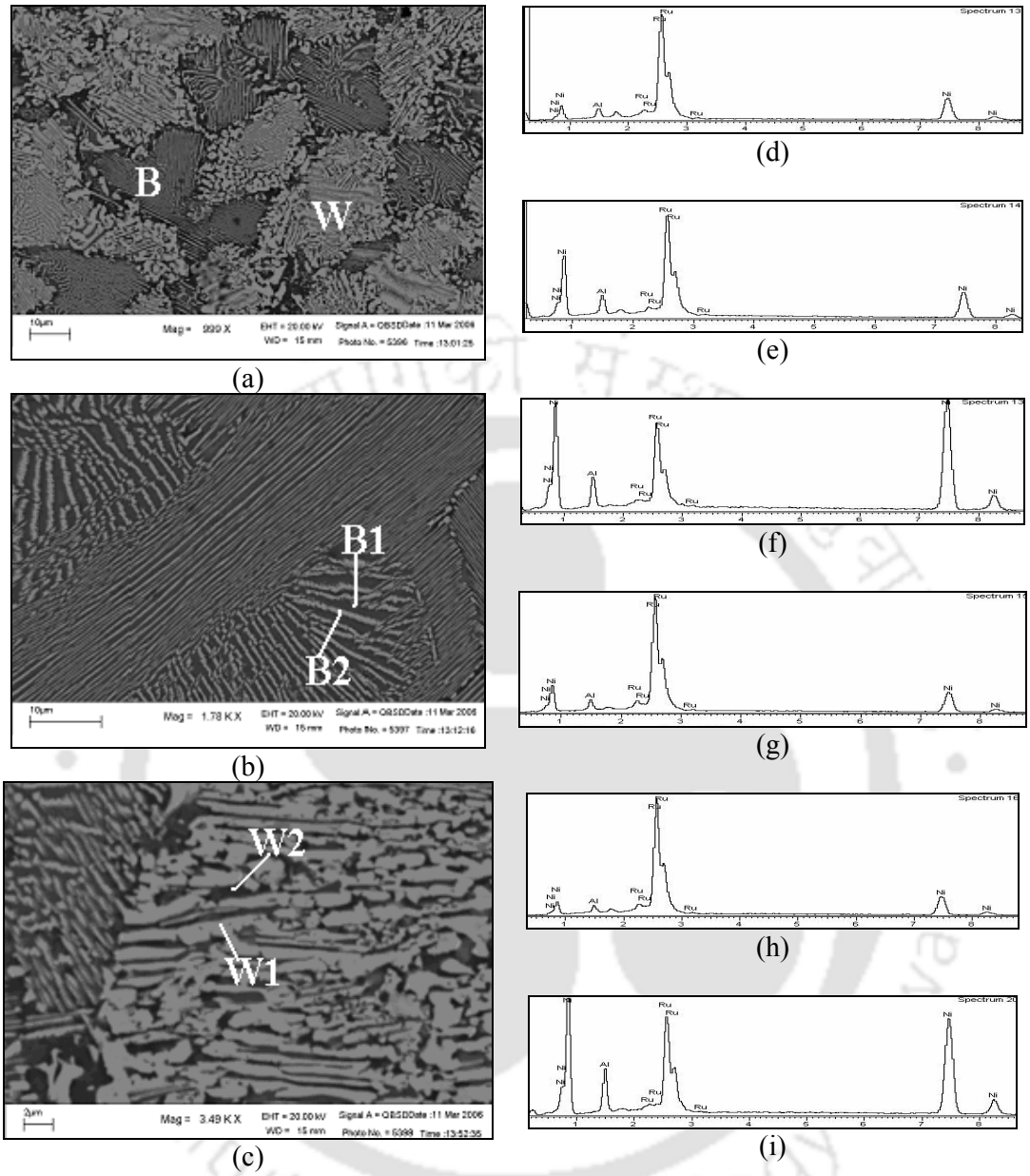

Figure 5.42: SEM micrographs of $Ru_{38.5}Al_{16.5}Ni_{45}$ alloy annealed at 1450 °C (a) at low magnification and (b-c) black and white lamellae [labelled as "B" and "W" in Figure (a)] at high magnification, respectively; EDS spectra corresponding to the (d-e) overall compositions for the regions "W" and "B" in Figure 5.42 (a), respectively, (f-g) regions "B1" and "B2" in Figure 5.42 (b), respectively and (h-i) regions "W1" and "W2" in Figure 5.42 (c), respectively

The overall composition of the alloy ($Ru_{39}Al_{13}Ni_{48}$) falls in the three-phase (γ + β_2 + Ru) field and also in the neighbourhood of the two-phase (γ + Ru) field of the isothermal phase diagrams at 1250 °C and 1000 °C [53]. The present studies on cast

alloy annealed at 1450 °C suggest that there is a shift in the two-phase (γ + Ru) field towards the three-phase (γ + β_2 + Ru) field as well as toward the γ-phase field (of Figure 3.10). Higher annealing temperature used in the present study (1450 °C) might have resulted in this shifting of the two-phase (γ + Ru) field towards the three-phase (γ + β_2 + Ru) field.

The microstructural studies on cast and annealed alloy revealed two types of lamellar structures, each with unique overall compositions. These lamellae consist of mixtures γ + Ru phases with distinct compositions for each constituent phase. The presence of two distinct lamellar structures gives an indication that there are two eutectoid compositions. It was also observed that the [Ru] phase in the two lamellae gave slightly varying compositions, *viz.*, $Ru_{56}Al_{10}Ni_{34}$ and $Ru_{59}Al_7Ni_{34}$. The corresponding compositions of the γ phases are $Ru_{17}Al_{13}Ni_{70}$ and $Ru_{19}Al_{19}Ni_{62}$, respectively. It has been pointed out that the slow inter-diffusion of Ru in Ni alloys [75] as well as slow homogenization in Ru-Al-Ni alloys [74] might result in a inhomogeneous structure unless annealed for very long periods of time. Since the γ + Ru phase compositions corresponding to the two lamella structures are close, it might be possible to obtain a single lamellar structure by prolonged annealing.

5.9.3 Hardness measurement of the $Ru_{38.5}Al_{16.5}Ni_{45}$ cast alloy

Overall hardness values corresponding to the as-cast and cast and annealed $Ru_{38.5}Al_{16.5}Ni_{45}$ alloy were determined to be 557 VHN and 763 VHN, respectively. The average microhardness values of the white (region W) and black (region B) lamella regions in the cast and annealed alloy [shown in Figure 5.42 (a)] were determined at a load of 5 gmf. These regions exhibited microhardness values of 825 VHN and 750 VHN, respectively.

The alloy exhibited an increase in the overall hardness values in annealed condition than in as-cast condition. Since there is no report on the hardness of this alloy composition in the literature, no comparison is possible. However, overall hardness values reported for $Ru_{25}Al_{25}Ni_{50}$ alloy [53,73] are given in the Table 5.2. The softening of alloy after annealing has been interpreted [53] in the same manner as explained in the earlier section [*cf.* section 5.5.3]. The overall hardness value obtained for the alloy in as-cast condition in the present studies is comparable to the hardness values given in Table

5.2. However in the present case, the composition lies in the two-phase (γ + Ru) region of the ternary phase diagram. On annealing, there is an increase in the overall hardness value in this alloy unlike the case of the $Ru_{25}Al_{25}Ni_{50}$ alloy. Although, there is only a slight change in the overall composition of the respective phases in as-cast alloy had occurred after annealing, the lamellar structure observed in these regions might have resulted in the increase in the overall hardness values. The white lamella region exhibited higher microhardness value (825 VHN) as compared to the black lamella region (750 VHN) in the cast and annealed alloy. The presence of more amount of *hcp* [Ru] in the white lamella region has resulted in the higher microhardness than the black lamella region.

Table 5.2: Overall hardness value for $Ru_{25}Al_{25}Ni_{50}$ alloy [53,73]

Treatment	Hardness, VHN	Phases present
As-cast	554±52 [73], 515 [52]	γ + β_2
1000 °C	489 [52]	γ + β_2 + Ru
1250 °C	414 [52]	γ + β_2 + Ru

5.9.4 Electrical resistivity

Electrical resistivity (ρ) measurement on $Ru_{38.5}Al_{16.5}Ni_{45}$ cast-and-annealed alloy indicated a resistivity of 119 μΩ-cm at room temperature, which increased to 191 μΩ-cm at 600 ºC. Figure 5.43 shows an approximately linear dependency of electrical resistivity vs. temperature up to 600 ºC. Linear fit to the data yielded a temperature coefficient of resistivity (α) value of 0.13 $ºC^{-1}$.

The cast-and-annealed $Ru_{38.5}Al_{16.5}Ni_{45}$ alloy exhibited a lower resistivity as compared to the cast-and-annealed $Ru_{43}Al_{39}Ni_{18}$ alloy (144 μΩ-cm at room temperature to 269 μΩ-cm at 600 ºC). The presence of Ni-rich γ-phase might have resulted in the lower resistivity in this alloy as compared to the cast-and-annealed $Ru_{43}Al_{39}Ni_{18}$ alloy.

5.10 Summary and Conclusions

The highlights and new finding in the current investigations on $Ru_{38.5}Al_{16.5}Ni_{45}$ alloy are summarised below:

- SEM-EDS studies on the milled powders revealed the formation of $Ru_{48}Al_{45}Ni_7$ after 5 hours of milling.

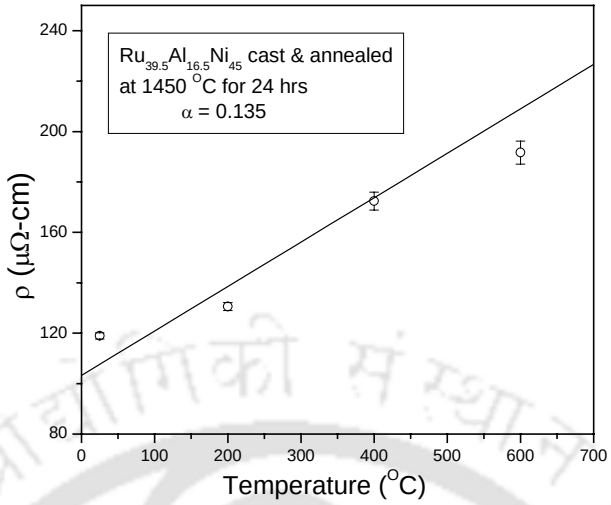

Figure 5.43: Plot of electrical resistivity with temperature for the cast $Ru_{38.5}Al_{16.5}Ni_{45}$ alloy annealed at 1450 °C

- The milled powders could be cold compacted and well sintered. The sintered alloy exhibited 94% theoretical density.
- The milled, compacted and sintered alloy exhibited lower electrical resistivity than the binary Ru-Al alloy. But this value was slightly higher than the sintered $Ru_{43}Al_{39}Ni_{18}$ alloy. However, the cast alloy after annealing exhibited a higher electrical resistivity, which is more than four times higher than that of the P/M, processed alloy. The temperature coefficient of resistivity of the P/M processed alloy was the lowest among all Ru-Al alloys reported, which shows that this alloy exhibits the least change in resistivity with temperature.
- The microstructure of the cast and annealed alloy revealed two lamellar structures each with a slight different composition. Prolonged annealing might result in inter-diffusion between the two lamellar regions resulting in a single a lamellar structure.
- Annealing of the cast alloy resulted in an increase in the overall hardness, which could be attributed the formation of the lamellar structure.

Summary of discussion on ternary Ru-Al-Ni alloys

Table 5.3 shows the compositions of the constituent phases in the three ternary Ru-Al-Ni alloys after annealing at 1450 °C. The corresponding positions of the constituent and overall phase compositions superimposed on 1250 °C Ru-Al-Ni phase

diagram proposed by Chakravorty and West [53] are shown in Figure 5.44. It is evident from the figure that annealing $Ru_{39}Al_{13}Ni_{48}$ alloy at 1450 °C results in the formation of two phases: a Ni-rich γ-phase and a Ru-rich phase. Moreover, with respect to the 1250 °C isothermal phase diagram, the 1450 °C phase diagram is expected that the γ + Ru two-phase field extends towards the γ + β_2 + Ru three-phase region as well as towards the γ-phase fields.

Table 5.3: Constituent phases and hardness values of the analysed both as-cast and cast and annealed ternary Ru-Al-Ni alloys

Alloy composition determined by EDS (at.%)	Treatment of alloy	Phases present	Phase composition (at.%)	Micro-hardness of phase (VHN)	Overall hardness of alloy (VHN)
1) $Ru_{39}Al_{45}Ni_{16}$ ($Ru_{32}Al_{50}Ni_{18}$)	As-cast	β_2	$Ru_{46}Al_{45}Ni_9$	570	528
		β_1	$Ru_{17}Al_{37}Ni_{46}$	629	
	Annealed	β_2	$Ru_{45}Al_{45}Ni_{10}$		
		β_2	$Ru_{38}Al_{45}Ni_{17}$	660	640
		[Ru] (around porosity)	$Ru_{87}Al_2Ni_{11}$	774	
2) $Ru_{46}Al_{35}Ni_{19}$ ($Ru_{43}Al_{39}Ni_{18}$)	As-cast	β_2	$Ru_{47}Al_{44}Ni_9$	636	696
		γ	$Ru_{37}Al_{40}Ni_{23}$	-	
		[Ru]	$Ru_{64}Al_{12}Ni_{24}$	-	
	Annealed	β_2	$Ru_{34}Al_{43}Ni_{23}$	848• (796)°	835
		γ	$Ru_{39}Al_{37}Ni_{24}$	-	
		[Ru]	$Ru_{80}Al_4Ni_{16}$	896↑	
		Precipitated needles	$Ru_{60}Al_{13}Ni_{27}$	-	
3) $Ru_{39}Al_{13}Ni_{48}$ ($Ru_{38.5}Al_{16.5}Ni_{45}$)	As-cast	γ	$Ru_{28}Al_{15}Ni_{57}$	-	557
		[Ru]	$Ru_{66}Al_7Ni_{27}$	-	
		[Ru]	$Ru_{56}Al_9Ni_{35}$	-	
	Annealed	γ	$Ru_{17}Al_{13}Ni_{70}$	-	763
		γ	$Ru_{19}Al_{19}Ni_{62}$	-	
		[Ru]	$Ru_{56}Al_{10}Ni_{34}$	-	
		[Ru]	$Ru_{59}Al_7Ni_{34}$	-	

Starting composition of the alloys are shown within brackets
• Precipitated region
° Precipitate free region
↑ Hardness value reported for lamellar regions
Lamellar regions consist of γ and Ru

γ - Ni solid solution
β_2 – RuAl phase
β_1 – NiAl phase

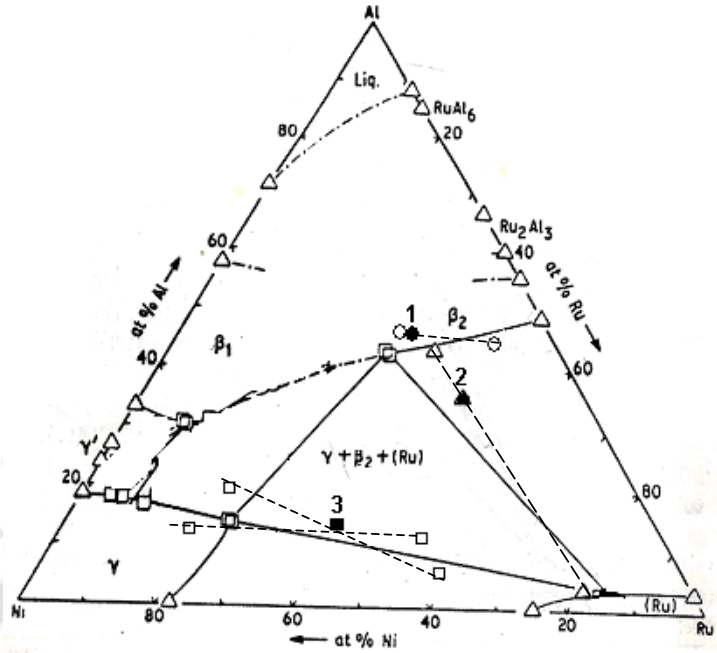

Figure 5.44: Overall and phase compositions in the partial isothermal diagram at 1250 °C [53]. The overall compositions are shown with filled symbols and the constituent phases are shown with open symbols.

$Ru_{39}Al_{45}Ni_{16}$ alloy and $Ru_{46}Al_{35}Ni_{19}$ alloys annealed at 1450 °C contained a [Ru] phase with compositions $Ru_{87}Al_2Ni_{11}$ and $Ru_{80}Al_4Ni_{16}$, respectively, whereas Chakravorty and West found a composition of $Ru_{85}Al_3Ni_{12}$ for the same phase in $Ru_{50}Al_{25}Ni_{25}$ alloy [53] annealed at 1250 °C. The present study indicates that the [Ru] phase field expands to accommodate up to 16 at.% Ni when annealed at 1450 °C. Composition analysis of $Ru_{46}Al_{35}Ni_{19}$ alloy annealed at 1450 °C indicates an expansion of the three-phase ($\gamma + \beta_2$ + Ru) region towards the two-phase (β_2 + Ru) region with respect to the isothermal phase diagram at 1250 °C [53].

In the case of $Ru_{39}Al_{13}Ni_{48}$ alloy, the microstructure studies revealed presence of two distinct lamellar structures having two different overall compositions. These lamellae consist of mixtures of γ + [Ru] phases with distinct compositions for each constituent phase. The varying overall as well as the constituent compositions in the two lamellae could be attributed to slow inter-diffusion of Ru in Ni alloys and slow homogenization in Ru-Al-Ni alloys reported in the literatures [74,75].

The binary Ru-Al alloy in the present study exhibited overall hardness values of 290 VHN and 334 VHN in the as-cast and annealed conditions, respectively. The

overall hardness values of the multiphase Ru-Al-Ni ternary alloys were higher than that of the binary Ru-Al alloy. This increase in the overall hardness values can be attributed to one or more of the following reasons: (i) the solid solution strengthening of RuAl phase by addition of nickel, (ii) presence of Ni-rich γ-phase in the alloy, and (iii) increase in the micro-hardness of the β_2-RuAl phase due to precipitation of Ru-rich needles on heat treatment.

Figure 5.45 shows the comparison of electrical resistivity values obtained as a function of temperature up to 600 °C, for three ternary cast Ru-Al-Ni alloys annealed at 1450 °C. Out of the three ternary Ru-Al-Ni alloy compositions, the $Ru_{39}Al_{45}Ni_{16}$ alloy exhibited the lowest electrical resistivity values followed by $Ru_{39}Al_{13}Ni_{48}$ and $Ru_{46}Al_{35}Ni_{19}$ alloy samples.

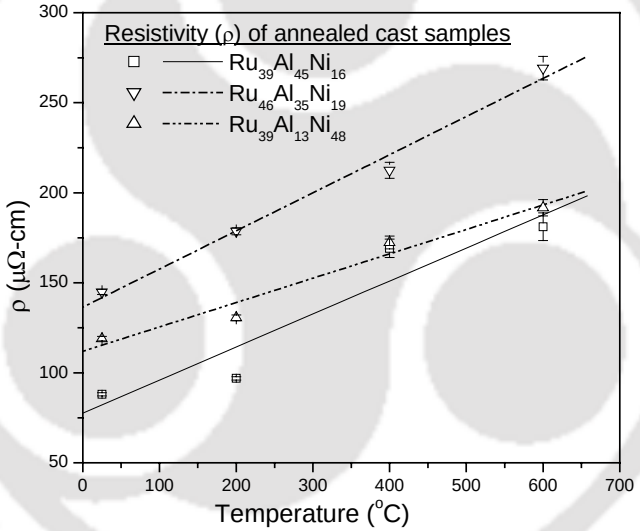

Figure 5.45: Comparison of electrical resistivity of cast and annealed Ru-Al-Ni alloy

The lowest electrical resistivity values exhibited by the $Ru_{39}Al_{45}Ni_{16}$ alloy could be attributed to the single (β_2) phase structure of the alloy. On the other hand $Ru_{46}Al_{35}Ni_{19}$ and $Ru_{39}Al_{13}Ni_{48}$ alloys showed a two-phase structure consisting of (β_2 + Ru) and (γ + Ru) phases, respectively, and hence higher resistivity values as compared the $Ru_{39}Al_{45}Ni_{16}$ alloy. Of these two alloys, lower resistivity is exhibited by $Ru_{39}Al_{13}Ni_{48}$ alloy as compared to the $Ru_{46}Al_{35}Ni_{19}$ alloy, which could be attributed to the presence of conductive Ni-rich γ-phase in the former. The needle shaped precipitates in the β_2-phase and the lamellar structure of the [Ru] phase in the

$Ru_{46}Al_{35}Ni_{19}$ alloy might have resulted in the highest electrical resistivity observed in this alloy. Moreover, $Ru_{39}Al_{13}Ni_{48}$ alloy exhibited the lowest temperature coefficient of resistivity (α = 0.13 $°C^{-1}$) as compared to the values obtained for $Ru_{39}Al_{45}Ni_{16}$ (α = 0.164 $°C^{-1}$) and $Ru_{46}Al_{35}Ni_{19}$ (α = 0.21 $°C^{-1}$) alloys. All the three annealed Ru-Al-Ni alloys exhibited higher resistivity values compared to annealed RuAl alloy (resistivity of 54 μΩ-cm and 90 μΩ-cm at room temperature and at 600 °C, respectively). The increase in the resistivity values in the ternary Ru-Al-Ni alloys as compared to the binary RuAl alloy may to be attributed to presence of Ni enriched phases in the ternary alloys.

5.8 Summary and Conclusions

The highlights and new finding in the current investigations on Ru-Al-Ni alloys are summarised below:

- The average crystallite size of Ru was found to be of the same order in $Ru_{43}Al_{39}Ni_{18}$ powder mixture as that of the $Ru_{32}Al_{50}Ni_{18}$ after 50 hours of milling. However, the crystallite size obtained for Ru in $Ru_{38.5}Al_{16.5}Ni_{45}$ powder mixture after 50 hours was found to be lower than the above two powder compositions.
- The micro-strains observed in the three milled Ru-Al-Ni powder compositions, *viz.*, $Ru_{32}Al_{50}Ni_{18,}$ $Ru_{43}Al_{39}Ni_{18}$ and $Ru_{38.5}Al_{16.5}Ni_{45}$ did not reveal any systematic trend. The micro-strain in Ru was found to be of the same order in these three milled powder compositions after 50 hours of milling.
- XRD analysis of all the three milled Ru-Al-Ni powder mixtures did not reveal any new phase formation even after milling up to 50 hours. However, SEM studies of $Ru_{43}Al_{39}Ni_{18}$ and $Ru_{38.5}Al_{16.5}Ni_{45}$ powder mixtures milled for 25 and 5 hours, respectively, revealed the formation of (Ru,Ni)Al phases. The small amount of these phases formed during milling might have eluded the detection by XRD.
- The green compacts obtained from $Ru_{32}Al_{50}Ni_{18}$ powder mixtures milled for 50 hours exhibited very poor adhesion between the powder grains and hence suitable samples for sintering could not be obtained. The sintered alloys obtained from $Ru_{43}Al_{39}Ni_{18}$ and $Ru_{38.5}Al_{16.5}Ni_{45}$ powder mixtures milled for 50 hours exhibited 85.5% and 94% theoretical densities. The sintered alloy obtained from cold compacted $Ru_{43}Al_{39}Ni_{18}$ powder mixture exhibited voids due to removal of some

weekly bound grains during polishing stage whereas that of obtained from $Ru_{38.5}Al_{16.5}Ni_{45}$ powder mixture resulted in a well-sintered alloy.

- All the three cast Ru-Al-Ni alloys exhibited an increase in the overall hardness values after annealing.
- Cast-and-annealed $Ru_{39}Al_{45}Ni_{16}$ alloy (starting composition $Ru_{32}Al_{50}Ni_{18}$) exhibited lower electrical resistivity values as compared to the $Ru_{46}Al_{35}Ni_{19}$ (starting composition $Ru_{43}Al_{39}Ni_{18}$) and $Ru_{39}Al_{13}Ni_{48}$ (starting composition $Ru_{38.5}Al_{16.5}Ni_{45}$) within the temperature range from room temperature to 600 ºC. Moreover, $Ru_{39}Al_{13}Ni_{48}$ alloy exhibited the lowest temperature coefficient of resistivity.
- Ru-rich needle shaped precipitates was observed in the β_2-RuAl phase in the cast $Ru_{46}Al_{35}Ni_{19}$ alloy after heat treatment. This phase undergoes precipitation hardening during annealing treatment.

Chapter-6

Results and discussion on Ru-Al-Co alloy system

6.1 Introduction

The partial isothermal section of Ru-Al-Co alloy system at 500 °C reported earlier [77] is shown in Figure 3.11. Two alloy compositions of Ru-Al-Co system, *viz.*, $Ru_{32.5}Al_{32.5}Co_{35}$ (point "1" in the Figure 3.11) and $Ru_{23.5}Al_{21.5}Co_{55}$ (point "2" in the Figure 3.11) were processed by powder metallurgy as well as by casting routes using the procedures outlined in chapter 3. $Ru_{32.5}Al_{32.5}Co_{35}$ falls in the two-phase ($\beta + \gamma$) region, and $Ru_{23.5}Al_{21.5}Co_{55}$ falls in the three-phase ($\alpha + \beta + \gamma$) region of Figure 3.11, respectively. A survey of the literatures shows that both these alloy compositions have not been investigated earlier and none of the Ru-Al-Co alloys have been processed by powder metallurgy route. The results of the microstructural investigations, hardness testing and electrical resistivity measurements of the alloys are presented in the following sub-sections.

6.2 Processing of $Ru_{23.5}Al_{21.5}Co_{55}$ alloy by powder metallurgy route

The elemental powder mixture of Ru + Al + Co corresponding to the composition $Ru_{23.5}Al_{21.5}Co_{55}$ was attrition milled for 50 hours. The XRD pattern and SEM micrographs of the powder mixture milled for 50 hours were studied and the results obtained are presented in the following sub-sections.

6.2.1 Milling characteristics

XRD pattern for the $Ru_{23.5}Al_{21.5}Co_{55}$ elemental powder mixture is shown in Figure 6.1. In the XRD pattern, the reflections from Co planes were not discernible in both starting (as-mixed) as well as 50 hours milled powder mixture. The as-received Co powder (Aldrich Chemical Company, Product No. 26664-7, purity 99.9+ %) did not show any XRD peaks, which might be due to the amorphous nature of the powder. The presence of Co in the powder mixture has however been confirmed from SEM-EDS studies detailed in the section 6.1.2. Reflections from Al plane could not be observed in the XRD pattern of the powder mixture obtained after 50 hours of milling. However,

there was evidence of broadening of Ru peaks after 50 hours of milling. Since the reflections from the planes of Co could not be obtained in the as-mixed powder and the earlier studies on Ru-Al-Ni showed the absence of reflections from Al planes after 10 hours of milling, no systematic study of the evolution of the mechanical alloying process was attempted in the Ru-Al-Co alloy system. Hence, XRD patterns obtained for as-mixed and powders milled for 50 hours are depicted in Figure 6.1.

In the starting powder mixture (as-mixed), the peak observed at 2θ value of 38.66° corresponds to overlapping reflections from Ru (100) and Al (111) planes. Similarly, the peak observed at 2θ value of 78.61° corresponds to overlapping reflections from Ru (103) and Al (311) planes. Reflections from Al planes were not discernible in the XRD pattern for the powder mixture milled for 50 hours. There was no evidence of any new phase formation in the XRD pattern milled for 50 hours. Since no new peaks were observed in the XRD pattern corresponding to the powder mixture milled for 50 hours, it can be presumed that there is no evidence of any new phase formation in the powders. However, broadening of the peaks indicative of crystallite size reduction and increase in micro-strain were evident in the XRD patterns of the milled powders. Analysis of the W-H plot shown in Figure 6.2 for the Ru peaks revealed that the Ru crystallite size was 75 nm and the strain induced in Ru crystallites was 0.00264 after 50 hours of milling.

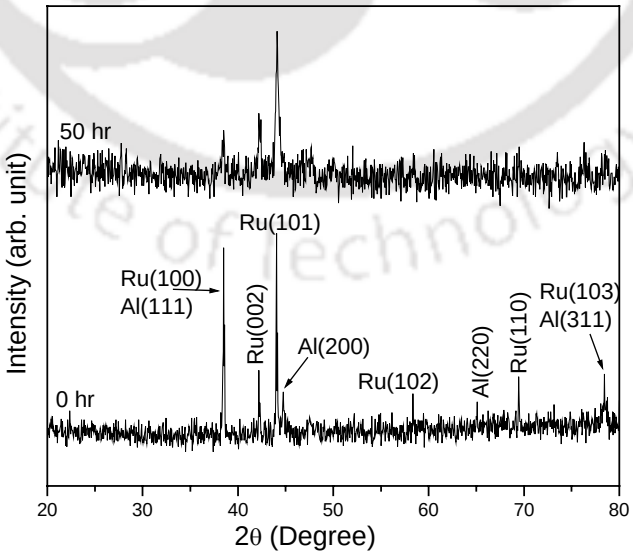

Figure 6.1: XRD pattern for as- milled $Ru_{23.5}Al_{21.5}Co_{55}$ elemental powder mixture

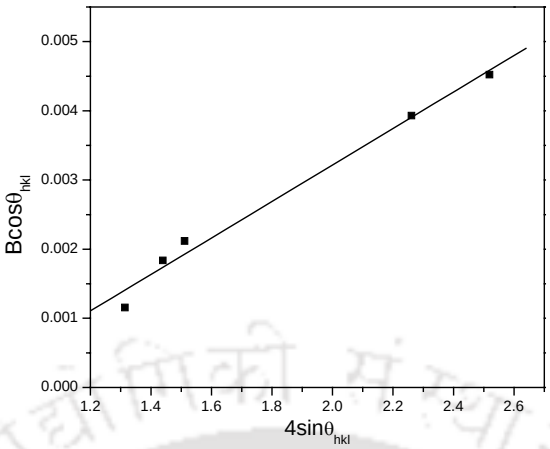

Figure 6.2: W-H plot corresponding to Ru in the $Ru_{23.5}Al_{21.5}Co_{55}$ powder mixture milled for 50 hours

6.2.2 Milled powder microstructure

SEM micrographs of as-milled $Ru_{23..5}Al_{21.5}Co_{55}$ powder mixture milled for 50 hours is shown in Figures 6.3 (a-b). Agglomerations of very fine powder particles were observed. The average size of the powder particles was less than 2 μm. The powder particles were mostly flaky in shape. The EDS analysis shown in Figure 6.3 (c) revealed an overall composition $Ru_{22}Al_{23}Co_{55}$ for the powder mixture.

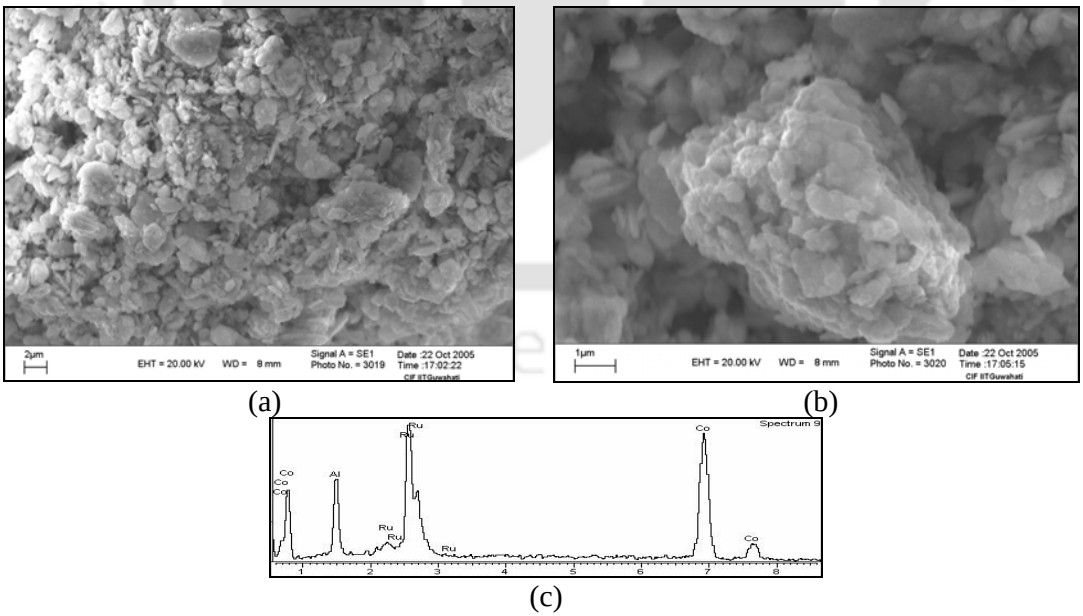

Figure 6.3: (a-b) SEM micrographs of as-milled $Ru_{23.5}Al_{21.5}Co_{55}$ powder mixture milled for 50 hours at low and high magnifications, respectively and (c) EDS spectrum corresponding to the overall composition of the powder mixture

6.2.3 Cold compaction

The $Ru_{23.5}Al_{21.5}Co_{55}$ powder mixture milled for 50 hours exhibited very poor adhesion even under a pressure of 500 MPa and hence could not be cold compacted. The green compacts exhibited very poor bonding and hence compacts could not be obtained. Hence sintering studies could not be carried out in this system.

6.3 Alloy processed by casting technique

$Ru_{23.5}Al_{21.5}Co_{55}$ alloy was prepared by arc melting high purity elemental powders in an arc-melting furnace. The structure, microstructure, microhardness and electrical resistivity of the cast $Ru_{23.5}Al_{21.5}Co_{55}$ alloy was investigated both in the as cast as well as annealed conditions. The results obtained are presented in the following sub-sections.

6.3.1 XRD analysis of cast $Ru_{23.5}Al_{21.5}Co_{55}$ alloy

XRD patterns for the both as-cast and cast and annealed $Ru_{23.5}Al_{21.5}Co_{55}$ alloy are shown in Figure 6.4. Reflections seen in the XRD pattern appear at 2θ values that are very close to the positions of the reflections from β_2-RuAl and hexagonal Co crystal. The lack of precise matching of the positions of the reflections suggests that these reflections are not from pure RuAl and Co crystal planes, but rather from RuAl-rich and Co-rich phases. On annealing at 900 ºC for 8 hours, one extra peak at 2θ value of 44.24 ° was seen in the XRD pattern for the annealed alloy. This peak is very close to the (111) reflection from hexagonal Co (PDF No. 1-1278). The reduction of peak width on annealing might have resolved this peak, which was overlapping with the RuAl peak in the cast sample. The presence of a β_2-phase of composition $Ru_{40}Al_{43}Co_{17}$ and a γ-phase of composition $Ru_{23}Al_{13}Co_{64}$ have been identified by EDS analyses in this alloy in support of these arguments.

6.3.2 SEM microstructural study of cast $Ru_{23.5}Al_{21.5}Co_{55}$ alloy

SEM micrographs shown in Figures 6.5 (a-b) reveal a dendritic structure in the as-cast $Ru_{23.5}Al_{21.5}Co_{55}$ alloy. The EDS spectrum for the overall composition of the alloy is given in Figure 6.5 (c). EDS analysis indicated an overall composition of $Ru_{25}Al_{21}Co_{54}$ for the alloy. Black spots seen in the SEM micrographs are micro-

porosities, which are uniformly distributed in the matrix. Concentration variation in the as-cast alloy is evident from the contrast in the backscattered SEM micrograph [*cf.* Figure 6.5 (a)]. Figure 6.5 (b) shows the microstructure at high magnification revealing two phases, one labelled as "C" and the other labelled as "A" and "B". The EDS spectra of these regions are shown in Figures 6.5 (d-e), respectively. The phase labelled as "C" was identified as β_2-phase of composition $Ru_{40}Al_{43}Co_{17}$. The regions "A" and "B" in spite of showing contrast differences were identified as γ-phase with an average composition of $Ru_{23}Al_{13}Co_{64}$.

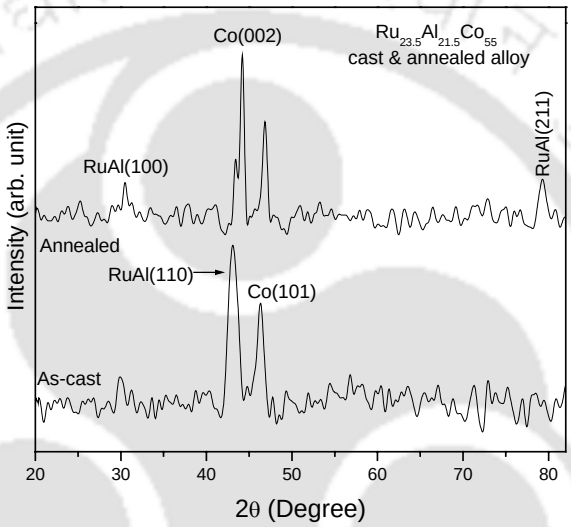

Figure 6.4: XRD pattern corresponding to the cast $Ru_{23.5}Al_{21.5}Co_{55}$ alloy in as-cast as well as annealed conditions

Figures 6.6 (a-b) show the microstructure of the cast $Ru_{23.5}Al_{21.5}Co_{55}$ alloy after annealing at 900 °C for 8 hours. The microstructural features of the annealed alloy were similar to the as-cast alloy, as evident from the low magnification SEM micrograph shown in Figure 6.6 (a). The EDS spectra for the two phases labelled as "C" and "B" as seen in Figure 6.6 (b) are given in Figures 6.6 (c-d), respectively. The regions "C" and "B" were identified as β_2-phase of composition $Ru_{41}Al_{40}Co_{19}$ and γ-phase of composition $Ru_{22}Al_{12}Co_{66}$, respectively. There was only a marginal variation in the composition of the two phases on annealing.

Discussion

The overall composition of the alloy falls within the three-phase [β {(Ru,Co)Al} + γ + α] field as shown in the ternary Ru-Al-Co partial isothermal section

at 550 °C [77]. XRD and SEM analyses of as cast structure of this alloy showed two phases, *viz.*, β-RuAl and γ. These phases had composition $Ru_{40}Al_{43}Co_{17}$ and $Ru_{23}Al_{13}Co_{64}$, respectively. On the other hand, the [Co] phase (α - phase) was not observed in SEM-EDS analysis. This indicates that the α-phase is not present in the isothermal section at 900 °C. This possibility cannot be ruled out since the extent of the α-phase in the isothermal section at 550 °C is very small. Only a marginal variation in the composition of the β and γ phases was observed on annealing at 900 °C. The low diffusion at 900 °C might have been the reason for this observation. β and γ phases of the annealed alloy are denoted by symbols β1and γ1, respectively and the overall composition with filled circle in the Figure 6.7.

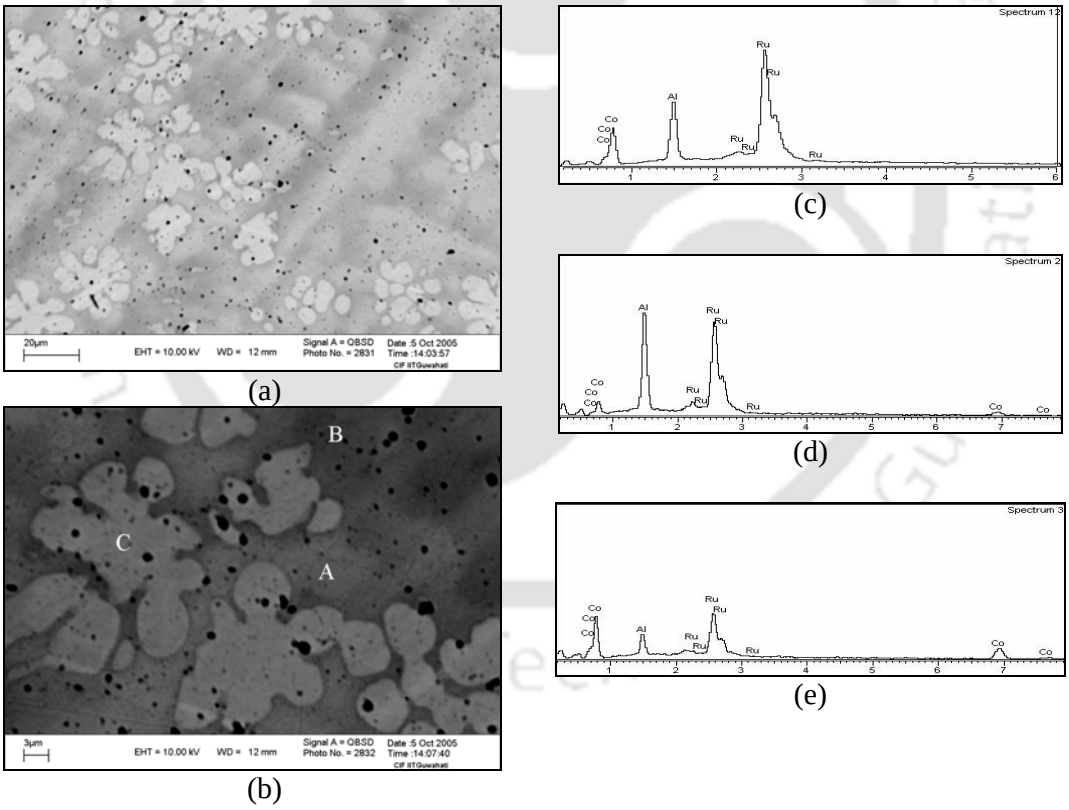

Figure 6.5: (a-b) SEM micrographs of the as-cast $Ru_{23.5}Al_{21.5}Co_{55}$ alloy at low and high magnification, respectively; EDS spectra corresponding to the (c) overall composition of the alloy, (d) region "C" and (e) regions "A" and "B" in (b)

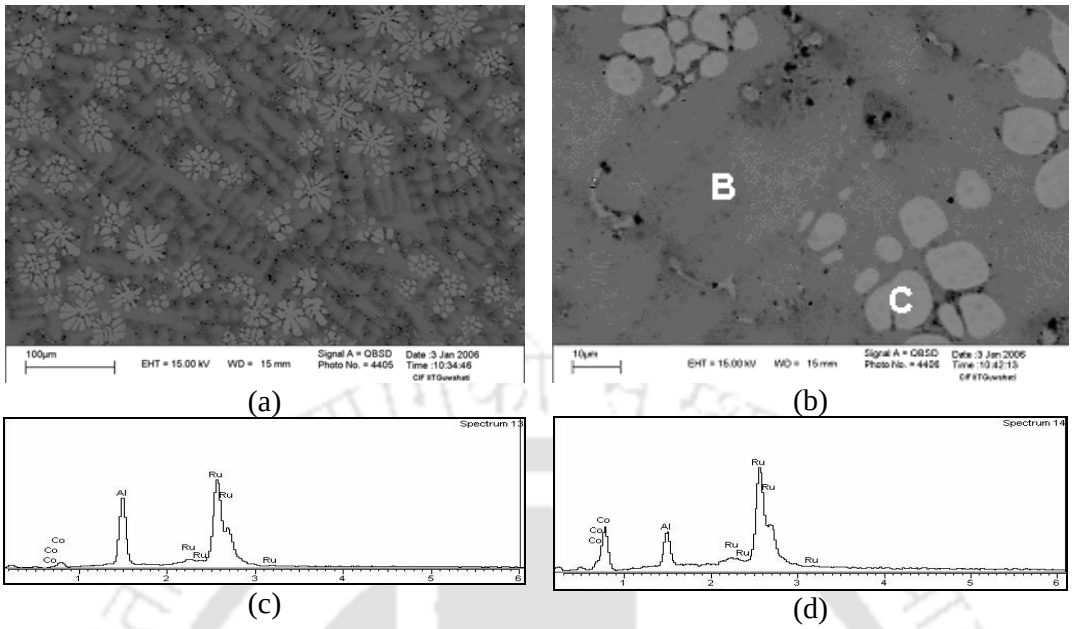

Figure 6.6: (a-b) SEM micrographs of the cast $Ru_{23.5}Al_{21.5}Co_{55}$ alloy annealed at 900 °C at low and high magnification, respectively; EDS spectra corresponding to the (c) region "C" and (d) region "B" in Figure 6.6 (b)

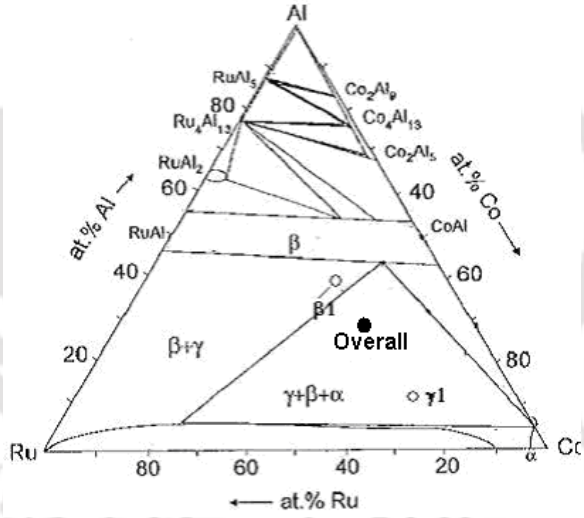

Figure 6.7: Partial isothermal section [77] showing positions the constituent phases and the overall composition of the annealed $Ru_{23.5}Al_{21.5}Co_{55}$ alloy

6.3.3 Hardness measurement of the cast $Ru_{23.5}Al_{21.5}Co_{55}$ alloy

The overall hardness values for as-cast and annealed $Ru_{23.5}Al_{21.5}Co_{55}$ alloy were determined to be 521 VHN and 533 VHN respectively. The average microhardness values for the regions "C" (β_2-phase) and "B" (γ-phase) [*cf.* Figure 6.6 (b)] determined

at a load of 100 gmf in the cast and annealed $Ru_{23.5}Al_{21.5}Co_{55}$ alloy sample were found to be 572 VHN and 512 VHN, respectively.

Since there is no report on the hardness of this alloy composition in the literature, no direct comparison is possible. The alloy exhibited a marginal increase in the overall hardness value after annealing treatment. EDS analysis showed Co-content increased in the two phases, *viz.*, β and γ respectively by 5 at.% and 11 at.% which might have resulted in the increase in the overall hardness of the alloy.

6.3.4 Electrical resistivity

Variation of electrical resistivity (ρ) of the cast and annealed $Ru_{23.5}Al_{21.5}Co_{55}$ alloy is shown in Figure 6.8. The electrical resistivity of the alloy exhibited a linear dependence on temperature up to 400 °C. Within this temperature range electrical resistivity increases from 91 μΩ-cm at room temperature to 106 μΩ-cm at 400 °C. At 600 °C, the recorded value of electrical resistivity was 162 μΩ-cm.

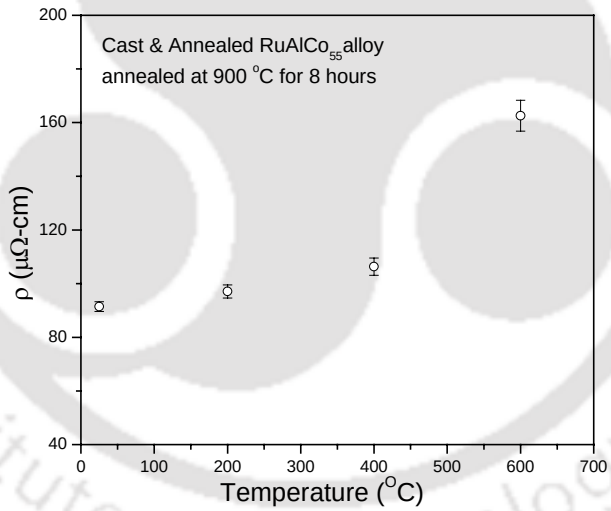

Figure 6.8: Plot of electrical resistivity with temperature for cast $Ru_{23.5}Al_{21.5}Co_{55}$ alloy annealed at 900 °C

6.4 Processing of $Ru_{32.5}Al_{32.5}Co_{35}$ alloy by powder metallurgy route

The elemental powder mixture of Ru + Al + Co corresponding to the composition of $Ru_{32.5}Al_{32.5}Co_{35}$ was attrition milled for 100 hours. The XRD pattern and SEM micrographs of the powder mixture milled for 100 hours were studied and the results obtained are presented in the following sub-sections.

6.4.1 Milling characteristics

Figure 6.9 shows the XRD pattern of the milled $Ru_{32.5}Al_{32.5}Co_{35}$ powder mixture. As observed in the milling of $Ru_{23.5}Al_{21.5}Co_{55}$ powder mixture, the XRD reflections from the Co planes were not observed in the starting powder mixture (as-mixed). Since there was no evidence of any new phase formation in the milling of $Ru_{23.5}Al_{21.5}Co_{55}$ powder mixture, this powder composition was milled up to 100 hours. In the XRD pattern of the as mixed powder, the peak observed at 2θ value of 38.66° corresponds to overlapping reflections from Ru (100) and Al (111) planes. Similarly, the peak observed at 2θ value of 78.61° corresponds to overlapping reflections from Ru (103) and Al (311) planes. Reflections from Al planes were not discernible in the XRD pattern of powder mixture milled for 100 hours. Since no new peaks were observed in the XRD pattern of powders milled for 100 hours, it can be presumed that there is no evidence of any new phase formation in the powders. However, broadening of the peaks indicative of crystallite size reduction and increase in micro-strain were evident in the XRD patterns of the milled powders. Analysis of the W-H plot shown in Figure 6.10 for the Ru peaks revealed that the Ru crystallite size was 27 nm and the micro-strain induced in Ru crystallites was 0.00405 after 100 hours of milling.

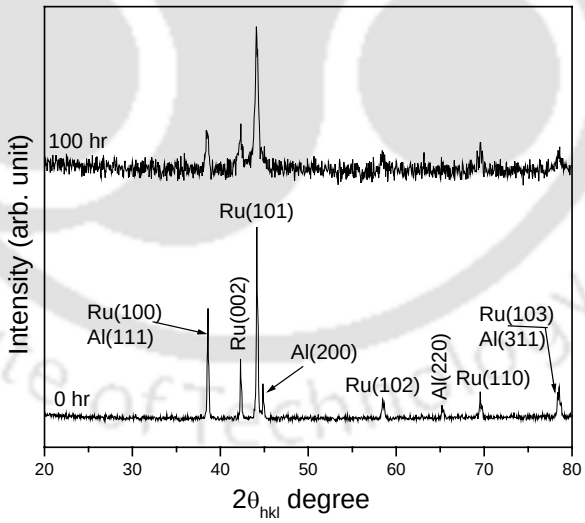

Figure 6.9: XRD patterns for the elemental powder mixture of composition $Ru_{32.5}Al_{32.5}Co_{35}$

6.4.2 Milled powder microstructure

SEM micrographs of $Ru_{32.5}Al_{32.5}Co_{35}$ powder mixture milled for 100 hours are shown in Figures 6.11 (a-b). The milled powder mixture consisted of aggregates of very fine particles. The sizes of the aggregates were in the range of 100 - 800 nm. The

surface feature of the milled powder was indicative of extensive plastic deformation and cold welding. EDS analyses revealed an overall composition of $Ru_{33}Al_{32}Co_{35}$ for the powder mixture and the composition of the powder agglomerate labelled as "A" in Figure 6.11 (a) as $Ru_{33}Al_{32}Co_{35}$. The EDS spectra for the overall composition and the composition of the powder agglomerate (region "A") are shown in Figures 6.11 (c-d), respectively.

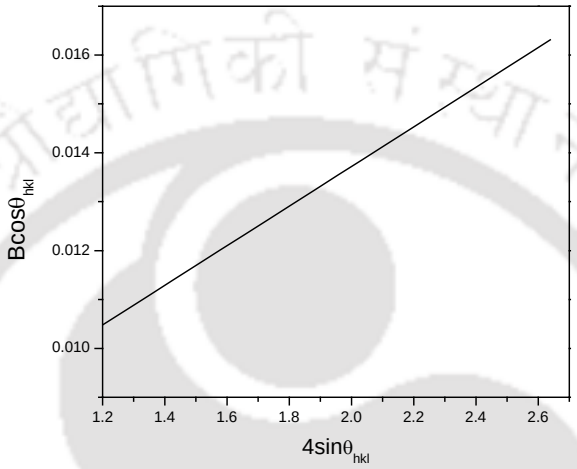

Figure 6.10: W-H plot corresponding to Ru in the $Ru_{32.5}Al_{32.5}Co_{35}$ powder mixture milled for 100 hours

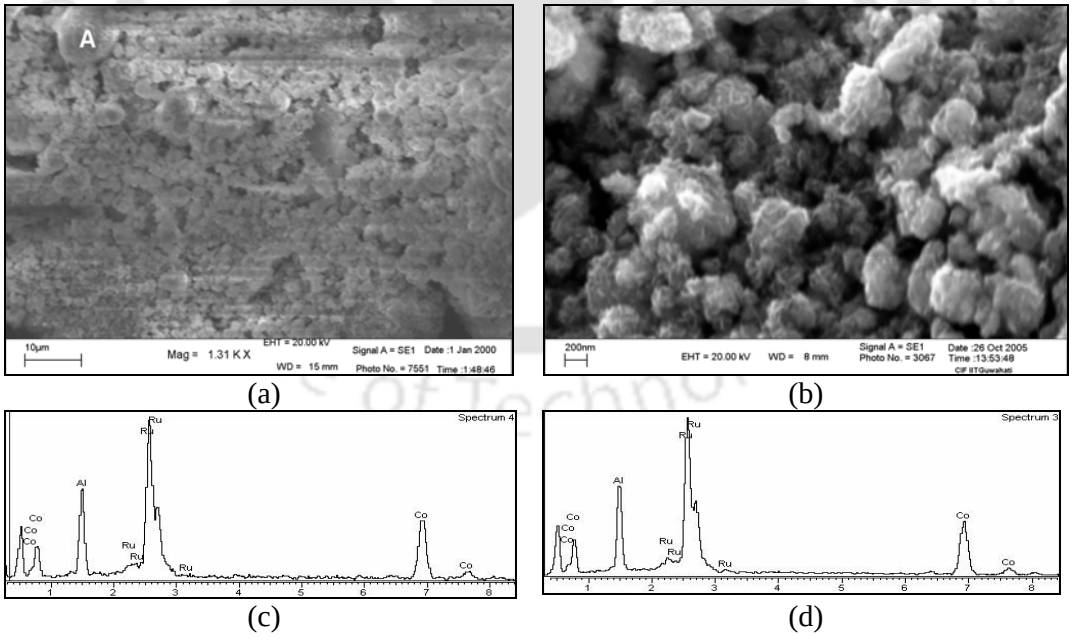

Figure 6.11: (a-b) SEM micrographs of $Ru_{32.5}Al_{32.5}Co_{35}$ powder mixture milled for 100 hours at low and high magnification, respectively; EDS spectra corresponding to the (c) overall composition (d) powder agglomerate labelled as "A" shown in Figure (a)

Discussion

The XRD pattern (*cf.* Figure 6.9) did not reveal any evidence of formation of any new phase for this powder mixture on milling up to 50 hours. In order to verify if further milling would help in crystallite size reduction amenable for alloying, milling was continued for 100 hours for this powder mixture. As compared to the $Ru_{23.5}Al_{21.5}Co_{55}$ powder composition (milled for 50 hours), Ru crystallite size of 27 nm was obtained in this powder mixture milled for 100 hours with no trace of alloying. Liu *et al.* [55] have reported the formation of (Ru,Ni)Al phase by mechanical alloying elemental powders. They reported an average crystallite size of ~ 10 nm in their milled powder mixture. Hence, it can be presumed that crystallite size ~ 10 nm is required for phase formation during milling, which could not be obtained in this system.

6.4.3 Cold compaction

The $Ru_{32.5}Al_{32.5}Co_{35}$ powder mixture milled for 100 hours exhibited very poor adhesion even under a pressure of 500 MPa and hence could not be cold compacted. Attempts to hot press the compacts failed mainly due to fusion of the powders with the die-and-punch assembly as a result of the exothermic reaction following the formation of RuAl above 700 °C. Hence cold compacts suitable for sintering work could not be prepared in this alloy system.

6.5 Alloy processed by casting technique

Structure, microstructure, microhardness and electrical resistivity of the cast $Ru_{32.5}Al_{32.5}Co_{35}$ alloy was investigated both in the as cast as well as annealed conditions. The results obtained are summarised in the following sub-sections.

6.5.1 XRD analysis of cast $Ru_{32.5}Al_{32.5}Co_{35}$ alloy

Figure 6.12 shows the XRD patterns for the $Ru_{32.5}Al_{32.5}Co_{35}$ alloy in as-cast and annealed conditions. There is not much variation in the XRD patterns obtained for both the as-cast as well as cast and annealed alloys. This shows that there is not much change in the structure of the alloy after annealing at 900 °C for 8 hours. XRD patterns revealed that the cast alloy consisted of RuAl and [Co] phases in both as-cast and annealed conditions. The presence of a β-phase of composition $Ru_{43}Al_{44}Co_{13}$ and γ-phase of composition $Ru_{21}Al_{11}Co_{68}$ have been identified by EDS analysis in this alloy.

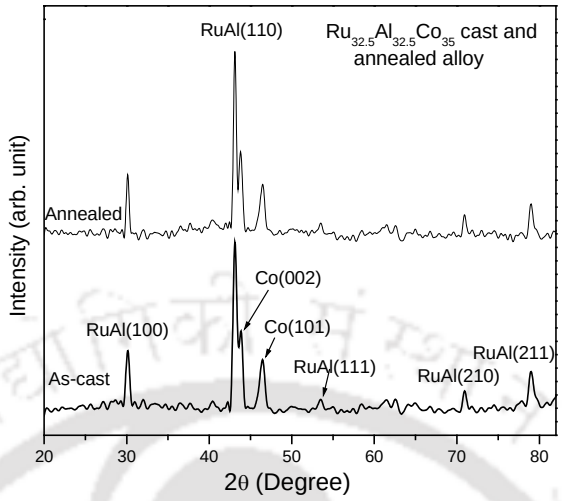

Figure 6.12: XRD patterns corresponding to the both as-cast as well as cast and annealed $Ru_{32.5}Al_{32.5}Co_{35}$ alloy

6.5.2 SEM microstructural study of cast $Ru_{32.5}Al_{32.5}Co_{35}$ alloy

SEM micrographs of the as-cast $Ru_{32.5}Al_{32.5}Co_{35}$ alloy shown in Figures 6.13 (a-b) revealed dendritic structure. The microstructure consists of two phases, labelled as "B" and "D" in Figure 6.13 (b). Very fine porosities labelled as "P" could also be observed. Figures 6.13 (c-e) show the EDS spectra corresponding to the overall composition of the alloy, the regions "B" and "D", respectively. EDS analysis revealed an overall composition of $Ru_{33}Al_{32}Co_{35}$ for the alloy. The regions "B" and "D" were identified as β-phase of composition $Ru_{43}Al_{44}Co_{13}$ and γ-phase of composition $Ru_{21}Al_{11}Co_{68}$, respectively.

Microstructure of $Ru_{32.5}Al_{32.5}Co_{35}$ cast alloy annealed at 900 ^{o}C for 8 hours is shown in Figures 6.14 (a-b). It can be seen that there are no marked differences in the microstructural features when compared to the as-cast case. However, small composition differences in the constituent phases were observed after heat-treatment. EDS spectra for the regions labelled as "B" and "D" in Figure 6.14 (b) are shown in Figures 6.14 (c-d), respectively. The average compositions of the regions "B" and "D" were determined as $Ru_{44}Al_{41}Co_{15}$ and $Ru_{24}Al_{10}Co_{66}$, respectively.

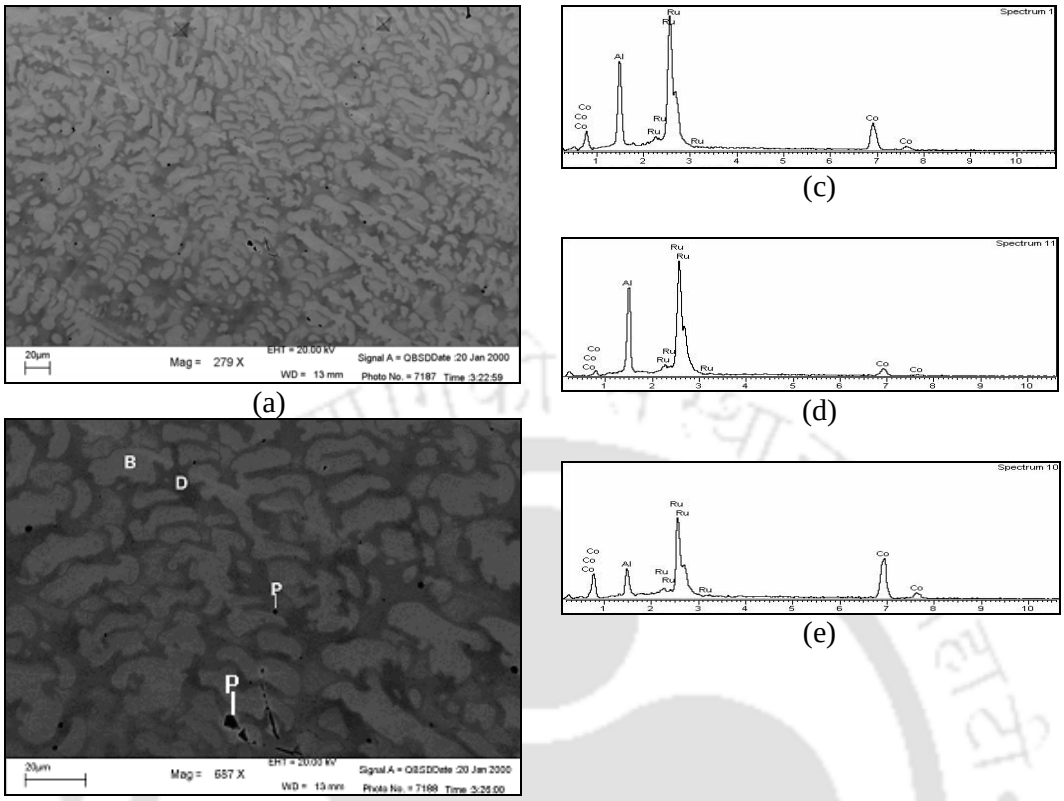

Figure 6.13: (a-b) Backscattered micrographs of as-cast $Ru_{32.5}Al_{32.5}Co_{35}$ alloy at low and high magnification, respectively; EDS spectra corresponding to the (c) overall composition, (d) region "B" and (e) region "D" in Figure 6.13 (b)

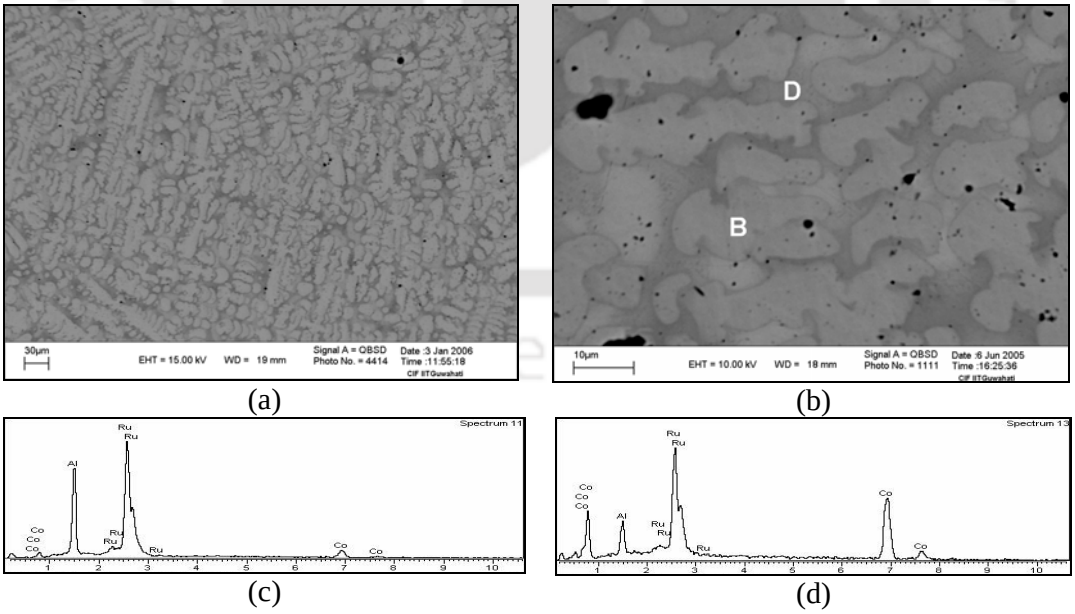

Figure 6.14: (a-b) SEM micrographs for the cast and annealed $Ru_{32.5}Al_{32.5}Co_{35}$ alloy at low and high magnification, respectively; EDS spectra corresponding to the (c) region "B" and (d) region "D"

Discussion

The overall composition of the alloy falls within the two-phase [β (Ru,Co)Al + γ] region of the Ru-Al-Co partial isothermal section at 550 °C [77]. Both XRD and SEM studies revealed that the as-cast alloy consisted of β-RuAl and [Co] phases. Non-equilibrium cooling during solidification in the arc-melting furnace could have resulted in the in the formation of two phases, *viz.*, β-RuAl [region "B" of composition $Ru_{43}Al_{44}Co_{13}$ in Figure 6.13 (b)] and Co-rich γ-phase [region "D" of composition $Ru_{21}Al_{11}Co_{68}$ in Figure 6.13 (b)]. Annealing at 900 °C resulted in 'β' ($Ru_{44}Al_{41}Co_{15}$) and 'γ' ($Ru_{24}Al_{10}Co_{66}$) phases with minor composition variations. Since the composition variation obtained from analysis of SEM-EDS spectra is very small (~ 1 at.%), it is not conclusive whether there is a change in the compositions of the phases on annealing.

6.5.3 Hardness measurement of cast $Ru_{32.5}Al_{32.5}Co_{35}$ alloy

The overall hardness values corresponding to the as-cast and cast and annealed $Ru_{32.5}Al_{32.5}Co_{35}$ alloys were determined to be 475 VHN and 479 VHN, respectively. Microhardness testing was carried out on the cast and annealed alloy using a load of 100 gmf. The microhardness values obtained for the β-phase and γ-phase of the annealed alloy were 560 VHN and 521 VHN, respectively. Microhardness testing of constituent phases of the as-cast alloy could not be carried out due to the poor visibility of the indentations. A marginal increase in the overall hardness was observed after annealing of the alloy. This marginal increase in the overall hardness on annealing suggests that the small variations observed in the compositions of the 'β' and 'γ' phases as indicated by SEM-EDS analyses may be correct.

Since there is no report on the hardness of this alloy composition in the literature, no direct comparison is possible with the above results. However, an overall hardness value of 385 ± 12 VHN and 428 ± 10 VHN were reported for as-cast $Ru_{20}Al_{50}Co_{30}$ and $Ru_{10}Al_{50}Co_{40}$ alloys, respectively [77]. In the present study, increase in the overall hardness in as-cast $Ru_{25}Al_{21}Co_{54}$ alloy (521 VHN) was observed as compared to the as-cast $Ru_{32.5}Al_{32.5}Co_{35}$ alloy (475 VHN). This observation is in good agreement with the reported linear increase in the overall hardness in the ternary Ru-Al-Co alloys with the increase in the Co-content [77].

A marginal increase in the microhardness value was observed in the γ-phase of the two cast and annealed alloys of overall compositions $Ru_{25}Al_{21}Co_{54}$ (512 VHN) and $Ru_{33}Al_{32}Co_{35}$ (521 VHN) in the present investigation. Since, similar compositions ($Ru_{22}Al_{12}Co_{66}$ and $Ru_{24}Al_{10}Co_{66}$) for the γ-phase in the two alloys were obtained, this marginal increase in the microhardness value is expected.

6.5.4 Electrical resistivity

Electrical resistivity (ρ) measurement on $Ru_{32.5}Al_{32.5}Co_{35}$ cast-and-annealed alloy indicated a resistivity of 74 μΩ-cm at room temperature, which increased to 186 μΩ-cm at 600 °C. Figure 6.15 shows a linear fit to the electrical resistivity vs. temperature up to 600 °C. Linear fit to the data yielded a temperature coefficient of resistivity (α) value of ~ 0.2 °C $^{-1}$.

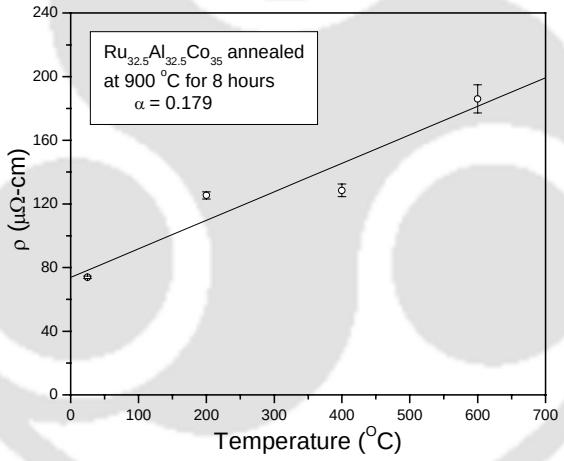

Figure 6.15: Plot of electrical resistivity with temperature of the cast and annealed $Ru_{32.5}Al_{32.5}Co_{35}$ alloy annealed at 900 °C

6.6 Summary and Conclusions

The conclusions drawn from the present investigations on Ru-Al-Co alloys are summarised below:

- Milling of both the Ru-Al-Co powder compositions, *viz.*, $Ru_{23.5}Al_{21.5}Co_{55}$ and $Ru_{32.5}Al_{32.5}Co_{55}$ did not result any new phase formation for milling up to 50 hours. Continued milling of the $Ru_{32.5}Al_{32.5}Co_{55}$ powder mixture up to 100

hours resulted in the reduction in the average crystallite size of Ru and an increase in the micro-strain in Ru as compared to the $Ru_{23.5}Al_{21.5}Co_{55}$ milled for 50 hours.

- Green compacts obtained from the milled Ru-Al-Co powder mixtures exhibited very poor adhesion between the powder grains.
- No marked difference in the microstructure of the cast Ru-Al-Co alloys after annealing at 900 ºC.
- An increase in the overall hardness values was observed in the Ru-Al-Co alloys with an increase in the Co-concentration.
- Ru-Al-Co alloys with higher Co content exhibited higher electrical resistivity.

Chapter-7

Conclusions and future scope of the work

7.1 Conclusions

Three Ru-Al alloy systems, *viz.*, Ru-Al, Ru-Al-Ni and Ru-Al-Co were processed by powder metallurgy as well as by casting techniques. Six alloy compositions belonging to these three alloy systems were processed and characterised. Of these, the ternary alloy compositions have not been investigated earlier. This work is the first attempt to process the above alloys by powder metallurgy as well as casting techniques, thereby providing a means to compare the properties of the alloys processed by both the routes. Hence, most part of the studies reported in this thesis on these alloy compositions are entirely new and correspond to the unreported results. It is worth mentioning that at present no information is available in the literature on sintering characteristics of the binary Ru-Al and ternary Ru-Al-X (X= Ni, Co) alloys processed from milled powder mixtures.

The salient results obtained in the course of the present investigations are summarised below:

- XRD patterns of as-milled powder mixture of composition $Ru_{47}Al_{53}$ revealed the formation of RuAl phase after 7 hours of milling. However, ternary alloy systems consisting of Ru-Al-Ni and Ru-Al-Co did not reveal any new binary or ternary phase formation up to 50 hours of milling under the same experimental conditions. Analysis of crystallite size reduction during the milling process leads to the conclusion that the crystallite sizes of the order of 10 nm are required for the formation of alloy phases. The inability to attain this critical size limit is expected to be the reason for the lack of alloy formation in the ternary powder mixtures.
- Average crystallite size of 17 nm was obtained for the RuAl phase during milling. Tailoring of the crystallite RuAl size up to 83 nm was possible with appropriate heat treatment.
- Microstructural study on the as-milled Ru-Al powder mixture revealed the formation of RuAl phase even after 2 hours of milling. Since the percentage of

alloy formed was less, it could not be detected by XRD. EDS analysis on the powders milled for 7 hours showed the formation of the RuAl phase (of composition $Ru_{48}Al_{52}$), a [Ru] phase (of composition $Ru_{95}Al_5$) and a metastable Ru_2Al phase (of composition $Ru_{67}Al_{33}$). Sintering of the cold compacted powder mixture led to elimination of the metastable phase and resulted in the RuAl phase (of composition $Ru_{56}Al_{44}$) and [Ru] phase (of composition $Ru_{95}Al_5$). Since the RuAl phase with composition $Ru_{56}Al_{44}$ has also been reported by other researchers as well, this confirms that the RuAl phase extends up to 56 at. % Ru in the binary Ru-Al phase diagram.

- Sintered Ru-Al powder compacts exhibited a low electrical resistivity value (83 μΩ-cm) at room temperature with a low temperature coefficient of resistivity (0.07 $°C^{-1}$). This alloy is a potential candidate for high temperature electrical contact application such as aircraft spark-plug electrode material.
- Microstructural observation of as-cast and heat-treated alloys revealed the presence of multiple phases together with porosities formed due to volatilisation of Al. Sintered alloy powder compacts showed better homogeneity and less Al loss. However, all the milled powders could not be cold compacted for sintering and the ones that could be cold compacted required to be sintered at higher temperatures and for longer time periods.
- In the cast and annealed Al rich alloys (RuAl, $Ru_{32}Al_{50}Ni_{18}$ and $Ru_{43}Al_{39}Ni_{18}$) a Ru-rich layer was observed around macro porosities. Aluminium diffusion into the free surface (porosity) from the surrounding matrix results in the formation of the Ru-rich layer in the region surrounding the porosity.
- Composition analysis of the $Ru_{46}Al_{35}Ni_{19}$ alloy annealed at 1450 °C indicated an expansion of the three-phase ($\gamma + \beta_2 + Ru$) region towards the two-phase ($\beta_2 + Ru$) region with reference to the isothermal phase diagram at 1250 °C. Similar analysis on the $Ru_{38.5}Al_{16.5}Ni_{45}$ alloy annealed at 1450 °C indicated expansion of the two-phase ($\gamma + Ru$) region towards the three-phase ($\gamma + \beta_2 + Ru$) as well as the γ-phase regions with reference to the isothermal phase diagram at 1250 °C.
- All the cast alloys exhibited higher overall hardness values in comparison to their milled and sintered counterparts.

- The overall hardness values of the Ru-Al-Ni and Ru-Al-Co cast alloys were higher than that of the binary Ru-Al alloy. Ni and Co additions to Ru-Al alloy resulted in an increase in the overall hardness as well as microhardness of the different constituent phases present in the cast alloys.
- Ru-rich needle shaped precipitates was observed in the cast Ru-Al and $Ru_{43}Al_{39}Ni_{18}$ alloys after heat treatment. This indicates the occurrence of precipitation hardening in Ru-Al and Ru-Al-Ni alloys, which results in the large increase in the overall hardness of the alloy.
- Additions of Ni and Co were found to increase the electrical resistivity in these alloys as compared to the binary Ru-Al alloy. Lower electrical resistivity was observed in mechanically alloyed and sintered Ru-Al-Ni samples as compared to the cast samples. Cast and annealed $Ru_{32}Al_{50}Ni_{18}$ alloy with a single-phase microstructure exhibited the lowest electrical resistivity among all the cast and annealed Ru-Ni-Al alloys.
- Alloys processed by powder metallurgy as well as casting routes showed variations in structure and microstructure. These variations resulted in pronounced differences in their physical properties as well. The above study provides a means to choose a more appropriate processing route for a particular application.

7.2 Future scope of the work

The results of the present study reveal lot of scopes for further studies in the binary Ru-Al, ternary Ru-Al-Ni and Ru-Al-Co alloy systems. A few of such areas in which further research can be carried out are mentioned below:

- The ruthenium rich end of the binary Ru-Al phase diagram (Ru content > 50 at.%) has not been explored in detail. A through investigation of this part of the phase diagram brings insight into the various properties and microstructure.
- Only a few binary and ternary alloy compositions of Ru-Al alloys have been studied by the powder metallurgy route. In-depth studies can be extended to explore the properties of the sintered alloys from the viewpoint of applications.
- The present studies revealed precipitation behavior in binary Ru-Al alloys having ruthenium content in the range of 55 at.% to 70 at.%. The precipitation hardening characteristics of these alloys, *viz.*, precipitation kinetics,

precipitation mechanisms, structure-property correlation during heat-treatment, etc. are required to be investigated in-depth.

- It would also be interesting to investigate the ternary isothermal sections of Ru-Al-Ni and Ru-Al-Co alloy systems at higher temperatures. Study of more alloy composition in those regions of the phase diagram can substantiate the work reported in the present study on the expansion of the phase regions of the isothermal phase diagrams at elevated temperatures.
- The present study can be extended to study the effects of higher sintering temperatures and time on the sintering characteristics and its effect on the microstructure and properties of the alloys.
- Hot pressing or hot isostatic pressing of the milled powders may lead to higher density compact with better mechanical properties. This prompts further research on the hot compatibility and sintering characteristics of binary and ternary alloys of Ru-Al, Ru-Al-Ni and Ru-Al-Co systems.
- There is a general lack of diffusion data on binary as well as ternary Ru-Al alloys. A rigorous investigation of the diffusion mechanism and diffusivity data is required for both experimental as well as computational research.

References

1. M.R. Winstone, Microstructure and alloy developments in nickel-based super alloys, in Microstructural stability of creep resistant alloys for high-temperature plant applications, edited by A. Stang *et al.*, London: IOM Communication, 1998, 27-47.
2. M. McLean, Nickel-base super alloys: current status and potential, High-Temperature Structural Materials, Editors- R.W. Cahn, A.G. Evans and M. McLean, Chapman and Hall (First Edition) 1996.
3. Carl H. Lund, The aging alloys have matured, in Processing and design issues in high temperature materials, Edited by N.S. Stoloff and R.H Jones, The Minerals, Metals and Materials Society, 1997, 91-105
4. F.M. Yang, X.F. Sun, H.R. Guan and Z.Q. Hu, High-Temperature low cycle fatigue behaviour of K40S cobalt-base superalloy, Metall. and Mater. Trans. A, Vol. 34 A (2003) 979.
5. Structure and Properties of Engineering Materials, edited by Daniel Henkel and Alan W. Pense, 5th edition-Boston: MGH (2002) 368-371.
6. N.S. Stoloff, "Wrought and P/M super alloys" in ASM Handbook, Vol. 1, "Properties and selection: Irons, Steels and High-Performance Alloys", Materials Park, OH, ASM International (1990) 950-980.
7. C.T Liu and J.O. Stiegler, "Ordered Intermetallics" in ASM Handbook, Vol. 2, "Properties and selection: Non-ferrous alloys and special purpose materials", Materials Park, OH, ASM International (1990) 913-942.
8. M. Yamaguchi, Overview, High temperature intermetallics-with particular emphasis on TiAl, Mater. Sci. Tech. Vol. 8 (1992) 299-307.
9. R.L Fleischer, Review- High-Strength, high-temperature intermetallic compounds, Journal of Materials Sci. 22 (1987) 2281-2288.
10. S. Djanarthany, J. C. Viala and J. Bouix, Review, An overview of monolithic titanium alumides bases on Ti_3Al and TiAl, Materials chemistry and physics 72 (2001) 301-319.

11. G. Sauthoff, “Structure and properties of nonferrous alloys” in Materials science and technology, Edited by R.W Cahn, P. Haasen and E.J. Kramer, Vol. 8, VCH New York (1996).
12. Shigehisa Naka, Advanced titanium-based alloys, Current opinion in solid state & materials science 1 (1996) 333-337
13. S. Kerry and M.R. Winstone, Creep behaviour Ti3Al-based titanium aluminide containing molybdenum, Mater. Sci. & Engg. A 192/193 (1995) 856-861
14. F. Appel, M. Oehring and R. Wagner, Novel design concepts for gamma-base titanium aluminide alloys , *Intermetallics, Volume 8, Issues 9-11, September 2000, Pages 1283-1312*
15. M. Yamaguchi, H. Inui and K. Ito, High-temperature structural intermetallics, Acta mater. 48 (2000) 307-322.
16. C. Colinet and A. Pasturel, Ab initio calculation of the formation energies of $L1_2$, $D0_{22}$, $D0_{23}$ and one dimensional long period structures in $TiAl_3$ compound, Intermetallics 10 (2002) 751-764.
17. D.B. Miracle, Overview: The physical and mechanical properties of NiAl, Acta Metall. Mater. Vol. 41 (1993) 649-684
18. R.W. Cahn, Multiphase intermetallics, in High-temperature structural materials, edited by R.W. Cahn, A.G. Evans and M. McLean, Chapman & Hall, First edition (1996) p 81 (79-90).
19. D. Golberg, M. Demura and T. Hirano, Effect of Al-rich off-stoichiometry on the yield stress of binary Ni_3Al single crystals, Acta mater. Vol. 46, No. 8 (1998) 2695-2703.
20. S. Naka, M. Thomas and T. Khan, Potential and prospects of some intermetallic compounds for structural applications, Material science and technology, Vol. 8 (1992) 291-298.
21. S. Hanada, S. Watanabe, W.Y. Kim, N. Masahashi ans M.S. Kim, Microstructure control and ductility in Ni_3Al polycrystals, Mater. Sci. Engg. A 239-240 (1997) 309-316.

22. C.T. Liu, Recent advanced in ordered intermetallics, Materials Chemistry and Physics 42 (1995) 77-86.
23. C.B. Jiang, Hong Li, J. Tan, S.D. Wu, L.J. Rong, S. Patu, A dramatic decrease of the dislocation velocity in Ni_3Al single crystals under the influence of hydrogen, Intermetallics 9 (2001) 355-360.
24. R.D. Noebe, R.R. Bowman and M.V. Nathal, Physical and mechanical properties of the B2 compound NiAl, Int. Mater. Review, Vol. 38, No. 4 (1993) 193-232.
25. M.R. Harmouche and A. Wolfenden, Temperature and composition dependence of Young's modulus in polycrystalline B2 NiAl, Journal of Testing and Evaluation, JTEVA, Vol. 15, No. 2 (1987) 101-104.
26. Yoshihiro Terada, Kenji Ohkubo, Kiyotaka Nakagawa, Tetsuo Mohri and Tomoo Suzuki, Thermal conductivity of B2-type aluminides and titanides, Intermetallics 3 (1995) 341-355.
27. C.Y. Cui, J.T. Guo, Y.H. Qi and H.Q. Ye, High tensile elongation of a directionally solidified NiAl multiphase alloy at high temperatures, Mater. Sci. Engg. A 396 (20015) 194-201.
28. Y.L. Wang, R.E. Smallman, I.P. Jones, Effect of ternary iron addition on the creep behaviour of NiAl, Materials Science and Engineering A329–331 (2002) 847–851.
29. I. Baker and P.R. Munroe, Mechanical properties of FeAl, Int. Mater. Rev., Vol. 42, No. 5 (1997) 181-205.
30. S. Gedevanishvili and S.C. Deevi, Processing of iron aluminide by pressure less sintering through Fe + Al elemental route, Mater. Sci. Engg. A 325 (2002) 163–176.
31. J.L. Jordan and S. C. Deevi, Review vacancy formation and effects in FeAl, Intermetallics 11 (2003) 507-528.
32. C.T. Liu, E.P. George, P.J. Maziasz and J.H. Schneibel, Recent advances in B2 iron aluminide alloys: deformation, fracture and alloy design, Mater. Sci. Engg. A 258 (1998) 84-98.

33. D.G. Morris and M.A. Morris-Muñoz, The influence of microstructure on the ductility of iron aluminides, Intermetallics 7 (1999) 1121-1129.
34. David G. Morris, Maria A. Muñoz-Morris and Jesus Chao, Development of high strength, high ductility and high creep resistant iron aluminide, Intermetallics 12 (2004) 821–826.
35. M. Salazar, A. Albiter, G. Rosas and R. Pérez, Structural and mechanical properties of AlFe intermetallic alloy, Materials Science and Engineering A351 (2003) 154-159.
36. Marian Kupka, Temperature dependence of the yield stress of an FeAl base alloy, Materials Science and Engineering A336 (2002) 320–322.
37. S.C. Sundar and S.C. Deevi, High-temperature strength and creep resistance of FeAl, Materials Science and Engineering A357 (2003) 124-133.
38. C. Zanotti, P. Giuliani and F. Maglia, Combustion synthesis of Co–Al and Ni–Al systems under reduced gravity, Intermetallics 14 (2006) 213–219.
39. Ryusuke Nakamura and Yoshiaki Iijima, Self-diffusion of cobalt in B2 type intermetallic compound CoAl, Intermetallics 13 (2005) 163–167.
40. Yoshisato Kimura, Masaru Takahashi, Hideki Hosoda, Seiji Miura and Yoshinao Mishima, Compressive mechanical properties of multi-phase alloys based on B2 CoAl and $E2_1$ Co_3AlC, Intermetallics 8 (2000) 749-757.
41. Yoshisato Kimura, Yoshinao Mishima and C.T. Liu, Microstructure control and tensile properties of three-phase alloys based on the E21 Co3 AlC and B2 CoAl, Intermetallics 9 (2001)1069-1078.
42. Yoshinao Mishima, Masaharu Kato, Yoshisato Kimura, Hideki Hosoda and Seiji Miura, Improvement in room temperature ductility of intermetallic alloys through microstructural control, Intermetallics 4 (1996) S171-S179.
43. S. Mi, B. Grushko, C. Dong and K. Urban, A study of the ternary phase diagrams of Al–Co with Cu, Ag and Au, Journal of Alloys and Compounds 354, (2003),148-152.
44. I.M. Wolff, Toward a Better Understanding of Ruthenium Aluminide, JOM, January, (1997), 34-39.

45. R.L. Fleischer, R.D. Field and C.L. Briant, Mechanical Properties of High Temperature Alloys of RuAl, Metall. Trans. A, Vol. 22A (1991) 404-414.
46. R.L. Fleischer and D.W. McKee, Mechanical and oxidation properties of RuAl based high temperature alloys, Metall. Trans. A, Vol. 24A (1993) 769-763.
47. I.M. Wolff, G. Sauthoff, L.A. Cornish, H. DeV. Steyn and R. Coetzee, Structure-property-application relationship in ruthenium aluminide RuAl, Structural Intermetallics, Edited by M.V. Nathal, R. darolia, C.T. Liu, P.L. martin, D.B. Miracle, R. Wagner, M. Yamaguchi, The Minerals, Metals and Materials Society (1997) 815-823.
48. F. Mucklich and N. Ilic, RuAl and its alloys. Part I. Structure, physical properties, microstructure and processing, Intermetallics 13 (2005) 5-21.
49. W. Lin, Jian-hua Xu and A.J. Freeman, Cohesive properties, electronic structure, and bonding characteristics of RuAl – A comparison to NiAl, Journal of Mater. Res., Vol. 7, No. 3, (1992), 592-604.
50. R.L. Fleischer, Substitutional solutes in AlRu-I. Effects of solute on moduli, lattice parameters and vacancy production, Acta Metall. Mater., Vol. 41, No 3 (1993) 863-869.
51. H.A. Gobran, K.W. Liu, D. Heger and F. Mucklich, Investigation on point defect in single-phase B2 type RuAl alloys by lattice parameter measurements, Scripta Mater. 49 (2003) 1097-1102.
52. S. Chakravorty and D.R.F. West, Phase equilibria between NiAl and RuAl in the Ni-Al-Ru system, Scripta Metall., Vol. 19 (1985) 1355-1360.
53. S. Chakravorty and D.R.F. West, The constitution of Ni-Al-Ru system, J. of Mater. Sci., 21 (1986) 2721-2730.
54. I.J. Horner, N. Hall, L.A. Cornish, M.J. Witcomb, M.B. Cortie and T.D. Boniface, An investigation of the B2 phase between AlRu and AlNi in the Al–Ni–Ru ternary system, Journal of Alloys and Compounds 264 (1998) 173–179.
55. K.W. Liu, F. Mucklich, W. Pitschke, R. Barringer and K. Wetzig, Formation of nanocrystalline B2 structured (Ru, Ni)Al in the ternary system by mechanical alloying and its thermal stability, Mater. Sci. Engg A313 (2001) 178-197.

56. Pablo Gargano, Hugo Mosca, Guillermo Bozzolo and Ronald D. Noebe, Atomistic modeling of RuAl and (RuNi)Al alloys, Scripta Materialia 48 (2003) 695-700.
57. P.J. Hill, L.A. Cornish and M.L. Witcomb, Constitution of the Al-Ir-Ru system, Journal of Alloys and Compounds 291 (1999) 130–144.
58. J. Hohls, P.J. Hill, and I.M. Wolff, Hardness behaviour in B2 pseudo-binary systems, Materials Sci. Engg. A329–331 (2002) 504–512.
59. S. Mi and B. Grushko, Investigation of the high-Al region of Al-Cu-Ru, Intermetallics 12 (2004) 425-435.
60. B. Massalski (ed.), Binary Alloy Phase Diagrams, ASM International, USA, 2nd edition (1990) p. 204.
61. T.D. Boniface and L.A. Cornish, Investigation of the aluminium-ruthenium phase diagram above 25 at.% ruthenium, J. of alloys and compounds 234 (1996) 275-279.
62. S.N. Prins, L.A. Cornish, W.E. Stumpf and B. Sundman, Thermodynamic assessment of Al-Ru system, Calphad, Vol. 27, No. 1 (2003) 79-90.
63. N. Ilic´, R. Rein, M. Göken, M. Kempf, F. Soldera, F. Mücklich, Properties of eutectic Ru–Al alloy produced by ingot metallurgy. Mater. Sci. Engg. A 329-331 (2202) 38-44.
64. S. Mi, S. Balanetskyy and B. Grushko, A study of A-rich part of the Al-Ru alloy system, Intermetallics 11 (2003) 643-649.
65. E.G. Smith and C.I. Lang, High Temperature Resistivity and Thermo-EMF of RuAl, Scripta Mater., Vol. 33, No. 8 (1995) 1225-1229.
66. S.A. Anderson and C.I. Lang, Thermal conductivity of ruthenium aluminide (RuAl), Scripta Mater., Vol. 38, No. 3 (1998) 493-497.
67. B. Tryon, T.M. Pollock, M.F.X. Gigliotti and K. Hemker, Thermal expansion behaviour of ruthenium aluminides, Scripta Mater. 50 (2004) 845-848.
68. I.M. Wolff and G. Sauthoff, High-temperature behaviour of precious metal base composites, Metall. Mater. Trans. A, Vol. 27A (1996) 2642-2652.
69. R.L. Fleischer, statistics of solubilities of ternary elements in intermetallic compounds, Journal of Mater. Sci. Letters 7 (1988) 525-526.

70. R.L. Fleischer, Substitutional solutes in AlRu-II. Hardening and correlations with defect structure, Acta Metall. Mater., Vol. 41, No 4 (1993) 1197-1205.
71. R.L. Fleischer, Boron and off-stoichiometry effects on the strength and ductility of AlRu, Metall. Trans. A, Vol. 24A, (1993), 227-230.
72. R.L. Fleischer, The distribution of boron in AlRu: Effect on ductility and toughness, Acta Mater., 53 (2005) 2623-2627.
73. I.M. Wolff and G. Sauthoff, Mechanical properties of Ru-Al-Ni alloys, Metall. Mater. Trans. A, Vol. 27A (1996) 1395-1400.
74. B. Tryon and T.M. Pollock, Experimental assessment of the Ru-Al-Ni ternary phase diagram at 1000 °C and 1100 °C, Mater. Sci. and Engg. A, Vol. 430 (2006) 266-276.
75. M.S.A. Karunaratne and R.C. Reed, Interdiffusion of the platinum-group metals in nickel at elevated temperatures, Acta Materialia 51 (2003) 2905–2919.
76. A. Khataee, H.M. Flower and D.R.F West, Constitution of Ti-Al-Ru system, Mater. Sci. Tech., 5 (1989) 632-643.
77. I.M. Wolff and G. Sauthoff, Role of an intergranular phase in RuAl with substitutional additions, Acta Mater. Vol. 45, No.7 (1997) 2949-2969.
78. T.D. Reynolds and D.R. Johnson, Microstructure and Mechanical Properties of Ru-Al-Mo Alloys, Intermetallics 12 (2004) 157-164.
79. K. Eow, D. Lu and T.M. Pollock, Rate sensitivities for low temperature deformation in ruthenium aluminide alloys, Scripta Mater., Vol. 38, No. 7 (1998) 1065-1069.
80. D.C. Lu and T.M. Pollock, Low temperature deformation and dislocation substructure of ruthenium aluminide polycrystals, Acta Mater., Vol. 47, No. 3 (1999) 1035-1042.
81. T.M. Pollock, D.C. Lu, X. Shi and K. Eow, A comparative analysis of low temperature deformation in B2 aluminides, Materials Sci. Engg. A317 (2001) 241-248.
82. T.K. Nandy, Q. Feng and T.M. Pollock, Deformation of a platinum-containing RuAl intermetallic by $<111>$ dislocations, Scripta Mater., 48 (2003) 1087-1092.

83. T.K. Nandy, Q. Feng and T.M. Pollock, Elevated temperature deformation and dynamic aging in polycrystalline RuAl alloys, Intermetallics 11 (2003) 1029-1038.
84. Q. Feng, T.K. Nandy, B. Tryon and T.M. Pollock, Deformation of Ru-Al-Ta ternary alloys, Intermetallics 12 (2004) 755-762.
85. Anil Borah, P.S. Robi, A. Srinivasan, Ajit L. Mujumdar, Processing and characterization of ruthenium aluminide alloys by powder metallurgy and solidification techniques, International Conference on Powder Metallurgy at IIT Bombay, February 2005.
86. I.M. Wolff, Synthesis of RuAl by Reactive Powder Processing, Metall. Mater. Trans. A, Vol. 27A (1996) 3688-3699.
87. H.A. Gobran, N. Ilic, F. Mucklich, Effects of particle size and pressure on the reactive sintering of RuAl intermetallic compound, Intermetallics 12 (2004) 555-562.
88. M.B. Cortie and T.D. Boniface, Synthesis and Processing of Ruthenium Aluminide, Journal of Mater. Synthesis and Processing, Vol. 4, No. 6 (1996) 413-428.
89. L. Lu and M.O. Lai, Mechanical Alloying, Kluwer Academic Publishers, (1997), London, 204.
90. E. Hellstern, H.J. Fecht, Z. Fu and W.L. Johnson, Structural and thermodynamic properties of heavily mechanically deformed Ru and AlRu, Journal of Applied Physics, 65 (1) (1989) 305-310.
91. K.W. Liu, F. Mucklich and R. Birringer, Synthesis of nano RuAl by Mechanical Alloying, Intermetallics 9 (2001) 81-88.
92. K.W. Liu and F. Mucklich, Synthesis and Thermal Stability of nano-RuAl by Mechanical Alloying, Mater. Sci. and Engg. A329-331 (2002) 112-117.
93. K.W. Liu and F. Mucklich, Thermal stability of nano-RuAl produced by mechanical alloying, Acta Mater. Vol. 49 (2001) 395-403.
94. K.W. Liu and F. Mucklich, Synthesis of RuAl/ZrO_2 nanocomposite by mechanical alloying and subsequent annealing, Scripta Mater., 49 (2003) 207-212.

95. Yu Rosenberg, V. Sh Machavariani, A. Voronel, S. Garber and A. Rubshtein, Strain energy density in the x-ray powder diffraction from mixed crystal and alloys, J. Phys: Condens. Matter 12 (2000) 8081-8088.
96. B.D. Cullity, Elements of X-ray diffraction, Addition-Wesley publishing company, Second edition (1978), 284.
97. L.J. van der Pauw, A Method of Measuring Specific Resistivity and Hall Effects of Discs of Arbitrary Shape, Philips Res.Repts.,13 (1958)1-9.
98. Low Level Measurements Hand Book, 6th Edition, Keithley Instruments, Inc., Section-4, 26-31.

.

List of Publications from the Present Work

1. Anil Borah, A. Srinivasan, P. S. Robi and P. K. Gudla, Processing of Ru-Al alloys by Mechanical Alloying, Proceedings of the National Conference on Recent Advances in Materials Processing (RAMP), September 7-8, 2001, Page 335-341, Annamalai University, Tamil Nadu.
2. Anil Borah, P. P. Singha, P. S. Robi and A. Srinivasan, Powder Metallurgy Processing of Ruthenium Aluminium Alloys, Journal of Materials Processing Technology, 153-154 (2004), page 952-957.
3. Anil Borah, P. P. Singha, P. S. Robi and A. Srinivasan, Powder Metallurgy Processing of Ruthenium Aluminium Alloys, Proceedings of the International Conference on Advances in Materials and Processing Technologies 2003, Dublin City University, Ireland, 8-11 July, 2003, Page 1234-1237.
4. Anil Borah, A. L. Mujumdar, P. S. Robi and A. Srinivasan, Processing and characterization of Ruthenium Aluminide alloys by Powder Metallurgy and Solidification Techniques, International Conference on Powder Metallurgy at IIT Bombay, February 2005. (Adjudged as best paper).
5. Anil Borah, A. L. Mujumdar, P. S. Robi and A. Srinivasan, Processing and Characterisation of Ruthenium Aluminide Alloys by Powder Metallurgy and Solidification Techniques, Transactions of Powder Metallurgy Association of India, Vol. 31, 2005, Page 01- 06.